THE UNIVERSITY *of* EDINBURGH

CO_2 Reduction via Photo- and Photo-Thermo Coupled Heterogeneous Catalytic Reaction

Ke Wang

THE UNIVERSITY *of* EDINBURGH

Thesis submitted for the degree of
Doctor of Philosophy

The University of Edinburgh

2021

CO_2 Reduction via Photo- and Photo-Thermo Coupled Heterogeneous Catalytic Reaction

By

Ke Wang

Supervised by

Prof. Xianfeng Fan (Principal, The University of Edinburgh)

Dr. Cher Hon Lau (Assistant, The University of Edinburgh)

Prof. Ying Zheng (Assistant, Western University)

Declaration

Hereby, I declare that all the experiments and simulations in this thesis have been solely performed and written by myself. The helps and contributions of others have been clearly indicated and acknowledged. This work has not been submitted for any other degree or qualification in this or any other institution or university.

Ke Wang

August 2021

Abstract

CO_2 has been seen as a green-house gas mainly responsible for the global climate change. According to National Oceanic and Atmospheric Administration (NOAA), CO_2 emission since 1980 contributes to half of the CO_2 increases in the last 300 years and 25% of the CO_2 concentration rise is attributed to the emission since 2000. The CO_2 concentration is increasing faster than ever now. Instant and effective actions are urgently required to curb the trend in order to constrain the global temperature increase lower than 1.5 °C. Besides CO_2 capture and storage, CO_2 catalytic conversion to value-added chemicals is another important strategy to reduce its concentration in the atmosphere.

Solar light is one of the massive and widespread sustainable energy sources on the Earth. Using solar energy to drive CO_2 reduction is a promising and green way to reduce CO_2 concentration in atmosphere. The main challenges in practical implementation of the CO_2 conversion in large-scale are the relatively slow reaction rates and poor selectivity to more valuable products. The key to address these issues relies on better understanding of the reaction and photoexcitation mechanisms. This thesis focuses on building the correlation between the microstructure of catalysts, light induced excitation, reaction pathway, product selectivity and reaction rate.

The research work presented in this thesis starts from investigating the CO_2 photocatalytic reduction with H_2O over g-C_3N_4 (Chapter 3). A comprehensive optimisation of molecular and electronic structure of pristine g-C_3N_4 is conducted. The designed modification of co-doped K, B and N Vacancy (N_V) enhances light absorption, excited-electron/hole separation, CO_2 adsorption, therefore the overall significantly increases the photocatalytic CO and CH_4 production rate by 527% and 161% comparing with the pristine g-C_3N_4. The reaction mechanism has been investigated via *in-situ* DRIFTS. An important correlation is found between activated CO_2* concentration on catalyst surface

and reaction rate. The enhanced capability to activate the adsorbed CO_2* is the key guidance for future photocatalysts design.

Most of the current CO_2 photocatalytic reduction with H_2O can only produce CH_4 and CO. Therefore, Chapter 4 focuses on how to promote higher hydrocarbon production via CO_2 photocatalytic reduction with H_2O over Au/TiO_{2-x} with abundant oxygen vacancies (V_O). The reaction performances are compared under UV and green light irradiation conditions. The UV light-driven CO_2 reduction shows primary product of CO; by comparison, the green light-driven CO_2 reduction produces 20% C_2H_6 and 80% CH_4. The electronic structure and microstructure of Au/TiO_{2-x} are investigated by a series of *in-situ* spectroscopy methods. The involvement of V_O is found indispensable for this reaction. The different product selectivity under ultraviolet (UV) or green light irradiation is derived from the different excitation mechanism. The UV light bandgap excitation induces negatively charged Au that retards CO* adsorption; on the contrary, the green light plasmonic excitation causes positively charged Au that stabilises CO* adsorption. The stability of CO* key reaction intermediate is essential for higher hydrocarbon production.

The two chapters mentioned above have demonstrated the feasibility to significantly improve the photocatalytic CO_2 reduction rate by optimising the catalysts. However, the photocatalytic reaction rate is still far from comparable with traditional thermocatalytic CO_2 reduction. The H_2O has been proven as a less effective proton donor in Chapter 4 and the role of H_2O needs further investigations. Therefore, in the Chapter 5 & 6, CO_2 hydrogenation to CO, known as the reversed water gas shift reaction (RWGS reaction), is investigated under photo-thermo coupled catalytic reaction condition. The external light promoted thermocatalytic RWGS reaction performances are compared over two typical catalysts: Au/TiO_2 and $Au/\gamma\text{-}Al_2O_3$. The reducible TiO_2 and non-reducible $\gamma\text{-}Al_2O_3$ supports are fundamentally different on whether the plasmonic hot electrons transfer to the support. The CO_2 reduction rates are found significantly higher over Au/TiO_2 than Au/Al_2O_3 on either pure thermocatalytic or photo-thermo coupled catalytic reaction conditions.

Moreover, the plasmonic enhancement efficiency is also superior on Au/TiO_2 over Au/Al_2O_3.

In Chapter 5 & 6, the RWGS reaction mechanism in dark and photo-thermo coupled conditions are investigated via a series of *in-situ* spectroscopy and isotope kinetic analyses. The plasmonic enhancement mechanisms are also investigated via both experimental and theoretical approaches. The reaction mechanisms are proven to be quite different over Au/TiO_2 and Au/Al_2O_3. RWGS reaction follows a redox pathway with CO_2 self-dissociation at the V_O site of Au/TiO_2. By comparison, the RWGS reaction mechanism over Au/Al_2O_3 is a mixture of formate and carboxyl reaction pathways. Accordingly, the plasmonic enhancement mechanisms are different too. In the case of Au/TiO_2, plasmonic hot electrons mainly facilitate the V_O generation; while on Au/Al_2O_3, the formate pathway, especially the formate in bridged configuration, is preferentially promoted by plasmonic excitations.

Overall, this thesis has expanded and deepened the understandings of the photocatalytic and photo-thermo coupled catalytic CO_2 reductions. The mechanisms elucidated in this thesis can inspire future works on designing and developing more efficient and economically-feasible CO_2 utilisation to address climate change challenge.

Lay Summary

CO_2 is an important greenhouse gas responsible for global warming issues and also related to the floods and draughts happened more often recently than ever. The Intergovernmental Panel on Climate Change (IPCC), a United Nations body, released its lasted report in 2021 warning that “immediate, rapid and large-scale” actions are severely needed now to prevent the global temperature rise exceeding the 1.5 °C target. Besides CO_2 capture and storage technology, catalytic CO_2 conversion to value-added fuels is also an important supplement. Taking advantage of sustainable energy to drive the catalytic conversion is the only way to make this reaction process environmentally and economically feasible. Solar light as one of the most abundant green energy sources is promising to drive the CO_2 conversion reaction in a green way.

This thesis focuses on the catalytic CO_2 conversion driven by external light. There are two key scientific questions underpinning this topic: new catalysts design and reaction mechanism understandings. These two aspects closely relate to each other. New catalysts usually bring new reaction mechanisms; reaction mechanism understanding can guide rational design of new catalysts.

g-C_3N_4 and TiO_2 are environmentally friendly catalysts, which show promising photocatalytic CO_2 conversion capability. With detailed investigations on the molecular and electronic structure of these catalysts, their UV-Visible light photocatalytic CO_2 reduction with H_2O mechanism is elucidated. Conventional photocatalysis comparing with thermocatalysis suffers from slow reaction kinetics and is hardly implemented in industrial level. Therefore, introducing sustainable light energy to boost the thermocatalytic reaction and lower the energy consumption is a promising way. This area is still at its early stage with either reaction mechanism and light enhancement mechanism being less understood. This thesis sheds light onto the fundamental aspects of photo and

thermal catalysts coupling over typical model catalysts Au/TiO_2 and Au/Al_2O_3 widely used in industry.

In both cases, the understanding of the mechanisms achieved in this thesis will provide further references and guidance for future developing the high-efficient solar light-driven catalysts.

Acknowledgements

Foremost I would like to express my sincere thanks to my supervisor Prof. Xianfeng Fan for his consistent supports and tireless guidance throughout my PhD study in Edinburgh. He has been a constant source of inspirations, helpful advices and constructive feedbacks. His efforts and contributions are essential and indispensable to my PhD study.

I also thank Prof. Ying Zheng who was my principal supervisor during my first year of PhD student here and acted as the co-supervisor during the following years. She kindly provided the precious opportunity to study in the University of Edinburgh on this intriguing research field of catalysis. I would also like to thank my co-supervisor Dr. Sam Lau on his very constructive advice on experimental designs and paper organisations. I learned a lot from these suggestions. I am also super grateful to Dr. Francisco Garcia Garcia, who kindly shared his great insights and knowledge about heterogeneous catalysts with me. Many thanks to Dr. Ignacio Tudela for his many helpful advice on both research and academic career developments. I would also like to express my greatest appreciation to Dr. Guanjie He and Dr. Leonardo Rios Solis, who kindly reviewed my thesis and provided insightful questions and recommendations. Your kindest helps greatly improved the quality of this thesis.

There are many academics and students who have helped me during my PhD study. Great thanks to Prof. Neil Robertson and Dr. Gary Nichol from the school of chemistry for helping me so much on UV-Vis DRS and XRD characterizations. Dr. Laetitia Pichevin and Dr. Nicola Cayzer from the school of geoscience are much appreciated for helping on ICP-OES and SEM tests. Thanks to Dr. David Miller from the University of St. Andrews and Dr. Jiangbo Lu from Shaanxi Normal University for the excellent STEM characterizations. All of the works in this thesis cannot be accomplished without the kindest supports from the colleagues in the school of engineering. Mr. Fergus Dingwall

provided invaluable and countless technical supports in our lab. I also have to thank Mr. Alex Kirkland, Mr. Andy Banks, Mr. Jamie Graham, Mr. Mark Mason, Mr. Kevin Tierney and Mr. Kevin Baines. The scientific ideas can never be practically implemented without your helps. The school of engineering is very much appreciated for providing scholarship funding my PhD study.

Lastly, I would like to thank every member of Prof. Fan's group and all the friends in the lab. I am so grateful for your numerous helps inside and outside the lab. It has been a great pleasure to work together with you. I also cannot thank my family enough. Your trusts and encouragements support me overcome all the hard time during pursuing this PhD degree.

Publications During PhD Study

1. **Wang, K.**, M Cao, J. Lu, Y. Lu, C.H. Lau, Y. Zheng, X. Fan*, Operando DRIFTS-MS Investigation on Plasmon-Thermal Coupling Mechanism of CO_2 Hydrogenation on Au/TiO_2: The Enhanced Generation of Oxygen Vacancies. *Appl. Catal., B,* **2021**, *296*, 120341.
2. **Wang, K.**, J. Lu, Y. Lu, C.H. Lau, Y. Zheng*, X. Fan*, Unravelling the C-C coupling in CO_2 photocatalytic reduction with H_2O on Au/TiO_{2-x}: Combination of plasmonic excitation and oxygen vacancy, *Appl. Catal., B*, **2021**, *292*, 120147.
3. **Wang, K.**; Fu, J.; Zheng, Y.*, Insights into photocatalytic CO_2 reduction on C_3N_4: Strategy of simultaneous B, K co-doping and enhancement by N vacancies. *Appl. Catal., B* **2019,** *254*, 270-282.
4. **Wang, K.**; Smith, D.; Zheng, Y.*, Electron-driven heterogeneous catalytic synthesis of ammonia: Current states and perspective. *Carbon Resources Conversion* **2018,** *1* (1), 2-31. (**Review**)
5. Guo, Y.; Zhang, C.; Zhang, J.; Dastafkan, K.; **Wang, K.***; Zhao, C.*; Shi, Z.*, Metal–Organic Framework-Derived Bimetallic NiFe Selenide Electrocatalysts with Multiple Phases for Efficient Oxygen Evolution Reaction. *ACS Sustainable Chem. Eng.* **2021,** *9* (5), 2047-2056.
6. Li, Z.; **Wang, K.***; Ge, B.; Zhang, Z.; Wei, Z.; Shi, Z.*; Qiao, G., Synergistic enhancement of sinterability and corrosion resistance of $ZnCr_2O_4$ spinel by TiO_2 addition for carbon-free aluminum electrolysis. *Chem. Eng. J.* **2020,** *400*, 125924.
7. Guo, Y.; Guo, D.; Ye, F.; **Wang, K.***; Shi, Z.*; Chen, X.; Zhao, C.*, Self-Supported $NiSe_2$ Nanowire Arrays on Carbon Fiber Paper as Efficient and Stable Electrode for Hydrogen Evolution Reaction. *ACS Sustainable Chem. Eng.* **2018,** *6* (9), 11884-11891.
8. Cao, M.; **Wang, K.***; Tudela, I.; Fan, X.*, Improve photocatalytic performance of g-C_3N_4 through balancing the interstitial and substitutional chlorine doping. *Appl. Surf. Sci.* **2021,** *536*, 147784.

9. Cao, M.; **Wang, K.***; Tudela, I.; Fan, X.*, Synthesis of Zn doped g-C_3N_4 in KCl-$ZnCl_2$ molten salts: The temperature window for promoting the photocatalytic activity. *Appl. Surf. Sci.* **2020,** *533*, 147429.

10. Fu, J.; Ren, D.; Xiao, M.; **Wang, K**.; Deng, Y.; Luo, D.; Zhu, J.; Wen, G.; Zheng, Y.*; Bai, Z.*; Yang, L.; Chen, Z.*, Manipulating Au-CeO_2 Interfacial Structure Toward Ultrahigh Mass Activity and Selectivity for CO_2 Reduction. *ChemSusChem* **2020,** 24, 6621-6628.

11. Dong, X.; Akram, A.; Comesaña-Gándara, B.; Dong, X.; Ge, Q.; **Wang, K.**; Sun, S. P.; Jin, B.; Lau, C. H.*, Recycling Plastic Waste for Environmental Remediation in Water Purification and CO_2 Capture. *ACS Appl. Polym. Mater.* 2020, 2 (7), 2586-2593.

12. García-Vázquez, M.; **Wang, K.**; González-Carballo, J. M.; Brown, D.; Landon, P.; Tooze, R.; García-García, F. R.*, Iron and chromium-based oxides for residual methane abatement under realistic conditions: A study on sulfur dioxide poisoning and steam-induced inhibition. *Appl. Catal., B* **2020,** *277*, 119139.

13. Burnett, L.; Rysakova, M.; **Wang, K.**; González-Carballo, J.; Tooze, R. P.; García-García, F. R.*, Isothermal cyclic conversion of methane to methanol using copper-exchanged ZSM-5 zeolite materials under mild conditions. *Appl. Catal., A* **2019,** *587*, 117272.

Table of Contents

List of Figures

List of Tables

List of Abbreviations

Abbreviation	Definition
0D	Zero-Dimensional
1D	One-Dimensional
2D	Two-Dimensional
3D	Three-Dimensional
AIM	Atom in Molecule
AIMD	Ab Initio Molecular Dynamics
BET	Brunauer–Emmett–Teller
BID	Barrier discharge Ionization Detector
BOMD	Born-Oppenheimer Molecular Dynamics
CASSCF	Complete Active Space Self Consistent Field
CB	Conduction Band
CBM	Conduction Band Minimum
CDD	Charge Density Difference
CID	Chemical Interface Damping
CIS	Chemical Interface Scattering
CI-NEB	Climbing Image Nudged Elastic Band
COHP	Crystal Orbital Hamilton Population
CW	Continuous-Wave
DCDA	Dicyandiamide
DFT	Density Functional Theory
DFT-D	Density Functional Theory with Dispersion Correction
DFT+U	Density Functional Theory with Hubbard Correction
DICTT	Direct metal-to-semiconductor Interfacial Charge-Transfer Transition
DIMET	Desorption Induced by Multiple Electronic Transition
DOS	Density of States
DP	Deposition-Precipitation
DRIFTS	Diffuse Reflectance Infrared Fourier-Transform Spectroscopy
DSC	Differential Scanning Calorimeter
E_a	Activation energy
E_F	Fermi Energy
EDS	Energy Dispersive Spectroscopy
EMSI	Electronic Metal Support Interaction
ETEM	Environmental Transmission Electron Microscope
EXAFS	Extended X-ray Absorption Fine Structure
fcc	Face-centered cubic
FID	Flame Ionization Detector
fs	Femtosecond
GC	Gas Chromatography/Gas Chromatograph
GGA	Generalized Gradient Approximation

HAADF	High Angle Angular Dark Field
HF	Hartree-Fock
HSE	Heyd-Scuseria-Ernzerhof
HOMO	Highest-Occupied Molecular Orbital
ICP-OES	Inductively Coupled Plasma Optical Emission Spectroscopy
KS	Kohn-Sham
LDA	Local Density Approximation
LSPR	Localized Surface Plasmon Resonance
LUMO	Lowest-Unoccupied Molecular Orbital
MD	Molecular Dynamics
MOF	Metal-Organic Framework
MS	Mass Spectroscopy/Mass Spectrometer
MvK	Mars van Krevelen
NP	Nano Particle
ns	nanosecond
N_V	Nitrogen Vacancy
OSC	Oxygen Storage Capability
PAW	Projector-Augmented Wavefunction
PBE	Perdew-Burke-Ernzerhof
PCET	Proton-Coupled Electron Transfer
PDOS	Projected Density of States
PICTT	Plasmon-Induced Interfacial Charge-Transfer Transition
PID	Proportional–Integral–Derivative
PIRET	Plasmon-Induced Resonance Energy Transfer
PHET	Plasmon-induced Hot-Electron Transfer
PL	Photoluminence
ps	Picosecond
PTI	Poly(Triazine Imide)
QM	Quantum Mechanics
QY	Quantum Yields
RWGS	Reverse-Water-Gas-Shift
RHE	Reversible Hydrogen Electrode
SCF	Self-Consistent Field
SEM	Scanning Electron Microscope
SHE	Standard Hydrogen Electrode
SIE	Self-Interaction Error
SFLP	Solid Frustrated-Lewis-Pair
SMSI	Strong Metal Support Interaction
SSA	Specific Surface Area
SSITKA	Steady-State Isotope Transient Kinetics Analyses
STM	Scanning Tunnelling Microscope
STS	Scanning Tunnelling Spectroscopy
STEM	Scanning Transmission Electron Microscope
TAP	Temporal Analysis of Products
TCD	Thermal Conductivity Detector
TDDFT	Time Dependent Density Functional Theory
rt-TDDFT	real time-Time Dependent Density Functional Theory

TDOS	Total Density of States
TEM	Transmission Electron Microscope
TGA	Thermogravimetric Analysis
TPD	Temperature-Programmed Desorption
TPSR	Temperature-Programmed Surface Reaction
TOF	Turnover Frequency
VB	Valence Band
VBM	Valence Band Maximum
vdW	van der Waals
V_O	Oxygen Vacancy
WGSR	Water Gas Shift Reaction
WN	Nano-Wire
XANES	X-ray Absorption Near-Edge Structure
XPS	X-ray Photoelectron Spectroscopy/Spectrometer
XRD	X-ray Diffraction/Diffractometer
XC	Exchange-Correlation

Chapter 1. Introduction and Literature Review

1.1 Overview

1.1.1 Motivations

Reducing carbon dioxide (CO_2) emission is one of the central topics in the first twenty years of the twenty-first century. More and more researches on climate change have drawn to the same conclusion that the CO_2 emission derived from Human activities is the main reason for the significant global warming.[1-3] The strategies made by policy makers aim to constrain the temperature increase within the limit of 1.5 °C by 2100 and achieve the zero net CO_2 emission in 2050.[4-7] Although carbon capture and storage is a promising strategy to reduce CO_2 emission, converting CO_2 to other products is another pathway to achieve the net zero emission target.[8-9] In 2019, the global CO_2 emission due to the anthropogenic activity hits a new record of 43.1±3.2 Giga-tonnes;[10] the UN Emission Gap Report in 2019 warns that we are failing to meet the target of 1.5 °C.[11] The severe climate challenge makes the CO_2 conversion a necessity to achieve a sustainable future.

Heterogeneous catalytic CO_2 conversion to value-added products is attracting widespread interest among the research community in recent years. The thermocatalytic CO_2 hydrogenation has proven the capability to convert CO_2 into desired products including CO, CH_4, CH_3OH, C_2H_5OH, and higher alkanes, olefins, alcohols. However, the traditional thermocatalytic process requires the external heat energy to drive the reaction, which results in the CO_2 emission. Therefore, a cleaner energy resource is more desirable to replace or partially replace the thermal energy to drive the CO_2 conversion to achieve a real negative CO_2 emission. Solar energy is one of the most promising candidates

due to its high total energy amount, easy accessibility and feasible implementation in the catalytic process.

However, due to the complicated processes and limited systematic investigations, the reaction mechanism of CO_2 conversion especially under excitation by external light is still not fully understood. CO_2 is a stable molecule and hard to be activated. Its further conversion to other products involves multiple steps and reaction intermediates. The lack of understanding of the reaction mechanism is the main obstacle hindering the design for efficient photocatalysts and photocatalytic process for CO_2 conversion. In this thesis, I focus on the CO_2 catalytic conversion driven or promoted by external light energy to produce value-added products. In addition to catalysts design, the reaction mechanism for the CO_2 activation and conversion are highlighted in this research. While the solar energy-driven or promoted CO_2 conversion technology is still many years away from practical implementation in industry, this work hopes to provide insights to help the design of more efficient photocatalytic and photo-promoted thermocatalytic CO_2 conversion technique and catalysts for both the catalysis research community and industry.

1.1.2 Thesis organization

This thesis is formed by seven chapters:

Chapter 1 is the general introduction and literature review of photo- and thermo- catalytic CO_2 conversion into value-added products. The principle and catalysts design for photo- and thermo- catalytic CO_2 reduction are briefly summarized and discussed.

Chapter 2 introduces the theoretical background of methods used throughout the thesis.

The following four chapters (Chapter 3 to 6) are the main science chapters, including a short introduction on the research background on specific scientific questions, research results, discussions and conclusions.

Chapter 3 focuses on the design and preparation of g-C_3N_4 based photocatalyst for CO_2 reduction with H_2O. The effects of modification on the photocatalytic CO_2 reduction performance are investigated. Additionally, the reaction mechanism is proposed based on theoretical and experimental evidence.

Chapter 4 focuses on how to alter the product selectivity of photocatalytic CO_2 reduction with H_2O. CO_2 photocatalytic reduction performances are evaluated over Au/TiO_2 with either bandgap or plasmonic excitation mechanisms. The reaction pathways, especially the C-C coupling mechanisms, are investigated.

Chapter 5 presents the detailed investigation of the CO_2 hydrogenation mechanism over Au/TiO_2 at photo- and thermo- coupled reaction condition. The critical role of V_O in determining the reaction performance and mechanism is highlighted. The promotion effects of incident light on the CO_2 hydrogenation reaction are unravelled via both experimental and theoretical investigations.

Chapter 6 investigates the CO_2 hydrogenation at photo-thermo coupled catalytic condition over Au/Al_2O_3. The fundamental differences between Chapter 5 & 6 are the reducibility and electronic structure of the oxide supports. The catalytic performance and reaction mechanism are investigated. The differences between reducible and non-reducible oxide supports for Au NPs in the photo-thermal catalytic CO_2 hydrogenation are compared.

The final chapter 7 makes a summary of the main conclusions of the works in this thesis. Improvements and perspectives are proposed at the end of this chapter.

1.2 Photocatalysts with bandgap excitation

1.2.1 Conventional metal oxide semiconductor

In the pioneering investigations on photocatalysis, the catalysts are mainly transition metal oxide semiconductors. In 1979, Inoue and Fujishima et al.[12-13] proved the capability of metal oxide semiconductors to reduce CO_2 and H_2O

to valuable products under UV light irradiation. Since then, more semiconductors, not limited to oxides, have been investigated on their photocatalytic performances including ZnO,[14-15] CuO,[16-17] MoS_2,[18-19] WO_3,[20-21] etc. Among them, the TiO_2 draws more attention from researchers due to its prominent photocatalytic activity and industrialized manufacture. As a result, the TiO_2-P25 (a product from Evonik (Degussa) company) is still frequently used as the benchmark for evaluating new photocatalysts.[22-23] TiO_2 has three most conventional phases known as rutile, anatase and brookite, which show different photocatalytic performances at different circumstances.[24-25] The rutile is thermodynamically more stable than anatase phase and anatase will transform to rutile at the transformation temperature of 600 to 700 °C.[26] Generally, it is believed the better photocatalytic performance of anatase than rutile and brookite is derived from their different electronic structures. The anatase is an indirect semiconductor; By contrast, rutile and brookite are direct semiconductors. Because the recombination of photo-excited electrons and holes in indirect semiconductor needs the assistances of phonon, which causes the longer lifetime of photo-excited charge carriers in anatase.[27]

1.2.2 Graphitic carbon nitride

Besides conventional transition metal oxides, organic semiconductors are attracting more and more attention. Graphitic carbon nitride (g-C_3N_4) is a relatively new organic semiconductor showing a vdW layered structure. Since Wang et al.[28] reported that the g-C_3N_4 was capable of driving H_2 photocatalytic production via water splitting in 2009, g-C_3N_4 has drawn a lot of interest from researchers. The g-C_3N_4 exhibits several attractive features including the moderate bandgap of ~2.7 eV; transition metal-free chemical composition; suitable VB, CB edge potentials.

Since g-C_3N_4 is a polymer semiconductor usually synthesized via the polymerization of organic precursors, the low crystallinity and abundance of defects make a clear understanding of g-C_3N_4 structure very difficult.[29-30] Due to different synthesis methods, the reported structure of g-C_3N_4 can be

summarized into following four categories:[31] (a) triazine-based g-C_3N_4, (b) heptazine-based g-C_3N_4, (c) melon-based g-C_3N_4, and (d) PTI-based g-C_3N_4 (seen in **Figure 1.1**). The chemical structures of triazine and heptazine motifs are plotted in **Figure 1.1**(e, f). The stacking of the layers is illustrated in **Figure 1.1**(g). The heptazine, triazine and melon-based g-C_3N_4 are usually synthesized via the thermal polymerization of N-rich organic molecules including melamine, dicyandiamide, cyanamide, urea etc. in ambient atmosphere. Comparatively, the PTI-g-C_3N_4 is a highly crystalline polymorph, which is usually synthesized via the polycondensation of melamine in KCl-LiCl molten salts. In literature, most of the g-C_3N_4 is synthesized via the polycondensation method in the static air. Therefore, the heptazine-based structure with high stability is focused in the following paragraph.

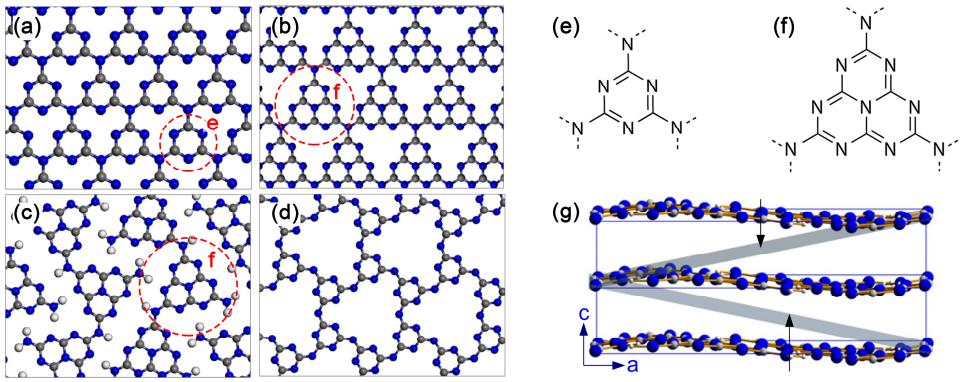

Figure 1.1. The structures of single-layer g-C_3N_4 prepared via different methods: (a) triazine-based, (b) heptazine-based, (c) melon-based, (d) PTI-based g-C_3N_4, respectively. Reproduced with permission from ref. 31, Copyright 2016, American Chemical Society. The chemical structures of (e) triazine, (f) heptazine units. (g) The scheme of multiple layers stacking. Reproduced with modification with permission from ref. 30. Copyright 2013, IOP Publishing.

1.2.3 Optimization of g-C_3N_4 for promoting photocatalytic performance

Heteroatom doping was developed to improve the catalytic performance by modifying the electronic structures of g-C_3N_4. Many elements such as B,[32-34] O,[35-36] P,[37] S,[38] Cl,[39-40] K [41-42] etc. have been reported as dopants. The main improvements are summarized herein including optimisation of band edge

positions, facilitation of carrier generation and transfer, suppression of carrier recombination and enhancement of adsorption of reactants.[43-44] Beyond single element doping discussed above, multi-element doping is a relatively new strategy in enhancing performance. S-P,[45] Fe-P,[46] O-Na,[47] O-K,[48] B-P,[49] B-F,[50] N-P-B,[51] K-I,[52] C-O,[53] etc. co-doping systems have been reported to enhance the catalytic performance of g-C_3N_4. Ideally, the multiple dopants should provide a comprehensive approach to overcome different intrinsic shortcomings of g-C_3N_4 simultaneously. Each of the dopants is supposed to play its unique role in modifying material structure or electronic structure properties. However, co-doping elements in current works usually have similar energy-favourable doping sites and act duplicated functions. For example, when the doping elements that have large diameters, such as Na, K, P, F, Cl, Br and I etc., usually prefer to dope at the interstitial sites of g-C_3N_4.[40, 43] Doping elements such as S, P, F, Pt, Fe, Co, Ni etc. tend to generate the mid-gap dopant states that in turn promotes carrier recombination.[38, 40, 50, 54-57] The substitutional dopants having smaller Mulliken electronegativity than C, N (eg. S, P, B,) are believed to upshift the CBM while the substitutional dopants with larger Mulliken electronegativity (eg. F, Cl, O) behave the opposite.[58-60] Atoms contain more valence electrons than C and N (eg. O, S, P, Cl etc) will generate an electron donor state near the CBM. On the other hand, the dopants with less valence electrons will produce electron adaptor states near the VBM.[61] In literature, neither the rationale of choosing co-doped elements nor the interaction between the co-dopants have been clearly understood. The corresponding effects of different modification factors on catalytic performance need further elucidation.

Besides heteroatom doping, the approach of vacancy introduction,[41, 62-65] creating atom vacancies in the lattice of g-C_3N_4, has also been proven as an alternative effective way. The N_v shows high efficiency in narrowing bandgap and generating active sites compared to heteroatom doping. However, only appropriate amount of N_v can function positively.[66-68] N_v always generates an extra state in the middle of bandgap, which is deemed as the main recombination centre for the excited electron and holes in g-C_3N_4. Excessive

N_v, especially the loss of N at the intersection of heptazine unit, could retard the electrical conductivity of g-C_3N_4. Thermal treatment of g-C_3N_4 under H_2 atmosphere is the most commonly used method to generate N_v.[65-66] However, it is an uncontrollable way for N_v introduction due to the usage of excessive H_2.

Photocatalytic CO_2 reduction with H_2O is an attractive application for g-C_3N_4 since it addresses greenhouse gas emission challenge and produces profitable fuel at the same time.[69-71] How to increase the photocatalytic CO_2 reduction performance of g-C_3N_4 and keep the catalysts free of transition metals are the main challenges. To be specific, an optimized g-C_3N_4 is expected to have the following features: (1) enhanced CO_2 adsorption and activation ability; (2) reduced bandgap for utilizing more light energy; (3) relatively high CBM as CO_2 reduction requires a high reduction potential to activate; (4) fast transfer of excited electrons on and across g-C_3N_4 layers; (5) the long lifetime of charge carriers. Modification of the molecular and electronic structure of g-C_3N_4 via doping and vacancy creation is proven to be a very promising approach.[72] For example, Sagara et al.[32] successfully prepared B-doped g-C_3N_4 that exhibited superior activities on CO_2 photoelectrochemical reduction. It was attributed to the enhanced water oxidation potentials achieved by the doping approach. Fu et al.[35] doped O into g-C_3N_4 so that light energy adsorption was promoted and carrier recombination was retarded.

Since CO_2 is a Lewis acid, basic sites are preferred for the CO_2 adsorption.[73] Sun et al.[42, 74] reported their etching method with KOH at high temperature to increase the catalytic performance of g-C_3N_4. The doped K along with more amino groups brought by etching were able to promote the activation of CO_2 over g-C_3N_4. Xia et al.[75] generated amine functional group via annealing bulk g-C_3N_4 under NH_3 atmosphere to improve its capability of CO_2 adsorption and the CO_2 conversion was significantly increased.

Other main shortcomings of pristine g-C_3N_4 include the limited SSA, fast excited electron-hole recombination and unoptimized band positions. The bulk g-C_3N_4 synthesized via the conventional thermal polymerization method in static air generates the very limited SSA of ~10 m^2 g^{-1}.[43, 76-77] The most

effective way to increase the SSA of g-C_3N_4 is using hard templates[78] or soft templates[79-81] to introduce mesopores into the particles. Another popular method is to decrease the dimension of the g-C_3N_4 crystal to 2D,[82-83] 1D[84-85] and 0D.[86-87]

The issue of fast recombination of photoexcited electrons and holes can be addressed by multiple strategies. For instance, the doping of heteroatoms at the interlayer position can facilitate the interlayer charge transfer and suppress the recombination.[43, 48] Reducing the interlayer distance can enhance the interlayer charge carrier transfer and retard the recombination.[88] Moderate doping can introduce a doping energy level inside the bandgap, which temporally traps the photoexcited electrons and suppresses the recombination.[41] Additionally, building the heterostructure between g-C_3N_4 and another semiconductor or cocatalysts can efficiently facilitate the electron-hole separation.[89]

1.2.4 The dynamics of photoexcited electron transfer from semiconductor to metal NP

One of the keys to improving the efficiency of photocatalysts is to retard the excited electron/hole recombination. For photocatalysts using bandgap excitation mechanism, loading transition metal cluster onto semiconductor is a classic and successful design. When a semiconductor is illuminated by light with larger energy than the bandgap of the semiconductor, the electrons in VB can be excited into the CB and leave holes inside the VB. The photoexcited electrons and holes can migrate to the surface of the semiconductor and react with the reactants to drive the reaction. With metal NP cocatalyst, the electron will usually inject into the metal NP. The whole process is schemed in **Figure 1.2**(a, b) for the most conventional combination of metal NP and N-type semiconductor. Loading metal NP as cocatalysts onto semiconductor surface show two main advantages: (i) the heterostructure can significantly enhance the charge separation; (ii) the metal NP shows good catalytic performance

itself. In this section, only bandgap excitation is considered and the plasmonic excitation within the metal NP will be discussed in section 1.3.

Hisatomi et al.[90] proposed a kinetic model to describe the generation, transportation, heterostructure injection, recombination and participation (as shown in **Figure 1.2**(c)). Following elementary steps are used to describe the whole photocatalytic process of a semiconductor with cocatalysts. The generation and recombination of photoexcited electron-hole pairs can be expressed with:

$$h\nu \longrightarrow e^- + h^+ \tag{1.1}$$

$$e^-_{\mathrm{bulk}} + h^+_{\mathrm{bulk}} \longrightarrow E_{\mathrm{recomb}} \tag{1.2}$$

$$e^-_{\mathrm{bulk}} + h^+_{\mathrm{surf}} \longrightarrow E_{\mathrm{recomb}} \tag{1.3}$$

$$e^-_{\mathrm{surf}} + h^+_{\mathrm{bulk}} \longrightarrow E_{\mathrm{recomb}} \tag{1.4}$$

$$e^-_{\mathrm{surf}} + h^+_{\mathrm{surf}} \longrightarrow E_{\mathrm{recomb}} \tag{1.5}$$

Among all four kinds of recombination, the equation (1.3) is predominant in n-type semiconductors. Therefore, the rate of recombination (r_{recomb}) in a n-type semiconductor can be approximated as:

$$r_{\mathrm{recomb}} \approx k_r([e^-_{\mathrm{bulk}}] + [e^-_{\mathrm{dark}}])[h^+_{\mathrm{surf}}]; \tag{1.6}$$

where $[e^-_{\mathrm{bulk}}]$, $[h^+_{\mathrm{surf}}]$, $[e^-_{\mathrm{dark}}]$ are the concentrations of photoexcited electrons in the bulk of semiconductor, photoexcited holes trapped at semiconductor surface and intrinsic electron inside semiconductor at ground-state, respectively. k_r is the recombination rate constant. In n-type semiconductor the electrons are the majority carrier and the relation of $[e^-_{\mathrm{dark}}] \gg [e^-_{\mathrm{bulk}}]$ is usually satisfied. Therefore, $[e^-_{\mathrm{dark}}]$ can be treated as a *constant* and the equation (1.6) can be further approximated to:

$$r_{\mathrm{recomb}} \approx k_r([e^-_{\mathrm{dark}}])[h^+_{\mathrm{surf}}]; \tag{1.7}$$

Under such approximation, the r_{recomb} follows a pseudo-first-order kinetics. Based on a series of microkinetics analyses, Histatomi et al.[90] proposed the photocatalytic reaction rate (r_{react}) can be written as:

$$r_{\mathrm{react}} = \frac{wk_{\mathrm{e1}}k_{\mathrm{e2}}k_{\mathrm{R}}(k_{\mathrm{O}}+k_{\mathrm{r}}[e^{-}_{\mathrm{dark}}])(\sqrt{1+b}-1)}{2(k'_{\mathrm{e1}}(k'_{\mathrm{e2}}+k_{\mathrm{R}})+wk_{\mathrm{e2}}k_{\mathrm{R}})k_{\mathrm{r}}} \quad (1.8)$$

$$b = \frac{4(k'_{\mathrm{e1}}(k'_{\mathrm{e2}}+k_{\mathrm{R}})+wk_{\mathrm{e2}}k_{\mathrm{R}})k_{\mathrm{r}}k_{\mathrm{O}}}{wk_{\mathrm{e1}}k_{\mathrm{e2}}k_{\mathrm{R}}(k_{\mathrm{O}}+k_{\mathrm{r}}[e^{-}_{\mathrm{dark}}])^{2}}\alpha I \quad (1.9)$$

where k_{e1}, k'_{e1}, k_{e2}, k'_{e2}, k_{R}, k_{O} are the corresponding reaction rate constants for each elementary step (illustrated in **Figure 1.2**(c)); α is the average light absorption coefficient of the photocatalysts; I is the incident light intensity; *w* is a coefficient depending on the loading amount of cocatalysts. The equations (1.8) and (1.9) can be further simplified at two extreme conditions: (i) incident light is weak, ($\lim\ b \to 0$); (ii) incident light is strong ($\lim\ b \to \infty$):

$$r_{\mathrm{react}} = \sqrt{\frac{wK_{\mathrm{e1}}K_{\mathrm{e2}}k_{\mathrm{R}}k_{\mathrm{O}}\alpha I}{k_{\mathrm{r}}}},\ \lim\ b \to \infty \quad (1.10)$$

$$r_{\mathrm{react}} = \frac{k_{\mathrm{O}}}{k_{\mathrm{O}}+k_{\mathrm{r}}[e^{-}_{\mathrm{dark}}]}\alpha I,\ \lim\ b \to 0 \quad (1.11)$$

where K_{e1} and K_{e2} are the equilibrium constants for electron transfer between bulk/surface and surface/cocatalysts. Here, the authors approximated the term $\sqrt{1+b}-1$ with $\sqrt{b}$ and *b*/2 as b approaches infinite or zero, respectively. The importance of equations (1.10) and (1.11) is that the equations suggest that the correlation between reaction rate and incident light intensity can be separated into two ranges. When the light is strong, $r_{\mathrm{react}} \propto \sqrt{I}$;[91] by contrast, when light is weak, $r_{\mathrm{react}} \propto I$.

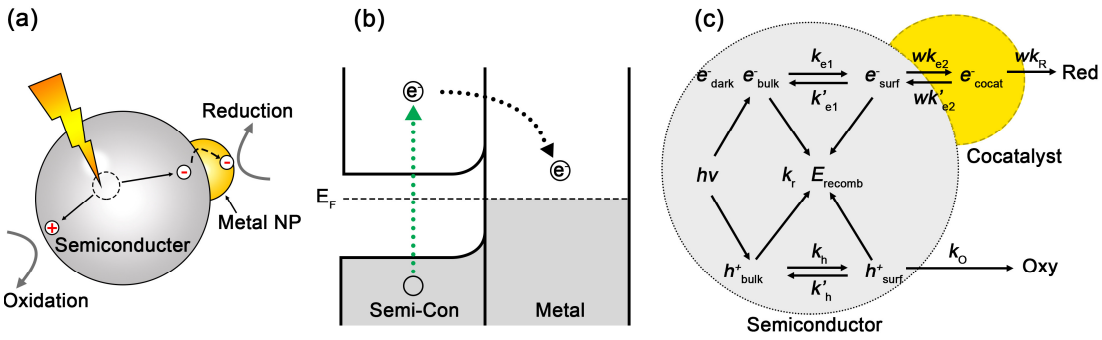

Figure 1.2. (a) Scheme of photocatalytic reaction process of semiconductor with cocatalysts. (b) Scheme of electron transfer between semiconductor (n-type) and metal NP cocatalysts with bandgap photo-excitation. (c) Kinetic model describing the electron-hole generation, recombination, diffusion and participation in photocatalytic reaction. Reproduced with modification with permission from ref. 92. Copyright 2013, American Chemical Society.

From the perspective of the timescale, the photoexcitation of electron-hole pairs and trapping of the charge carriers happen within fs scale; electron injection into metal NP occurs within ps scale; electron/hole-driving reaction and charge carrier recombination fall into the timescale of ns to μs.[93] Therefore, the key to achieving a high QY is to enhance the charge separation at the interface between semiconductor and metal NPs. The dynamics of charge separation at the interface is affected by the following factors:[94-96] (i) the size of cocatalyst NP; (ii) the loading of metal NP cocatalysts; (iii) the crystal phase and facet; (iv) the dopant and vacancy in the semiconductor.

Lee et al.[97] compared the PL decay dynamics of Au/ZnO with the Au NP diameter of 1.1, 1.6 and 2.8 nm, respectively. It was found the larger Au NP corresponded to a faster charge carrier separation. However, Wang et al.[98] found the charge separation efficiency correlated to many factors and not exclusively to metal NP size. The higher separation efficiency of larger Au NP on TiO_2 could be attributed to the higher capability of electrons storage and faster electron discharging to reactants. Ioannides et al.[99] proposed the metal-semiconductor contact models to describe the dynamics of electron transfer across the interface. The authors emphasized the influences of E_F, the electric field within the depletion area of semiconductor and the dopant concentrations

on the efficiency of charge transfer across the interface. Note that the explicit understanding of the electron transfer dynamics across the interface has not been achieved and too many involved factors make clear interpretations of experimental evidence difficult. A generally valid physical model has not been built yet.

1.3 Plasmonic photocatalysts

1.3.1 LSPR and its decays

For metal NPs, the free electrons can be excited by external light and reach a collective oscillation state, which is called the LSPR effects. The decay of LSPR is the energy resource for electron/hole excitation that can potentially drive photocatalytic reactions. Therefore, the decay process determines both the generation rate and energy distribution of the hot carriers. The total decay time constant (γ_{tot}) of the LSPR can be written as the sum of the contributions from the bulk (γ_{b}) and surface ($\gamma_{\mathrm{surface}}$) mechanisms:

$$\gamma_{\mathrm{tot}} = \gamma_{\mathrm{b}} + \gamma_{\mathrm{surface}} \tag{1.12}$$

Note that the $\gamma_{\mathrm{surface}}$ is the parameter strongly correlates with the size of the NP, because a smaller NP size ensures a larger surface to bulk ratio. The γ_{b} term can be written as the sum of the intraband and interband excitations.

$$\gamma_{\mathrm{b}} = \gamma_{\mathrm{Drude}} + \gamma_{\mathrm{interband}} \tag{1.13}$$

The intraband excitation has been well established using the Drude-Sommerfeld model; therefore, it is usually denoted as γ_{Drude}.[100] The bulk damping constant can be further split into three parts, electron-electron (e-e), electron-phonon (e-p) and electron-defects (e-d) interactions:

$$\gamma_{\mathrm{Drude}} = \gamma_{\mathrm{e\text{-}e}} + \gamma_{\mathrm{e\text{-}ph}} + \gamma_{\mathrm{e\text{-}d}} \tag{1.14}$$

For the Au NPs, the dielectric function within the intraband wavelength range can be written as:

$$\varepsilon_{\text{Drude}}(\omega) = \varepsilon_{\text{b,Drude}} - \frac{\omega_{p,\text{Drude}}^2}{\omega^2 + i\gamma_{\text{Drude}}\omega} \quad (1.15)$$

where ω is the frequency of light; $\omega_{p,\text{Drude}}$ is the plasmon frequency in bulk metal.

As described in equation (1.12), the size effects for the hot carriers generation are derived from the high ratio of surface atoms. It has been proposed that the surface damping constant γ_{surface} of spherical NPs can be further written as:

$$\gamma_{\text{surface}} = A\frac{v_F}{l_{\text{eff}}} \quad (1.16)$$

where *A* is a coefficient determined by theory and has little correlation with the damping process; therefore A can always be used as a fitting parameter.[101] l_{eff} is the effective path length for electrons; for spherical NP, l_{eff} is proportional to the radius of the sphere. v_F is the Fermi velocity and derived from the equation:

$$v_F = \sqrt{\frac{2E_F}{m_e}} \quad (1.17)$$

It is important to emphasize that when a metal cluster is as small as a few hundreds of atoms, a molecule-like rather than metallic electronic structure is exhibited. The rate of nonradiative decay ($k_{\text{non-rad}}$) follows the energy gap law:[102]

$$k_{\text{non-rad}} \propto e^{-\gamma\Delta E/\hbar\omega_M} \quad (1.18)$$

where γ is a term representing molecular parameters; ω_M is the highest energy vibrational mode involved in the non-radiative transition from the excited state to the ground state; ΔE is the energy gap between HOMO and LUMO.

1.3.2 Generation rate and energy distribution of hot carriers

As described in last paragraph, the LSPR decay and excite electrons from VB to CB and leave holes at VB. The excited electrons and holes are sometimes called the hot carriers. Taking Au as an example, as shown in **Figure 1.3**(a),

in Au electronic structure, the d-band is localised, while sp-band is relatively delocalised. Therefore, there are two kinds of electron excitations when Au NP is irradiated by external light. When the photon energy ($\hbar\omega$) is less than the energy difference between d-band and E_F, only electrons in sp-band can be excited to the unoccupied sp-band, which is called intraband excitation. By comparison, electrons in d-band can be excited into unoccupied sp-band, when incident light energy is high enough. It can be seen from the electronic structure that under the light irradiation with the same energy, the intraband excitation causes the photo-excited electrons with higher energy and leaves holes with relatively low energy; on the contrary, the interband excitation causes photo-excited holes with higher energy and photo-excited electrons with lower energy. More importantly, the electron excitation needs to satisfy the rule of crystal momentum conservation. For interband excitation, the electron-hole pair exhibits zero crystal momentum. It is the reason why the interband excitation is also called *direct excitation*. On the contrary, the electron-hole derived from intraband excitation has the net crystal momentum, which needs to be provided by either the phonons in bulk or on the surfaces. With the help of the surface, the linear momentum conversation is broken, which is the key mechanism for *high-energy* electrons formation. Therefore, for larger crystals, the interband excitation predominates; while in NPs, the intraband transition is more likely to happen.[103-104] The decay contribution from geometry (surface) increases significantly when the size of Au NP decreases. The energy distribution of hot carriers during the excitation and thermalisation after excitation is schemed in **Figure 1.3**(c).

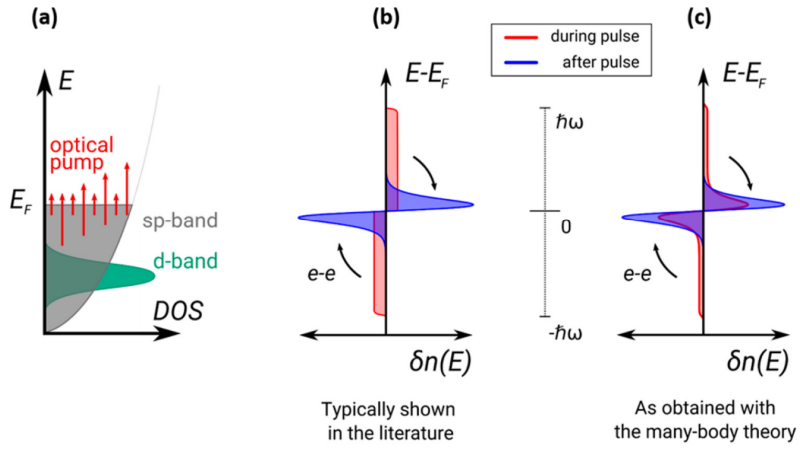

Figure 1.3. (a) Scheme of the electronic structure of Au NP and photo-excitation. (b, c) The energy distribution of hot carriers during and after the pulse of light irradiation. Reproduced with permission from ref.[105] Copyright 2017, American Chemical Society.

After briefing the LSPR induced hot carrier excitation qualitatively in the last paragraph, the quantitative descriptions of the hot carriers are described in the following paragraphs. The plasmonic electron excitation can be described using the following spectral functions:[106]

$$R_e(\varepsilon) = \frac{d^2 N_e}{dt\, d\varepsilon} \tag{1.19}$$

$$\delta n(\varepsilon) = \frac{dN_e}{d\varepsilon} \tag{1.20}$$

where the $R_e(\varepsilon)$ provides the spectral information on the carriers' generation rate and $\delta n(\varepsilon)$ describes the density distribution of the non-equilibrium carrier population (before full relaxation to Fermi-Dirac distribution); the N_e is the number of excited electrons. The total rate of excited carrier generation ($Rate_{\text{tot}}$) can be calculated by:

$$Rate_{\text{tot}} = \int_{E_F}^{\infty} R_e(\varepsilon) d\varepsilon = \frac{dN_e}{dt} \tag{1.21}$$

The calculated energy distribution of excited electrons in spherical Au NP is shown in **Figure 1.4**.[105] The most important feature in this diagram is that there are two kinds of excited electrons: (1) low energy Drude electrons/holes near the E_F; (2) the high-energy electrons/holes show a plateau shape. The high-energy electrons/holes are derived from the surface-assisted excitation with

the breaking of linear momentum conservation, which is also called Landau damping mechanism.

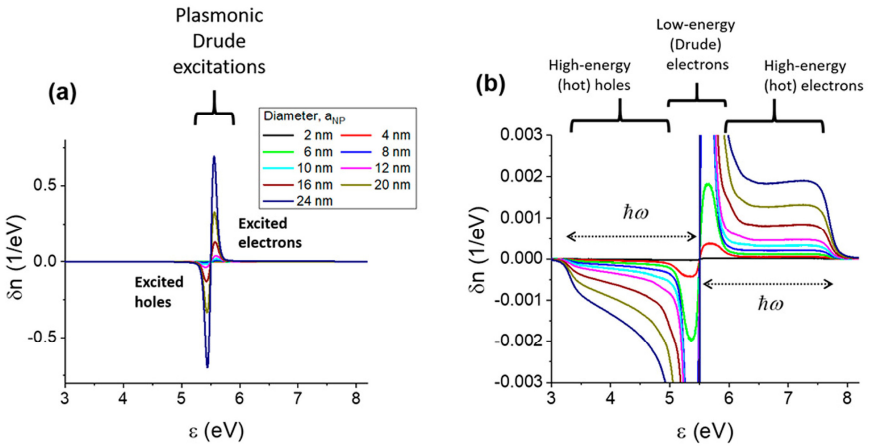

Figure 1.4. (a) Distribution of excited electrons and holes in spherical Au NP with different diameters. (b) The magnification of (a). Reproduced with permission from ref. 105. Copyright 2017, American Chemical Society.

Since only the hot electrons (high-energy electrons) have a high probability to drive reactions, the term hot-electron production efficiency ($\mathrm{Eff}_{\text{hot-electrons}}$) is defined as:

$$\mathrm{Eff}_{\text{hot-electrons}} = \frac{Q_{\text{hot-electrons}}}{Q_{\text{tot}}} \tag{1.22}$$

$$Q_{\text{tot}} = Q_{\text{hot-electrons}} + Q_{\text{classical}} \tag{1.23}$$

where $Q_{\text{hot-electrons}}$, $Q_{\text{classical}}$ and Q_{tot} are the light absorbed corresponding to hot electrons generation, classical light absorption and total absorption by the Au NP. The classical absorption in Au NP can be written as:

$$Q_{\text{classical}} = Q_{\text{Drude}} + Q_{\text{interband}} \tag{1.24}$$

$$Q_{\text{Drude}} = \frac{\omega}{2\pi} \cdot \frac{4\pi R_0^3}{3} |E_{\text{inside}}|^2 \mathrm{Im}(\varepsilon_{\text{Drude}}) \tag{1.25}$$

$$Q_{\text{Drude}} = \frac{\omega}{2\pi} \cdot \frac{4\pi R_0^3}{3} |E_{\text{inside}}|^2 \mathrm{Im}(\varepsilon_{\text{interband}}) \tag{1.26}$$

where $\varepsilon_{\text{Drude}}$ and $\varepsilon_{\text{interband}}$ are the dielectric functions of the Drude and the interband excitation, respectively; $\frac{4\pi R_0^3}{3}$ is the volume of the spherical Au NP. The $Q_{\text{classical}}$ contains both the Drude intraband and interband dissipation in *bulk* metals, which is described using classical theory. Within quasi-static approximation, the total electric field inside a small Au spherical NP can be written as:

$$E_{\text{inside}} = E_0 \frac{3\varepsilon_{\text{matrix}}}{2\varepsilon_{\text{matrix}}+\varepsilon_{\text{metal}}} \tag{1.27}$$

where $\varepsilon_{\text{metal}}$ and $\varepsilon_{\text{matrix}}$ are the dielectric functions of the metal and the matrix, respectively. E_0 is the external electric field of light, and the corresponding amplitude shows the following relation with the incident flux of light energy (I_0), light speed (C_0) and dielectric constant of matrix ($\varepsilon_{\text{matrix}}$):[107]

$$E_0 = \frac{2\pi I_0}{C_0\sqrt{\varepsilon_{\text{matrix}}}} \tag{1.28}$$

On the contrary, the $Q_{\text{hot-electrons}}$ term is derived from the quantum confinement effects and can be expressed by the following equation:

$$Q_{\text{hot-electrons}} = \frac{1}{\tau_\varepsilon}\int d\varepsilon \cdot (\varepsilon - E_F) \cdot \delta n(\varepsilon)\,, |\varepsilon - E_F| > \delta E_{\text{crit}} \tag{1.29}$$

where the $\delta n(\varepsilon)$ is the distribution of non-thermal electrons (hot electrons) in the NP under CW light irradiation; τ_ε is the energy relaxation time; δE_{crit} is the energy threshold accounting for the hot electrons:

$$\delta E_{\text{crit}} = \sqrt{\left(b_1 \frac{\hbar v_F \pi}{R_{\text{NP}}}\right)^2 + (b_2 k_B T_0)^2} \tag{1.30}$$

where T_0 is the temperature of quasi-equilibrium electron gas; k_B is the Boltzmann constant; v_F is the Fermi velocity; R_{NP} is the diameter of the NP.

Additionally, it is assumed that the hot-electrons are activated by the *electric field* normal to the surface of Au NP; Therefore, the distribution function of hot electrons $\delta n(\varepsilon)$ is written as:

$$\delta n(\varepsilon) = \pm \frac{2}{\pi^2} \cdot \tau_\varepsilon \frac{e^2 E_F^2}{\hbar} \frac{1}{(\hbar\omega)^4} \int |E_{\text{normal}}(\theta, \varphi)|^2 ds \quad (1.31)$$

where the *ds* is the unit surface area; θ and φ are the spherical angles.

The generation rates of hot electrons and Drude electrons in spherical Au NPs can be written with the following equations:[107]

$$Rate_{\text{hot-electrons}} = \frac{2}{\pi^2} \frac{e^2 E_F^2}{\hbar} \frac{1}{(\hbar\omega)^3} \frac{4\pi}{3} R_{NP}^2 \left| \frac{3\varepsilon_{\text{matrix}}}{2\varepsilon_{\text{matrix}} + \varepsilon_{\text{metal}}} \right| {E_0}^2 \quad (1.32)$$

If only consider the hot electrons with energy higher than ΔE_b, where ΔE_b is usually considered as the barrier height for hot electrons transfer from Au NPs to attached objects (eg. semiconductor support, adsorbed molecules), equation (1.32) is further written as:

$$Rate_{\text{hot-electrons}} = \frac{2}{\pi^2} \frac{e^2 E_F^2}{\hbar} \frac{(\hbar\omega - \Delta E_b)}{(\hbar\omega)^4} \frac{4\pi}{3} R_{NP}^2 \left| \frac{3\varepsilon_{\text{matrix}}}{2\varepsilon_{\text{matrix}} + \varepsilon_{\text{metal}}} \right| {E_0}^2 \quad (1.33)$$

The low electron generation rate has the classical form:

$$Rate_{\text{Drude}}(\varepsilon) = Q_{\text{Drude}} \frac{d^2 f_{\text{F}}}{d\varepsilon^2} \quad (1.34)$$

$$Q_{\text{Drude}} = \int_{-\delta E_{\text{crit}}}^{\delta E_{\text{crit}}} R_{\text{Drude}}(\varepsilon) d\varepsilon = \frac{\gamma_p \omega_{p,\text{Drude}}^2}{\omega^2} \frac{1}{2\pi} \frac{4\pi}{3} R_{NP}^2 \left| \frac{3\varepsilon_{\text{matrix}}}{2\varepsilon_{\text{matrix}} + \varepsilon_{\text{metal}}} \right| {E_0}^2 \quad (1.35)$$

Summarizing all the arguments mentioned above, following results can be achieved:

$$\frac{Rate_{\text{Hot-electrons}}}{Rate_{\text{Drude}}} = constant \frac{l_{\text{mfp}}}{R_0} \frac{v_F / R_0}{\omega} \quad (1.36)$$

$$\frac{Q_{\text{Hot-electrons}}}{Q_{\text{Drude}}} = \frac{\gamma_{\text{hot-electrons}}}{\gamma_p} = constant' \frac{l_{\text{mfp}}}{R_0} \quad (1.37)$$

where l_{mfp} is the mean free path of electrons, R_0 and v_F are the diameter and Fermi velocity of NP, respectively; ω is the optical frequency. It can be seen that the l_{mfp}/R_0 is the critical parameter in both ratios. For noble metals, the l_{mfp} for Au and Ag are ~10 nm and ~40 nm, respectively, at room temperature.[107] As shown in **Figure 1.5**(a, b), both the hot electrons and Drude electrons generation rates increase when Au NP size rises. However, the

generation rate ratio of hot electrons to Drude electrons shows a negative correlation with Au NP size. It means the higher portion of hot electrons is generated in smaller Au NPs. The similar relations can be found between *QY*, *QP* with Au NP diameter, as shown in **Figure 1.5**(c, d). Here, the *QP* is defined with the following equation:[106, 107]

$$QP_{\text{plasmon}} = \frac{Q_{\text{Hot-electrons}}}{Q_{\text{tot}}} = \frac{Rate_{\text{Hot-electrons}}}{Rate_{\text{abs,photons}}} \tag{1.38}$$

In summary, an optimal plasmonic photocatalytic performance can only be achieved with trade-offs. Considering the intrinsic catalytic activity is also related to the size of the NP due to the number of low-coordinated atoms, the optimal size for Au NPs in the photocatalytic reaction is still an open question.

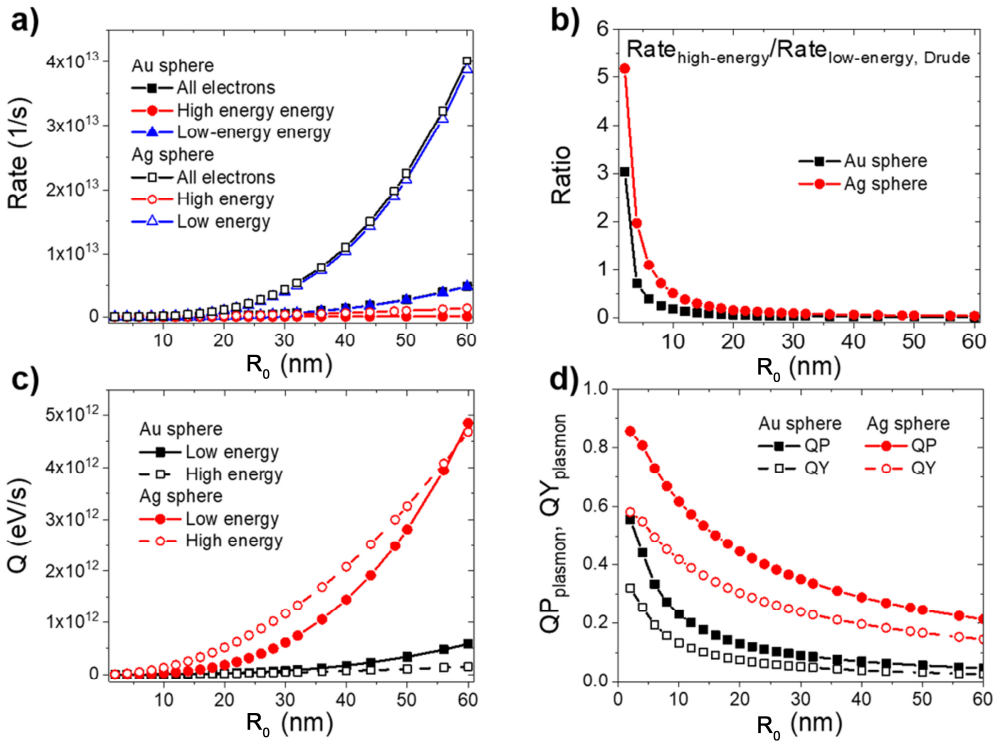

Figure 1.5. (a) High energy (hot) electron and low energy (Drude) electrons generation rates in Au and Ag NPs of different diameters. (b) Ratio of the High energy (hot) electron to low energy (Drude) electrons generation rates in Au and Ag NPs of different diameters. (c) Dissipations related to the generation of different kinds of electrons. (d) Quantum yield (QY) and quantum parameter (QP) in different diameters. Reproduced with permission from ref. [106-107]. Copyright 2017, American Chemical Society.

1.3.3 Timescale of excited electrons in plasmonic catalysts

The full life cycle of charge carriers in plasmonic catalyst is illustrated in **Figure 1.6**. The electrons in the dark are in thermalized distribution follows the classical Fermi-Dirac distribution. Under light irradiation, the electrons exhibit the collective oscillation, which is known as plasmonic resonance in metal NPs. The decay of plasmon follows different mechanisms, as mentioned in Section 1.3.1. The surface-assisted damping (Landau damping) shows a timescale ranging from 1 to 100 fs, which is responsible for the generation of 'hot' electrons (high-energy electrons).[108] The other two damping mechanisms show different timescales too. The electron-electron resistive damping shows the timescale of 0.1 to 1 ps and electron-phonon damping shows the timescale ranging from 1 to 10 ps. The further thermalization of electrons to the thermalized state takes 100 ps to 10 ns with energy dissipation in the form of heat.[109] If the metal NPs are supported by semiconductors, the hot electrons can inject into the CB of semiconductors, which possesses a timescale of ~ 20 fs.[110] When molecules are adsorbed on the plasmonic metal NP surface, the direct transfer of hot electrons to the LUMO of molecule shows a timescale ranging from 5 fs to 100 fs. The summary of the timescales is illustrated in **Figure 1.7**. The importance of clarifying the timescales is due to their correlation to the probability of the electron transfer process. For example, the hot electron injection to a semiconductor is a very fast process (~20 fs), which is faster than the thermalization (100 ps to 10 ns). It means the hot electrons have a high possibility to transfer to the semiconductor before thermalization. Similarly, the CID that the direct plasmonic generation of electrons in the LUMO of adsorbed molecules is a fast process too (~ 5 fs to 100 fs). On the contrary, the CIS that transfer of electrons from metal NPs to adsorbed molecules is less likely due to the longer timescale (~ 100 fs to 10 ps).

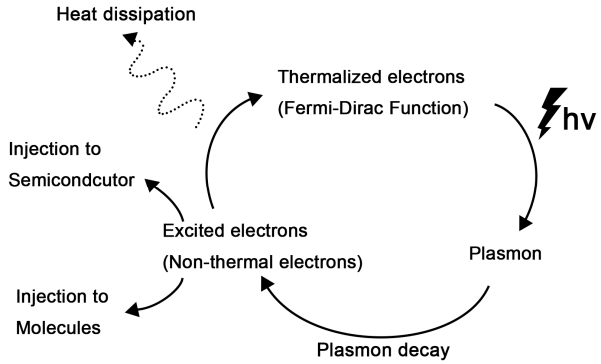

Figure 1.6. The scheme of electron excitation and thermalization process in plasmonic catalysts.

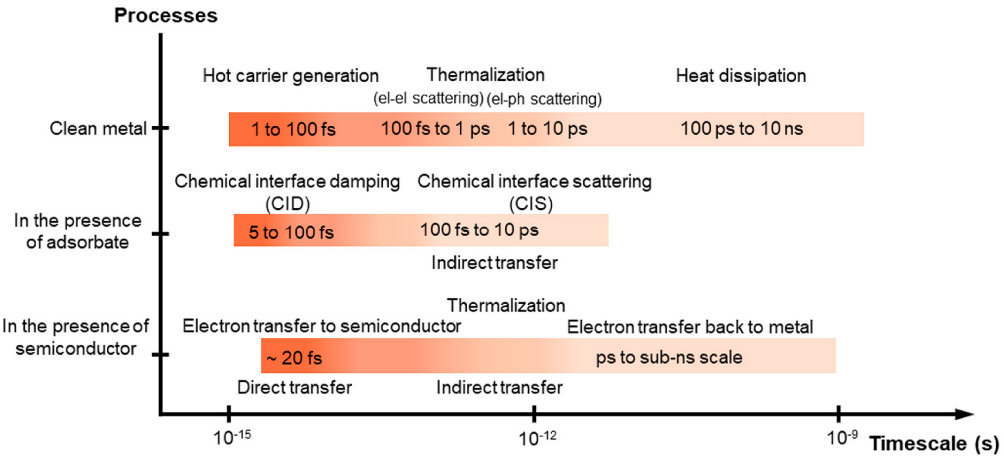

Figure 1.7. Timescale of possible processes during the plasmonic photocatalysis. Reproduced with permission from ref. 111. Copyright 2013, American Chemical Society.

1.3.4 Classification of plasmonic catalytic process.

Plasmonic catalysis can be classified into three main categories in terms of the hot electrons transfer path. In the first category, the electrons transfer from metal to adsorbed molecules and drive the reaction; in the second category, the electrons firstly inject into semiconductors and further migrate to adsorbed molecules; the last type is the nano-antenna effect without electron transfer.

1.3.4.1 Electron transfer from metal to adsorbed molecules

The first electron transfer path from metal NPs to the molecule can be further divided into two kinds: direct and indirect mechanisms. As schemed in **Figure**

1.8(a), the indirect mechanism is a two-step process that electrons are firstly excited by plasmon decay and the hot electrons are then injected into the adsorbed molecules. The other mechanism is called the direct electron transfer mechanism. When the molecule is strongly chemisorbed on the metal NPs, new orbitals are formed due to the hybridization between metal and molecules. Due to the CID, the electrons in metal NP are directly excited to the unoccupied hybridized orbital between molecule-metal, as shown in **Figure 1.8**(c). When the chemisorption is weak, there is no hybridized orbital. The optical excitation happens inside the molecule alone, which is called the direct intramolecular photoexcitation (**Figure 1.8**(b)). The difference between the CID and intramolecular excitation mechanisms is whether the hybridized orbitals are formed.

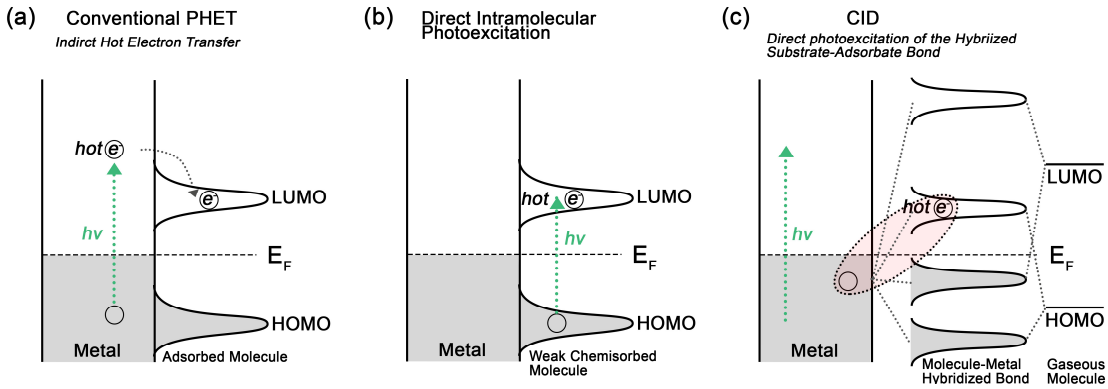

Figure 1.8. Plasmon-excited electron transfer between metal NPs and adsorbed molecules: (a) indirect transfer mechanism; (b) Photoexcitation inside weakly adsorbed molecule; (c) Chemical interface damping (CID) mechanism with electron excited from metal directly to chemisorbed molecules. The CID happens on the condition that hybridized orbitals formed between adsorbate and metal NPs.

Indirect transfer mechanism

The indirect plasmonic electron transfer from metal NPs to adsorbed molecules mechanism is a two-step process: (i) the plasmon decay excites electrons inside metal NPs; (ii) the hot electrons transfer into the LUMO of the weakly adsorbed molecule. The rate of electron injection into the adsorbed molecule can be described with following equations:[112]

$$Rate_{\mathrm{e}} = \gamma_{\mathrm{tun}} \frac{\delta n_e(\varepsilon_{\mathrm{mol}})}{n_{\mathrm{DOS}}(\varepsilon_{\mathrm{mol}})} \tag{1.39}$$

$$\gamma_{\mathrm{tun}} = 2\pi w_t^2 \rho_{\mathrm{DOS}}(\varepsilon_{\mathrm{mol}}) \tag{1.40}$$

where $Rate_{\mathrm{e}}$ represents the number of the electrons transferred to the molecule per second; γ_{tun} is the tunneling rate; $n_{\mathrm{DOS}}(\varepsilon_{\mathrm{mol}})$ is the density of states in metal NP at the energy of $\varepsilon_{\mathrm{mol}}$; $\delta n_e(\varepsilon_{\mathrm{mol}})$ is the distribution function of excited electrons at the energy of $\varepsilon_{\mathrm{mol}}$, which is defined in equations (1.20) and (1.31).

The efficiency of charge transfer ($\mathrm{eff}(\omega)$) can be calculated by dividing the energy density of hot electrons injected into the molecule by the total absorbed light energy:

$$\mathrm{eff}(\omega) = \frac{Rate_e(\omega)\cdot\hbar\omega}{\sigma_{\mathrm{NP}} I_0} \tag{1.41}$$

where the total absorbed energy is calculated by the product of metal NP cross section (σ_{NP}) and incident light energy (I_0). A recent experimental result supports this mechanism by quantitatively measuring the hot carriers with probe molecules.[113]

Direct transfer mechanism

The direct mechanism is featured by the direct excitation of hot electrons in metal NPs to the hybrid orbital between the molecule and metal NP. Experimental evidence of the direct electron transfer mechanism was reported by Boerigter et al.[114] The methylene blue molecules were absorbed on Ag nanocubes, and the Raman vibration spectra were characterized with incident light of 532 and 785 nm. For molecules in the dark, the Anti-stokes line in Raman spectra showed an exponentially weaker intensity than the Stokes line, because more molecules were at ground-state (**Figure 1.9**(a)). On the contrary, when the methylene blue/Ag sample was excited by 785 nm rather than 532 nm laser, the anti-stokes line was remarkably enhanced (**Figure 1.9**(b)). Moreover, the signal ratio of anti-stokes to stokes line showed a linear response to the incident light intensity. The evidence strongly proved the direct

charge transfer mechanism. Because if indirect charge transfer could excite the methylene blue molecule, excitation effects were expected to be observed under 532 nm light irradiation too. However, no Raman spectra change was observed for MB/Ag under 532 nm light excitation.

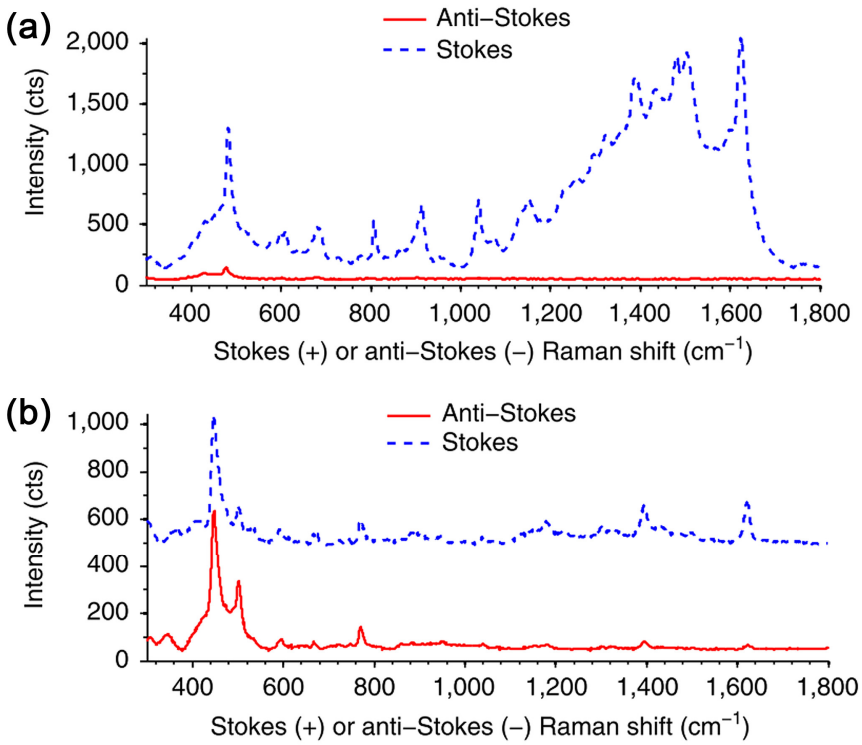

Figure 1.9. Stokes and anti-stokes spectra of Methylene Blue molecules adsorbed on Ag nanocubes with irradiation light wavelength of (a) 532 nm and (b) 785 nm. Reproduced with permission from ref. 114. Creative Commons CC BY license.

Similarly, Kale et al.[115] investigated the plasmon-enhanced CO preferential oxidation over Pt NPs in H_2-rich atmosphere. The direct and selective electron transfer from Pt NP to Pt-CO hybridized orbitals was adopted to explain the high selectivity to CO oxidation other than H_2 oxidation. The experimental evidence to support this mechanism was the wavelength-dependent QY data. The experimentally determined wavelength-dependent QY was in high consistency with the measured CO-adsorption induced UV-Vis DRS (**Figure 1.10**(a)). As shown in **Figure 1.10**(b), the wavelength-dependent QY calculated from the *Electron Scattering Model*[116-117] on RDS matched the trend determined by experiments.

The factors influencing the efficiency of direct electron transfer mechanism are complicated. For example, Qian et al.[118] suggested the larger Au NP size (~40 nm) were active for water splitting under visible light irradiation (λ > 430 nm). It was attributed to the higher LSPR intensity achieved by the larger NP. By contrast, some researchers[119-121] reported the smaller Au NPs could induce the more efficient charge transfer at the interface under visible light (λ > 430 nm). Additionally, in Priebe's work[122], the defects and band edge of TiO_2 support rather than the particle size of Au exhibited a more significant impact on the final H_2 production rate in the experiments driven by visible light (λ > 430 nm).

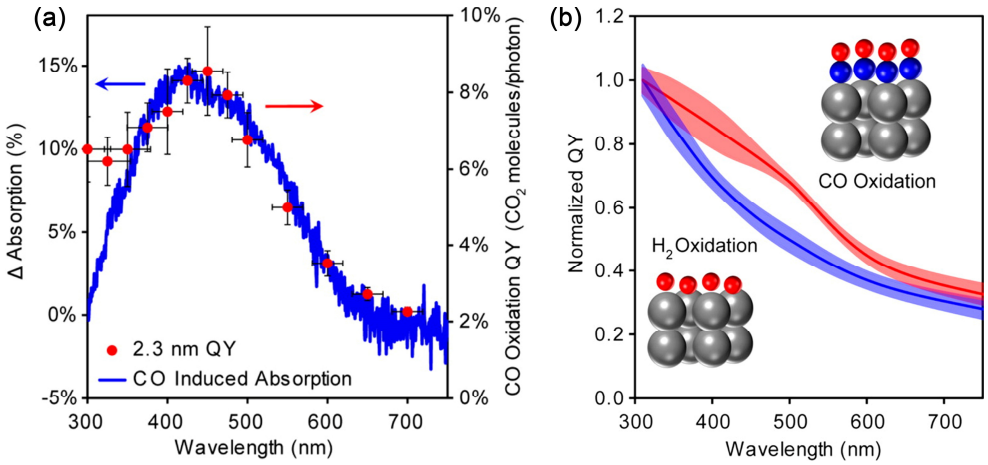

Figure 1.10. (a) Comparison between experimental Wavelength-dependent yields (QY) of CO oxidation and measured CO-induced UV-Vis spectrum; (b) Calculated wavelength-dependent QY from the two-temperature model. Reproduced with permission from ref. 115. Copyright 2014, American Chemical Society.

1.3.4.2 Electron transfer from metal to semiconductor supports

Similar to plasmon-induced hot carrier transfer between metal NP and molecules, the hot carrier transfer from metal NP to semiconductor can also be classified into direct and indirect pathways. The indirect mechanism is illustrated in **Figure 1.11**(a); the direct transfer mechanism is shown in **Figure 1.11**(b,c). The DICTT mechanism is featured of direct excitation of an electron from metal to CB of the semiconductor (**Figure 1.11**(b)). The other direct mechanism is the PICTT mechanism, as shown in **Figure 1.11**(c). The

plasmon-excited electron and holes are generated simultaneously in semiconductor and metal, respectively. It is due to the strong interdomain coupling and mixing of the metal and semiconductor energy levels, which is similar to the CID mechanism mentioned in section 1.3.4.1.

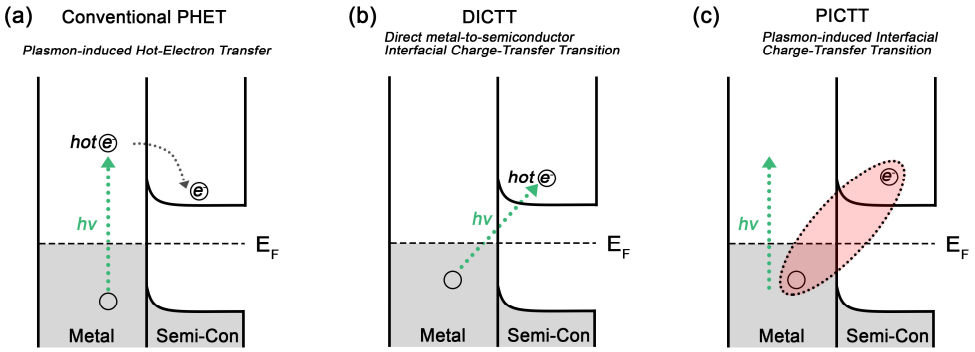

Figure 1.11. Scheme of different mechanism of plasmon-induced charge transfer between metal NP and semiconductors.

Indirect mechanism

It has been mentioned in section 1.3.3, the transfer of hot electrons to semiconductor is a fast process with high possibility. Two conditions have to be satisfied for a successful electron injection process: (i) energy condition: the energy of the hot electrons has to be higher than the Schottky barrier height (ϕ_B); (ii) momentum condition: ***k***-vector of hot electron needs to fall inside the emission cone in the momentum space (***k***-space).[123] The energy and momentum conditions are illustrated in **Figure 1.12**(a,b). The electrons excited by LSPR show the energy distribution described by the EDJDOS, $\mathcal{D}(E, \hbar\omega)$.[124] For simplicity, it is popular in literature to assume that hot electrons with isotropic momentum distribution and only a fraction of electrons possessing high enough perpendicular velocity ($\varepsilon_z = \frac{p_z^2}{2m} > E_B$). As a result, the current density generated due to the plasmonic electrons penetrating to the semiconductor follows the Fowler's equation:[111-112]

$$QY(\omega) = c(\hbar\omega - E_B)^n \cdot \frac{1}{\hbar\omega} \tag{1.42}$$

where *c* is the Fowler emission coefficient and *n* is a parameter related to the materials. For metal/semiconductor interface with Schottky barrier, E_B is usually the Schottky barrier energy, ϕ_B. For small metal NPs, the Fowler function can be adapted with suitable fitting coefficients:[112, 125-130]

$$QY(\omega) = c_{\text{geometry}}(\hbar\omega - E_B)^2 \cdot \frac{1}{4E_F\hbar\omega} \tag{1.43}$$

However, in small metal NPs ($R_0 < l_{\text{mfp}}$) the momentum of LSPR is not isotropic and the deviation from Fowler function becomes significant. To achieve a more accurate description, more sophisticated treatment, such as quantum mechanics formalization, needs to be implemented.[130-133] In the end, it is also noted that the tunnelling effects are negligible for the transmission of hot carries over the Schottky barrier.[134]

As described in section 1.3.2, the total hot electrons generation rate decreases while the ratio of hot electrons to all plasmonic electrons increases when metal NP size becomes smaller. Therefore, there must be an optimal Au NP size for the highest QY in theory. In an early study by Tetsuma et al.[135], the smaller size of Au (~15 nm) has a higher electron transfer efficiency to semiconductor than those with larger diameters. Additional study on Au LSPR induced solar-cell efficiency investigation with a wide range of Au NP sizes further proves a monotonic increase of apparent quantum efficiency with the decrease of Au size from 40 nm to 5 nm.[136] However, it is still an open question and more investigations are needed to achieve an explicit result.

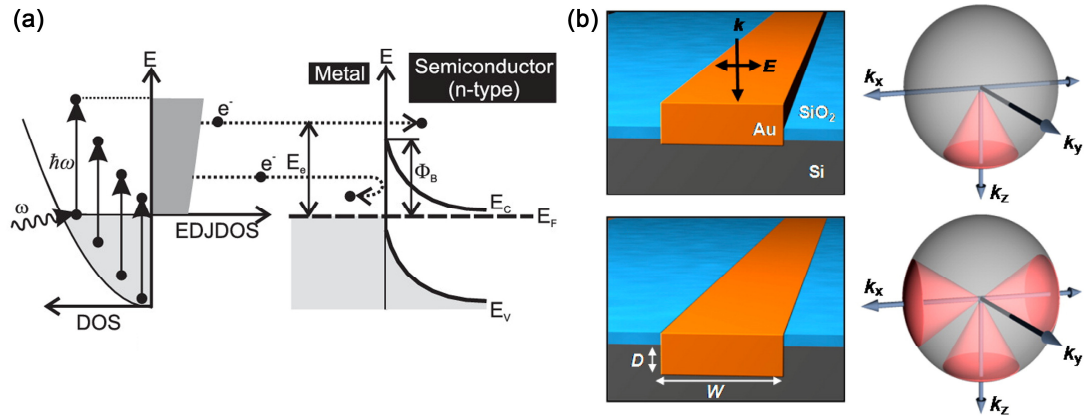

Figure 1.12. (a) Scheme of metal/semiconductor interface and Schottky barrier. (b) The scheme of cone in ***k***-space required by electron transfer across the interface. Reproduced with permission from ref.124, 137. Copyright 2011, American Chemical Society. Copyright 2012, AIP Publishing.

Direct mechanism

The direct mechanism also exists in the transfer of plasmonic electrons from metal NP to semiconductor, which is similar to the CID mechanism. Wu et al.[125] demonstrated that electron could be directly excited by plasmon decay from the metal to the strongly coupled CdSe. A high QE of 24% was reached during this so-called PICTT mechanism. The key evidence supporting the PICTT mechanism was that the QY was independent from the incident light wavelength, which was completely different from the conventional PHET mechanism.

1.3.4.3 Antenna effects

As suggested by the name, the metal NPs act as the light absorber (antenna) and transfer the plasmonic energy to adsorbed molecule or semiconductor. There is no electron transfer but energy transfer between metal NPs and molecule/semiconductor. As a result, it is also called the PIRET process.[138] For PIRET, the energy transfer rate can be calculated using the following equations:[139]

$$k_{\text{transfer}} = \left(\frac{R_0}{R}\right)^6 \cdot \frac{1}{\tau_{\text{donor}}} \tag{1.44}$$

$$R_0 = 0.2108(k^2_{\text{orientation}} \Phi_0 n^{-4} J)^{1/6} \tag{1.45}$$

$$J = \int F_D(\lambda) \times \varphi_A(\lambda) \times \lambda^4 d\lambda \quad (1.46)$$

where τ_{donor} is the radiative lifetime of energy donor; *n* is the refractive index; Φ_0 is the QY of the donor; J is the normalized overlap integral between the donor spectrum ($F_D(\lambda)$) and the acceptor spectrum ($\varphi_A(\lambda)$).

1.3.5 Mechanism of plasmonic hot carriers driven reactions

The LSPR-induced hot carriers can significantly affect the electronic state of catalysts. Therefore, the ***adsorption*** of small molecules on the surface of plasmonic catalysts can be remarkably affected by the LSPR induced hot carriers. For example, Liu et al.[140-141] found both the UV and visible light induced LSPR could enhance the CO adsorption on Au/TiO_2 and concluded the electrons could activate the CO molecules for further reaction. In a comparative investigation, Yang et al.[142] found that there was no enhancement of CO adsorption on the Au/Al_2O_3 under visible light irradiation. It was attributed to the positive charge or electron deficiency of the Au NPs. In addition to the plasmonic enhancement on adsorption, the hot electron induced ***desorption*** has also been reported. In a simplified model, the catalyst surface consists of two heat baths, the phonons (lattice vibration) and the electrons. The energy transfer between the two baths is through the electron-phonon coupling with a typical equilibrium time in the ps scale. The fs two-pulse correlation (pump-probe) measurements have been used to distinguish the hot electrons induced desorption from thermal effects induced desorption. Because the electron-phonon equilibrium time is in ps scale, if the time intervals between the two light pulses are shorter than the equilibrium time, combination effects are expected. The response of electron-mediated desorption should be remarkably faster than phonon-mediated desorption. There are two theoretical models to describe the electron transfer during the desorption.[143] The desorption induced by DIMET model is used to describe the hot electrons induced desorption. In DIMET model, the hot electrons excite the adsorbate by creating a transient negative ion resonance and the decay of excited negative ion to neutral causes the vibrational excitation in the molecule-metal bond. Another popular model, the frictional model, treats the

energy transfer between substrate and adsorbate in terms of friction, which can be used to describe both the electron and phonon-mediated desorption.[143] CO desorption was found driven by hot electrons on Cu[144] and phonons on Ru.[145] While in some cases, both the electrons and phonons contribute to the desorption.[146-147] Recently, Olsen et al.[117] further developed the DIMET model with the implementation of density functional theory (DFT) calculation to describe the enhancement of hot electrons on CO and NO desorption from Pt surface. Isotope effects are another indicator to distinguish the electron or phonon-mediated desorption: the electron-mediated mechanism usually shows a large isotope effect and the phonon-mediated one shows weak or absence of isotope effects.[145, 148]

In addition to the remarkable influences of hot carriers on molecule sorption, the plasmonic hot carriers also significantly affect specific reaction step, which results in the alteration of reaction rate and product selectivity. For example, Quiroz et al.[149] reported the controlling product selectivity of phenylacetylene hydrogenation with the help of plasmonic hot carriers. Based on the electronic structure analysis, the authors claimed that the hot carriers preferred to interact with triple-bond in phenylacetylene rather than the double-bond in styrene. Therefore, the further hydrogenation of styrene is relatively hindered. Kolobov et al.[150] investigated the hot carriers enhanced CO oxidation reaction. The authors believed that the hot electrons promoted the O_2 activation was ascribed to the enhanced reaction rate. Bonn et al.[151] reported the hot electrons-enhanced CO oxidation on Ru (0001) surface. By taking advantage of fs laser light source and monitoring the CO desorption and CO_2 formation timescale, it was found the CO_2 formation was an order of magnitude faster than the CO desorption and comparable with the electron excitation process. The experimental result indicated that the CO_2 formation was driven by the hot electrons, while the CO desorption was caused by the phonon effects derived from the electron-phonon coupling.

H_2 dissociative adsorption on the surface is an important step for CO_2 hydrogenation reaction. Yang et al.[142] pointed out the dissociative adsorption

of H_2 was suppressed at $Au^{\delta-}$ sites of Au/TiO_2 under visible light irradiation. While the electron-deficient $Au^{\delta+}$ could promote the dissociative adsorption of H_2 on the Au/Al_2O_3. On the contrary, the work from Mukherjee et al.[152] proved that the LSPR induced hot electrons on Au/TiO_2 contributed to the H_2 dissociation on the surface. As shown in **Figure 1.13**(a, b), the electrons were excited due to the plasmon decay in Au NP under visible light irradiation. The hot electron energy distribution overlapped with the antibonding orbitals of adsorbed H_2. Therefore, it was likely for the hot electrons in Au to transfer to the antibonding orbital. The negatively charged H_2 molecule ($H_2^{\delta-}$) showed an even lower activation energy for H_2 dissociation, which had a higher possibility to dissociate into two adsorbed H atoms (**Figure 1.13**(c)). A following up research by the same group[153] replaced the support for Au NP from TiO_2 to Al_2O_3 and SiO_2. Comparing with Au/TiO_2, the plasmon-induced H_2/D_2 dissociation rates on Au/SiO_2 was enhanced by almost 2 orders of magnitude. The authors ascribed the faster H_2 dissociation on Au/SiO_2 than Au/TiO_2 to the process of hot electrons transfer to TiO_2, which was competitive to hot electron transfer to H_2 molecules.

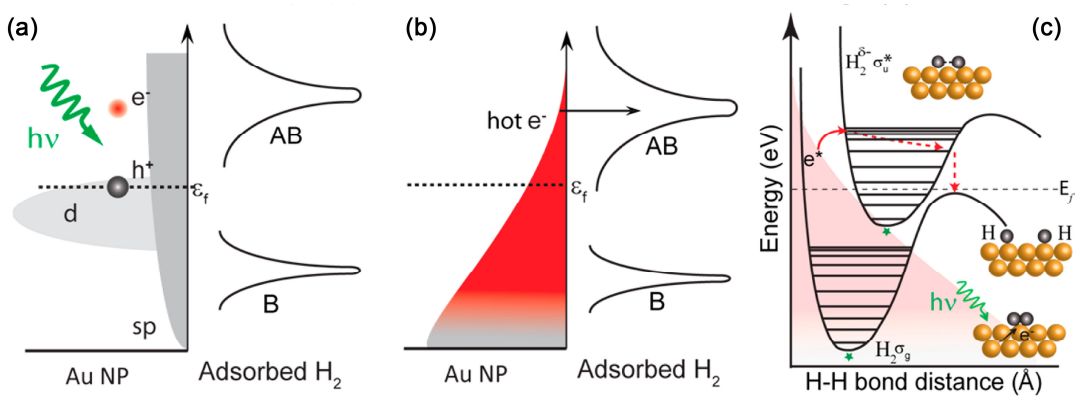

Figure 1.13. Schemes of hot electrons (a) excitation and (b) transfer to the antibonding orbital of adsorbed H_2. Proposed mechanism of hot electrons induced H_2 dissociation on Au surface. Reproduced with permission from ref. 152. Copyright 2013, American Chemical Society.

1.4 Principles of Au-based thermal catalysts

1.4.1 The electronic structure of Au

Au has been believed as an inert transition metal for quite a long history. The inertness can be generally explained by its electronic structure. Nørskov et al.[154-157] have proposed a successful model to explain this phenomenon: the *d-band theory*. A d-band centre position can act as a descriptor of the catalytic activity. For bulk Au, the d-band edge is located at 2~2.4 eV below the Fermi energy achieved by both DFT calculation[158] and photoemission spectroscopy experiment.[159-160] As shown in **Figure 1.14**(a, b), when H atom is adsorbed on the surface of metal NP, the orbitals between metal surface and H* atom hybridize and generate the bonding and antibonding orbitals. Comparing with Ni, Cu, Pt, the relatively low position of the d-band centre of Au results in the lower position of the Au-H antibonding orbital, which causes the weak adsorption to H atom (**Figure 1.14**(c)). In addition, the Au shows the largest coupling matrix, which makes the d-states more tightly bound. These two factors contribute together to the weak adsorption of H on Au surface. Similar d-band position-dependent adsorption strength has also been found valid for other atoms and small molecules.[157, 161-164] Although the d-band theory is very successful, it is important to emphasize that there are still experimental results against the trends predicted by DFT calculations. The limitation of d-band theory is still an open question.[165-166] Additionally, in real catalysts, the Au (or other metal) NP shows surface atoms with different coordination numbers, such as corner, edge, surface atoms etc. The electronic properties of the atoms at different sites are slightly different from each other. It will cause the deviation from the d-band model relying on relatively bulk property.

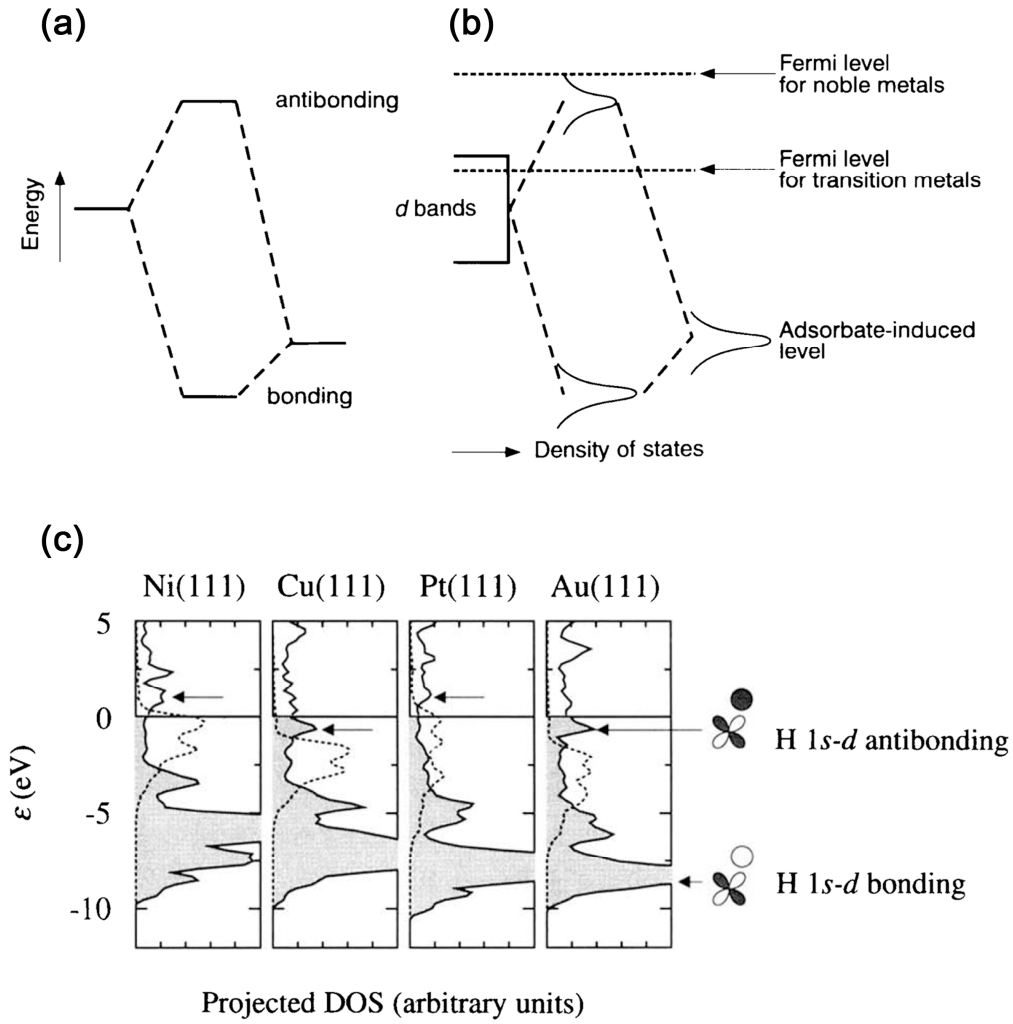

Figure 1.14. (a) Scheme and (b) formation of bonding and antibonding states for chemisorbed H* with metal surface. (c) The DOS plot for H adsorbed on the (111) surfaces of Ni, Cu, Pt and Au. The dash line represents the d-band of clean metal surface. Reproduced with permission from ref. 154. Copyright 1995, Nature Publishing Group.

The electronic structure of Au NP alone varies with the size (number of atoms), as presented in **Figure 1.15**. The small Au cluster exhibits the discrete energy levels; with increasing atom number in Au NP, the nondegenerate energy levels become close to each other. When the nondegenerate energy is close enough, the quasi-continuum of the energy levels is called the energy band. When the Au cluster is small, the spacing between the discrete energy levels (δ) can be expressed with dividing the fermi energy E_F by the number of atoms in a cluster (N):

$$\delta = E_F \cdot \frac{1}{N} \tag{1.47}$$

For nanocluster with limited atom numbers, the HOMO and LUMO exist due to the discrete energy levels. The energy gap between HOMO and LUMO exhibits an important correlation with stability and chemical reactivity.[167] For instance, the large energy gap induces high stability, and the phenomenon was observed for the cluster with 'magic number' of atoms.[168-170] The CO adsorption was enhanced on Au nanocluster with the magic number and the CO oxidation activation energy was lowered.[171] When Au size grows larger, the HOMO-LUMO gap becomes smaller.[102, 172] As mentioned in the earlier paragraph, the d-band position and d-band width are important descriptors of catalytic performance. The band position and width are also NP size-dependent. According to theoretical calculation results, the d-band position shifted towards E_F when the NP size decreased.[173-175] However, there is still experimental investigation suggesting a different correlation between NP size and d-band position. Visikovskiy et al.[176] used photoelectron spectroscopy to investigate the electronic structure of Au NP supported by carbon. It was found that the d-band centre position and d-band width of Au NP were close to the values in bulk, when the Au atom number exceeded 150 atoms/NP (~2.6 nm in diameter). When the atom number in the cluster decreased, the d-band position shifted away from E_F; while all the d-band positions of Au NP were higher than the bulk value.

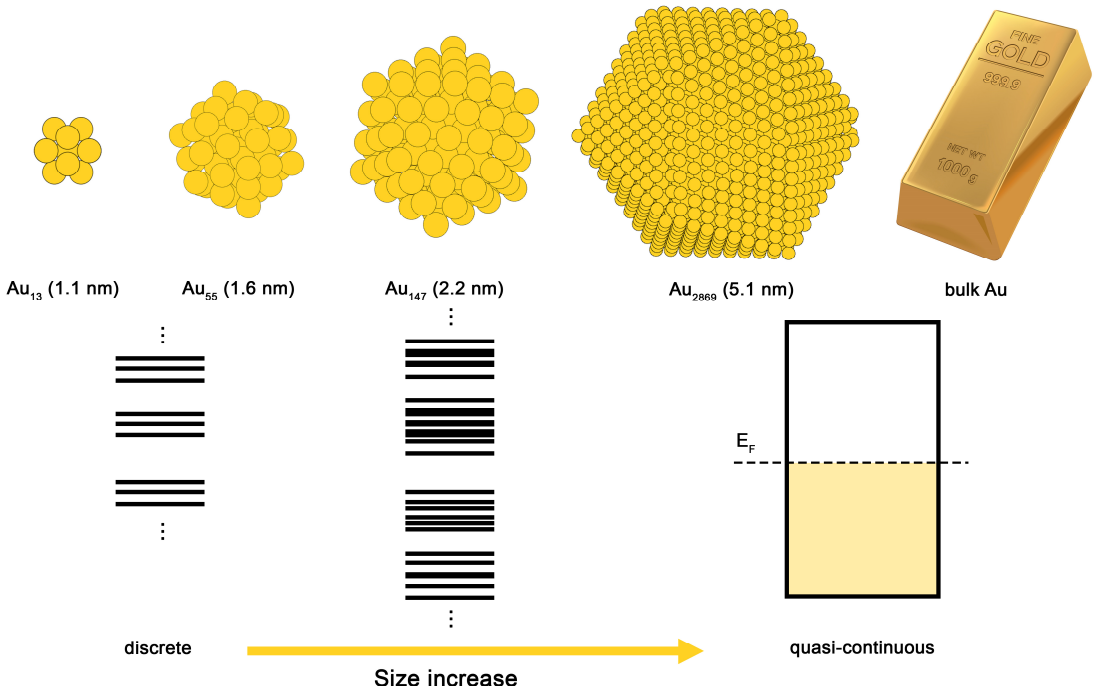

Figure 1.15. Scheme of the electronic structure of Au cluster, NP, bulk structure.

1.4.2 The interaction between Au nanoparticles and oxides supports

For gas phase heterogeneous catalytic reaction, the metal NPs are usually dispersed on the oxides support. The oxide support not only acts as the substrate of the metal NPs, it can also contribute to the catalytic reaction via different ways including electronic interaction with metal NPs, providing active sites and even exchanging atoms with the reactants. When metal NPs are loaded onto oxides, especially *reducible* oxides, the interaction between metal NP and oxides is complex and strongly affects the catalytic performance of the metal NP. As a result, the term SMSI is proposed by Tauster et al.[177-179] to describe the phenomena observed when group VIII metals interact with *reducible* oxides.

The phenomena of the classical SMSI can be summarized with following features:[180-181] (i) the metal NPs are wetted on the oxide support forming strong bonding, which results in a well-dispersion of metal NPs on the surface; (ii) the

decrease or even complete loss of the adsorption of small molecules, eg. CO and H_2; (iii) significant electron transfers between metal NPs and oxides supports; (iv) the formation of SMSI is reversible. The formation of the classical SMSI can be induced by pre-treatment at high temperature with different atmospheres. In the most conventional high-temperature reduction (above 300 °C), the treatments can form the suboxide of the reducible support, which further migrates to the metal particle forming the encapsulation. In summary, from a fundamental perspective, the results of SMSI can be classified into two categories: (i) geometry changes; (ii) electronic structure changes;

1.4.2.1 SMSI between Au NPs and supports

Although the SMSI has been observed between other VIII group metals and TiO_2 as early as the 1970s, the formation of SMSI between Au and reducible oxides was not accepted as a consensus until very recently.

Geometry evolution

In 2017, research on the Au/TiO_2 SMSI in the real reaction condition was conducted by Tang et al.[182] As shown in **Figure 1.16**(a, b), it was found the 10%H_2/He treatment at temperature 300 to 500 °C could result in the encapsulation phenomenon as well as the loss of CO adsorption ability over Au/TiO_2. And the encapsulation retreated under the re-oxidation by 10%O_2/He treatment at 400 °C. The same mass interaction, encapsulation, has been observed using *in-situ* ETEM technology by Kuwauchi et al. in 2012.[183] As shown in **Figure 1.16**(c-e), both the O_2 environment and large flux of incident electron beam could induce the reorganization of the TiO_2 support forming the thin layer covering the Au NPs. The O_2-induced encapsulation phenomena have been observed between Au and other metal oxide supports too. For example, Liu et al.[184] reported the formation of the SMSI between the ZnO nanorods and Au NPs. The ZnO partially covered the Au NPs when treated in O_2 atmosphere at 300 °C, and the encapsulation was reversely removed by treating in H_2 atmosphere at the same temperature.

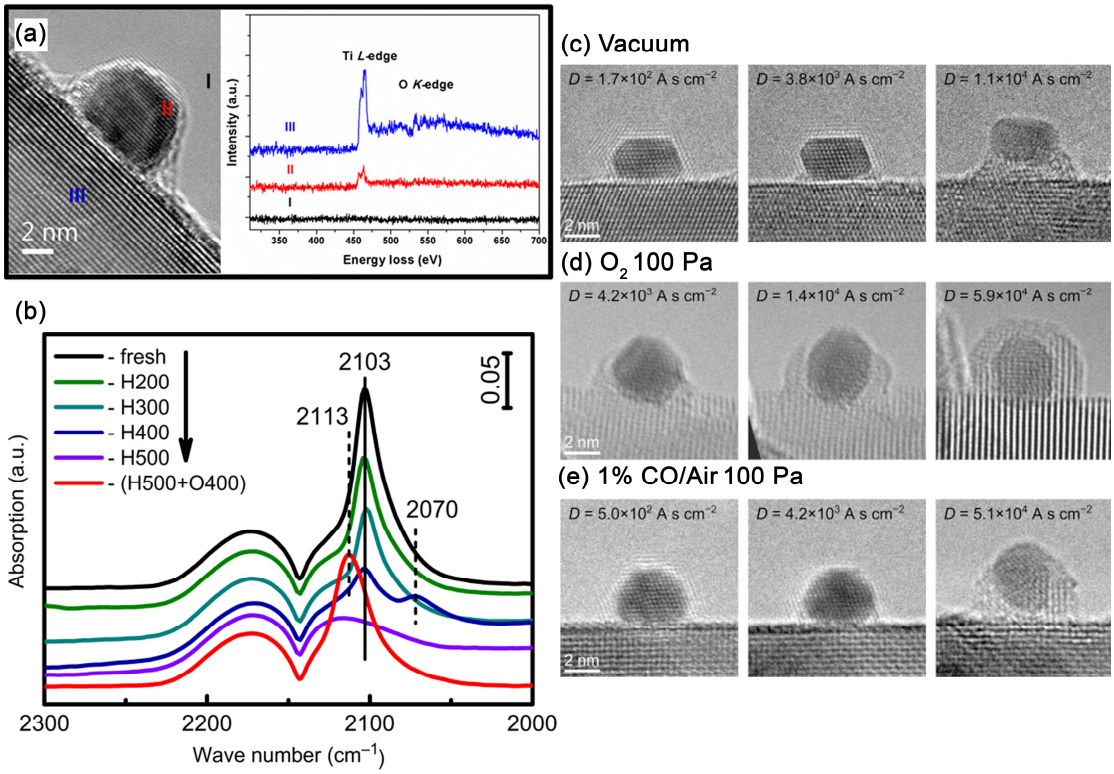

Figure 1.16. (a) TEM image and corresponding EELS of Au/TiO_2 after H_2 treatment at 500 °C. (b) In-situ FTIR spectra of CO adsorption on Au/TiO_2 after being treated under different conditions. Reproduced with permission from ref. 182. Creative Commons Attribution NonCommercial License 4.0 (CC BY-NC). ETEM images of Au/TiO_2 at atmospheres of (c) vacuum, (d) 100 Pa O_2 and (e) 1%CO/Air 100 Pa. Reproduced with permission from ref. 183. Copyright 2012, WILEY-VCH Verlag GmbH & Co. KGaA, Weinheim.

As proposed by Fu et al.[185], the encapsulation of the metal NP by oxides needed to meet two conditions: (1) the Vo defects in oxides and (2) metal nanocluster with large work function could induce electron transfer from TiO_2 to metal; the resulted electric field could drive the outward diffusion of Ti cations and further caused the encapsulation. One of the proposed reasons to explain the harder formation of SMSI between Au and oxides is the low activity of Au in splitting H_2. And the active H* is believed to be indispensable for the reduction of TiO_2 and following reorganisation.

The half-covering of the metal by oxide support in SMSI shows positive aspects due to the high stability against sintering. However, the loss of the ability for small molecule adsorption is the main drawback since it mainly decreases the catalytic activity. The blocking of the metal NP is usually

believed as one of the reasons for the vanishing of small molecules chemisorption.[186-188]

The electron transfer between the metal and oxides support

The electronic interaction between metal cluster and semiconductor interface results in two results: electron transfer and Schottky barrier. Theoretically, when metal and semiconductor having different work functions attach together, their Fermi energy level will achieve equilibrium by electron transferring: the electrons will move from the higher Fermi energy level to lower Fermi energy level.[189] If the metal has the larger work function interacts with an intrinsic n-type semiconductor, for example Au/TiO_2, the electron will transfer from the TiO_2 to Au. The depletion of electrons in the TiO_2 side of interface causes a potential energy barrier for electron transport, which is often termed as the Schottky barrier.[185] In realistic metal/semiconductor, the defects at the interface (surface states) will play a critical role.[190] In the covalent semiconductor-metal interface, it has been found the Schottky barrier height is almost independent from the choice of metal,[191] which is now known as the "Fermi level pinning" effect.

The electron transfer between Au and TiO_2 is not as straightforward as it looks.[99] Although the Schottky model predicts in theory that the electron transfer from TiO_2 to Au due to the larger work function of Au (~5.3 eV) than TiO_2 (~4.2 eV),[192-194] theoretical calculation suggested bulk Au and stoichiometric TiO_2 had negligible electronic interaction.[195-197] Following several factors are supposed to be considered on the topic of electronic interaction between Au and TiO_2. (i) The crystal phase of the TiO_2. The anatase exhibited a higher affinity (or larger work function) than rutile by ~0.4 eV.[198-199] (ii) Au cluster size. The shift of Au XPS binding energy to higher value was just the initial state effects. The XANES experiments (free of charging effects) suggested there was negligible electron transfer between bulk Au and bulk TiO_2. Only when the Au size was small enough, the electronic interaction became significant.[200-202] The small size of Au nanocluster exhibits non-metal property, which shows the shift of Fermi energy. (3) V_O in TiO_2. DFT calculation

results suggested the work function of TiO_2 became smaller when the surface was reduced.[203] Direct *in-situ* XPS evidence proved that the negatively charged Au was attributed to the electron transfer from the reduced rutile (110) surface.[204-205, 186] (4) The adsorbed molecules. Theoretical *ab-initio* molecular dynamics (AIMD) calculation results found that the reduced rutile (110) surface showed similar work function with Au_{20} NP (5.1 eV vs 5.0 eV, respectively). Therefore the electron transfer was easily affected by the adsorbed molecules and atmosphere.[206] As reported by Manzoli et al.[207], the Au NP supported by CeO_2 exhibited cationic state under oxidizing atmosphere while anionic state under reducing atmosphere.

However, not all researchers believe that electrons would transfer from TiO_{2-x} to Au. Using *in-situ* XPS, Yu et al.[195] reported the positively charged Au when SMSI was significant between Au and TiO_2 with V_O. On the contrary, Au presented metallic state when interacted with stoichiometric TiO_2 surface, where the interaction was weak.

1.4.2.2 The interaction between Au and non-reducible oxides

Comparing with the reducible metal oxide support, the interaction between Au NP with non-reducible metal oxide support is relatively simple and weak.[208] Reducible oxides are featured of the capability to exchange the O with environments with small energy barrier; while nonreducible metal oxides do not easily lose O. Generally, the reducible metal oxides include TiO_2, Fe_2O_3, WO_3, NiO, CeO_2, ZnO, etc.; the nonreducible metal oxides include SiO_2, Al_2O_3, etc.[209] In the case of geometry evolution, the encapsulation is seldomly observed due to the less mobility of O in the crystal. On the other hand, the electronic interaction between Au and nonreducible metal oxides are weak but still exists. The nonreducible metal oxides are usually wide bandgap semiconductors or insulators. It is hard to generate V_O on the surface of nonreducible metal oxides. Because of the surface charge on SiO_2 and its weak interaction with Au, it is difficult to achieve a homogeneous distribution of Au NPs on SiO_2, which causes detrimental effects on the catalytic performance.[194]

1.4.3 Effects of metal-support interaction on catalytic performance

As mentioned in theprevious section, the static electron transfer between metal clusters and oxide support is sometimes termed as “EMSI”, which strongly affects the catalytic performances.[210-211] In the literature, the electronic interaction effects are also discussed as the Au oxidation state effects.[212]

CO oxidation reaction is an important application for Au catalysts. However, in the literature, metallic, anionic and cationic Au NP were all claimed active for CO oxidation.[212-214] The Au oxidation states have significant influences on CO oxidation performance, because the CO is mainly adsorbed on Au.

The DFT calculations on CO and O_2 adsorptions on Au NPs are well-documented. Most of the researches suggested the CO was more strongly bonded to positively charged small Au clusters; while O_2 intended to bond to neutral/negatively charged Au NP.[215-219] However, Gao et al.[171] compared the CO/O_2 adsorption on relatively larger Au clusters with neutral and anionic oxidation states. The authors claimed that both the CO and O_2 more strongly adsorbed on anionic cluster than on the neutral counterparts. Additionally, the activation energy for CO oxidation reaction was smaller on the negatively charged Au clusters. Therefore, the controversy about the Au oxidation state effects on CO oxidation performance is likely due to different RDSs of this reaction on specific catalysts.

As mentioned earlier, the V_O can donate the extra electrons to the Au and make the Au negatively charged, which is a typical kind of EMSI. Wang et al.[220-221] reported that the CO could reduce the TiO_2 support and induce V_O on the surface, which resulted in the negatively charged Au NPs. The CO oxidation capability was found significantly suppressed due to the retarded CO adsorption. With reaction proceeding, the V_O was gradually replenished and the CO oxidation reaction rate recovered. Guzman et al.[222] took advantage of *in-situ* XANES to investigate the effects of Au oxidation states on the CO oxidation reaction rate over Au/MgO. It was found that the higher ratio of the cationic gold cluster associated with higher CO oxidation activity.

On the contrary, Chenakin et al.[223] reported a higher CO oxidation reaction rate correlated with more negatively charged Au NP due to the abundance of V_O in TiO_2 support. Similarly, Yoon conducted the comparison of CO oxidation performance between Au clusters loaded on stoichiometric and reduced MgO (001) surfaces. The negatively charged Au due to the V_O outperformed the cationic Au supported by stoichiometric MgO. The phenomenon was attributed by the authors to the poor O_2 adsorption on cationic Au. Kung et al.[224] compared the CO oxidation performance of oxidized Au and reduced Au supported by TiO_2. It was found that the oxidized Au supported by TiO_2 showed poor CO oxidation capability and the metallic Au was proposed as the active site. Similarly, Green et al.[225] investigated the CO oxidation reaction at 120 K over Au/TiO_2 with different metal oxidation states. A 22-times faster oxidation rate was observed over reduced Au/TiO_2 than the pre-oxidised one.

1.4.4 Effects of Au NP size on catalytic performance

Au has a long history been deemed as inert for catalytic reaction until 1980s, Haruta[226-227] and Hutchings[228] independently reported the high activity of Au catalysts when the Au size decreased to a few nanometres.[229] When Au NP supported on the metal oxides surface, the Au NPs usually exhibit three basic geometries: cuboctahedron, decahedron and icosahedron, as shown in **Figure 1.17**(a-f). As the size of the Au NP decreases, the fraction of under-coordinated atoms increases. The under-coordinated atoms in NP can be classified into the following kinds: corner atoms, edge atoms, surface atoms and perimeter atoms. Their fraction evolutions as a function of Au NP size are shown in **Figure 1.17**(g). The difference in catalytic behaviours of Au atoms at different locations are derived from their different coordination conditions.

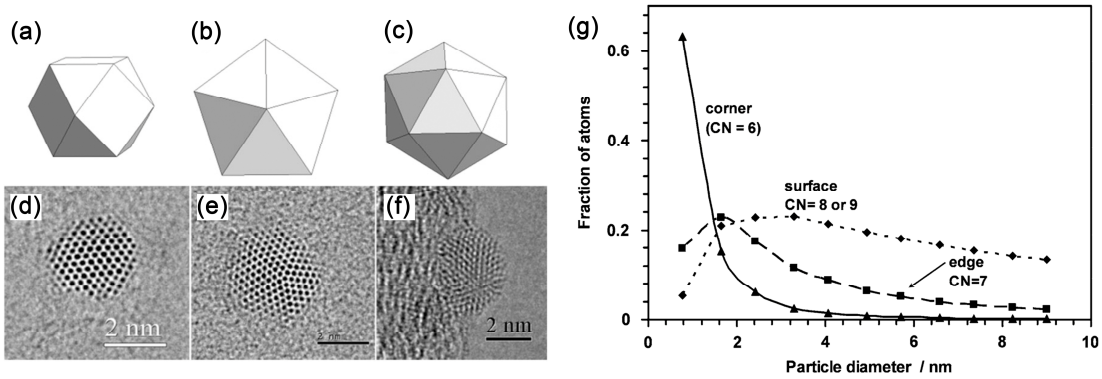

Figure 1.17. Schematic diagrams and corresponding TEM images of Au NPs in cuboctahedron (a, d), decahedron (b, e) and icosahedron (c, f), respectively. Reproduced with permission from ref. 230. Copyright 2016, Royal Society of Chemistry. (g) Calculated fraction of atoms on corner, edge, surface in Au NP as a function of Au NP particle diameter. The calculation is based on the half-truncated octahedron model. Reproduced with permission from ref. 231. Copyright 2007, Springer Science Business Media, LLC.

It is more fundamental to understand the mechanism underpinning the size effects on catalytic activity. Based on the investigation on the correlation between the number of Au atoms at different sites and CO oxidation rate, the active sites for the reaction can be revealed. For example, Fujitani and Nakamura[232] reported the CO oxidation performance evaluation over both the powder Au/TiO_2 catalysts and model catalysts Au/TiO_2(110). As shown in **Figure 1.18**(a, b), at 300 K, the TOF showed a linear correlation with the number of atoms at perimeter site; while at 400 K, the TOF correlated directly with the number of surface atoms. These results suggested that at different temperatures, the active sites were different, which was due to the different reaction mechanisms. Williams et al.[233] reported the investigation on WGS reaction on Au/TiO_2 and found smaller Au NP size resulted in a higher reaction rate. Moreover, the reaction rate correlated with the number of corner atoms in Au NPs.

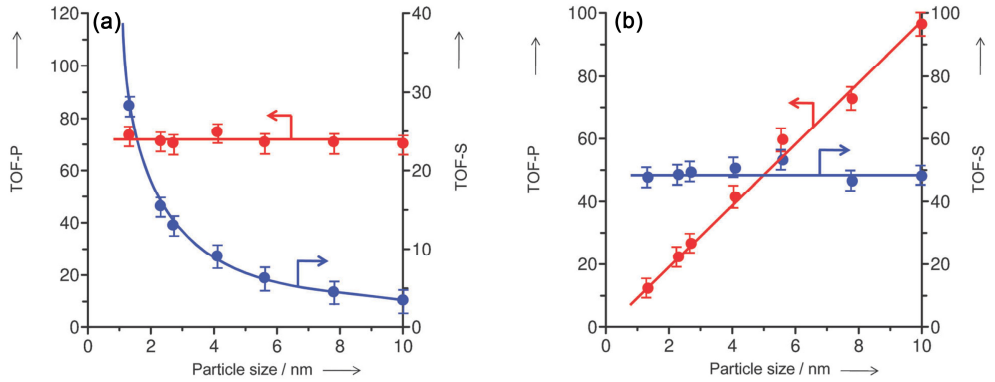

Figure 1.18. TOF-P (normalized by perimeter atom number) and TOF-S (normalized by surface atoms) for CO_2 formation over Au/TiO_2 (110) at (a) 300 K and (b) 400 K, respectively. Reproduced with permission from ref. 232. Copyright 2011, WILEY-VCH Verlag GmbH & Co. KGaA, Weinheim.

Similar phenomena are found on hydrogenation reaction on Au-based catalysts. H/D exchange experiments over Au/TiO_2 reported by Fujitani et al.[234] unravelled a direct correlation between Au cluster size and its ability in H_2 heterolytic dissociation. It was found that the higher HD production rate was achieved when Au NP size became smaller; moreover, the TOF of HD formation was consistent with the number of perimeter sites at the Au-TiO_2 interface.

It is important to emphasize that some researchers believe that an optimal Au NP size exists for the highest catalytic performance. For instance, Valden et al.[235] used scanning tunnelling microscope/scanning tunnelling spectroscopy (STM/STS) to investigate the CO oxidation performance over Au/TiO_2 with Au NP size ranging from 1 to 6 nm. It was found in CO/O_2 mixture of a total pressure of 40 Torr, the optimal Au NP size was ~3.5 nm. Qian et al.[236] investigated the Au cluster size-dependent CO oxidation performance over Au/SiO_2. It was found that supported Au clusters within the size range of 3-4.5 nm showed the highest performance, which was due to the bulk-like electronic structure and abundance of low-coordinated atoms, as shown in **Figure 1.19**.

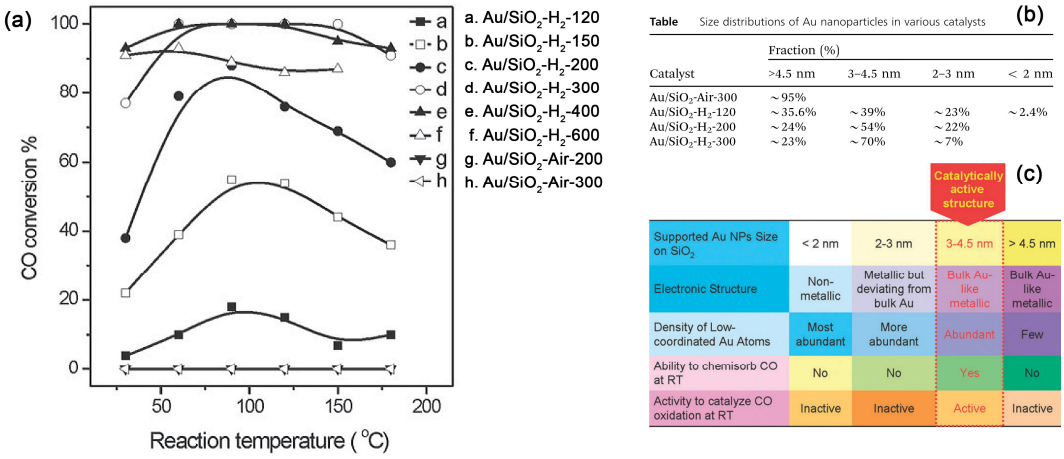

Figure 1.19. (a) CO oxidation catalytic performance of Au/SiO_2 with different pretreatments. (b) Size distributions of Au clusters after different pretreatments. (c) The correlation between Au size, electronic structure, density of low-coordination atoms and CO oxidation performance. Reproduced with permission from ref. 236. Copyright 2013, Royal Society of Chemistry.

1.4.5 The role of oxide support in heterogeneous catalytic reaction

1.4.5.1 Perimeter as active sites

As already mentioned in section 1.4.4, the model of metal-support perimeter as active site is very successful in explaining the Au metal NP size effects.[237] However, the reason why the perimeter site is more active than the surface site is not explained. One of the excellent examples to explain the role of oxide support is the H_2 dissociation. H_2 dissociation is a well-documented process in homogeneous catalysis, which can be classified into two categories: homolytic and heterolytic dissociation. On the Au NPs alone, the Au atoms at different site of the NP exhibit similar affinity to electrons.. Therefore, the H_2 dissociation on Au NP alone is homolytic. On the contrary, at the perimeter site, one of the H atoms bonds to the O in the oxides, while the other H atom adsorbed on Au NP. Due to the different electronegatively of Au and O atoms, the H_2 molecule is polarized. As a result, the E_a of heterolytic dissociation is much smaller than the homolytic dissociation.[238-241]

1.4.5.2 Oxygen Vacancy

The V_O is the most important surface feature on reducible metal oxides surface. As the electron-donating effect of V_O has already been described in former

section 1.4.2, this section focuses on the direct involvement of V_O in the reaction. Taking TiO_2 as an example, the existence of V_O makes TiO_2 a n-type semiconductor intrinsically. The recent direct evidence from STM and STS methods suggested the creation of V_O left two extra electrons trapped at adjacent Ti atoms forming polaron.[242] Ti^{3+} state derived from the localization of extra electron locates at ~1.1 eV below E_F, which was revealed by the VB spectra using resonant photoemission experiments.[243-244] The existence of V_O also induced magnetism to TiO_{2-x} due to the localised excessive electrons to adjacent Ti atoms.[245] The experimental results suggest the ferromagnetism of both reduced anatase[246] and rutile.[247] Atomic level understanding the magnetism of TiO_{2-x} is still an open question. Both ferromagnetic[248-250] and antiferromagnetic[251] states have been suggested by DFT calculation. And the magnetism is site- and facet-dependent for the V_O.[252-253] The V_O on the surface with excessive electrons shows strong adsorption to Lewis acid molecules (eg. CO_2) and electrophilic molecules (eg. O_2, H_2O). The V_O site with extra electrons also promoted the dissociation of O_2 and facilitated the MvK mechanism.[254-256] The V_O on the surface could even help to form the solid frustrated-Lewis-pair, which could remarkably lower the E_a of H_2 heterolytic dissociation.[257]

Besides the atomistic description on the role of V_O, the parameters representing the macroscopic property of oxides support are sometimes useful descriptors too. The OSC is a measurable parameter representing the capability of O transfer between the metal oxides and reactants.[258] As described in sections 1.4.4 and 1.4.5.1, researchers have found the reaction rate is directly related to the Au atoms at perimeter size, while the fundamental reasons are not unravelled. Kotobuki et al.[259] took advantages of TAP reactor to analyse the kinetics of CO oxidation on Au/TiO_2 catalyst. The CO conversion at 80 °C on Au/TiO_2 linearly correlated with $Au\text{-}TiO_2$ perimeter length. Additionally, it is found the linear relationship between interface perimeter length and OSC of TiO_2 (**Figure 1.20**(a)). Therefore, the experimental evidence suggested the CO oxidation reaction was highly related to the oxygen transfer at the perimeter sites. OSC is also useful to unravel the effects

of reducibility of metal oxides support on catalytic performance. Widmann et al.[260] investigated the CO oxidation performance on Au NPs supported by Al_2O_3, TiO_2, ZnO, ZrO_2 supports and determined the OSC of the different catalysts. As shown in **Figure 1.20**(b), although the relation between CO conversion and OSC of different catalysts were not linear, it was still rational to claim the strong correlation between activity and OSC of the metal oxides support.

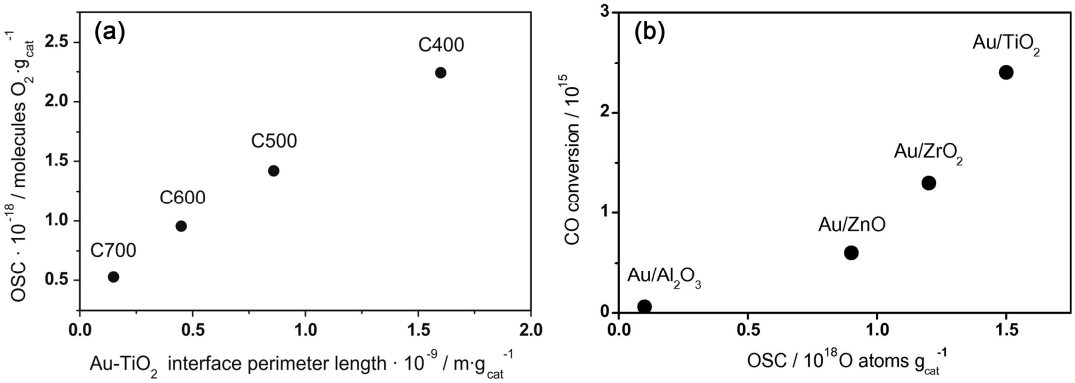

Figure 1.20. (a) The correlation between OSC and length of Au-TiO_2 interface perimeter. Reproduced with permission from ref. 259. Copyright 2009 Elsevier Ltd. (b) CO conversion versus OSC of different catalysts. Reproduced with permission from ref. 260. Copyright 2010 Elsevier Ltd.

1.4.5.3 The acidity, basicity of the metal oxide support.

The acidity and basicity are important topics for γ-Al_2O_3, which are used to explain the catalytic performance. Although still under debate,[261-262] the most widely accepted atomistic level understanding of the surface structure and property of γ-Al_2O_3 are reported by Krokidis et al.[263] and Digne et al.[264-265] The bulk γ-Al_2O_3 crystal structure is inherited from boehmite (γ-AlOOH) through dehydration process. The resulting γ-Al_2O_3 exhibited a fcc sublattice of oxygen atoms, which generates octahedral (75%) and tetrahedra (25%) interstices. In addition, the (110) surface predominated the surface of γ-Al_2O_3 with 74% of the total area; (100) surface constituted 16% and (111) surface contributed to the rest 10%. The structure proposed by the authors showed the important feature of no structural vacancies. Another important feature of γ-Al_2O_3 surface

is the adsorbed OH*. The complete dehydroxylation requires calcination at about 1000 °C.[266]

Due to the nature of ionic bond between Al-O, the under-coordinated Al and O atoms on the surface provide acidic and basic sites for the reaction. Additionally, the adsorbed OH* group also acts as the basic site too. The straightforward method to determine the acid and basic sites on the surface of γ-Al_2O_3 is to introduce probe molecules, such as ammonia, CO_2, CO, pyridine, etc, and analyse the adsorption via spectroscopy or TPD process. Most of the researchers believe there are at least three types of Lewis acid sites existing on the surface of γ-Al_2O_3, namely the weak, medium and strong Lewis acid sites.[267-271] The origin of Lewis acidity is the empty 3p orbitals of unsaturated Al atoms on the surface including Al_{3C}, Al_{4C} and Al_{5C}, where the subscript denotes the coordination number of Al atoms. The Brønsted acid sites are weakly observed on the surface via pyridine adsorption experiments, which are derived from the surface OH* species adsorbed at under-coordinated Al atoms.[265-266] For γ-Al_2O_3, the Lewis acidity predominates over the basicity on the surface.[261] In the end, it is important to point out the acid and base sites can work synergistically and show high activity.

1.5 Mechanism of photocatalytic CO_2 conversion on heterogeneous catalysts

From the perspective of photocatalytic CO_2 reduction, there are generally two aspects to consider: the thermodynamics and kinetics. In the case of thermodynamics, considering the photocatalytic reduction and oxidation are driven by the photoexcited electrons and holes respectively, the CBM and VBM need to be more negative than the reduction potential of CO_2 and more positive than and the oxidation potential of proton source (usually water, H_2) respectively. Though such kind of comparison is over-simplified and only based on the thermodynamic data in standard condition, it is a good method to quickly screen out the candidate photocatalysts. The CBM, VBM of

semiconductor candidates and the redox potentials of CO_2 reduction and H_2O splitting are summarized in **Figure 1.21**.

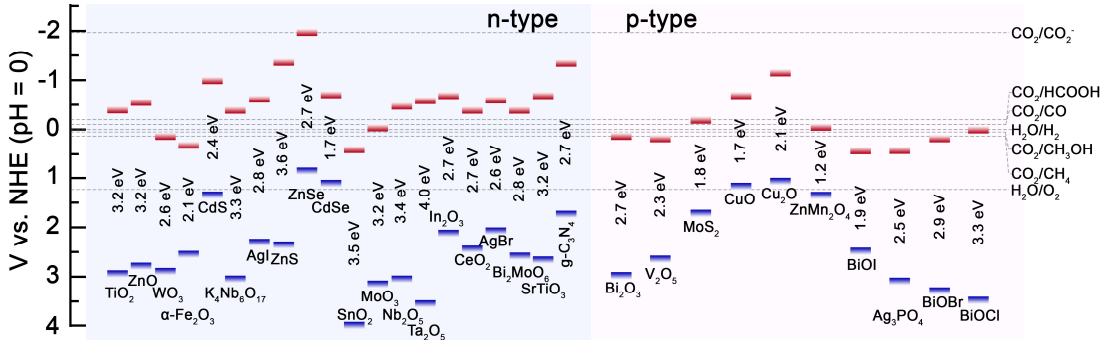

Figure 1.21. The CBM and VBM positions of conventional semiconductors and the redox potentials of CO_2 reductions and H_2O splitting.

During the photocatalytic CO_2 reduction with H_2O, the reduction potentials to common products can be expressed with the following equations (vs. NHE, pH=7, 25 °C):[73, 272]

$$CO_2 + e^- \rightarrow CO_2^{\cdot-},\ E^0 = -1.90\ V \quad (1.48)$$

$$2H_2O + 2e^- \rightarrow 2OH^- + H_2,\ E^0 = -0.41\ V \quad (1.49)$$

$$2H_2O + 4h^+ \rightarrow 4H^+ + O_2,\ E^0 = +0.817\ V \quad (1.50)$$

$$CO_2 + 2H^+ + 2e^- \rightarrow CO + H_2O,\ E^0 = -0.51\ V \quad (1.51)$$

$$CO_2 + 2H^+ + 2e^- \rightarrow HCOOH,\ E^0 = -0.61\ V \quad (1.52)$$

$$CO_2 + 6H^+ + 6e^- \rightarrow CH_3OH + H_2O,\ E^0 = -0.38\ V \quad (1.53)$$

$$CO_2 + 8H^+ + 8e^- \rightarrow CH_4 + 2H_2O,\ E^0 = -0.24\ V \quad (1.54)$$

$$2CO_2 + 14H^+ + 14e^- \rightarrow C_2H_6 + 4H_2O,\ E^0 = -0.27\ V \quad (1.55)$$

$$2CO_2 + 12H^+ + 12e^- \rightarrow C_2H_5OH + 3H_2O,\ E^0 = -0.33\ V \quad (1.56)$$

Another important concern is the kinetic issue on the amount of the protons needed for the reaction. It can be seen from the equations above that the formation of CO and HCOOH requires two protons and the formations of CH_3OH, CH_4 and C_2H_6 need 6, 8, 14 protons, respectively. Generally, the electron and proton transfers (PCET) are believed concerted, which means

only a pair of electron and proton is transferred each time.[273] Therefore, the CO and HCOOH formations are usually faster, although their reduction potentials are lower. Recently, several works proposed a multiple PCET mechanism that ensures more than one pair of electron and proton transfer per time. The multiple PCET mechanism is very promising for CO_2 reduction to higher products (eg. equations (1.55) and (1.56)), which requires more electrons and protons.

1.5.1 CO_2 adsorption and activation

The reduction of CO_2 is challenging because of its high stability. CO_2 is a linear molecule that two equivalent C=O double bonds forming a angle of 180°.[274-275] The CO_2 physically adsorbed will remain its linear structure. By contrast, the chemisorbed CO_2 usually exhibits a bent structure due to electronic interaction with absorbent. As a Lewis acid, the first step of CO_2 activation is adding an electron to CO_2 forming CO_2^-. Based on theoretical calculation,[274, 276] the activated CO_2^- shows a bent structure with O-C-O angle of 138°. After activation, the C-O bond length of CO_2^- increases by 0.07 Å comparing with the ground-state CO_2. More importantly, the bent structure will lower the LUMO energy level, which can further enhance the electron transfer from the catalyst surface to adsorbed CO_2.[272] As indicated by equation (1.48), the direct transfer of an electron to CO_2 requires a high potential of -1.90 eV, which locates above the CBM of most semiconductors (**Figure 1.21**). Therefore, the bent configuration of the adsorbed CO_2 will facilitate the electron transfer process. The strategies to enhance the CO_2 adsorption and activation include enlarging SSA, creating basic sites and introducing vacancies, which will be discussed in the following section.

As shown in **Figure 1.22**, the CO_2 can adsorb on the surface in linear and bent configurations. Although there is no explicit boundary between physical and chemical adsorption, it is generally believed that the physisorption shows the linear structure and chemisorption generates bent configuration. Moreover, an activation energy barrier exists for the CO_2 transforming between these two

configurations.[277] In addition, it is very common to observe the CO_2 adsorption on the surface in the forms of carbonate and bicarbonate, which are derived from the CO_2 reacting with surface OH* or H* species.

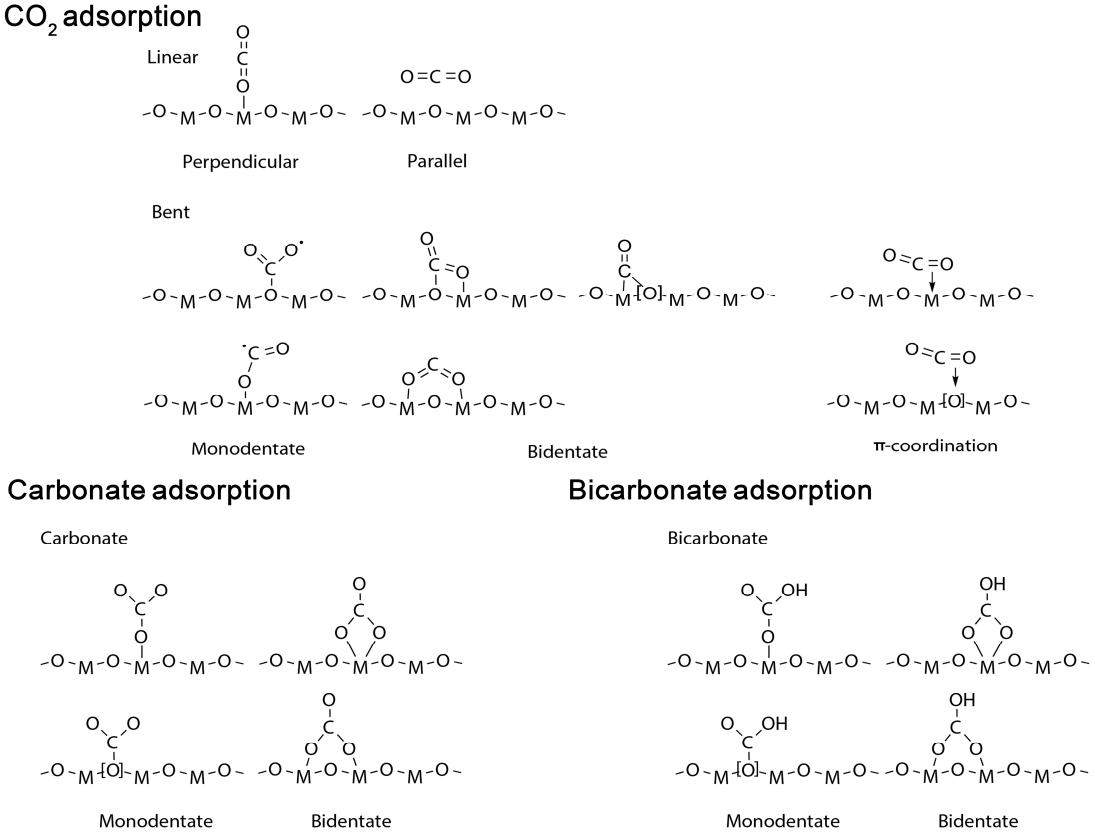

Figure 1.22. Configurations of CO_2 adsorption on catalyst surface. The M, O and [O] represent metal, oxide and oxide vacancy site, respectively.[278-280]

1.5.2 Photocatalytic CO_2 reduction reaction pathway

During the recent twenty years of research on the photocatalytic CO_2 reduction with H_2O, most of the research works focus on the developments of photocatalysts. However, the reaction mechanisms are relatively less investigated. In 2010, Yang et al.[281] presented the isotope-labelling experimental evidence to support the feasibility of CO_2 photocatalytic reduction with H_2O. Using $^{13}CO_2$ as feedstock, the primary product was found to be ^{13}CO, which proved the feedstock CO_2 rather than the C pool on the catalyst surface was the C source. The explicit role of H_2O is even less investigated, despite

its abundance on the surface of the catalysts, reactor or gas supply system. Moreover, the H_2 and O_2 products in trace amounts during the CO_2 photocatalytic reduction are difficult to quantitatively determine simultaneously. Therefore, a clear understanding of H_2O needs to use the ultraclean reaction evaluation equipment. In addition, the H_2O is not a perfect proton donor, and the photo-oxidation of H_2O is actually a sluggish reaction. Only until recently, Dilla et al.[91, 282-283] designed an ultraclean photocatalytic flow reactor with an on-line GC-BID system. Their works proved that H_2O was indispensable for CH_4 production on P25. However, the O_2 was absent in the effluent gas stream. Moreover, H_2 was also not detected during the photocatalytic CO_2 reduction with water, which was out of expectation since H* should be more easily reduced to H_2 than the formation of CH_4. The author proposed the V_O replenishment mechanism, which provided the protons for CH_4 formation. Their works challenge the conventional understanding that H_2O oxidation is the proton source for CO_2 reduction. Another relevant work was reported by Ji and Luo,[284] they used DFT calculation to support a plausible mechanism that the proton was directly transferred from H_2O to CO_2 on TiO_2 surface with the generation of OH* on the surface. This mechanism avoided the H_2O oxidation steps.

One of the most popular proposed CO_2 reduction pathways is featured by the key role of CO_2^-.[24, 285-286] The CO_2^- is believed to be able to form CO, HCOOH and further produce CH_4. The key experimental evidence is the observation of CO_2^- via DRIFTS technique. The limitation of this reaction pathway is the difficulty of the first step of CO_2 reduction (equation (1.48)).[24] Additionally, the carbene pathway has been proposed to describe the mechanism of CO_2 conversion on the semiconductor surface with the key radicals of C* and CO_2^-.[272, 287-288] The key experimental results supporting this pathway is the detection of *C signal in ESR spectroscopy.[289] Another reaction pathway is called the formaldehyde or formate pathway with formate and formyl as the main intermediates, which can be converted to CH_4 and CO.[24, 290-291] The last proposed reaction pathway is called the glyoxal pathway. The glyoxal is believed to be generated via the combination of two formyl species.[288] Based

on the DFT calculations, Ji et al.[284, 292-293] proposed two reaction pathways for CO_2 reduction on the surface: the fast-hydrogenation and the fast deoxygenation pathways. The authors found the initial of CO_2 photocatalytic reduction was the formation of CO* and the HCOO* was hard to be further hydrogenated. Additionally, the existence of V_O on the surface was found critical in determining the exact reaction pathway.

In the end, it is worth emphasizing that the exact reaction pathway is still an open question. The difficulties lay in the researches on the reaction mechanism are mainly due to the slow reaction rate of photocatalytic reaction and co-existence of reduction and oxidation on the surface.

1.5.3 Recent advances for photocatalytic CO_2 reduction driven by bandgap excitation

The strategies to increase the photocatalytic CO_2 reduction with bandgap excitation mechanism can be generally classified into two categories: (i) photocatalysts optimization; (ii) strategy targeting the reaction. In the following sections, recent researches in the literature using these two kinds of strategies are reviewed separately.

1.5.3.1 Strategies to optimize photocatalysts

The strategy to increase the QY of photocatalysts is theoretically valid to promote all the photocatalytic reactions. In the case of CO_2 reduction with H_2O, it is necessary to meet the thermodynamic condition that the photoexcited electrons and holes are able to drive the CO_2 reduction and H_2O oxidation. Strategies to increase the QY of photocatalysts can be further classified into three categories based on the different photocatalysis stages: electron-hole pair excitation, charge carrier transfer and surface reaction.

Firstly, to enhance the electron-hole pair excitation means to make the most usage of solar light. The bandgap of semiconductor is the parameter directly related to the threshold of solar energy that can be absorbed by the semiconductor. As a result, many researches work on reducing the bandgap

of semiconductors. For instance, the TiO_2 is known as a promising candidate for the photocatalytic CO_2 reduction, however it can only adsorb UV light due to the relatively wide bandgap of ~3.2 eV. Creating vacancies in the TiO_2 lattice can effectively reduce the bandgap energy.[294-295] Doping with heteroatoms is another effective way to increase the light absorption by creating the mid-bandgap defect energy levels.[296] In addition to the doping effects, Chen et al.[297-298] introduced the surface disorder and H dopants into the TiO_2 by calcinating the TiO_2 in H_2-rich atmosphere and fabricated the 'black-TiO_2' with significantly enhanced solar light absorption. Inspired by this work, other dopants such as Al,[299] Zn,[300] Mg[301] and non-metal elements[302] etc. were reported to prepare TiO_2 with different colours. Besides, adding sensitization cocatalysts onto semiconductor including dyes and plasmonic metal NPs can also enhance the solar light absorption.

After the excitation of electron-hole pairs, the strategies to suppress the recombination during the carrier transfer includes the nanostructure engineering and electrical field introduction. The nanostructure engineering aims to decrease the charge carrier diffusion path length, which can decrease the recombination possibility. Various kinds of 1D[35, 303-304] and 2D[305-307] structures have been successfully synthesized and reported to utilise the solar light effectively. Another way is to increase the crystallinity of semiconductor, because excessive defects can enhance the recombination. For instance, Bhunia et al.[308] prepared the triazine-based g-C_3N_4 with high-crystallinity via ionic melted salts polycondensation method. High apparent QE of 15% was achieved at 400 nm. Recently, a strategy called internal electric field is proposed to drive the electron-hole separation inside photocatalyst crystal.[309] For example, Xing et al.[310] synthesized mesoporous F doped TiO_2 and a build-in electric field was formed due to F dopants. The photocatalytic CO_2 reduction was facilitated, and CH_4 production rate was enhanced by 13 times. In the case of g-C_3N_4, which is a vdW structure, the electrons and holes can hardly transfer across the layers. As a result, intercalating a heteroatom between the layers could bridge the inter-layer charge transfer, which suppresses the recombination.[43, 94]

When the charge carrier reaches the surface, it transfers either to the adsorbed molecule or to another part of the photocatalysts (eg. cocatalyst). On the semiconductor surface, following strategies have been used to increase the efficiency of excited charge carrier usages. Adding a cocatalyst or another semiconductor onto the semiconductor to build a heterostructure has been proven as an efficient method to separate the charge carriers. Since the CBM of semiconductor is usually higher than the E_F of metal NP, the excited electrons intend to inject into the metal NPs. Moreover, as already discussed in section 1.4.2, when metal NP as cocatalyst interacts with a n-type semiconductor, a Schottky barrier is formed, which can prevent the back-transfer of electrons from the metal to semiconductor. Additionally, if a metal NP builds contact with a p-type semiconductor, the built-in electric field in the depletion area of the semiconductor can also enhance the charge separation on the surface.[94, 311] For semiconductor/semiconductor interface, a p-n junction is deemed as an efficient way to separate the charge carriers due to the internal electric field. Numerous p-n junctions[312] have been reported to improve the photocatalytic CO_2 reduction including g-C_3N_4-NiO,[313] CuO-$TiO_{2-x}N_x$,[314] etc. Another special kind of heterostructure is called the 'Z-scheme' structure,[315] which is featured by the direct recombination of the photogenerated electrons and holes at the semiconductor interface. As a result, the photoexcited electrons and holes with high potentials are separated at different sides of the interface. The latest Z-scheme heterostructure design has reached the third generation, which is featured by the absence of charge diffusion layer at the interface. The key to successfully building this kind of Z-scheme structure is to choose the semiconductors with appropriate CBM, VBM levels. A few examples include Fe_2O_3/Cu_2O,[316] BiOI/g-C_3N_4,[317] Fe_2O_3/g-C_3N_4,[318] $BiVO_4$/Cu_2O,[319] etc.

1.5.3.2 Strategies targeting the CO_2 reduction reaction

Besides the general strategy to increase the QY of photocatalysts described in the previous section, there are strategies directly targeting to enhance the CO_2 photocatalytic reaction: enhance CO_2 adsorption and activation, using

cocatalysts, using hole scavengers, etc. Although using hole scavengers that quickly consume the photoexcited holes can significantly enhance the QY of the photocatalysts, it is also infamous for bringing intervention to the reaction mechanism investigations and violation of the sustainable fuel production goal of photocatalysis. So, this strategy is not discussed here.

Enhancing the CO_2 adsorption and activation is a straightforward method to increase the CO_2 reduction rate. The creation of anionic vacancies can enhance both CO_2 adsorption and activation. V_O on the TiO_2 surface can leave two extra electrons localised at the adjacent Ti^{3+} sites. The CO_2 intend to adsorb on the V_O sites with bent configuration.[320-321] The same principle is valid for other metal oxides too. For example, Pu et al.[322] designed a heterostructure of Cu_2O/CeO_{2-x} for photocatalytic CO_2 reduction. The abundance of V_O on CeO_{2-x} was proven to significantly enhance the CO_2 adsorption and generation of $CO_2^{\delta-}$ radicals. In_2O_{3-x} is another efficient photocatalytic to convert CO_2 to value-added products. Qi et al.[323] reported the light-induced V_O generation in amorphous In_2O_3 and a high CO production rate was achieved with nearly 100% selectivity. Moreover, a similar phenomenon was observed on g-C_3N_4 with more electrons transferred to CO_2* on V_N sites than the stoichiometric surface.[324] Since the CO_2 is a Lewis acid, the enrichment of basic sites can simultaneously facilitate the CO_2 adsorption and activation, which is due to the donation of electrons from catalysts to the CO_2*. Alkali metal elements as the most conventional promoters to increase the surface basicity of catalysts have been proven valid for CO_2 adsorption enhancement too. For example, Tang et al.[325] investigated the alkali and alkali-earth elements doping into the titanate nanotubes and the enhanced CO_2 adsorption and photocatalytic reduction rates were observed. Meng et al.[326] treated TiO_2 with NaOH and created Na^+ modified surface sites on TiO_2, which significantly enhanced the CO_2 chemisorption and activation. Liao et al.[327] decorated the amine functional groups onto the surface of TiO_2 and an increased CO_2 adsorption capability was observed. The CO_2 photocatalytic reduction to CH_4 was also accelerated. In the case of g-C_3N_4, creation of basic sites is more versatile due to the organic structure of g-C_3N_4. For example, Liu et al.[328] reported the synthesis

of P-doped g-C_3N_4 nanotubes with an abundance of amine group, which is ascribed to remarkably increased CO_2 adsorption and photocatalytic reduction rates. Wang et al.[329] doped K elements into g-C_3N_4, which increased the CO_2 photocatalytic reduction rate by 25 times comparing with pristine g-C_3N_4.

Co-catalysts are another very important factor.[311] In this paragraph, only metal NP is discussed, because metal NP affects not only the CO_2 photocatalytic reduction rate but also the product selectivity. In addition, I focus on the effects of metal NP cocatalysts on the reaction in this paragraph, since its benefits on charge separation have been discussed in the previous section. Firstly, some transition metal NP is nucleophilic and can be partially oxidized and helps to activate the CO_2. For example, the Cu NP supported by reduced TiO_2 can induce the spontaneous dissociation to CO.[330] Lyemperumal et al.[331] investigated the CO_2 adsorption and activation on Cu/TiO_2 catalyst via DFT calculations. The authors found the CO_2 intended to adsorb at the perimeter with bend structure with high stability and C-O bond length was elongated after adsorption. Secondly, the metal NP can enhance the reducibility of the metal oxides, which means the high concentration of V_O is reached on the surface.[209] Lastly, it is important to emphasize that some transition metal NPs (Pd,[332] Pt[333-334] etc.) show high activity towards H_2 production, which will suppress CO_2 reduction because of the competing effects.

1.5.4 Recent advances on LSPR-driven photocatalytic CO_2 reduction

The CO_2 plasmonic reduction has been proven possible on metal NPs without supports. Kumari et al.[335] took advantage of *in-situ* Raman spectroscopy to investigate the CO_2 photocatalytic reduction mechanism. It was found that the plasmon-induced hot electrons can directly transfer into and activate CO_2*. In addition, the COOH* was believed as the main reaction intermediates for the CO and HCOOH products. Similarly, Yu et al.[336] reported the direct conversion of C-C coupling during the CO_2 plasmonic reduction with the formation of CH_4 and C_2H_6. A direct $CO_2^{\bullet-}$ dimerization mechanism was proposed to explain the

formation of C_2H_6. Some researches only use Au NPs as light absorbers but not the catalysts. For example, Kumar et al.[337] synthesized the Au NP@TiO_2 core-shell catalysts with Pt NP loaded onto the TiO_2 surface. Using Pt NPs with high efficiency for H_2O dissociation significantly increased the photocatalytic CO_2 reduction rate by 312 times. Tu et al.[338] prepared Au@TiO_2 yolk-shell hollow sphere structure. It was found a high production rate of C_2H_6 was achieved besides the primary product CH_4. Since the Au was covered by TiO_2 shell structure, the LSPR induced electric field was ascribed to the C_2H_6 production. Kumar et al.[339] prepared Au NPs covered with graphene layers and a relatively high HCOOH production rate was reported under visible light irradiation.

The reaction pathway and plasmonic enhancement mechanism can be very different for plasmonic metal NP with oxide support. In 2011, a pioneering work by Hou et al.[340] reported the CO_2 reduction by H_2O over Au/TiO_2 under light irradiation with different wavelengths. When pure intraband excitation mechanism predominated, the CH_4 was the only product. While under UV excitation and interband excitation existed, more attractive products including C_2H_6, CH_3OH and HCHO were detected. Size is always a key topic in plasmonic photocatalysis. As discussed in 1.3.2, smaller Au NP generates 'hotter' electrons, while larger NP generates more plasmonic electrons. Qian et al.[118] compared the plasmon-driven water splitting on small Au (4.4±1.7 nm) and larger Au (67±17 nm) NPs supported by TiO_2. It was proven that the smaller Au NPs outperformed larger Au NPs under light irradiation with the wavelength shorter than 400 nm; on the contrary, larger Au NPs showed superior performance to smaller Au NPs when the light wavelength was longer than 435 nm. Lie et al.[341] investigated the effects of size on the photocatalytic CO_2 reduction performance over the Au NP/g-C_3N_4 and achieved similar conclusion. Zhao et al.[342] investigated the plasmonic CO_2 reduction on Au/ZnO under UV-Vis light irradiation and a 10-fold increase was observed for the CO_2 conversion. Moreover, a high selectivity to C_2H_6 was observed, which was attributed to the dehydrogenative coupling of CH_4 with C-H bond in CH_4 activation by LSPR induced local electric field.[343]

In recent years, the non-precious plasmonic materials attract more attention from researchers due to its abundance and low price. Al is one of the most abundant metal elements in the Earth's crust and shows reasonable plasmonic activity. Knight et al.[123, 344] successfully prepared Al NPs via solvothermal method and reported the photocatalytic reaction could be driven by plasmonic Al NPs. Huang et al.[345] investigated the CO_2 plasmonic reduction performance over Cu/ZnInS catalyst and CH_4 was measured as the primary product with 71.1% selectivity. Alloying Au with other non-precious metal is another effective way to reduce the usage of precious metal. Neatu et al.[346] reported the Au-Cu alloy NPs supported by TiO_2, which showed significantly increased photocatalytic CO_2 reduction rate comparing with Cu/TiO_2 or Au/TiO_2 alone. Similarly, Tahir et al.[347] reported the Au-Ag alloy NP supported by TiO_2 and a synergistic effect of Au-Ag alloy was observed on plasmonic CO_2 reduction.

1.6 Mechanism of CO_2 hydrogenation to fuels on thermal heterogeneous catalysts

Comparing with photocatalytic CO_2 reduction, CO_2 thermocatalytic hydrogenation is a reaction with much clearer evidence to support the arguments on the reaction mechanism. To date, the CO_2 hydrogenation over heterogeneous catalysts can produce CO, CH_4, CH_3OH, higher hydrocarbons and higher alcohols etc.

1.6.1 CO_2 hydrogenation to CO: reverse water gas shift reaction

The CO produced via RWGS reaction is an important product, which can be used as the feedstock for methanol and higher hydrocarbon production. As described in equation (1.57), the RWGS is an endothermal reaction and requires a high temperature for high conversion.

$$\mathrm{CO_2 + H_2 \leftrightarrow CO + H_2O}, \Delta H_{298\mathrm{K}} = 41.2\ \mathrm{kJ\ mol^{-1}} \quad (1.57)$$

In the presence of H_2, the CO_2 conversion can be generally divided into two different categories: (i) redox mechanism; (ii) associative mechanism. The latter mechanism can be further divided into carboxyl (COOH*, also called hydroxycarbonyl) pathway and formate (HCOO*) pathway.

For redox mechanism, CO_2 is believed to be an oxidative reagent that can oxidize the metal (eg. Cu, Fe, Ni) or the reducible catalysts support (eg. TiO_{2-x}, CeO_{2-x}) with itself being reduced to CO. The metal or support will restore to the original state with reducing agent. Gines et al.[348] proposed the redox pathway for RWGS over $Cu/ZnO/Al_2O_3$. The Cu metallic NP was successively oxidised and reduced by CO_2 and H_2, respectively with the formation of CO and H_2O. The similar mechanism was also supported by Fujita et al.'s work[349] with the CO adsorption IR spectroscopy evidence on the oxidation states of Cu. The V_O in metal oxide support shows the capability to reduce CO_2 and formation of CO, too. For instance, Wang et al.[350] proved that CO_2 could oxidise Au/CeO_{2-x} by conducting TAP experiments. Similarly, the IR spectroscopy evidence provided by Liu et al.[330] proved that the CO_2 could spontaneously dissociate at $Cu(I)/TiO_{2-x}$ interface. In summary, the redox mechanism highly associates with the properties of the catalysts, both metal NP and metal oxides (MO_x) support. For the metal $NP/MO_{x-\delta}$ easily oxidized by CO_2 is likely to be difficult to be reduced by H_2; similarly, the metal $NP/MO_{x-\delta}$ easily being reduced by H_2 usually shows the low capability to reduce CO_2. In summary, the synergistic effects of metal NP and metal oxide still need more investigations.

The associative mechanisms can be further divided into formate pathway and carboxyl pathway based on the key intermediates observed. Both the COOH* and HCOO* can further decompose into CO* and OH*. Bobadilla et al.[351] investigated the reaction pathway of RWGS over Au/TiO_2 and Au/Al_2O_3 with DRIFTS technique. The formate pathway dominated on Au/Al_2O_3, while carboxyl pathway dominated on the surface of Au/TiO_2. The author also emphasized the importance of V_O in Au/TiO_2 during the reaction. SSITKA-DRIFTS is a powerful tool to unravel the reaction mechanism, because it can

provide the kinetic parameters for individual species. For example, Goguet et al.[352] investigated the RWGS reaction over Pt/CeO_2 catalysts. The mean residence lifetime, τ, of CO*, CO_3* and HCOO* were characterized via SSITKA to be 48 ± 5, 54 ± 5 and 660 ± 30 s, respectively; on the other hand, the $\tau_{CO(g)}$ was determined via MS responses to be 54 ± 6 s. Based on the kinetic parameters, the authors claimed that the formate was the 'minor reaction intermediate' and the CO_3* was believed to be involved in the reaction. Similarly, Wang et al.[353] took advantage of SSITKA-DRIFTS technique to analyse the reaction mechanism of CO_2 hydrogenation over Pd/Al_2O_3. It was proven that the HCOO* was the intermediate, which was further converted to CO with the help of H*.

DFT calculations are very popular to provide theoretical insights on reaction mechanisms.[354-355] Sun et al.[356] conducted DFT calculations on the role of V_O in Au/TiO_2 during the CO_2 hydrogenation. The authors found that at the V_O of Au/TiO_2 perimeter, the E_a for the formation of HCOO* and COOH* from CO_2* and H* were 0.49 eV and 1.52 eV, respectively. Therefore, the COOH* pathway was excluded from the possible reaction mechanism. On the contrary, the E_a of COOH* formation from CO* and OH* was calculated to be as small as 0.13 eV on Au (100), which gives hints on the reason why many WGS reaction researches claimed the carboxyl pathway. Similarly, Liu et al.[357] reported the larger calculated E_a for COOH* formation than HCOO* formation at Cu/Al_2O_3 interface. On the contrary, Rodriguez et al.[358] reported their DFT calculation results on Au_{10}/TiO_2 that the E_a of COOH* formation from CO_2* and H* was ~0.3 eV. However, it is important to notice that in Rodriguez et al.'s work, the H* sources were adsorbed on the surface of TiO_2, which was against the generally believed assumption that the H* is usually at the transition metal surface. It is one of the differences between RWGS and WGS reactions.[359]

1.6.2 CO_2 thermocatalytic conversion to CH_4.

The CO_2 can be hydrogenated into methane and this conversion is also called methanation or Sabatier reaction:

$$CO_2 + 4H_2 \leftrightarrow CH_4 + 2H_2O, \Delta H_{298K} = -164.75\ \text{kJ mol}^{-1} \quad (1.58)$$

As suggested by the reaction formula, the CO_2 methanation is an exothermal reaction with the reduction of total moles of gases. Therefore, high pressure and low temperature are preferred to achieve high conversion. Although the CO_2 methanation is a thermodynamically spontaneous reaction with the reaction Gibbs free energy, $\Delta G^0_{298K} = -55.8\ \text{kJ mol}^{-1}$, the full methanation is an eight-electron transfer process, which faces up to remarkable kinetic limitations.

The reaction mechanism of CO_2 methanation can be classified into two different categories: (i) RWGS + CO methanation pathway; (ii) pathway without the formation of CO.

The first mechanism (RWGS + CO methanation) is featured with the formation of CO*, which can happen through the redox, formate, carboxyl pathways, as already mentioned in section 1.6.1. Therefore, in this section, the following CO hydrogenation to CH_4 is focused. The methanation of CO* must include the cleavage of C=O bond of CO, which is usually considered as the RDS of the methanation. The C=O bond cleavage can be classified into two main pathways:[360] direct CO* dissociation (equ. (1.59)) and H-assisted CO* dissociation (equ. (1.60) or (1.61)):

$$CO^* \rightarrow C^* + O^* \quad (1.59)$$

$$CO^* + xH^* \rightarrow H_{x-1}COH^* \rightarrow H_{x-1}C^* + OH^* \quad (1.60)$$

$$CO^* + xH^* \rightarrow H_xCO^* \rightarrow H_xC^* + O^* \quad (1.61)$$

The H assisted CO dissociations have been proposed to happen over VIII-group transition metals.[361-362] For example, Eckle et al.[363] proposed the direct CO_2* dissociative adsorption mechanism for CO_2 methanation over Ru/Al_2O_3. Based on the SSITKA results, the authors claimed the CHO* (formyl) species

as the reactive intermediate and ruled out the formate as reactive species on the surface. Similarly, Karelovic et al.[364] investigated the CO_2 methanation over Rh/TiO_2 with kinetic analyses and SSITKA experiments. The CO* was identified via the IR spectroscopy in a large amount. Additionally, the kinetics analyses proved that the H-assisted C-O bond break was the main reaction pathway.

For the second mechanism, the formation of CH_4 can initialise with CO_2 hydrogenation to HCOO* species at the metal/support interface. Therefore, it is sometimes called formate pathway. Theoretically, the COOH* is also the possible product for the first step of CO_2* hydrogenation. However, the COOH* intends to decompose to CO*, which makes the process belong to the first mechanism. In the case of HCOO* pathway, the detailed pathways differ from each other on the timing of C-O bond break:

$$\mathrm{HCOO^*} + x\mathrm{H^*} \rightarrow \mathrm{H}_x\mathrm{COOH^*} \rightarrow \mathrm{H}_x\mathrm{CO^*} + \mathrm{OH^*} \tag{1.62}$$

$$\mathrm{H}_x\mathrm{CO^*} + y\mathrm{H^*} \rightarrow \mathrm{H}_{x+y}\mathrm{C^*} + \mathrm{O^*} \tag{1.63}$$

$$\mathrm{H}_x\mathrm{CO^*} + y\mathrm{H^*} \rightarrow \mathrm{H}_{x+y-1}\mathrm{COH^*} \rightarrow \mathrm{H}_{x+y-1}\mathrm{C^*} + \mathrm{OH^*} \tag{1.64}$$

It can be seen from the equations that the C-O bond breaking is either a direct break or H-assisted break. Wang et al.[365] investigated the reaction pathway of CO_2 methanation over Ru/CeO_2. With the help of SSITKA-DRIFTS technique, the formation pathway was proposed and the formate hydrogenation was claimed to be the RDS. Similarly, Aldana et al.[366] investigated on the CO_2 methanation over $Ni/Ce_xZr_{1-x}O_2$ using SSITKA-DRIFTS technique. It was found the CO* was not the reaction intermediate and the main reaction pathway was the hydrogenation of CO_2* to HCOO*, which was further hydrogenated to CH_3O*.

1.6.3 CO_2 hydrogenation to methanol

As an alternative fuel, methanol is deemed as a preferred product for CO_2 hydrogenation. The reaction is described by the following equation:

$$\mathrm{CO_2} + 3\mathrm{H_2} \leftrightarrow \mathrm{CH_3OH} + \mathrm{H_2O}, \Delta H_{298\mathrm{K}} = -49.5\ \mathrm{kJ\ mol^{-1}} \quad (1.65)$$

Therefore, from the perspective of thermodynamics, the reaction prefers high pressure and low temperature. In the literature, the reaction conditions are usually between 200 to 300 °C; 0.1 to 5 MPa. The reaction pathways for CH_3OH formation can be classified into three categories: (i) formate pathway, (ii) RWGS pathway, (iii) carboxyl pathway, based on the different initial steps of CO_2 hydrogenation.

The formate mechanism is an important mechanism generally accepted by the research community. As discussed in section 1.6.1, the HCOO* is always more stable than COOH* thermodynamically, therefore it usually shows a higher E_a for HCOO* hydrogenation than COOH* hydrogenation. Liu et al.[357] conducted DFT calculations on CO_2 hydrogenation to methanol over Cu_4/Al_2O_3. The RDS was determined to be the hydrogenation of HCOO* with E_a of 1.18 eV. For the hydrogenation of HCOO* step, two products have been proposed: (i) H_2COO* and (ii) HCOOH*. Recently, Grabow and Mavrikakis[367] suggested that the formation of HCOOH* showed lower E_a than the formation of H_2COO*. The RWGS + CO hydrogenation pathway is another popular proposed reaction mechanism. CO* is produced from RWGS and further converted into the methanol via the CO hydrogenation to methanol mechanism. This reaction mechanism is straightforward, since there are already commercial catalysts for CO hydrogenation to methanol, such like $Cu/ZnO/Al_2O_3$.

Hartadi et al.[368-369] investigated the CO_2 hydrogenation on Au catalysts with different oxide supports including Al_2O_3, TiO_2, ZnO and ZrO_2 under moderate condition. The reaction was conducted under 5 Bar, 250 °C with $25\%CO_2/H_2$ at a flow rate of 20 sccm. It was found the methanol production rate increased with Au NP size decreased. However, the selectivity toward methanol also

reduced due to the decrease of Au NP size. In addition, van den Berg et al.[370-371] conducted experimental and theoretical investigations on the real active sites for methanol production. It was found the Cu-Zn alloy was the true active sites for methanol production. A more direct experimental evidence was reported by Kuld et al.[372] that a quantitative correlation could be found between methanol yields and Zn coverage on Cu, which was determined by H_2-TPD.[373] The Zn-Cu alloys were ascribed to stabilize the key intermediates, such as HCO*. The interaction between Cu and Zn were also confirmed on the commercial Cu/ZnO/Al_2O_3 catalysts through the SMSI.[374]

The nature of oxide support is another pivotal factor determining the methanol production. Hartadi et al.[368-369] found the methanol selectivity followed the order of Au/ZnO > Au/TiO_2 > Au/ZrO_2 > Au/Al_2O_3. Similarly, Vourros et al.[375] investigated the CO_2 hydrogenation to methanol over Au NPs supported by various metal oxide supports. It was found that the methanol formation rate showed the sequence of Au/CeO_2 > Au/ZnO > Au/Fe_2O_3 > Au/TiO_2 > Au/Al_2O_3; Au/CeO_2 and Au/ZnO showed the highest selectivity toward methanol. Sakurai et al.[376] summarized the effects of metal oxides on methanol yields as the surface acidity and basicity effects: more acidic support intended to induce higher methanol production rate but lower selectivity.

1.6.4 Summary

It is important to summarise some trends that describe the behaviours of different metal/oxide catalysts in CO_2 activation. The first factor is the CO_2 adsorption and activation, which is remarkably influenced by V_O. The role of V_O in metal oxide is highly affected by the property of the transition metal. [377-378] The higher metal-oxygen affinity is believed to be directly correlated to its better ability of CO_2 cleavage to CO,[379] which is roughly independent of the H_2 dissociation ability. Another important descriptor is the adsorption strength of CO* on the catalysts.[380] Since CO is a Lewis base and possesses a lone pair of electrons localised at C atom, the adsorption of CO* is mainly determined by metal NPs. Too weak CO adsorption decreases the chances to generate

the CH_4 and methanol. Additionally, it is important to keep the 'Sabatier principle' in mind, since too strong adsorption can cause poisoning. In the specific case of CO_2 hydrogenation, the common poison is the HCOO*. Due to the high stability of HCOO* on the surface, it is sometimes a spectator rather than an intermediate for the reaction.

1.7 Recent researches on photo-thermo coupled CO_2 reduction

1.7.1 Motivation in coupling thermo- and photo- catalysis

First of all, the thermo- and photo- catalysis are substantially different from the way the energy is delivered. In the case of thermocatalysis, the electrons are heated up homogeneously following the Fermi-Dirac distribution. On the other hand, in photocatalysis, the electrons are directly excited by the photon and reach a non-thermal distribution. The energy of electrons from different energy sources can be compared with the term k_BT in the Fermi-Dirac distribution function. Therefore, it can be seen that 1 eV equals to ~11604 K. Therefore, the photo-excitation is a more efficient energy input way. Moreover, the temperature can only homogeneously activate every component in the reactor; on the contrary, the photon energy can more selectively transfer to the targeted component, which may possibly divert the reaction pathway. However, the photocatalysis shows its own shortcomings including the slow reaction rate and low quantum efficiency.

There are three scenarios when combining thermo- and photo- catalytic reaction together:[381-382] (i) the photocatalytic and thermocatalytic half reactions take place sequentially and independently; (ii) the incident light is simply another energy source providing thermal energy; (iii) synergistic coupling between the photo- and thermo- catalytic reactions. Only the third scenario can make the coupling of thermo and photo- catalysis attractive. The key feature of the third scenario making it different from the other two counterparts is the utilisation of the 'hot carriers' in the reaction. Therefore, in the following

sections, I focus on reviewing and discussing the third scenario. The potential benefits include faster reaction rate, higher conversion, lower reaction temperature required and selectivity changes.

1.7.2 Mechanism of coupling thermal and photo-catalytic process

1.7.2.1 Photo-excitation mechanism

As introduced and discussed in sections 1.2 and 1.3, the photoexcited electrons can be classified into two mechanisms, bandgap excitation and plasmonic excitation. Since the key parameter for a successful thermo-photo coupling is the 'hot electrons', it is important to compare how 'hot' the electrons are photo-excited based on these two mechanisms. Here, the classical Au/TiO_2 catalyst is taken as an example for theoretical discussion. The bandgap of the TiO_2 is ~3.2 eV; TiO_2 is a n-type semiconductor, which makes the Fermi level closed to the CBM of TiO_2. The bandgap excitation requires the incident light with energy higher than ~3.2 eV. On the other hand, the LSPR effects of Au NPs can ensure the electrons excited directly from E_F. Moreover, the LSPR peak at ~2.4 eV can significantly enhance the light absorption. In summary, the LSPR can generate excited electron with higher energy than bandgap excitation.

1.7.2.2 Thermal effects

In practice, the clear separation of thermal effects and hot-electron induced effects (also called non-thermal effects) are very difficult.[383-387] As a kind of energy source, the incident light (CW) inevitably increases the temperature of the catalysts; especially the strong light with a power density as large as several W cm^{-2} is used in some works. For the reaction in solution, the thermal effects are less important, due to the large thermal capacity of the liquid medium and fast thermal transfer under agitation condition.[388] In the case of gaseous heterogeneous catalytic reaction, it is still a very challenging question. In literature, the following methods have been used to distinguish the thermal and nonthermal effects under CW light irradiation.

Firstly, the light-induced temperature increase is compensated by the heater during the control group experiment in dark. The main challenge for this method is accurate determination of the surface temperature under light irradiation. Li et al. and Zhang et al. [389-390] took advantage of a thermal couple underneath the surface of catalysts to monitor the surface temperature under light irradiation. The authors found the nonthermal CH_4 production rate showed a linear relationship with the temperature. This method shows the shortcomings of the lack of spatial distribution of the temperature reading. In work reported by Zhou et al.[151, 391-392], an IR camera was used to monitor the temperature of the catalysts surface. However, the temperature reading is largely affected by the surface emissivity property.[393]

Secondly, the theoretical model calculation is used to calculate the estimated temperature increase due to light irradiation. For example, Mukherjee et al.[152-153] proposed the LSPR induced temperature increase could be calculated with the following equation:

$$\Delta T = \frac{\sigma_{\mathrm{abs}} I}{4\pi R \beta \kappa_m} \tag{1.66}$$

where σ_{abs} is the integrated absorption cross-section; R is the radius of Au NP; β is the thermal capacity coefficient of Au NP ($\beta = 1$ for sphere); κ_m is the temperature-dependent thermal conductivity of the surrounding matrix. According to the equ. (1.66), the authors claimed that a temperature increase of only a few mK could be generated by an incident light as strong as 2 W cm^{-2}. Although the equation is explicit, it is significantly smaller than the measured surface temperature reported by Zhou et al.[151]

In summary, to date, there is no ideal method to adequately monitor and compensate the thermal effects brought by incident CW light during the catalytic performance evaluation. The explicit distinguishing between thermal and non-thermal effects are still under vigorous debate. A plausible solution can be fabricating the photocatalysts as an ultrathin coating with the thickness of a few microns, which is close to the penetration depth of incident light.

Additionally, the non-thermal mechanism of hot electrons driving the reaction is theoretically feasible as proven by many pump-probe experiments using fs light pulses (as discussed in section 1.3.5).

1.7.3 Recent researches on thermo-photo coupled catalytic process

The results of thermo-photo coupling can be classified into two categories: reaction rate enhancement; product selectivity alteration. There is still no consensus on the explicit mechanism causing the different coupling results. More detailed investigations are required.

1.7.3.1 The non-thermal enhancement of the reaction rate

CO_2 reduction with H_2O is deemed as a promising way to address the CO_2 emission issue. However, the photocatalytic process is too slow with the production rate at the magnitude of a few μmol g_{cat}^{-1} h^{-1}. By combining the photo-thermal catalytic reaction together, the reaction rate can be remarkably enhanced. For example, O'Brien et al.[394] investigated the methanation of CO_2 with H_2O over Ru/Si NW catalysts at photo-thermal condition. It was found the CH_4 production rate showed a linear relationship with incident light intensity when the light energy was higher than the bandgap of Si NW. An electron-assisted Ru-H activation mechanism was proposed based on the experimental results and literature. Zhang et al.[395] investigated the thermo- and photo-coupled catalytic CO_2 reduction with H_2O over Au-Ru/TiO_2. The CH_4 yields increased from 7.2 μmol g^{-1} h^{-1} in dark to 27.1 μmol g^{-1} h^{-1} under visible light irradiation. The positive coupling effects were demonstrated, while the mechanism was not clearly unravelled.

Photo-thermo coupled CO_2 reduction with H_2 can more efficiently convert CO_2 to value-added products. Lin et al.[396] investigated the CO_2 hydrogenation performance over Ru/$TiO_{(2-x)}N_x$ catalysts with and without visible light irradiation. The significantly enhanced CO_2 reduction rate enhancement by light was attributed to the facilitated V_O generation. Additionally, the electron-rich Ru due to light irradiation (bandgap excitation) could enhance the CO_2

adsorption. The only evidence supporting the enhanced V_O formation was the *ex-situ* XPS O 1s spectra, which are indirect and less reliable. Liu et al.[397] reported the plasmonic enhancement on CO_2 and CH_4 dry-reforming reaction. The closely located Au-Rh dimmer could generate strong electric field enhancement, which was ascribed to the enhanced CO_2 and CH_4 molecule activation. Novello et al.[398] reported CO oxidation was enhanced on Au/MgO under photo-thermal coupled reaction condition. The plasmon-excited electrons can facilitate the removal of carbonate absorbed on the surface, which significantly enhanced the lifetime of the catalysts. Ullah et al.[399] investigated the CO_2 methanation over Co_{10}/CeO_2 under photo-thermal coupled reaction condition. Under blue light irradiation, the CH_4 production rate was increased by 116% comparing with pure thermocatalytic condition at 300 °C. Additionally, over Cu_{10}/CeO_2 catalysts, the photo-thermal coupled reaction condition increased the CO production rate by 148%. On the contrary, the metal clusters supported by Al_2O_3 showed very limited light-induced enhancement. Therefore, the photo-enhancement was ascribed to the enhanced V_O generation on CeO_2. Wang et al.[400] reported the plasmon-enhanced CO_2 hydrogenation to methanol over Cu/ZnO. It was found the activation energy was reduced by 40% and methanol yields increased by 54%. The author claimed the same reaction pathway for both thermal and photothermal reaction condition. Kinetic analyses can provide insights on how light promotes the reaction. Upadhye et al.[401] reported the visible light enhanced RWGS over Au/TiO_2. It was found the reaction rate was enhanced by 1300% under visible light irradiation. Based on the kinetic analyses, the reaction rate enhancement was attributed to the promoted COOH* decomposition or OH* hydrogenation. Zhang et al.[402] investigated the CO_2 hydrogenation performance of Fe@C derived from MOF (MIL-101) structure. Under UV irradiation the Fe@C catalysts showed enhanced reaction rate and nearly 100% selectivity toward CO, which was attributed to the weak CO adsorption on C shell. Wang et al.[400] reported the enhancement of methanol production through CO_2 hydrogenation over Cu/ZnO under ambient pressure. The apparent activation energy was reduced by 40% and methanol production

rate increased by 54% under photo-thermal coupled catalytic condition comparing with pure thermocatalytic condition. The author believed the hot electrons excited by the LSPR effects could activate the reaction intermediates. However, no experimental or theoretical evidence clearly suggested which intermediate or how the intermediate was activated.

On the other hand, it is also important to emphasize that the coupling of photo and thermal reaction doesn't guarantee a positive effect on reaction rate. In the pioneering work of Westrich et al.,[403] the ethylene oxidation reaction was conducted over TiO_2 under thermo-photo coupled condition. The reaction rate increased with temperature rose at first and reached the maximum at the temperature of ~150 °C. Further temperature rise caused detrimental effects on the reaction rate. The authors proposed a kinetic description of the reaction with the following equations:

$$-r_{C_2H_4} = k_{app} P_{C_2H_4}^{\alpha} P_{O_2}^{\beta} P_{H_2O}^{\delta} I \left(k_{\Phi} \left(1 - e^{\frac{-\hbar\omega_p}{k_B T}} \right)^{-N_p} \right) \tag{1.67}$$

where k_{app} is the apparent reaction rate constant; P is the partial pressure; k_{Φ} is the temperature-independent quantum efficiency term; $\hbar\omega_p$ and N_p are the energy and number of the incident photon, respectively; I is the light intensity. The term in equ. (1.67) related to the light is based on the description of electron-hole non-radiative recombination rate (γ_{nonrad}):[404]

$$\gamma_{nonrad} = \gamma_{rad(T=0\ K)} \left(1 - e^{\frac{-\hbar\omega_p}{k_B T}} \right)^{-N_p} \tag{1.68}$$

where γ_{rad} is the rate of radiative recombination, which is independent from temperature. Therefore, the electron-hole utilised to drive the reaction ($\gamma_{products}$), which directly correlates with photocatalytic reaction rate ($-r_{photo}$), can be written as:

$$\frac{\gamma_{products}}{\gamma_{rad}+\gamma_{nonrad}+\gamma_{products}} \approx \frac{\gamma_{products}}{\gamma_{nonrad}}, (\gamma_{nonrad} \gg \gamma_{rad}+\gamma_{nonrad}+\gamma_{products}) \tag{1.69}$$

$$\gamma_{\text{products}} = \gamma_{\text{rad(T = 0 K)}} \left(1 - e^{\frac{-\hbar\omega_p}{k_B T}}\right)^{-N_p} \quad (1.70)$$

Similarly, Tan et al.[405] investigated the photothermal ethanol oxidation over Au/TiO_2. It was proven that the CO_2 formation rate showed a U-shape correlation with the temperature. Pudyal et al.[406] reported the CO_2 photocatalytic reduction with H_2O at 350 °C. The authors suggested the semiconductors with high Debye temperature could show less temperature-induced recombination.

1.7.3.2 Product selectivity alteration

Comparing with reaction rate enhancement, incident light-induced product selectivity alteration is more attractive. However, the researches reporting the successful product selectivity control by introducing incident light were much less. A few examples are presented as follows. Zhang et al.[407] reported the plasmon-induced product selectivity alteration for CO_2 hydrogenation. It was found the CH_4 became the primary product over Rh/Al_2O_3 when the catalysts were irradiated by light. It was proposed by the authors that the plasmon-induced selectivity alteration was due to the selective facilitation of the C-O cleavage in CHO* rather than CO* desorption. Based on the DFT calculation over CHO* on Ru (100) surface, the C-O antibonding orbital was positioned at ~ 2 eV above the E_F, which matched the energy of incident light. Moreover, an interesting phenomenon was observed in this work that the activation energy of the photo-thermal coupled reaction was independent of the incident light intensity. Robatjazi et al.[408-409] reported the plasmonic photocatalytic CO_2 reduction on $Al/Al_2O_3/Cu_2O$ structure. Comparing with pure thermal CO_2 hydrogenation, photo-thermal coupled CO_2 hydrogenation achieved a higher selectivity toward CO, which was ascribed to the enhanced CO desorption. Another recent work by Xie et al.[410] investigated the methanol production via CO_2 hydrogenation over $Cu/ZnO/Al_2O_3$ under photo-thermal coupled reaction condition. It was found the synergistic effects of UV and visible light were indispensable for the methanol production at ambient pressure. Using UV or

visible light alone could only promote the selectivity toward CO. Based on the electronic structure calculation of various possible reaction intermediates adsorbed on the catalyst surface, the band overlap between catalysts and adsorbates were used to unravel the possibility for electron transfer (a larger orbital overlap enhances the electron transfer). Reaction intermediates including CO_2*, HCOO* were believed activated due to filling hot electrons into the antibonding orbitals.

In summary, the photo-thermal coupling enhancement has been proven valid for CO_2 hydrogenation reaction over many catalysts. Moreover, the product selectivity can also be altered by coupling the light to thermocatalytic reaction. However, the exact enhancement mechanism is rarely investigated and whether the thermo-photo coupled reaction pathway is different is still an open question.

1.8 Summary

In chapter 1, the theoretical background and recent advances on photocatalytic and photo-thermo coupled catalytic CO_2 are reviewed. Although the CO_2 conversion to valuable chemicals is a promising approach, there are still challenges to resolve before moving to industrial implementation stage. There are also fundamental scientific questions remaining ambiguous.

The biggest challenges for pure photocatalytic CO_2 reduction include the low reaction rate and poor selectivity to more valuable products. The photocatalytic CO_2 reduction rate is usually smaller than thermocatalytic CO_2 reduction by 2-4 orders of magnitude. The production of CO_2 reduction with H_2O is limited to several C1 products including CO, HCOOH, CH_3OH and CH_4. Due to the complicated process of photocatalytic CO_2 reduction, its reaction mechanism is still not clear. The development of new catalysts largely relies on trials and experiences. The mechanism of photocatalytic CO_2 reduction is needed to give guidance on photocatalyst design.

The research of photo-thermo coupled CO_2 reduction is still at the early stage. Although it has shown a synergistic effect of photo- and thermo-catalysis with significantly faster CO_2 reduction rate than conventional thermocatalytic reduction, the catalysts are not fully optimised and the mechanism underpinning the enhancement is far from understanding. To figure out what exactly happens under photo-thermo coupled reaction condition, three scientific questions need to be answered: (1) mechanism of reaction under pure thermocatalytic condition; (2) mechanism of reaction under photo-thermo coupled catalytic reaction condition; (3) how the external light promotes the reaction.

The works in this thesis aim to address the challenges mentioned above:

(1) Investigating the optimisation strategy for a promising transition metal-free photocatalyst, g-C_3N_4, for CO_2 reduction with H_2O. Reaction mechanism and photocatalytic performance enhancement mechanism are correlated together to provide a guidance for future photocatalysts design. The results point out the increase of the coverage of activated CO_2 is critical for a fast photocatalytic CO_2 reduction. (Chapter 3)

(2) Investigating the possibility to get higher selectivity to more valuable products from photocatalytic CO_2 reduction with H_2O. By using Au/TiO_{2-x} with an abundance of V_O and plasmonic excitation mechanism, 20% selectivity to C_2H_6 is achieved. *In-situ* spectroscopy experimental results provide insights on the selectivity improvement mechanism and the most plausible reaction pathway. (Chapter 4)

(3) Investigating the photo-thermo coupled catalytic RWGS reaction over Au/TiO_2. In addition to demonstrating the synergistic effects of photocatalysis and thermocatalysis, this chapter focuses on the aforementioned three scientific questions of photo-thermo coupled catalytic CO_2 reduction. The reaction pathways of RWGS in pure thermocatalytic and photo- thermo coupled reaction conditions are elucidated by *in-situ* spectroscopy methods. The CO_2 dissociative adsorption is found at the V_O site of Au/TiO_2. The plasmonic

enhancement mechanism is proven as the facilitated V_O generation. (Chapter 5)

(4) Investigating the photo-thermo coupled RWGS mechanism over Au/Al_2O_3. Al_2O_3 is a typical non-reducible support, which is completely different from reducible TiO_2 from electronic structure point of view. Therefore, this work is important to achieve a more comprehensive understanding of photo-thermo coupled catalytic RWGS mechanism together with chapter 5. Also focusing on the mechanism, the work in this chapter proves that the LSPR shows preferential promotion effects on specific reaction intermediate and reaction pathway. The results suggest the potential to significantly alter the selectivity of products via coupling external light irradiation into thermocatalytic reaction. (Chapter 6)

1.9 References

1. Notz, D.; Stroeve, J., *Science* **2016,** 354 (6313), 747-750.
2. Meinshausen, M.; Meinshausen, N.; Hare, W.; Raper, S. C.; Frieler, K.; Knutti, R.; Frame, D. J.; Allen, M. R., *Nature* **2009,** 458 (7242), 1158-1162.
3. Oliveier, J. G. J.; Peters, J. A. H. W.; Janssens-Maenhout, G., Trends in global CO_2 emissions. 2012 Report. 2012.
4. Zheng, X.; Lu, Y.; Yuan, J.; Baninla, Y.; Zhang, S.; Stenseth, N. C.; Hessen, D. O.; Tian, H.; Obersteiner, M.; Chen, D., *Proc. Natl. Acad. Sci. U. S. A.* **2020,** 117 (1), 29-36.
5. Tapia Granados, J. A.; Spash, C. L., *Environmental Science & Policy* **2019,** 94, 262-266.
6. Teske, S., *Achieving the Paris Climate Agreement Goals*. 2019.
7. Allen, M. R.; Dube, O. P.; Solecki, W.; Aragón-Durand, F.; Cramer, W.; Humphreys, S.; Kainuma, M.; Kala, J.; Mahowald, N.; Mulugetta, Y.; Perez, R.; Wairiu, M.; Zickfeld, K., Global Warming of 1.5 °C. An IPCC Special Report on the impacts of global warming of 1.5 °C above pre-industrial levels and related global greenhouse gas emission pathways, in the context of strengthening the global response to the threat of climate change, sustainable development, and efforts to eradicate poverty. IPCC: 2018.
8. Creutzig, F.; Breyer, C.; Hilaire, J.; Minx, J.; Peters, G. P.; Socolow, R., *Energy Environ. Sci.* **2019,** 12 (6), 1805-1817.
9. Detz, R. J.; van der Zwaan, B., *Energy Policy* **2019,** 133, 110938.
10. Friedlingstein, P.; Jones, M. W.; O'Sullivan, M.; Andrew, R. M.; Hauck, J.; Peters, G. P.; Peters, W.; Pongratz, J.; Sitch, S.; Le Quéré, C.; Bakker, D. C. E.; Canadell, J. G.; Ciais, P.; Jackson, R. B.; Anthoni, P.; Barbero, L.; Bastos, A.; Bastrikov, V.; Becker, M.; Bopp, L.; Buitenhuis, E.; Chandra, N.; Chevallier, F.; Chini, L. P.; Currie, K. I.; Feely, R. A.; Gehlen, M.; Gilfillan, D.; Gkritzalis, T.; Goll, D. S.; Gruber, N.; Gutekunst, S.; Harris, I.; Haverd, V.; Houghton, R. A.; Hurtt, G.; Ilyina, T.; Jain, A. K.; Joetzjer, E.; Kaplan, J. O.; Kato, E.; Klein Goldewijk, K.; Korsbakken, J. I.; Landschützer, P.; Lauvset, S. K.; Lefèvre, N.; Lenton, A.; Lienert, S.; Lombardozzi, D.; Marland, G.; McGuire, P. C.; Melton, J. R.; Metzl,

N.; Munro, D. R.; Nabel, J. E. M. S.; Nakaoka, S.-I.; Neill, C.; Omar, A. M.; Ono, T.; Peregon, A.; Pierrot, D.; Poulter, B.; Rehder, G.; Resplandy, L.; Robertson, E.; Rödenbeck, C.; Séférian, R.; Schwinger, J.; Smith, N.; Tans, P. P.; Tian, H.; Tilbrook, B.; Tubiello, F. N.; van der Werf, G. R.; Wiltshire, A. J.; Zaehle, S., *Earth System Science Data* **2019,** 11 (4), 1783-1838.

11. Olhoff, A.; Christensen, J. M. *Emissions Gap Report 2019. United Nations Environment Programme*; 2019.
12. Inoue, T.; Fujishima, A.; Konishi, S.; Honda, K., *Nature* **1979,** 277 (5698), 637-638.
13. Fujishima, A.; Honda, K., *Nature* **1972,** 238 (5358), 37-38.
14. Chen, Y.; Zeng, D.; Zhang, K.; Lu, A.; Wang, L.; Peng, D. L., *Nanoscale* **2014,** 6 (2), 874-881.
15. Pan, L.; Wang, S.; Mi, W.; Song, J.; Zou, J.-J.; Wang, L.; Zhang, X., *Nano Energy* **2014,** 9, 71-79.
16. Li, J.; Zhang, Z.; Ji, Y.; Jin, Z.; Zou, S.; Zhong, Z.; Su, F., *Nano Res.* **2016,** 9 (5), 1377-1392.
17. Yang, Y.; Xu, D.; Wu, Q.; Diao, P., *Sci. Rep.* **2016,** 6, 35158.
18. Kang, Y.; Gong, Y.; Hu, Z.; Li, Z.; Qiu, Z.; Zhu, X.; Ajayan, P. M.; Fang, Z., *Nanoscale* **2015,** 7 (10), 4482-4488.
19. Ho, W.; Yu, J. C.; Lin, J.; Yu, J.; Li, P., *Langmuir* **2004,** 20 (14), 5865-5869.
20. Jin, J.; Yu, J.; Guo, D.; Cui, C.; Ho, W., *Small* **2015,** 11 (39), 5262-5271.
21. Huang, Z. F.; Song, J.; Pan, L.; Zhang, X.; Wang, L.; Zou, J. J., *Adv. Mater.* **2015,** 27 (36), 5309-5327.
22. Ohtani, B.; Prieto-Mahaney, O. O.; Li, D.; Abe, R., *J. Photochem. Photobiol., A* **2010,** 216 (2-3), 179-182.
23. Jiang, X.; Manawan, M.; Feng, T.; Qian, R.; Zhao, T.; Zhou, G.; Kong, F.; Wang, Q.; Dai, S.; Pan, J. H., *Catal. Today* **2018,** 300, 12-17.
24. Liu, L.; Zhao, H.; Andino, J. M.; Li, Y., *ACS Catal.* **2012,** 2 (8), 1817-1828.
25. Tran, H. T. T.; Kosslick, H.; Ibad, M. F.; Fischer, C.; Bentrup, U.; Vuong, T. H.; Nguyen, L. Q.; Schulz, A., *Appl. Catal., B* **2017,** 200, 647-658.
26. Hanaor, D. A. H.; Sorrell, C. C., *J. Mater. Sci.* **2010,** 46 (4), 855-874.
27. Zhang, J.; Zhou, P.; Liu, J.; Yu, J., *Phys. Chem. Chem. Phys.* **2014,** 16 (38), 20382-20386.
28. Wang, X.; Maeda, K.; Thomas, A.; Takanabe, K.; Xin, G.; Carlsson, J. M.; Domen, K.; Antonietti, M., *Nat. Mater.* **2009,** 8 (1), 76-80.
29. Fina, F.; Callear, S. K.; Carins, G. M.; Irvine, J. T. S., *Chem. Mater.* **2015,** 27 (7), 2612-2618.
30. Tyborski, T.; Merschjann, C.; Orthmann, S.; Yang, F.; Lux-Steiner, M. C.; Schedel-Niedrig, T., *J. Phys.: Condens. Matter* **2013,** 25 (39), 395402.
31. Lin, L.; Ou, H.; Zhang, Y.; Wang, X., *ACS Catal.* **2016,** 6 (6), 3921-3931.
32. Sagara, N.; Kamimura, S.; Tsubota, T.; Ohno, T., *Appl. Catal., B* **2016,** 192, 193-198.
33. Zhu, J.; Diao, T.; Wang, W.; Xu, X.; Sun, X.; Carabineiro, S. A. C.; Zhao, Z., *Appl. Catal., B* **2017,** 219, 92-100.
34. Wang, Y.; Li, H.; Yao, J.; Wang, X.; Antonietti, M., *Chem. Sci.* **2011,** 2 (3), 446-450.
35. Fu, J.; Zhu, B.; Jiang, C.; Cheng, B.; You, W.; Yu, J., *Small* **2017,** 13 (15), 1603938.
36. Huang, Z.-F.; Song, J.; Pan, L.; Wang, Z.; Zhang, X.; Zou, J.-J.; Mi, W.; Zhang, X.; Wang, L., *Nano Energy* **2015,** 12, 646-656.
37. Zhu, Y. P.; Ren, T. Z.; Yuan, Z. Y., *ACS Appl. Mater. Interfaces* **2015,** 7 (30), 16850-16856.
38. Wang, K.; Li, Q.; Liu, B.; Cheng, B.; Ho, W.; Yu, J., *Appl. Catal., B* **2015,** 176-177, 44-52.
39. Liu, C.; Zhang, Y.; Dong, F.; Reshak, A. H.; Ye, L.; Pinna, N.; Zeng, C.; Zhang, T.; Huang, H., *Appl. Catal., B* **2017,** 203, 465-474.
40. Zhu, B.; Zhang, J.; Jiang, C.; Cheng, B.; Yu, J., *Appl. Catal., B* **2017,** 207, 27-34.

41. Yu, H.; Shi, R.; Zhao, Y.; Bian, T.; Zhao, Y.; Zhou, C.; Waterhouse, G. I. N.; Wu, L. Z.; Tung, C. H.; Zhang, T., *Adv. Mater.* **2017,** 29 (16), 1605148.
42. Sun, Z.; Fischer, J. M. T. A.; Li, Q.; Hu, J.; Tang, Q.; Wang, H.; Wu, Z.; Hankel, M.; Searles, D. J.; Wang, L., *Appl. Catal., B* **2017,** 216, 146-155.
43. Xiong, T.; Cen, W.; Zhang, Y.; Dong, F., *ACS Catal.* **2016,** 6 (4), 2462-2472.
44. Cui, W.; Li, J.; Cen, W.; Sun, Y.; Lee, S. C.; Dong, F., *J. Catal.* **2017,** 352, 351-360.
45. Jiang, L.; Yuan, X.; Zeng, G.; Chen, X.; Wu, Z.; Liang, J.; Zhang, J.; Wang, H.; Wang, H., *ACS Sustainable Chem. Eng.* **2017,** 5 (7), 5831-5841.
46. Hu, S.; Ma, L.; You, J.; Li, F.; Fan, Z.; Lu, G.; Liu, D.; Gui, J., *Appl. Surf. Sci.* **2014,** 311, 164-171.
47. Fang, W.; Liu, J.; Yu, L.; Jiang, Z.; Shangguan, W., *Appl. Catal., B* **2017,** 209, 631-636.
48. Li, J.; Zhang, Z.; Cui, W.; Wang, H.; Cen, W.; Johnson, G.; Jiang, G.; Zhang, S.; Dong, F., *ACS Catal.* **2018,** 8 (9), 8376-8385.
49. Raziq, F.; Qu, Y.; Humayun, M.; Zada, A.; Yu, H.; Jing, L., *Appl. Catal., B* **2017,** 201, 486-494.
50. Ding, K.; Wen, L.; Huang, M.; Zhang, Y.; Lu, Y.; Chen, Z., *Phys. Chem. Chem. Phys.* **2016,** 18 (28), 19217-19226.
51. Zhao, S.; Liu, J.; Li, C.; Ji, W.; Yang, M.; Huang, H.; Liu, Y.; Kang, Z., *ACS Appl. Mater. Interfaces* **2014,** 6 (24), 22297-22304.
52. Guo, Y.; Liu, Q.; Li, Z.; Zhang, Z.; Fang, X., *Appl. Catal., B* **2018,** 221, 362-370.
53. Wu, J.; Li, N.; Zhang, X.-H.; Fang, H.-B.; Zheng, Y.-Z.; Tao, X., *Appl. Catal., B* **2018,** 226, 61-70.
54. Gao, G.; Jiao, Y.; Waclawik, E. R.; Du, A., *J. Am. Chem. Soc.* **2016,** 138 (19), 6292-6297.
55. Liu, J., *J. Alloys Compd.* **2016,** 672, 271-276.
56. Ran, J.; Ma, T. Y.; Gao, G.; Du, X.-W.; Qiao, S. Z., *Energy Environ. Sci.* **2015,** 8 (12), 3708-3717.
57. Zheng, Y.; Jiao, Y.; Zhu, Y.; Cai, Q.; Vasileff, A.; Li, L. H.; Han, Y.; Chen, Y.; Qiao, S. Z., *J. Am. Chem. Soc.* **2017,** 139 (9), 3336-3339.
58. Ma, X.; Lv, Y.; Xu, J.; Liu, Y.; Zhang, R.; Zhu, Y., *J. Phys. Chem. C* **2012,** 116 (44), 23485-23493.
59. Xu, Y.; Schoonen, M. A. A., *Am. Mineral.* **2000,** 85 (3-4), 543-556.
60. Butler, M. A.; Ginley, D. S., *J. Electrochem. Soc.* **2019,** 125 (2), 228-232.
61. Liu, G.; Wang, L.; Yang, H. G.; Cheng, H.-M.; Lu, G. Q., *J. Mater. Chem.* **2010,** 20 (5), 831-843.
62. Niu, P.; Liu, G.; Cheng, H.-M., *J. Phys. Chem. C* **2012,** 116 (20), 11013-11018.
63. Yang, P.; Zhao, J.; Qiao, W.; Li, L.; Zhu, Z., *Nanoscale* **2015,** 7 (45), 18887-18890.
64. Li, S.; Dong, G.; Hailili, R.; Yang, L.; Li, Y.; Wang, F.; Zeng, Y.; Wang, C., *Appl. Catal., B* **2016,** 190, 26-35.
65. Tay, Q.; Kanhere, P.; Ng, C. F.; Chen, S.; Chakraborty, S.; Huan, A. C. H.; Sum, T. C.; Ahuja, R.; Chen, Z., *Chem. Mater.* **2015,** 27 (14), 4930-4933.
66. Niu, P.; Yin, L. C.; Yang, Y. Q.; Liu, G.; Cheng, H. M., *Adv. Mater.* **2014,** 26 (47), 8046-8052.
67. Lan, H.; Li, L.; An, X.; Liu, F.; Chen, C.; Liu, H.; Qu, J., *Appl. Catal., B* **2017,** 204, 49-57.
68. Lau, V. W.-h.; Yu, V. W.-z.; Ehrat, F.; Botari, T.; Moudrakovski, I.; Simon, T.; Duppel, V.; Medina, E.; Stolarczyk, J. K.; Feldmann, J.; Blum, V.; Lotsch, B. V., *Adv. Energy Mater.* **2017,** 7 (12), 1602251.
69. Ong, W.-J.; Putri, L. K.; Tan, Y.-C.; Tan, L.-L.; Li, N.; Ng, Y. H.; Wen, X.; Chai, S.-P., *Nano Res.* **2017,** 10 (5), 1673-1696.
70. Li, W.; Hu, Y.; Rodríguez-Castellón, E.; Bandosz, T. J., *J. Mater. Chem. A* **2017,** 5 (31), 16315-16325.

71. Ye, L.; Wu, D.; Chu, K. H.; Wang, B.; Xie, H.; Yip, H. Y.; Wong, P. K., *Chem. Eng. J.* **2016,** 304, 376-383.
72. Wang, Y.; Silveri, F.; Bayazit, M. K.; Ruan, Q.; Li, Y.; Xie, J.; Catlow, C. R. A.; Tang, J., *Adv. Energy Mater.* **2018,** 8 (24), 1801084.
73. Chang, X.; Wang, T.; Gong, J., *Energy Environ. Sci.* **2016,** 9 (7), 2177-2196.
74. Sun, Z.; Wang, S.; Li, Q.; Lyu, M.; Butburee, T.; Luo, B.; Wang, H.; Fischer, J. M. T. A.; Zhang, C.; Wu, Z.; Wang, L., *Adv. Sustainable Syst.* **2017,** 1 (3-4), 1700003.
75. Xia, P.; Zhu, B.; Yu, J.; Cao, S.; Jaroniec, M., *J. Mater. Chem. A* **2017,** 5 (7), 3230-3238.
76. Yue, B.; Li, Q.; Iwai, H.; Kako, T.; Ye, J., *Sci. Technol. Adv. Mater.* **2011,** 12 (3), 034401.
77. Yan, S. C.; Li, Z. S.; Zou, Z. G., *Langmuir* **2009,** 25 (17), 10397-10401.
78. Groenewolt, M.; Antonietti, M., *Adv. Mater.* **2005,** 17 (14), 1789-1792.
79. Li, Y.; Jin, R.; Xing, Y.; Li, J.; Song, S.; Liu, X.; Li, M.; Jin, R., *Adv. Energy Mater.* **2016,** 6 (24), 1601273.
80. Wang, Y.; Jiang, Q.; Shang, J.-K.; Xu, J.; Li, Y.-X., *Acta Phys.-Chim. Sin.* **2016,** 32 (8), 1913-1928.
81. Wang, Y.; Wang, X.; Antonietti, M.; Zhang, Y., *ChemSusChem* **2010,** 3 (4), 435-439.
82. Bojdys, M. J.; Severin, N.; Rabe, J. P.; Cooper, A. I.; Thomas, A.; Antonietti, M., *Macromol. Rapid Commun.* **2013,** 34 (10), 850-854.
83. Dong, X.; Cheng, F., *J. Mater. Chem. A* **2015,** 3 (47), 23642-23652.
84. Chen, X.; Jun, Y.-S.; Takanabe, K.; Maeda, K.; Domen, K.; Fu, X.; Antonietti, M.; Wang, X., *Chem. Mater.* **2009,** 21 (18), 4093-4095.
85. Huang, Z.; Li, F.; Chen, B.; Lu, T.; Yuan, Y.; Yuan, G., *Appl. Catal., B* **2013,** 136-137, 269-277.
86. An, T.; Tang, J.; Zhang, Y.; Quan, Y.; Gong, X.; Al-Enizi, A. M.; Elzatahry, A. A.; Zhang, L.; Zheng, G., *ACS Appl. Mater. Interfaces* **2016,** 8 (20), 12772-12779.
87. Chen, X.; Liu, Q.; Wu, Q.; Du, P.; Zhu, J.; Dai, S.; Yang, S., *Adv. Funct. Mater.* **2016,** 26 (11), 1719-1728.
88. Zhang, G.; Li, G.; Lan, Z. A.; Lin, L.; Savateev, A.; Heil, T.; Zafeiratos, S.; Wang, X.; Antonietti, M., *Angew. Chem., Int. Ed.* **2017,** 56 (43), 13445-13449.
89. Ruan, Q.; Luo, W.; Xie, J.; Wang, Y.; Liu, X.; Bai, Z.; Carmalt, C. J.; Tang, J., *Angew. Chem., Int. Ed.* **2017,** 56 (28), 8221-8225.
90. Hisatomi, T.; Maeda, K.; Takanabe, K.; Kubota, J.; Domen, K., *J. Phys. Chem. C* **2009,** 113 (51), 21458-21466.
91. Dilla, M.; Mateblowski, A.; Ristig, S.; Strunk, J., *ChemCatChem* **2017,** 9 (23), 4345-4352.
92. Akimov, A. V.; Neukirch, A. J.; Prezhdo, O. V., *Chem. Rev.* **2013,** 113 (6), 4496-4565.
93. Mohamed, H. H.; Bahnemann, D. W., *Appl. Catal., B* **2012,** 128, 91-104.
94. Bai, S.; Jiang, J.; Zhang, Q.; Xiong, Y., *Chem. Soc. Rev.* **2015,** 44 (10), 2893-2939.
95. Qian, R.; Zong, H.; Schneider, J.; Zhou, G.; Zhao, T.; Li, Y.; Yang, J.; Bahnemann, D. W.; Pan, J. H., *Catal. Today* **2019,** 335, 78-90.
96. Zhang, L.; Mohamed, H. H.; Dillert, R.; Bahnemann, D., *J. Photochem. Photobiol., C* **2012,** 13 (4), 263-276.
97. Lee, J.; Shim, H. S.; Lee, M.; Song, J. K.; Lee, D., *J. Phys. Chem. Lett.* **2011,** 2 (22), 2840-2845.
98. Wang, N.; Tachikawa, T.; Majima, T., *Chem. Sci.* **2011,** 2 (5), 891-900.
99. Ioannides, T.; Verykios, X. E., *J. Catal.* **1996,** 161 (2), 560-569.
100. Ashcroft, N. W.; Mermin, N. D., *Solid State Physics*. Thomson Learning: 1976.
101. Kreibig, U.; Genzel, L., *Surf. Sci.* **1985,** 156, 678-700.
102. Kwak, K.; Thanthirige, V. D.; Pyo, K.; Lee, D.; Ramakrishna, G., *J. Phys. Chem. Lett.* **2017,** 8 (19), 4898-4905.

103. Brown, A. M.; Sundararaman, R.; Narang, P.; Goddard, W. A., 3rd; Atwater, H. A., *ACS Nano* **2016,** 10 (1), 957-966.
104. Sundararaman, R.; Narang, P.; Jermyn, A. S.; Goddard, W. A., 3rd; Atwater, H. A., *Nat. Commun.* **2014,** 5, 5788.
105. Hartland, G. V.; Besteiro, L. V.; Johns, P.; Govorov, A. O., *ACS Energy Lett.* **2017,** 2 (7), 1641-1653.
106. Besteiro, L. V.; Kong, X.-T.; Wang, Z.; Hartland, G.; Govorov, A. O., *ACS Photonics* **2017,** 4 (11), 2759-2781.
107. Kong, X. T.; Wang, Z.; Govorov, A. O., *Adv. Opt. Mater.* **2016,** 5 (15), 1600594.
108. Brongersma, M. L.; Halas, N. J.; Nordlander, P., *Nat. Nanotechnol.* **2015,** 10 (1), 25-34.
109. Zhang, Z.; Zhang, C.; Zheng, H.; Xu, H., *Acc. Chem. Res.* **2019,** 52 (9), 2506-2515.
110. Tatsuma, T.; Nishi, H.; Ishida, T., *Chem. Sci.* **2017,** 8 (5), 3325-3337.
111. Zhang, Y.; He, S.; Guo, W.; Hu, Y.; Huang, J.; Mulcahy, J. R.; Wei, W. D., *Chem. Rev.* **2018,** 118 (6), 2927-2954.
112. Govorov, A. O.; Zhang, H.; Gun'ko, Y. K., *J. Phys. Chem. C* **2013,** 117 (32), 16616-16631.
113. Yu, Y.; Wijesekara, K. D.; Xi, X.; Willets, K. A., *ACS Nano* **2019,** 13 (3), 3629-3637.
114. Boerigter, C.; Campana, R.; Morabito, M.; Linic, S., *Nat. Commun.* **2016,** 7, 10545.
115. Kale, M. J.; Avanesian, T.; Xin, H.; Yan, J.; Christopher, P., *Nano Lett.* **2014,** 14 (9), 5405-5412.
116. Christopher, P.; Xin, H.; Marimuthu, A.; Linic, S., *Nat. Mater.* **2012,** 11 (12), 1044-1050.
117. Olsen, T.; Gavnholt, J.; Schiøtz, J., *Phys. Rev. B* **2009,** 79 (3), 035403.
118. Qian, K.; Sweeny, B. C.; Johnston-Peck, A. C.; Niu, W.; Graham, J. O.; DuChene, J. S.; Qiu, J.; Wang, Y. C.; Engelhard, M. H.; Su, D.; Stach, E. A.; Wei, W. D., *J. Am. Chem. Soc.* **2014,** 136 (28), 9842-9845.
119. Teranishi, M.; Wada, M.; Naya, S.; Tada, H., *Chemphyschem* **2016,** 17 (18), 2813-2817.
120. Naya, S.-i.; Tada, H., *J. Catal.* **2018,** 364, 328-333.
121. Naya, S. I.; Tada, H., *J. Catal.* **2018,** 364, 328-333.
122. Priebe, J. B.; Radnik, J.; Lennox, A. J. J.; Pohl, M.-M.; Karnahl, M.; Hollmann, D.; Grabow, K.; Bentrup, U.; Junge, H.; Beller, M.; Brückner, A., *ACS Catal.* **2015,** 5 (4), 2137-2148.
123. Knight, M. W.; Wang, Y.; Urban, A. S.; Sobhani, A.; Zheng, B. Y.; Nordlander, P.; Halas, N. J., *Nano Lett.* **2013,** 13 (4), 1687-1692.
124. White, T. P.; Catchpole, K. R., *Appl. Phys. Lett.* **2012,** 101 (7), 073905.
125. Wu, K.; Chen, J.; McBride, J. R.; Lian, T., *Science* **2015,** 349 (6248), 632-635.
126. Chen, Q. Y.; Bates, C. W., Jr., *Phys. Rev. Lett.* **1986,** 57 (21), 2737-2740.
127. Schmidt-Ott, A.; Schurtenberger, P.; Siegmann, H. C., *Phys. Rev. Lett.* **1980,** 45 (15), 1284-1287.
128. Muller, U.; Burtscher, H.; Schmidt-Ott, A., *Phys Rev B* **1988,** 38 (11), 7814-7816.
129. Giugni, A.; Torre, B.; Toma, A.; Francardi, M.; Malerba, M.; Alabastri, A.; Proietti Zaccaria, R.; Stockman, M. I.; Di Fabrizio, E., *Nat. Nanotechnol.* **2013,** 8 (11), 845-852.
130. Govorov, A. O.; Zhang, H.; Demir, H. V.; Gun'ko, Y. K., *Nano Today* **2014,** 9 (1), 85-101.
131. Kumarasinghe, C. S.; Premaratne, M.; Bao, Q.; Agrawal, G. P., *Sci. Rep.* **2015,** 5, 12140.
132. Kumarasinghe, C. S.; Premaratne, M.; Gunapala, S. D.; Agrawal, G. P., *Phys. Chem. Chem. Phys.* **2016,** 18 (27), 18227-18236.
133. Zhang, H.; Govorov, A. O., *J. Phys. Chem. C* **2014,** 118 (14), 7606-7614.
134. Ratchford, D. C.; Dunkelberger, A. D.; Vurgaftman, I.; Owrutsky, J. C.; Pehrsson, P. E., *Nano Lett.* **2017,** 17 (10), 6047-6055.
135. Yu, K.; Tian, Y.; Tatsuma, T., *Phys. Chem. Chem. Phys.* **2006,** 8 (46), 5417-5420.
136. Reineck, P.; Brick, D.; Mulvaney, P.; Bach, U., *J. Phys. Chem. Lett.* **2016,** 7 (20), 4137-4141.

137. Mubeen, S.; Hernandez-Sosa, G.; Moses, D.; Lee, J.; Moskovits, M., *Nano Lett.* **2011,** 11 (12), 5548-5552.
138. Wu, N., *Nanoscale* **2018,** 10 (6), 2679-2696.
139. Cushing, S. K.; Li, J.; Meng, F.; Senty, T. R.; Suri, S.; Zhi, M.; Li, M.; Bristow, A. D.; Wu, N., *J. Am. Chem. Soc.* **2012,** 134 (36), 15033-15041.
140. Liu, J.; Si, R.; Zheng, H.; Geng, Q.; Dai, W.; Chen, X.; Fu, X., *Catal. Commun.* **2012,** 26, 136-139.
141. Dai, W.; Zheng, X.; Yang, H.; Chen, X.; Wang, X.; Liu, P.; Fu, X., *J. Power Sources* **2009,** 188 (2), 507-514.
142. Yang, K.; Liu, J.; Si, R.; Chen, X.; Dai, W.; Fu, X., *J. Catal.* **2014,** 317, 229-239.
143. Frischkorn, C.; Wolf, M., *Chem. Rev.* **2006,** 106 (10), 4207-4233.
144. Struck, L. M.; Richter, L. J.; Buntin, S. A.; Cavanagh, R. R.; Stephenson, J. C., *Phys. Rev. Lett.* **1996,** 77 (22), 4576-4579.
145. Oberg, H.; Gladh, J.; Marks, K.; Ogasawara, H.; Nilsson, A.; Pettersson, L. G.; Ostrom, H., *J. Chem. Phys.* **2015,** 143 (7), 074701.
146. Szymanski, P.; Harris, A. L.; Camillone, N., 3rd, *J. Phys. Chem. A* **2007,** 111 (49), 12524-12533.
147. Gladh, J.; Hansson, T.; Öström, H., *Surf. Sci.* **2013,** 615, 65-71.
148. Bonn, M.; Funk, S.; Hess, C.; Denzler, D. N.; Stampfl, C.; Scheffler, M.; Wolf, M.; Ertl, G., *Science* **1999,** 285 (5430), 1042-1045.
149. Quiroz, J.; Barbosa, E. C. M.; Araujo, T. P.; Fiorio, J. L.; Wang, Y. C.; Zou, Y. C.; Mou, T.; Alves, T. V.; de Oliveira, D. C.; Wang, B.; Haigh, S. J.; Rossi, L. M.; Camargo, P. H. C., *Nano Lett.* **2018,** 18 (11), 7289-7297.
150. Kolobov, N. S.; Svintsitskiy, D. A.; Kozlova, E. A.; Selishchev, D. S.; Kozlov, D. V., *Chem. Eng. J.* **2017,** 314, 600-611.
151. Zhou, L.; Swearer, D. F.; Zhang, C.; Robatjazi, H.; Zhao, H.; Henderson, L.; Dong, L.; Christopher, P.; Carter, E. A.; Nordlander, P.; Halas, N. J., *Science* **2018,** 362 (6410), 69-72.
152. Mukherjee, S.; Libisch, F.; Large, N.; Neumann, O.; Brown, L. V.; Cheng, J.; Lassiter, J. B.; Carter, E. A.; Nordlander, P.; Halas, N. J., *Nano Lett.* **2013,** 13 (1), 240-247.
153. Mukherjee, S.; Zhou, L.; Goodman, A. M.; Large, N.; Ayala-Orozco, C.; Zhang, Y.; Nordlander, P.; Halas, N. J., *J. Am. Chem. Soc.* **2014,** 136 (1), 64-67.
154. Hammer, B.; Norskov, J. K., *Nature* **1995,** 376 (6537), 238-240.
155. Nilsson, A.; Pettersson, L. G. M.; Hammer, B.; Bligaard, T.; Christensen, C. H.; Nørskov, J. K., *Catal. Lett.* **2005,** 100 (3-4), 111-114.
156. Hammer, B.; Nørskov, J. K., *Adv. Catal.* **2000,** 45, 71-129.
157. Norskov, J. K.; Abild-Pedersen, F.; Studt, F.; Bligaard, T., *Proc. Natl. Acad. Sci. U. S. A.* **2011,** 108 (3), 937-943.
158. Bernardi, M.; Mustafa, J.; Neaton, J. B.; Louie, S. G., *Nat. Commun.* **2015,** 6, 7044.
159. Eastman, D. E., *Phys. Rev. Lett.* **1971,** 26 (18), 1108-1110.
160. Clavero, C., *Nat. Photonics* **2014,** 8 (2), 95-103.
161. Jiang, T.; Mowbray, D. J.; Dobrin, S.; Falsig, H.; Hvolbæk, B.; Bligaard, T.; Nørskov, J. K., *J. Phys. Chem. C* **2009,** 113 (24), 10548-10553.
162. Lopez, N., *J. Catal.* **2004,** 223 (1), 232-235.
163. Tamura, M.; Kon, K.; Satsuma, A.; Shimizu, K.-i., *ACS Catal.* **2012,** 2 (9), 1904-1909.
164. Han, B. C.; Miranda, C. R.; Ceder, G., *Phys. Rev. B* **2008,** 77 (7), 075410.
165. Lu, C.; Lee, I. C.; Masel, R. I.; Wieckowski, A.; Rice, C., *J. Phys. Chem. A* **2002,** 106 (13), 3084-3091.
166. Hofmann, T.; Yu, T. H.; Folse, M.; Weinhardt, L.; Bär, M.; Zhang, Y.; Merinov, B. V.; Myers, D. J.; Goddard, W. A.; Heske, C., *J. Phys. Chem. C* **2012,** 116 (45), 24016-24026.

167. Taketoshi, A.; Haruta, M., *Chem. Lett.* **2014,** 43 (4), 380-387.
168. Tsunoyama, H.; Tsukuda, T., *J. Am. Chem. Soc.* **2009,** 131 (51), 18216-18217.
169. Li, J.; Li, X.; Zhai, H. J.; Wang, L. S., *Science* **2003,** 299 (5608), 864-867.
170. Li, H.; Li, L.; Pedersen, A.; Gao, Y.; Khetrapal, N.; Jonsson, H.; Zeng, X. C., *Nano Lett.* **2015,** 15 (1), 682-688.
171. Gao, Y.; Shao, N.; Pei, Y.; Chen, Z.; Zeng, X. C., *ACS Nano* **2011,** 5 (10), 7818-7829.
172. Beltrán, M. R.; Suárez Raspopov, R.; González, G., *The European Physical Journal D* **2011,** 65 (3), 411-420.
173. Phala, N. S.; van Steen, E., *Gold Bull.* **2007,** 40 (2), 150-153.
174. van Bokhoven, J. A.; Miller, J. T., *J. Phys. Chem. C* **2007,** 111 (26), 9245-9249.
175. Verga, L. G.; Aarons, J.; Sarwar, M.; Thompsett, D.; Russell, A. E.; Skylaris, C. K., *Faraday Discuss.* **2018,** 208 (0), 497-522.
176. Visikovskiy, A.; Matsumoto, H.; Mitsuhara, K.; Nakada, T.; Akita, T.; Kido, Y., *Phys. Rev. B* **2011,** 83 (16), 165428.
177. Tauster, S. J.; Fung, S. C.; Garten, R. L., *J. Am. Chem. Soc.* **2002,** 100 (1), 170-175.
178. Tauster, S. J.; Fung, S. C.; Baker, R. T.; Horsley, J. A., *Science* **1981,** 211 (4487), 1121-1125.
179. Tauster, S. J., *Acc. Chem. Res.* **2002,** 20 (11), 389-394.
180. Pacchioni, G., *Phys. Chem. Chem. Phys.* **2013,** 15 (6), 1737-1757.
181. Jimenez-Izal, E.; Alexandrova, A. N., *Annu. Rev. Phys. Chem.* **2018,** 69 (1), 377-400.
182. Tang, H.; Su, Y.; Zhang, B.; Lee, A. F.; Isaacs, M. A.; Wilson, K.; Li, L.; Ren, Y.; Huang, J.; Haruta, M.; Qiao, B.; Liu, X.; Jin, C.; Su, D.; Wang, J.; Zhang, T., *Sci. Adv.* **2017,** 3 (10), e1700231.
183. Kuwauchi, Y.; Yoshida, H.; Akita, T.; Haruta, M.; Takeda, S., *Angew. Chem., Int. Ed.* **2012,** 51 (31), 7729-7733.
184. Liu, X.; Liu, M. H.; Luo, Y. C.; Mou, C. Y.; Lin, S. D.; Cheng, H.; Chen, J. M.; Lee, J. F.; Lin, T. S., *J. Am. Chem. Soc.* **2012,** 134 (24), 10251-10258.
185. Fu, Q.; Wagner, T., *Surf. Sci. Rep.* **2007,** 62 (11), 431-498.
186. Hadjiivanov, K. I.; Klissurski, D. G., *Chem. Soc. Rev.* **1996,** 25 (1), 61-69.
187. Haller, G. L.; Resasco, D. E. Metal–Support Interaction: Group VIII Metals and Reducible Oxides, Academic Press Inc.: 1989.
188. Bonanni, S.; Aït-Mansour, K.; Brune, H.; Harbich, W., *ACS Catal.* **2011,** 1 (4), 385-389.
189. McCaldin, J. O.; McGill, T. C., *Annu. Rev. Mater. Sci.* **1980,** 10 (1), 65-83.
190. Tung, R., *Appl. Phys. Rev.* **2014,** 1 (1), 011304.
191. Waldrop, J. R., *Appl. Phys. Lett.* **1984,** 44 (10), 1002-1004.
192. Cai, Y.; Feng, Y. P., *Prog. Surf. Sci.* **2016,** 91 (4), 183-202.
193. Imanishi, A.; Tsuji, E.; Nakato, Y., *J. Phys. Chem. C* **2007,** 111 (5), 2128-2132.
194. Ma, Z.; Dai, S., *Heterogeneous Gold Catalysts and Catalysis*. the Royal Society of Chemistry: 2014.
195. Klyushin, A. Y.; Jones, T. E.; Lunkenbein, T.; Kube, P.; Li, X.; Hävecker, M.; Knop-Gericke, A.; Schlögl, R., *ChemCatChem* **2018,** 10 (18), 3985-3989.
196. Okazaki, K.; Morikawa, Y.; Tanaka, S.; Tanaka, K.; Kohyama, M., *Phys. Rev. B* **2004,** 69 (23), 235404.
197. Okazaki, K.; Ichikawa, S.; Maeda, Y.; Haruta, M.; Kohyama, M., *Appl. Catal., A* **2005,** 291 (1-2), 45-54.
198. Scanlon, D. O.; Dunnill, C. W.; Buckeridge, J.; Shevlin, S. A.; Logsdail, A. J.; Woodley, S. M.; Catlow, C. R.; Powell, M. J.; Palgrave, R. G.; Parkin, I. P.; Watson, G. W.; Keal, T. W.; Sherwood, P.; Walsh, A.; Sokol, A. A., *Nat. Mater.* **2013,** 12 (9), 798-801.
199. Deák, P.; Aradi, B.; Frauenheim, T., *J. Phys. Chem. C* **2011,** 115 (8), 3443-3446.
200. Okazawa, T.; Kohyama, M.; Kido, Y., *Surf. Sci.* **2006,** 600 (19), 4430-4437.

201. Chusuei, C. C.; Lai, X.; Luo, K.; Goodman, D. W., *Top. Catal.* **2000,** 14 (1/4), 71-83.
202. Howard, A.; Clark, D. N. S.; Mitchell, C. E. J.; Egdell, R. G.; Dhanak, V. R., *Surf. Sci.* **2002,** 518 (3), 210-224.
203. Cai, Y.; Bai, Z.; Chintalapati, S.; Zeng, Q.; Feng, Y. P., *J. Chem. Phys.* **2013,** 138 (15), 154711.
204. Jiang, Z.; Zhang, W.; Jin, L.; Yang, X.; Xu, F.; Zhu, J.; Huang, W., *J. Phys. Chem. C* **2007,** 111 (33), 12434-12439.
205. Minato, T.; Susaki, T.; Shiraki, S.; Kato, H. S.; Kawai, M.; Aika, K.-i., *Surf. Sci.* **2004,** 566-568, 1012-1017.
206. Wang, Y. G.; Yoon, Y.; Glezakou, V. A.; Li, J.; Rousseau, R., *J. Am. Chem. Soc.* **2013,** 135 (29), 10673-10683.
207. Manzoli, M.; Boccuzzi, F.; Chiorino, A.; Vindigni, F.; Deng, W.; Flytzanistephanopoulos, M., *J. Catal.* **2007,** 245 (2), 308-315.
208. Nilius, N.; Ganduglia-Pirovano, M. V.; Brazdova, V.; Kulawik, M.; Sauer, J.; Freund, H. J., *Phys. Rev. Lett.* **2008,** 100 (9), 096802.
209. Ruiz Puigdollers, A.; Schlexer, P.; Tosoni, S.; Pacchioni, G., *ACS Catal.* **2017,** 7 (10), 6493-6513.
210. Campbell, C. T., *Nat. Chem.* **2012,** 4 (8), 597-598.
211. Bruix, A.; Rodriguez, J. A.; Ramirez, P. J.; Senanayake, S. D.; Evans, J.; Park, J. B.; Stacchiola, D.; Liu, P.; Hrbek, J.; Illas, F., *J. Am. Chem. Soc.* **2012,** 134 (21), 8968-8974.
212. Hutchings, G. J., *ACS Cent. Sci.* **2018,** 4 (9), 1095-1101.
213. Fierro-Gonzalez, J. C.; Gates, B. C., *Chem. Soc. Rev.* **2008,** 37 (9), 2127-2134.
214. Min, B. K.; Friend, C. M., *Chem. Rev.* **2007,** 107 (6), 2709-2724.
215. Prestianni, A.; Martorana, A.; Labat, F.; Ciofini, I.; Adamo, C., *J. Phys. Chem. B* **2006,** 110 (25), 12240-12248.
216. Okumura, M.; Kitagawa, Y.; Haruta, M.; Yamaguchi, K., *Appl. Catal., A* **2005,** 291 (1-2), 37-44.
217. Wu, X.; Senapati, L.; Nayak, S. K.; Selloni, A.; Hajaligol, M., *J. Chem. Phys.* **2002,** 117 (8), 4010-4015.
218. Roldan, A.; Ricart, J. M.; Illas, F.; Pacchioni, G., *Phys. Chem. Chem. Phys.* **2010,** 12 (36), 10723-10729.
219. Vittadini, A.; Selloni, A., *J. Chem. Phys.* **2002,** 117 (1), 353-361.
220. Wang, Y.; Widmann, D.; Behm, R. J., *ACS Catal.* **2017,** 7 (4), 2339-2345.
221. Wang, Y.; Widmann, D.; Heenemann, M.; Diemant, T.; Biskupek, J.; Schlögl, R.; Behm, R. J., *J. Catal.* **2017,** 354, 46-60.
222. Guzman, J.; Gates, B. C., *J. Am. Chem. Soc.* **2004,** 126 (9), 2672-2673.
223. Chenakin, S.; Kruse, N., *J. Catal.* **2018,** 358, 224-236.
224. Kung, M. C.; Davis, R. J.; Kung, H. H., *J. Phys. Chem. C* **2007,** 111 (32), 11767-11775.
225. Green, I. X.; Tang, W.; McEntee, M.; Neurock, M.; Yates, J. T., Jr., *J. Am. Chem. Soc.* **2012,** 134 (30), 12717-12723.
226. Haruta, M.; Kobayashi, T.; Sano, H.; Yamada, N., *Chem. Lett.* **1987,** 16 (2), 405-408.
227. Haruta, M., *J. Catal.* **1989,** 115 (2), 301-309.
228. Hutchings, G., *J. Catal.* **1985,** 96 (1), 292-295.
229. Ishida, T.; Murayama, T.; Taketoshi, A.; Haruta, M., *Chem. Rev.* **2020,** 120 (2), 464-525.
230. Villa, A.; Dimitratos, N.; Chan-Thaw, C. E.; Hammond, C.; Veith, G. M.; Wang, D.; Manzoli, M.; Prati, L.; Hutchings, G. J., *Chem. Soc. Rev.* **2016,** 45 (18), 4953-4994.
231. Janssens, T. V. W.; Clausen, B. S.; Hvolbæk, B.; Falsig, H.; Christensen, C. H.; Bligaard, T.; Nørskov, J. K., *Top. Catal.* **2007,** 44 (1-2), 15-26.
232. Fujitani, T.; Nakamura, I., *Angew. Chem., Int. Ed.* **2011,** 50 (43), 10144-10147.

233. Williams, W. D.; Shekhar, M.; Lee, W. S.; Kispersky, V.; Delgass, W. N.; Ribeiro, F. H.; Kim, S. M.; Stach, E. A.; Miller, J. T.; Allard, L. F., *J. Am. Chem. Soc.* **2010,** 132 (40), 14018-14020.
234. Fujitani, T.; Nakamura, I.; Akita, T.; Okumura, M.; Haruta, M., *Angew. Chem., Int. Ed.* **2009,** 48 (50), 9515-9518.
235. Valden, M.; Lai, X.; Goodman, D. W., *Science* **1998,** 281 (5383), 1647-1650.
236. Qian, K.; Luo, L.; Bao, H.; Hua, Q.; Jiang, Z.; Huang, W., *Catal. Sci. Technol.* **2013,** 3 (3), 679-687.
237. Cargnello, M.; Doan-Nguyen, V. V.; Gordon, T. R.; Diaz, R. E.; Stach, E. A.; Gorte, R. J.; Fornasiero, P.; Murray, C. B., *Science* **2013,** 341 (6147), 771-773.
238. Yang, B.; Cao, X. M.; Gong, X. Q.; Hu, P., *Phys. Chem. Chem. Phys.* **2012,** 14 (11), 3741-3745.
239. Weiher, N.; Beesley, A. M.; Tsapatsaris, N.; Delannoy, L.; Louis, C.; van Bokhoven, J. A.; Schroeder, S. L., *J. Am. Chem. Soc.* **2007,** 129 (8), 2240-2241.
240. Sun, K.; Kohyama, M.; Tanaka, S.; Takeda, S., *J. Phys. Chem. C* **2014,** 118 (3), 1611-1617.
241. Nelson, N. C.; Szanyi, J., *ACS Catal.* **2020,** 10 (10), 5663-5671.
242. Setvin, M.; Franchini, C.; Hao, X.; Schmid, M.; Janotti, A.; Kaltak, M.; Van de Walle, C. G.; Kresse, G.; Diebold, U., *Phys. Rev. Lett.* **2014,** 113 (8), 086402.
243. Thomas, A. G.; Flavell, W. R.; Mallick, A. K.; Kumarasinghe, A. R.; Tsoutsou, D.; Khan, N.; Chatwin, C.; Rayner, S.; Smith, G. C.; Stockbauer, R. L.; Warren, S.; Johal, T. K.; Patel, S.; Holland, D.; Taleb, A.; Wiame, F., *Phys. Rev. B* **2007,** 75 (3), 035105.
244. Thomas, A. G.; Flavell, W. R.; Kumarasinghe, A. R.; Mallick, A. K.; Tsoutsou, D.; Smith, G. C.; Stockbauer, R.; Patel, S.; Grätzel, M.; Hengerer, R., *Phys. Rev. B* **2003,** 67 (3), 035110.
245. Zhang, Z.; Yates, J. T. *Defects at Oxide Surfaces*, Springer International Publishing: 2015.
246. Yoon, S. D.; Chen, Y.; Yang, A.; Goodrich, T. L.; Zuo, X.; Arena, D. A.; Ziemer, K.; Vittoria, C.; Harris, V. G., *J. Phys.: Condens. Matter* **2006,** 18 (27), L355-L361.
247. Parras, M.; Varela, Á.; Cortés-Gil, R.; Boulahya, K.; Hernando, A.; González- Calbet, J. M., *J. Phys. Chem. Lett.* **2013,** 4 (13), 2171-2176.
248. Kim, D.; Hong, J.; Park, Y. R.; Kim, K. J., *J. Phys.: Condens. Matter* **2009,** 21 (19), 195405.
249. Ha, M. A.; Alexandrova, A. N., *J. Chem. Theory Comput.* **2016,** 12 (6), 2889-2895.
250. Finazzi, E.; Di Valentin, C.; Pacchioni, G.; Selloni, A., *J. Chem. Phys.* **2008,** 129 (15), 154113.
251. Yang, K.; Dai, Y.; Huang, B.; Feng, Y. P., *Phys. Rev. B* **2010,** 81 (3), 033202.
252. Cheng, H.; Selloni, A., *J. Chem. Phys.* **2009,** 131 (5), 054703.
253. Selcuk, S.; Selloni, A., *Nature Mater.* **2016,** 15, 1107.
254. Duan, Z.; Henkelman, G., *ACS Catal.* **2015,** 5 (3), 1589-1595.
255. Duan, Z.; Henkelman, G., *ACS Catal.* **2018,** 8 (2), 1376-1383.
256. Schlexer, P.; Widmann, D.; Behm, R. J.; Pacchioni, G., *ACS Catal.* **2018,** 8 (7), 6513-6525.
257. Zhang, S.; Huang, Z. Q.; Ma, Y.; Gao, W.; Li, J.; Cao, F.; Li, L.; Chang, C. R.; Qu, Y., *Nat. Commun.* **2017,** 8, 15266.
258. Li, P.; Chen, X.; Li, Y.; Schwank, J. W., *Catal. Today* **2019,** 327, 90-115.
259. Kotobuki, M.; Leppelt, R.; Hansgen, D. A.; Widmann, D.; Behm, R. J., *J. Catal.* **2009,** 264 (1), 67-76.
260. Widmann, D.; Liu, Y.; Schüth, F.; Behm, R. J., *J. Catal.* **2010,** 276 (2), 292-305.
261. Busca, G., *Catal. Today* **2014,** 226, 2-13.
262. Ferreira, A. R.; Martins, M. J. F.; Konstantinova, E.; Capaz, R. B.; Souza, W. F.; Chiaro, S. S. X.; Leitão, A. A., *J. Solid State Chem.* **2011,** 184 (5), 1105-1111.
263. Krokidis, X.; Raybaud, P.; Gobichon, A.-E.; Rebours, B.; Euzen, P.; Toulhoat, H., *J. Phys. Chem. B* **2001,** 105 (22), 5121-5130.

264. Digne, M.; Sautet, P.; Raybaud, P.; Euzen, P.; Toulhoat, H., *J. Catal.* **2002,** 211 (1), 1-5.
265. Digne, M., *J. Catal.* **2004,** 226 (1), 54-68.
266. Tanabe, K.; Misono, M.; Hattori, H.; Ono, Y., *New Solid Acids and Bases: Their Catalytic Properties*. Elsevier Science: 1990.
267. Morterra, C.; Magnacca, G., *Catal. Today* **1996,** 27 (3-4), 497-532.
268. Haneda, M.; Emmanuel Joubert, c.; Me´ne´zo, J.-C.; Duprez, D.; Barbier, J.; Bion, N.; Daturi, M.; Saussey, J.; Lavalley, J.-C.; Hamada, H., *Phys. Chem. Chem. Phys.* **2001,** 3 (7), 1366-1370.
269. Majors, P. D.; Ellis, P. D., *J. Am. Chem. Soc.* **2002,** 109 (6), 1648-1653.
270. Kawakami, H.; Yoshida, S., *J. Chem. Soc., Faraday Trans. 2* **1985,** 81 (7), 1117-1127.
271. Kawakami, H.; Yoshida, S., *J. Chem. Soc., Faraday Trans. 2* **1985,** 81 (7), 1129-1137.
272. Habisreutinger, S. N.; Schmidt-Mende, L.; Stolarczyk, J. K., *Angew. Chem., Int. Ed.* **2013,** 52 (29), 7372-7408.
273. Saveant, J. M., *Annu Rev Anal Chem* **2014,** 7, 537-560.
274. Taifan, W.; Boily, J.-F.; Baltrusaitis, J., *Surf. Sci. Rep.* **2016,** 71 (4), 595-671.
275. Freund, H. J.; Roberts, M. W., *Surf. Sci. Rep.* **1996,** 25 (8), 225-273.
276. He, H.; Zapol, P.; Curtiss, L. A., *J. Phys. Chem. C* **2010,** 114 (49), 21474-21481.
277. Zhou, L.; Kandratsenka, A.; Campbell, C. T.; Wodtke, A. M.; Guo, H., *Angew. Chem., Int. Ed.* **2019,** 58 (21), 6916-6920.
278. Mino, L.; Zecchina, A.; Martra, G.; Rossi, A. M.; Spoto, G., *Appl. Catal., B* **2016,** 196, 135-141.
279. Mino, L.; Spoto, G.; Ferrari, A. M., *J. Phys. Chem. C* **2014,** 118 (43), 25016-25026.
280. Jia, J.; Qian, C.; Dong, Y.; Li, Y. F.; Wang, H.; Ghoussoub, M.; Butler, K. T.; Walsh, A.; Ozin, G. A., *Chem. Soc. Rev.* **2017,** 46 (15), 4631-4644.
281. Yang, C. C.; Yu, Y. H.; van der Linden, B.; Wu, J. C.; Mul, G., *J. Am. Chem. Soc.* **2010,** 132 (24), 8398-8406.
282. Dilla, M.; Jakubowski, A.; Ristig, S.; Strunk, J.; Schlogl, R., *Phys. Chem. Chem. Phys.* **2019,** 21 (29), 15949-15957.
283. Dilla, M.; Schlögl, R.; Strunk, J., *ChemCatChem* **2017,** 9 (4), 696-704.
284. Ji, Y.; Luo, Y., *J. Phys. Chem. C* **2019,** 123 (5), 3019-3023.
285. Liu, L.; Li, Y., *Aerosol Air Qual. Res.* **2014,** 14 (2), 453-469.
286. Liu, L.; Jiang, Y.; Zhao, H.; Chen, J.; Cheng, J.; Yang, K.; Li, Y., *ACS Catal.* **2016,** 6 (2), 1097-1108.
287. Sun, Z.; Talreja, N.; Tao, H.; Texter, J.; Muhler, M.; Strunk, J.; Chen, J., *Angew. Chem., Int. Ed.* **2018,** 57 (26), 7610-7627.
288. Shkrob, I. A.; Marin, T. W.; He, H.; Zapol, P., *J. Phys. Chem. C* **2012,** 116 (17), 9450-9460.
289. Anpo, M.; Yamashita, H.; Ichihashi, Y.; Ehara, S., *J. Electroanal. Chem.* **1995,** 396 (1-2), 21-26.
290. Dimitrijevic, N. M.; Vijayan, B. K.; Poluektov, O. G.; Rajh, T.; Gray, K. A.; He, H.; Zapol, P., *J. Am. Chem. Soc.* **2011,** 133 (11), 3964-3971.
291. Kar, P.; Farsinezhad, S.; Mahdi, N.; Zhang, Y.; Obuekwe, U.; Sharma, H.; Shen, J.; Semagina, N.; Shankar, K., *Nano Res.* **2016,** 9 (11), 3478-3493.
292. Ji, Y.; Luo, Y., *J. Am. Chem. Soc.* **2016,** 138 (49), 15896-15902.
293. Ji, Y.; Luo, Y., *ACS Catal.* **2016,** 6 (3), 2018-2025.
294. Guo, Y.; Chen, S.; Yu, Y.; Tian, H.; Zhao, Y.; Ren, J. C.; Huang, C.; Bian, H.; Huang, M.; An, L.; Li, Y.; Zhang, R., *J. Am. Chem. Soc.* **2019,** 141 (21), 8407-8411.
295. Wang, S.; Pan, L.; Song, J. J.; Mi, W.; Zou, J. J.; Wang, L.; Zhang, X., *J. Am. Chem. Soc.* **2015,** 137 (8), 2975-2983.
296. Abdullah, H.; Khan, M. M. R.; Ong, H. R.; Yaakob, Z., *J. CO2 Util.* **2017,** 22, 15-32.
297. Chen, X.; Liu, L.; Huang, F., *Chem. Soc. Rev.* **2015,** 44 (7), 1861-1885.

298. Chen, X.; Liu, L.; Yu, P. Y.; Mao, S. S., *Science* **2011,** 331 (6018), 746-750.
299. Wang, Z.; Yang, C.; Lin, T.; Yin, H.; Chen, P.; Wan, D.; Xu, F.; Huang, F.; Lin, J.; Xie, X.; Jiang, M., *Energy Environ. Sci.* **2013,** 6 (10), 3007-3014.
300. Zhao, Z.; Tan, H.; Zhao, H.; Lv, Y.; Zhou, L. J.; Song, Y.; Sun, Z., *Chem. Commun.* **2014,** 50 (21), 2755-2757.
301. Sinhamahapatra, A.; Jeon, J.-P.; Yu, J.-S., *Energy Environ. Sci.* **2015,** 8 (12), 3539-3544.
302. Lin, T.; Yang, C.; Wang, Z.; Yin, H.; Lü, X.; Huang, F.; Lin, J.; Xie, X.; Jiang, M., *Energy Environ. Sci.* **2014,** 7 (3), 967-972.
303. Kar, P.; Zeng, S.; Zhang, Y.; Vahidzadeh, E.; Manuel, A.; Kisslinger, R.; Alam, K. M.; Thakur, U. K.; Mahdi, N.; Kumar, P.; Shankar, K., *Appl. Catal., B* **2019,** 243, 522-536.
304. Ge, H.; Zhang, B.; Liang, H.; Zhang, M.; Fang, K.; Chen, Y.; Qin, Y., *Appl. Catal., B* **2020,** 263.
305. Sheng, L.; Liao, T.; Kou, L.; Sun, Z., *Mater. Today Energy* **2017,** 3, 32-39.
306. Tang, S.; Yin, X.; Wang, G.; Lu, X.; Lu, T., *Nano Res.* **2018,** 12 (2), 457-462.
307. She, H.; Zhou, H.; Li, L.; Zhao, Z.; Jiang, M.; Huang, J.; Wang, L.; Wang, Q., *ACS Sustainable Chem. Eng.* **2018,** 7 (1), 650-659.
308. Bhunia, M. K.; Yamauchi, K.; Takanabe, K., *Angew. Chem., Int. Ed.* **2014,** 53 (41), 11001-11005.
309. Guo, Y.; Shi, W.; Zhu, Y., *EcoMat* **2019,** 1 (1), e12007.
310. Xing, M.; Zhou, Y.; Dong, C.; Cai, L.; Zeng, L.; Shen, B.; Pan, L.; Dong, C.; Chai, Y.; Zhang, J.; Yin, Y., *Nano Lett.* **2018,** 18 (6), 3384-3390.
311. Li, X.; Yu, J.; Jaroniec, M.; Chen, X., *Chem. Rev.* **2019,** 119 (6), 3962-4179.
312. Galperin, M., *Chem. Soc. Rev.* **2017,** 46 (13), 4000-4019.
313. Tang, J.-y.; Guo, R.-t.; Zhou, W.-g.; Huang, C.-y.; Pan, W.-g., *Appl. Catal., B* **2018,** 237, 802-810.
314. In, S. I.; Vaughn, D. D., 2nd; Schaak, R. E., *Angew. Chem., Int. Ed.* **2012,** 51 (16), 3915-3918.
315. Zhang, W.; Mohamed, A. R.; Ong, W. J., *Angew. Chem., Int. Ed.* **2020,** 59 (51), 22894-22915.
316. Wang, J. C.; Zhang, L.; Fang, W. X.; Ren, J.; Li, Y. Y.; Yao, H. C.; Wang, J. S.; Li, Z. J., *ACS Appl. Mater. Interfaces* **2015,** 7 (16), 8631-8639.
317. Wang, J. C.; Yao, H. C.; Fan, Z. Y.; Zhang, L.; Wang, J. S.; Zang, S. Q.; Li, Z. J., *ACS Appl. Mater. Interfaces* **2016,** 8 (6), 3765-3775.
318. Jiang, Z.; Wan, W.; Li, H.; Yuan, S.; Zhao, H.; Wong, P. K., *Adv. Mater.* **2018,** 30 (10), 1706108.
319. Kim, C.; Cho, K. M.; Al-Saggaf, A.; Gereige, I.; Jung, H.-T., *ACS Catal.* **2018,** 8 (5), 4170-4177.
320. Huygh, S.; Bogaerts, A.; Neyts, E. C., *J. Phys. Chem. C* **2016,** 120 (38), 21659-21669.
321. Sorescu, D. C.; Al-Saidi, W. A.; Jordan, K. D., *J. Chem. Phys.* **2011,** 135 (12), 124701.
322. Pu, Y.; Luo, Y.; Wei, X.; Sun, J.; Li, L.; Zou, W.; Dong, L., *Appl. Catal., B* **2019,** 254, 580-586.
323. Qi, Y.; Song, L.; Ouyang, S.; Liang, X.; Ning, S.; Zhang, Q.; Ye, J., *Adv. Mater.* **2020,** 32 (6), e1903915.
324. Wang, K.; Fu, J.; Zheng, Y., *Appl. Catal., B* **2019,** 254, 270-282.
325. Tang, Q.; Sun, Z.; Wang, P.; Li, Q.; Wang, H.; Wu, Z., *Appl. Surf. Sci.* **2019,** 463, 456-462.
326. Meng, X.; Ouyang, S.; Kako, T.; Li, P.; Yu, Q.; Wang, T.; Ye, J., *Chem. Commun.* **2014,** 50 (78), 11517-11519.
327. Liao, Y.; Cao, S. W.; Yuan, Y.; Gu, Q.; Zhang, Z.; Xue, C., *Chem. - Eur. J.* **2014,** 20 (33), 10220-10222.

328. Liu, B.; Ye, L.; Wang, R.; Yang, J.; Zhang, Y.; Guan, R.; Tian, L.; Chen, X., *ACS Appl. Mater. Interfaces* **2018,** 10 (4), 4001-4009.
329. Wang, S.; Zhan, J.; Chen, K.; Ali, A.; Zeng, L.; Zhao, H.; Hu, W.; Zhu, L.; Xu, X., *ACS Sustainable Chem. Eng.* **2020,** 8 (22), 8214-8222.
330. Liu, L.; Zhao, C.; Li, Y., *J. Phys. Chem. C* **2012,** 116 (14), 7904-7912.
331. Iyemperumal, S. K.; Deskins, N. A., *Phys. Chem. Chem. Phys.* **2017,** 19 (42), 28788-28807.
332. Zhu, Y.; Gao, C.; Bai, S.; Chen, S.; Long, R.; Song, L.; Li, Z.; Xiong, Y., *Nano Res.* **2017,** 10 (10), 3396-3406.
333. Tasbihi, M.; Kočí, K.; Edelmannová, M.; Troppová, I.; Reli, M.; Schomäcker, R., *J. Photochem. Photobiol., A* **2018,** 366, 72-80.
334. Bazzo, A.; Urakawa, A., *ChemSusChem* **2013,** 6 (11), 2095-2102.
335. Kumari, G.; Zhang, X.; Devasia, D.; Heo, J.; Jain, P. K., *ACS Nano* **2018,** 12 (8), 8330-8340.
336. Yu, S.; Wilson, A. J.; Heo, J.; Jain, P. K., *Nano Lett.* **2018,** 18 (4), 2189-2194.
337. Kumar, D.; Park, C. H.; Kim, C. S., *ACS Sustainable Chem. Eng.* **2018,** 6 (7), 8604-8614.
338. Tu, W.; Zhou, Y.; Li, H.; Li, P.; Zou, Z., *Nanoscale* **2015,** 7 (34), 14232-14236.
339. Kumar, D.; Lee, A.; Lee, T.; Lim, M.; Lim, D. K., *Nano Lett.* **2016,** 16 (3), 1760-1767.
340. Hou, W.; Hung, W. H.; Pavaskar, P.; Goeppert, A.; Aykol, M.; Cronin, S. B., *ACS Catal.* **2011,** 1 (8), 929-936.
341. Li, X.; Liu, C.; Wu, D.; Li, J.; Huo, P.; Wang, H., *Chin. J. Catal.* **2019,** 40 (6), 928-939.
342. Zhao, J.; Liu, B.; Meng, L.; He, S.; Yuan, R.; Hou, Y.; Ding, Z.; Lin, H.; Zhang, Z.; Wang, X.; Long, J., *Appl. Catal., B* **2019,** 256, 117823.
343. Meng, L.; Chen, Z.; Ma, Z.; He, S.; Hou, Y.; Li, H.-H.; Yuan, R.; Huang, X.-H.; Wang, X.; Wang, X.; Long, J., *Energy Environ. Sci.* **2018,** 11 (2), 294-298.
344. Knight, M. W.; King, N. S.; Liu, L.; Everitt, H. O.; Nordlander, P.; Halas, N. J., *ACS Nano* **2014,** 8 (1), 834-840.
345. Huang, H. B.; Yu, K.; Zhang, N.; Xu, J. Y.; Yu, X. T.; Liu, H. X.; Cao, H. L.; Lu, J.; Cao, R., *Nanoscale* **2020,** 12 (28), 15169-15174.
346. Neatu, S.; Macia-Agullo, J. A.; Concepcion, P.; Garcia, H., *J. Am. Chem. Soc.* **2014,** 136 (45), 15969-15976.
347. Tahir, M.; Tahir, B.; Amin, N. A. S., *Appl. Catal., B* **2017,** 204, 548-560.
348. Ginés, M. J. L.; Marchi, A. J.; Apesteguía, C. R., *Appl. Catal., A* **1997,** 154 (1-2), 155-171.
349. Fujita, S., *J. Catal.* **1992,** 134 (1), 220-225.
350. Wang, L. C.; Tahvildar Khazaneh, M.; Widmann, D.; Behm, R. J., *J. Catal.* **2013,** 302, 20-30.
351. Bobadilla, L. F.; Santos, J. L.; Ivanova, S.; Odriozola, J. A.; Urakawa, A., *ACS Catal.* **2018,** 8 (8), 7455-7467.
352. Goguet, A.; Meunier, F. C.; Tibiletti, D.; Breen, J. P.; Burch, R., *J. Phys. Chem. B* **2004,** 108 (52), 20240-20246.
353. Wang, X.; Shi, H.; Szanyi, J., *Nat. Commun.* **2017,** 8 (1), 513.
354. Li, Y.; Chan, S. H.; Sun, Q., *Nanoscale* **2015,** 7 (19), 8663-8683.
355. Xu, S.; Carter, E. A., *Chem. Rev.* **2019,** 119 (11), 6631-6669.
356. Sun, K.; Kohyama, M.; Tanaka, S.; Takeda, S., *J. Phys. Chem. C* **2017,** 121 (22), 12178-12187.
357. Liu, C.; Yang, B.; Tyo, E.; Seifert, S.; DeBartolo, J.; von Issendorff, B.; Zapol, P.; Vajda, S.; Curtiss, L. A., *J. Am. Chem. Soc.* **2015,** 137 (27), 8676-8679.
358. Rodríguez, J. A.; Evans, J.; Graciani, J.; Park, J.-B.; Liu, P.; Hrbek, J.; Sanz, J. F., *J. Phys. Chem. C* **2009,** 113 (17), 7364-7370.
359. Burch, R., *Phys. Chem. Chem. Phys.* **2006,** 8 (47), 5483-5500.

360. Miao, B.; Ma, S. S. K.; Wang, X.; Su, H.; Chan, S. H., *Catal. Sci. Technol.* **2016,** 6 (12), 4048-4058.
361. Solymosi, F., *J. Catal.* **1981,** 68 (2), 371-382.
362. Weatherbee, G., *J. Catal.* **1982,** 77 (2), 460-472.
363. Eckle, S.; Anfang, H.-G.; Behm, R. J., *J. Phys. Chem. C* **2010,** 115 (4), 1361-1367.
364. Karelovic, A.; Ruiz, P., *J. Catal.* **2013,** 301, 141-153.
365. Wang, F.; He, S.; Chen, H.; Wang, B.; Zheng, L.; Wei, M.; Evans, D. G.; Duan, X., *J. Am. Chem. Soc.* **2016,** 138 (19), 6298-6305.
366. Aldana, P. A. U.; Ocampo, F.; Kobl, K.; Louis, B.; Thibault-Starzyk, F.; Daturi, M.; Bazin, P.; Thomas, S.; Roger, A. C., *Catal. Today* **2013,** 215, 201-207.
367. Grabow, L. C.; Mavrikakis, M., *ACS Catal.* **2011,** 1 (4), 365-384.
368. Hartadi, Y.; Widmann, D.; Behm, R. J., *ChemSusChem* **2015,** 8 (3), 456-465.
369. Hartadi, Y.; Widmann, D.; Behm, R. J., *J. Catal.* **2016,** 333, 238-250.
370. van den Berg, R.; Prieto, G.; Korpershoek, G.; van der Wal, L. I.; van Bunningen, A. J.; Laegsgaard-Jorgensen, S.; de Jongh, P. E.; de Jong, K. P., *Nat. Commun.* **2016,** 7, 13057.
371. Behrens, M.; Studt, F.; Kasatkin, I.; Kuhl, S.; Havecker, M.; Abild-Pedersen, F.; Zander, S.; Girgsdies, F.; Kurr, P.; Kniep, B. L.; Tovar, M.; Fischer, R. W.; Norskov, J. K.; Schlogl, R., *Science* **2012,** 336 (6083), 893-897.
372. Kuld, S.; Thorhauge, M.; Falsig, H.; Elkjaer, C. F.; Helveg, S.; Chorkendorff, I.; Sehested, J., *Science* **2016,** 352 (6288), 969-974.
373. Kuld, S.; Conradsen, C.; Moses, P. G.; Chorkendorff, I.; Sehested, J., *Angew. Chem., Int. Ed.* **2014,** 53 (23), 5941-5945.
374. Lunkenbein, T.; Schumann, J.; Behrens, M.; Schlogl, R.; Willinger, M. G., *Angew. Chem., Int. Ed.* **2015,** 54 (15), 4544-4548.
375. Vourros, A.; Garagounis, I.; Kyriakou, V.; Carabineiro, S. A. C.; Maldonado-Hódar, F. J.; Marnellos, G. E.; Konsolakis, M., *J. CO2 Util.* **2017,** 19, 247-256.
376. Sakurai, H.; Tsubota, S.; Haruta, M., *Appl. Catal., A* **1993,** 102 (2), 125-136.
377. Rodriguez, J. A.; Wang, X.; Liu, P.; Wen, W.; Hanson, J. C.; Hrbek, J.; Pérez, M.; Evans, J., *Top. Catal.* **2007,** 44 (1-2), 73-81.
378. Tibiletti, D.; Fonseca, A. A.; Burch, R.; Chen, Y.; Fisher, J. M.; Goguet, A.; Hardacre, C.; Hu, P.; Thompsett, D., *J. Phys. Chem. B* **2005,** 109 (47), 22553-22559.
379. Dietz, L.; Piccinin, S.; Maestri, M., *J. Phys. Chem. C* **2015,** 119 (9), 4959-4966.
380. Kattel, S.; Yan, B.; Yang, Y.; Chen, J. G.; Liu, P., *J. Am. Chem. Soc.* **2016,** 138 (38), 12440-12450.
381. Wang, Z. J.; Song, H.; Liu, H.; Ye, J., *Angew. Chem., Int. Ed.* **2020,** 59 (21), 8016-8035.
382. Vu, N. N.; Kaliaguine, S.; Do, T. O., *ChemSusChem* **2020,** 13 (16), 3967-3991.
383. Baumberg, J. J., *Faraday Discuss.* **2019,** 214, 501-511.
384. Sivan, Y.; Un, I. W.; Dubi, Y., *Faraday Discuss.* **2019,** 214, 215-233.
385. Kuppe, C.; Rusimova, K. R.; Ohnoutek, L.; Slavov, D.; Valev, V. K., *Adv. Opt. Mater.* **2019,** 8 (1), 1901166.
386. Baffou, G.; Bordacchini, I.; Baldi, A.; Quidant, R., *Light: Sci. Appl.* **2020,** 9, 108.
387. Dubi, Y.; Sivan, Y., *Light: Sci. Appl.* **2019,** 8, 89.
388. Jain, P. K., *J. Phys. Chem. C* **2019,** 123 (40), 24347-24351.
389. Li, X.; Everitt, H. O.; Liu, J., *Nano Res.* **2019,** 12 (8), 1906-1911.
390. Zhang, X.; Li, X.; Reish, M. E.; Zhang, D.; Su, N. Q.; Gutierrez, Y.; Moreno, F.; Yang, W.; Everitt, H. O.; Liu, J., *Nano Lett.* **2018,** 18 (3), 1714-1723.
391. Zhou, L.; Swearer, D. F.; Robatjazi, H.; Alabastri, A.; Christopher, P.; Carter, E. A.; Nordlander, P.; Halas, N. J., *Science* **2019,** 364 (6439), eaaw9545.
392. Robatjazi, H.; Bao, J. L.; Zhang, M.; Zhou, L.; Christopher, P.; Carter, E. A.; Nordlander, P.; Halas, N. J., *Nat. Catal.* **2020,** 3 (7), 564-573.

393. Sivan, Y.; Baraban, J.; Un, I. W.; Dubi, Y., *Science* **2019,** 364 (6439), aaw9367.
394. O'Brien, P. G.; Sandhel, A.; Wood, T. E.; Jelle, A. A.; Hoch, L. B.; Perovic, D. D.; Mims, C. A.; Ozin, G. A., *Adv. Sci.* **2014,** 1 (1), 1400001.
395. Zhang, L.; Kong, G.; Meng, Y.; Tian, J.; Zhang, L.; Wan, S.; Lin, J.; Wang, Y., *ChemSusChem* **2017,** 10 (23), 4709-4714.
396. Lin, L.; Wang, K.; Yang, K.; Chen, X.; Fu, X.; Dai, W., *Appl. Catal., B* **2017,** 204, 440-455.
397. Liu, H.; Meng, X.; Dao, T. D.; Zhang, H.; Li, P.; Chang, K.; Wang, T.; Li, M.; Nagao, T.; Ye, J., *Angew. Chem., Int. Ed.* **2015,** 54 (39), 11545-11549.
398. Novello, P.; Varanasi, C. V.; Liu, J., *ACS Catal.* **2018,** 9 (1), 578-586.
399. Ullah, S.; Lovell, E. C.; Wong, R. J.; Tan, T. H.; Scott, J.; Amal, R., *ACS Sustainable Chem. Eng.* **2020,** 8 (13), 5056-5066.
400. Wang, Z.-j.; Song, H.; Pang, H.; Ning, Y.; Dao, T. D.; Wang, Z.; Chen, H.; Weng, Y.; Fu, Q.; Nagao, T.; Fang, Y.; Ye, J., *Appl. Catal., B* **2019,** 250, 10-16.
401. Upadhye, A. A.; Ro, I.; Zeng, X.; Kim, H. J.; Tejedor, I.; Anderson, M. A.; Dumesic, J. A.; Huber, G. W., *Catal. Sci. Technol.* **2015,** 5 (5), 2590-2601.
402. Zhang, H.; Wang, T.; Wang, J.; Liu, H.; Dao, T. D.; Li, M.; Liu, G.; Meng, X.; Chang, K.; Shi, L.; Nagao, T.; Ye, J., *Adv. Mater.* **2016,** 28 (19), 3703-3710.
403. Westrich, T. A.; Dahlberg, K. A.; Kaviany, M.; Schwank, J. W., *J. Phys. Chem. C* **2011,** 115 (33), 16537-16543.
404. Kaviany, M., *Heat Transfer Physics, Second Edition*. Cambridge University Press: 2014.
405. Tan, T. H.; Scott, J.; Ng, Y. H.; Taylor, R. A.; Aguey-Zinsou, K.-F.; Amal, R., *ACS Catal.* **2016,** 6 (3), 1870-1879.
406. Poudyal, S.; Laursen, S., *J. Phys. Chem. C* **2018,** 122 (15), 8045-8057.
407. Zhang, X.; Li, X.; Zhang, D.; Su, N. Q.; Yang, W.; Everitt, H. O.; Liu, J., *Nat. Commun.* **2017,** 8, 14542.
408. Robatjazi, H.; Zhao, H.; Swearer, D. F.; Hogan, N. J.; Zhou, L.; Alabastri, A.; McClain, M. J.; Nordlander, P.; Halas, N. J., *Nat. Commun.* **2017,** 8 (1), 27.
409. Robatjazi, H.; Bahauddin, S. M.; Doiron, C.; Thomann, I., *Nano Lett.* **2015,** 15 (9), 6155-6161.
410. Xie, B.; Wong, R. J.; Tan, T. H.; Higham, M.; Gibson, E. K.; Decarolis, D.; Callison, J.; Aguey-Zinsou, K. F.; Bowker, M.; Catlow, C. R. A.; Scott, J.; Amal, R., *Nat. Commun.* **2020,** 11 (1), 1615.

Chapter 2. Materials and Methodology

In this chapter, the theories of key experimental/calculation techniques are briefly introduced. The materials used in the thesis and the catalysts synthesis methods are summarised. The general physical characterizations of photocatalysts are also presented in this chapter. Since the *in-situ* spectroscopy characterizations, catalytical performance evaluation methods and calculation settings significantly vary chapter by chapter, they will be presented separately in each chapter.

2.1 Theoretical background

2.1.1 SSITKA-DRIFTS-MS technique

Known as a powerful *in-situ* investigation technology, the SSITKA is a method combining the transient and steady-state techniques. First developed by Happel, Bennett and Biloen et al.,[1-2] this technique is soon widely adopted by the catalysis community to elucidate the reaction mechanism.[3] Coupling SSITKA with DRIFTS provides a more insightful way to reveal the reaction mechanism in atomistic level. In the 1960s, Dalziel et al. and Tamaru et al. for the first time couple the *in-situ* spectroscopy method with kinetics analyses together, which is known as the spectrokinetic analyses.[4-6] The most significant improvement after combing the spectroscopy method into the framework of SSITKA is the ability to determine the reaction intermediates adsorbed on the surface of catalysts. In addition, the kinetic parameters of the intermediates can be measured via the SSITKA method, which provides solid evidence to distinguish the true intermediates and spectators.

Different from the transient techniques, SSITKA-DRIFTS ensures the analyses of the steady-state kinetics on the surface of the catalyst including the type, coverage, mean surface lifetime of adsorbed reaction intermediates and active sites, etc,[7] which are closer to the real reaction condition.

A simplified scheme of SSITKA/DRIFTS-MS reaction system is shown in **Figure 2.1**. The inlet feed stream with unlabelled reactant *R* is firstly introduced into the reactor. After reaching the steady-state reaction condition, the inlet feed stream is switched to the other inlet with isotope labelled reactant *R'* in the identical concentration via the switching valve. With reaction on the surface further proceeding, the new isotope labelled reactants and intermediates will replace the unlabelled ones. The decay of the unlabelled species and increase of labelled species can be monitored by DRIFTS on the surface and MS in the effluent gases. For a reversible heterogeneous catalytic reaction at steady-state, the transformation can be expressed by the following equation:

$$R \rightleftarrows X \rightleftarrows P \tag{2.1}$$

where *R, X, P* represent reactants, intermediates, products respectively.

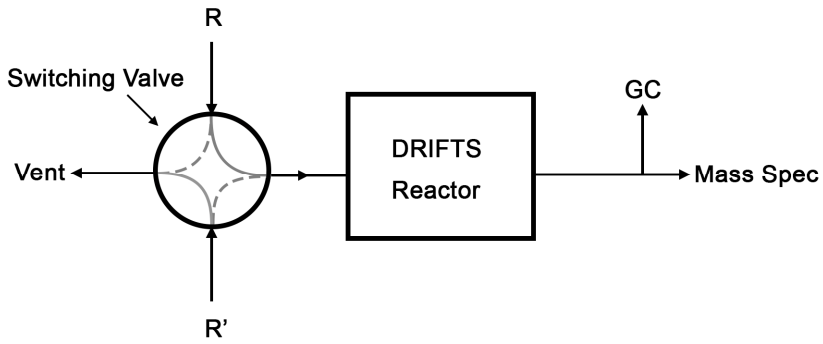

Figure 2.1. The scheme of SSITKA/DRIFTS-MS investigation setup.

The two most important parameters of interest can be directly calculated from the results of SSITKA experiments are amounts of adsorbed intermediates (N_p) and mean surface residence time (τ_p):

$$F_p(t) = \frac{r_p(t)}{r_p} = 1 - F_{p*}(t) \tag{2.2}$$

$$\tau_p = \int_0^\infty F_p(t)dt = \int_0^\infty \frac{r_p(t)}{r_p} dt = \frac{N_p}{r_p} \tag{2.3}$$

where the $F_p(t)$ and $F_{p*}(t)$ are the ***normalized*** transient responses of the unlabelled and isotope-labelled products, respectively. Other kinetic parameters derived from the experimental results are based on the theoretical

models.[3, 8] The differences between the kinetic models can easily be distinguished by the plot of $F_p(t)$ versus time, as schemed in **Figure 2.2** (a, b). Because the single pool model assumes the irreversible pseudo-first-order reaction kinetics, the decay of $F_p(t)$ in single pool model follows the first order exponential decay function:

$$F_p(t) = e^{-\frac{t}{\tau_p}} \tag{2.4}$$

Therefore the $\ln(F_p(t))$ shows a linear correlation to time and the slope is $-\frac{1}{\tau_p}$.

It is important to emphasize the SSITKA needs to be conducted under steady-state condition. Therefore, significant isotope effects need to be avoided. The isotopic element with large mass difference with respect to its most abundant counterpart, such as H_2/D_2 is extremely challenging in SSITKA experiments. Another difficult case is $^{16}O_2/^{18}O_2$, because the O atom exchange happens between intermediates and catalysts during the reaction.

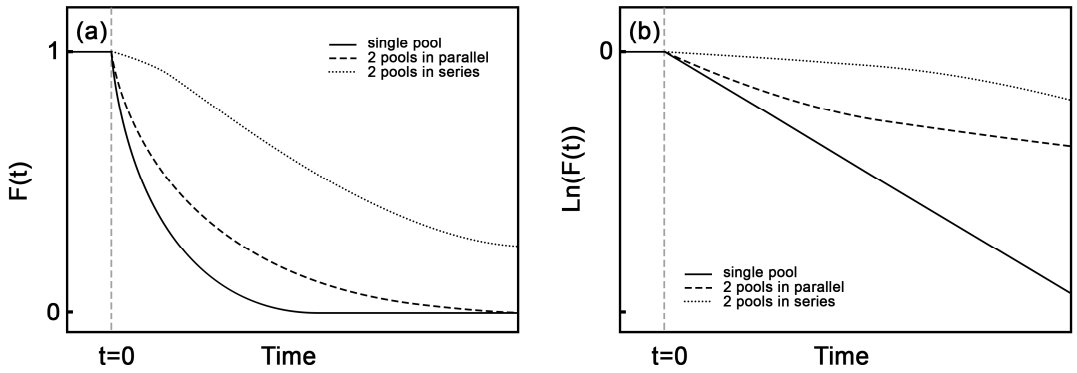

Figure 2.2. (a) Transient response and (b) logarithmic transient response plot in a function of time for the theoretical models of single pool, two pools in series and two pools in parallel, respectively.

2.1.2 *In-situ* DRIFTS-MS setup

The gas flow sheet of DRIFTS-MS setup used in this thesis is presented in **Figure 2.3**. **Figure 2.3**(a) is featured of introducing a water bubbler in the gas line, which was used in Chapter 3 & 4. The temperature of the bubbler is controlled by a PID temperature controller with a thermocouple inserted into

water. Since the Ar carrier gas is significantly smaller than the main stream, the water/vapour is close to equilibrium condition. Therefore, the water vapour concentration can be calculated by Antoine's equation:[9-11]

$$log_{10}\left(P_{H_2O}\right) = A - \frac{B}{T+C} \quad (2.5)$$

where *A*, *B*, *C* are constants and can be retrieved from the NIST webbook;[12] *T* is the temperature of the bubbler in Kelvin. **Figure 2.3**(b) shows the setup used in Chapter 5 & 6. In this setup, the two equivalent CO_2/H_2/Ar gas lines are switchable via the 4-way valve, which makes the SSITKA experiments feasible. The He gas line is used to provide reference and correction for the dead volume of the reactor.

The *in-situ* reactor used in the entire thesis is shown in **Figure 2.4**. A K-type thermocouple was inserted from the bottom of the sample cup into the powder to measure the temperature of the catalysts. 10 mg catalyst was loaded onto a stainless-steel mesh each time. The reactor was sealed with a dome with 3 windows for incident/reflecting light for spectrometers and the front window for external light driving the reaction.

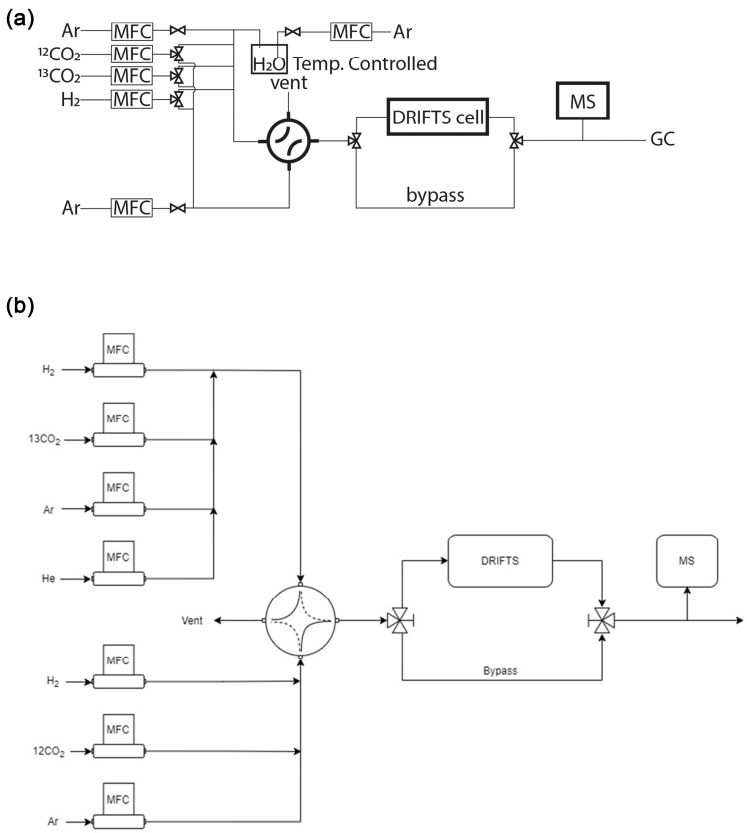

Figure 2.3. Flow diagram of in-situ DRIFTS cell used in (a) chapter 3, 4 and (b) chapter 5, 6 of this thesis.

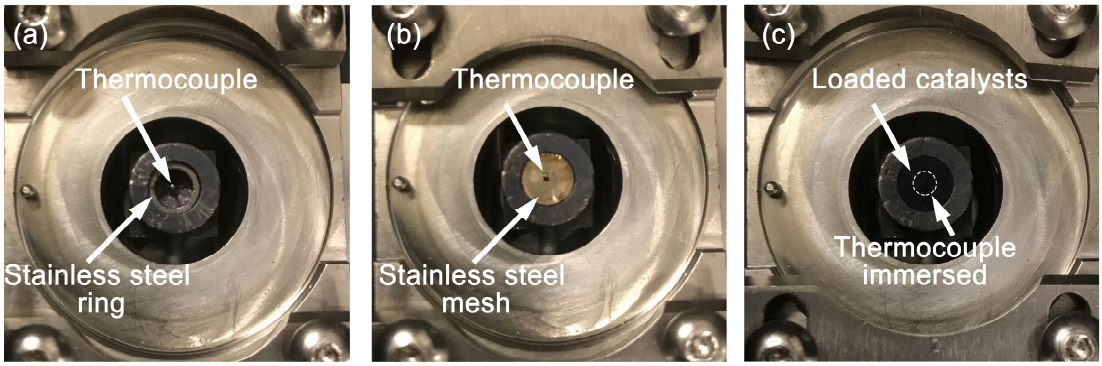

Figure 2.4. Digital pictures of *in-situ* reaction cell (praying mantis, Harrick) used in this work. A stainless-steel ring with O.D. of ~ 6 mm is used to support a stainless-steel mesh for catalysts loading. After loading 10 mg catalyst, the catalyst surface is at the similar height to the top surface of sample cup. A K-type thermocouple (RS pro, 0.5 mm diameter) is inserted into catalyst powder from bottom to monitor the real temperature of catalysts in dark or under light irradiation.

2.1.3 A Brief Introduction to Theoretical Investigations

In this thesis, the KS-DFT is used to investigate the structure of catalysts and the catalytic process theoretically. Therefore, an introductory level of DFT method overview is presented there.

2.1.3.1 Kohn-Sham Density Functional Theory

To describe the molecules and catalysts in the reaction, it is conventional to use the non-relativistic, time-independent Schrödinger equation (2.6) to describe the system:

$$\hat{\mathrm{H}}\Psi_i(\boldsymbol{x_1}, \boldsymbol{x_{12}}, \dots, \boldsymbol{x_N}, \boldsymbol{r_1}, \boldsymbol{r_2}, \dots, \boldsymbol{r_M}) = \mathrm{E}_i\Psi_i(\boldsymbol{x_1}, \boldsymbol{x_{12}}, \dots, \boldsymbol{x_N}, \boldsymbol{r_1}, \boldsymbol{r_2}, \dots, \boldsymbol{r_M}) \qquad (2.6)$$

where the E_i is the total energy of the system and Ψ_i is the wavefunction of the i'th state. The $\hat{\mathrm{H}}$ is called the Hamiltonian operator for the system containing M nuclei and N electrons. The Hamiltonian can be described by the following equation (2.7):[13]

$$\hat{\mathrm{H}} = -\frac{1}{2}\sum_{i=1}^{N}\nabla_i^2 - \frac{1}{2m_A}\sum_{A=1}^{M}\nabla_A^2 - \sum_{i=1}^{N}\sum_{A=1}^{M}\frac{Z_A}{\boldsymbol{r_{iA}}}$$

$$+ \sum_{i=1}^{N}\sum_{j<i}^{N}\frac{1}{\boldsymbol{r_{ij}}} + \sum_{A=1}^{N}\sum_{B<A}^{M}\frac{Z_A Z_B}{\boldsymbol{R_{AB}}} \qquad (2.7)$$

where the A, B represent the M nuclei; i, j denote the N electrons in the system and m_A is the mass of product of nucleus A and an electron. In equation (2.7), the ∇^2 is the Laplace operator and defined as the sum of differential operators in terms of coordinates in three dimensions. The first two terms describe the kinetic energy of electrons and nuclei, respectively; The rest three terms are the potentials derived from electron-nucleus, electron-electron and nucleus-nucleus interaction in sequence.

Since the electrons move considerably faster than the nuclei and the mass of proton or neutron is ~1836 time of the electron, it is a good approximation to treat the electrons and nuclei separately, which is well-known as the ***Born-Oppenheimer Approximation***. Under this approximation, the nuclei are

treated fixed with zero kinetic energy and constant nuclei-nuclei repulsion potential. Additionally, the electrons can be considered as moving in the electromagnetic field determined by the set of nuclei. As a result, the Schrödinger equation of the electrons in the field of fixed nuclei can be written as following equation (2.8):

$$\left[-\frac{1}{2}\sum_{i=1}\nabla_i^2+\sum_i\ V_n(\boldsymbol{r}_i)+\frac{1}{2}\sum_{i\neq j}\frac{1}{|\boldsymbol{r_i}-\boldsymbol{r_j}|}\right]\Psi=E\Psi \tag{2.8}$$

$$V_n(\boldsymbol{r})=-\sum_I\frac{Z_I}{|\boldsymbol{r_i}-\boldsymbol{R_I}|} \tag{2.9}$$

Inside square bracket, the three terms describe the kinetic energy of electrons, electron-nuclei interaction energy and electron-electron interaction energy, respectively. It is important to emphasize that the classical Coulomb interaction is also an approximation to describe the interaction between quantum particles. Note that the many-body Schrödinger equation is 3*N*-dimensional; therefore, approximation must be introduced to solve it practically.

To simplify the question, in the 1920s, the physicists (including Thomas, Fermi, Hartree et al.) propose the ***independent electron approximation*** that treats the electrons individually and neglect the interaction between the electrons. This approximation remarkably reduces the complex of many-body Schrödinger equation from 3*N* dimensional to *N* three-dimensional equations by assuming the wavefunction of the system is equal to the product of the wavefunctions of independent electrons:

$$\Psi(\boldsymbol{r_1},\boldsymbol{r_2},\dots\boldsymbol{r_n})=\phi_1(\boldsymbol{r_1})\phi_2(\boldsymbol{r_2})\dots\phi_n(\boldsymbol{r_n}) \tag{2.10}$$

$$\widehat{H}_0\phi_i(\boldsymbol{r_i})=\varepsilon_i\phi_i(\boldsymbol{r_i}) \tag{2.11}$$

The product shown in equation (2.10) is also called the ***Hartree product***. Although independent electron approximation described as equation (2.10) successfully simplifies the many-body problem, the reduction of complex has two important defects: (i) fails to follow Pauli's exclusion principle; (ii) the Coulomb interaction energy between electrons is too large to ignore.

The Pauli's exclusion principle describes one of the fundamental properties of the wavefunction of *fermions*, eg. electrons. It requires the sign changes of the wavefunction when variables of two electrons (spin and position) exchange. To meet this requirement, the wavefunctions under the *independent electron approximation* can be written in the format of the ***Slater determinant***. To improve the description of the electron-electron interaction, each independent electron is considered as immersing inside the electrostatic potential created by other electrons with fixed positions. It can be seen that the electrostatic potential here is a function of the spatial distribution of the electrons: the electron density $n(\boldsymbol{r})$. By taking the classical electrostatic potential in the form of Poisson's equation (2.12), the ***Hartree potential*** $V_H(\boldsymbol{r})$ is defined as the formal solution of (2.13):

$$\nabla^2 V_H(\boldsymbol{r}) = -4\pi n(\boldsymbol{r}) \tag{2.12}$$

$$V_H(\boldsymbol{r}) = \int d\boldsymbol{r}' \frac{n(\boldsymbol{r}')}{|\boldsymbol{r}-\boldsymbol{r}'|} \tag{2.13}$$

which represents the Coulomb potential generated by a charge of $-n(\boldsymbol{r}')d\boldsymbol{r}'$ at an element of volume of $d\boldsymbol{r}'$. Since the *Hartree potential* ($V_H(\boldsymbol{r})$) is defined as the average potentials for individual electrons, this approximation is also called the ***mean-field approximation***. After addressing these two shortcomings, single-electron wavefunction (equation (2.11)) can be improved as:

$$\left[-\frac{\nabla^2}{2} + V_n(\boldsymbol{r}) + V_H(\boldsymbol{r})\right]\phi_i(\boldsymbol{r}) = \varepsilon_i \phi_i(\boldsymbol{r}) \tag{2.14}$$

$$n(\boldsymbol{r}) = \sum_i |\phi_i(\boldsymbol{r})|^2 \tag{2.15}$$

$$\nabla^2 V_H(\boldsymbol{r}) = -4\pi n(\boldsymbol{r}) \tag{2.16}$$

It is important to point out the *mean-field approximation* derives from the classical treatment of the Coulomb repulsion, however not accurate enough to describe the interaction between the electrons, a kind of quantum particles.

In the 1930s, Fock further developed the description of the single-electron wavefunction, now known as the ***Hartree-Fock equation***:

$$\left[-\frac{\nabla^2}{2} + V_n(\boldsymbol{r}) + V_H(\boldsymbol{r})\right]\phi_i(\boldsymbol{r}) + \int d\boldsymbol{r}' V_X(\boldsymbol{r},\boldsymbol{r}')\,\phi_i(\boldsymbol{r}') = \varepsilon_i\phi_i(\boldsymbol{r}) \tag{2.17}$$

$$n(\boldsymbol{r}) = \sum_i |\phi_i(\boldsymbol{r})|^2 \tag{2.18}$$

$$\nabla^2 V_H(\boldsymbol{r}) = -4\pi n(\boldsymbol{r}) \tag{2.19}$$

In equation (2.17), an extra potential term is introduced into the single-electron wavefunction, V_X, which is expressed by summing up all the occupied single-electron states:

$$V_X(\boldsymbol{r},\boldsymbol{r}') = -\sum_j \frac{\phi_j^*(\boldsymbol{r}')\phi_j\,(\boldsymbol{r})}{|\boldsymbol{r}-\boldsymbol{r}'|^2} \tag{2.20}$$

The non-local potential $V_X(\boldsymbol{r},\boldsymbol{r}')$ is called the ***Fock exchange potential***, and its physical basis is the Pauli's exclusion principle. Although the Hartree-Fock equation is a step-change-improved description for single-electron wavefunction, the equation still misses the correlation term.

Twenty years later, two rigorously proven theorems from Kohn-Hohenberg build the foundations of DFT theory: "the ground-state energy of Schrödinger equation is a unique functional of the electron density; the true electron density corresponding to the solution of the Schrödinger equation minimizes the energy of the overall functional".[14-16] It is the reason why the method is called the density function theory. Inspired by all these important developments of simplifying and solving the many-body Schrodinger equation, Kohn and Sham proposed their approach in 1965.[14, 17] The ground-state energy of the system, under *independent electrons approximation*, *E* can be expressed in a functional of electron density, $n(\boldsymbol{r})$:

$$E = F[n] = \int d\boldsymbol{r}\, n(\boldsymbol{r})\, V_n(\boldsymbol{r}) - \sum_i \int d\boldsymbol{r}\, \phi_i^*(\boldsymbol{r})\frac{\nabla^2}{2}\,\phi_i\ (\boldsymbol{r})$$

$$+\frac{1}{2}\int\int d\boldsymbol{r}d\boldsymbol{r}'\,\frac{n(\boldsymbol{r})\,n(\boldsymbol{r}')}{|\boldsymbol{r}-\boldsymbol{r}'|} + E_{xc}[n] \tag{2.21}$$

On the right side of equation (2.21), the first term is the external potential derived from nuclei; the second term is the kinetic energy; the third term is the *Hartree energy;* the last is the exchange-correlation energy. Note that all the terms have already been expressed in terms of electron density, $n(\boldsymbol{r})$. By

keeping the *independent electron approximation* and leaving all the inaccurate parts to the XC term, the *KS equations* are written as follows:

$$\left[-\frac{1}{2}\nabla^2 + V_n(\boldsymbol{r}) + V_H(\boldsymbol{r}) + V_{xc}(\boldsymbol{r})\right]\phi_i(\boldsymbol{r}) = \varepsilon_i\phi_i(\boldsymbol{r}) \tag{2.22}$$

$$n(\boldsymbol{r}) = \sum_i |\phi_i(\boldsymbol{r})|^2 \tag{2.23}$$

$$V_n(\boldsymbol{r}) = -\sum_I \frac{Z_I}{|\boldsymbol{r}-\boldsymbol{R_I}|} \tag{2.24}$$

$$\nabla^2 V_H(\boldsymbol{r}) = -4\pi n(\boldsymbol{r}) \tag{2.25}$$

$$V_{xc}(\boldsymbol{r}) = \frac{\delta E_{xc}[n]}{\delta n} n(\boldsymbol{r}) \tag{2.26}$$

It is important to summarize the approximations used in KS equations again. First of all, in KS equations, the kinetic energy functional is the most important approximation, because the kinetic energy and total energy are of the same order of magnitude. In KS equations, the electrons are treated as independent and the so-called KS orbital ϕ_i are introduced. Although the introduction of the single-electron wavefunction increases the computational costs, the good approximation ensuring an accurate description of the kinetic energy is the foundation of the success of KS-DFT method. Secondly, the classical Coulomb interaction is not accurate enough to describe the interaction between the electrons and nuclei since they are quantum particles. Thirdly, in Hartree potential, the electron field approximation takes advantage of the classical poison's formulation. Lastly, all these approximations leave the inaccurate part to the XC term. Therefore, finding a good XC functional is the key to the success of KS-DFT method. Although the explicit expression of the XC functional is not possible to achieve, there are several good approximations that have already been proven capable of providing good accuracy with affordable computational costs. The two most commonly used levels of approximations are (i) LDA and (ii) GGA.

2.1.3.2 Limitation of KS-DFT method and remediation

2.1.3.2.1 Self-interaction error

The most important and well-known problem of KS-DFT method is so-called SIE, which is the source of many inaccuracies in KS-DFT calculation. The Hartree term in KS equations is a classical description of Coulomb repulsion between the electron and the mean-field of the system, which includes the trial electron itself. In HF method, the SIE is exactly cancelled by the exchange term. However, in KS-DFT, the explicit XC functional formulation is unknown. Due to the approximation used, the SIE cancellation is not complete. In the research field of catalysts, one of the most infamous failures of standard KS-DFT method is the description of energy, magnetic and electronic properties of transition metal oxides.[18-20] When defects exist in the crystal, the situation becomes worse. The standard LDA/GGA functional fails to correctly describe the localized electrons near the defects.[21-22] The physical origin is that standard KS-DFT tends to over-delocalize the *d* and *f* electrons in transition metal atoms.

The methods to solve the issue under the framework of KS-DFT include the Hubbard U correction (DFT+U),[23-24] meta-functional[25] and hybrid functional methods,[26-27] etc. Among them, the on-site Coulomb correction using Hubbard model shows excellent balance between accuracy and affordability. The added on-site potential correction shows the following form:

$$E = \frac{(U-J)}{2}\sum_{\sigma}\left(n_{m,\sigma} - {n_{m,\sigma}}^{2}\right) \tag{2.27}$$

$$U_{\text{eff}} = U - J \tag{2.28}$$

where *U* and *J* terms are the effective Coulomb repulsion and exchange parameters, respectively. *n* is the occupation number of a d orbital with number *m* and spin σ. For brevity, the difference between *U* and *J* is commonly denoted as the effective *U* (U_{eff}). One of the most essential challenges of DFT+U method is to determine the value of *U*. To date, there are two kinds of methods to determine the *U* value for transition metal oxides: (i) *ab initio*

method; (ii) calibration with experimental results. Developed by Cococcioni et al., the linear response approach and density functional perturbation theory is implemented to calculate the *U* value.[28-30] Although the self-consistent calculation of Hubbard parameter has a clear physical meaning and fully *ab initio*, the value it produces sometimes cannot fully generate 'accurate' correction to match the properties determined via experiments. Moreover, the methods show limitations in theory and can't be applied to all the transition metal systems. The other way, on the contrary, is to calibrate the U value by letting the properties of interest match the experimental results.[22, 31-32] However, the U determined by this method sometimes is not physically meaningful.

2.1.3.2.2 van der Waals forces

The dispersion interaction is extremely important in the catalysis research field, since the nature of reaction is the interaction of small molecules adsorbed on the catalyst surface. In the 1930s, London firstly investigates this relatively weak interaction and shows the formulation of the long-range interaction between two atoms treated as spheres:

$$V_{dispersion}(r) = -\frac{C_6}{R^6} \tag{2.29}$$

where *r* is the interatomic distance and *C* is a collection of constants. However, the most widely used density functionals or standard density functionals (eg. PBE, PW91, B3LYP) fail to describe the long-range interaction correctly.[33]

For now, there are two prevailing strategies to address to dispersion force problem: (i) vdW-functionals;[34] (ii) introducing a semiclassical correction describing the $-C_6R^{-6}$ term. For the first kind of method, the correction to consider the nonlocal dispersion energy (E_c^{NL}) is directly implemented within the XC functional:

$$E_{xc} = E_x^{LDA/GGA} + E_c^{LDA/GGA} + E_c^{NL} \tag{2.30}$$

The main advantages of the vdW-Functionals method are its independence from empirical parameters, which makes the calculation more '*ab initio*';

additionally, the dispersion interaction also considers the specific electronic structure of the investigated system. The main drawback of this method is the modification also affects local interaction and might cause the 'double-counting problem'. In addition, due to the complexity of calculating the dispersion force via QM approach, it is in a complicated formulation and adding extra burdens to the calculation. Some popular functionals are vdW-DF2,[35] optB88b-vdW,[36] etc. The other prevailing method is to add a semiclassical correction term without modifying the standard functionals. Therefore, it is also written as DFT-D method with D for dispersion. The general form of the dispersion energy as a correction to the KS-DFT energy is:

$$E_{disp}^{DFT-D} = -\sum_{AB}\sum_{n=6,8,10,\dots} s_n \frac{C_n^{AB}}{R_{AB}^n} f_{damp}(R_{AB}) \quad (2.31)$$

Where the E_{disp}^{DFT-D} is the sum up of all atomic pairs in the system, C_n^{AB} is the *n*th-order dispersion coefficient for atom pair AB with the internuclear distance of R_{AB}. s_n is a scaling factor dependent on the type of XC functional. The damping function, f_{damp} is set to avoid double-counting effects at the intermediate interatom distances.[37] With the more accurate determination of the dispersion coefficient and damping function, the 3rd version of Grimme's DFT-D3[38] with BJ damping[39] has been adopted as the most popular dispersion force correction method. The advantage of Grimme's DFT-D method is its significant improvement on the description of nonlocal dispersion energy under DFT method with nearly no extra requirement on computational resources. The trade-off is the neglection of the electronic structures since only the geometry is considered till the DFT-D3 version. To further improve the accuracy, the DFT-D4 version has been developed and published in 2019.[40] After taking the charge into consideration, the DFT-D4 method is reported consistently better than DFT-D3 method.

2.2 Materials

All chemicals used in this work were analytical grade or equivalent without further purification. Dicyandiamide (DCDA), KBH_4, KNO_3, $HAuCl_4{\cdot}3H_2O$ (ACS

reagent) and urea (99%) were purchased from the Acros Organics. Acetaldehyde (anhydrous), glyoxylic acid (50wt% in H_2O), glyoxal (40wt% in H_2O), formic acid (reagent grade, stabilized by 2.5% water), acetic acid (99.8%-100.5%, Ph. Eur.), formaldehyde (37wt% in H_2O, contains 10-15% Methanol as stabilizer) and B_2O_3 was purchased from the Sigma Aldrich. Oxalic acid dihydrate (analytical grade) were from the Fisher Scientific. TiO_2 NP used as the catalyst support is the commercially available Aeroxide® P25 (Sigma Aldrich) with ~80% anatase and ~20% rutile. γ-Al_2O_3 catalyst supports were supplied by Alfa-Aesar. Ultrapure water (resistivity ≥18.2 MΩ) was used through our experiments.

High purity He (zero grade), Ar (CP grade), N_2 (zero grade), CO (research grade), H_2 (zero grade), O_2 (Zero grade) and CO_2 (research grade) used in this study are supplied by BOC Limited, UK. $^{13}CO_2$ (99 atom % ^{13}C, <3 atom % ^{18}O) and Deuterium (99.8% atom D_2) for isotope labelling experiments was purchased from Sigma Aldrich.

2.3 Catalysts synthesis

2.3.1 g-C_3N_4 (Chapter 3)

For the synthesis of K, B co-doped g-C_3N_4 with N_v due to in situ H_2 treatment (KBH-C_3N_4), 4g DCDA was transferred into an agate mortar to mix with specific amounts of KBH_4 by 30 min grinding. The powder was then placed inside a ceramic crucible with a lid. After annealing inside a muffle furnace at 550 °C for 2h (ramping rate 2.3 °C min^{-1}), the KBH-C_3N_4 was successfully prepared. The syntheses of the control group samples, K doped C_3N_4 (3% K-C_3N_4), B doped C_3N_4 (3% B-C_3N_4) followed the same process except replacing the KBH with KNO_3 or B_2O_3. To verify the role of N_v, another control group B, K co-doped C_3N_4 without N_v (3% KB-C_3N_4) was synthesized via drying the DCDA and KBH_4 aqueous solution together at 100 °C to completely convert the KBH_4 to KBO_2 before thermal polymerization process. Pristine g-C_3N_4 was synthesized with DCDA only.

2.3.2 Au/TiO_2 (chapter 4 & 5)

DP method with urea[41] was used to prepare the Au/TiO_2 with two different loadings: 1 g TiO_2 was added into (1) 100 mL water containing 0.5 mmol $HAuCl_4 \cdot 3H_2O$, 50 mmol urea and (2) 100 mL water containing 1.5 mmol $HAuCl_4 \cdot 3H_2O$, 150 mmol urea, respectively. The two beakers containing the solution were wrapped with aluminium foil to prevent the photo-decomposition of Au-precursors. The solution under continuous stirring was heated up to 80 °C and kept for 5 h in an oil bath. After cooling down to room temperature, the NPs were separated from the solution using a centrifuge at 8000 rpm for 5 min. Further resining by water and collecting by centrifuging 8 times was to remove the residual Cl^- ions as much as possible. The washed powders were transferred into a vacuum oven and dried under vacuum, 60 °C overnight. Finally, the samples were calcinated in a muffle furnace at 400 °C for 2h under ambient atmosphere. The ramping rate was set to 1 °C per minute. *In-situ* pretreatment was applied to the samples either inside DRIFTS reactor or our photocatalytic reactor before experiments. The pretreatments include treating samples at 300 °C for 0.5 h under flowing Ar, O_2 or H_2 with the flow rate of 20 sccm. The corresponding samples are denoted as $Au/TiO_2(Ar)$, $Au/TiO_2(O_2)$ and $Au/TiO_2(H_2)$ respectively. The sample directly used after calcination in the muffle furnace without further pretreatment is denoted as $Au/TiO_2(UP)$ with 'UP' for *unpretreated*.

2.3.3 $Au/\gamma\text{-}Al_2O_3$ (chapter 6)

$Au/\gamma\text{-}Al_2O_3$ was prepared following the conventional DP method too. 2 mmol $HAuCl_4 \cdot 3H_2O$ and 200 mmol urea were dissovlved in 100 mL water and agitated with a magnetic stirrer bar. The beaker with solution was wrapped with aluminium foil to rule out the interference from ambient light. The solution was heated to 80 °C and held for 5 h in an oil bath. The catalysts were separated from solution using a vacuum filtration method. Ultrapure water was used to resin the catalyst for 8 times to remove residual Cl^- ions. The powder was dried in a vacuum oven at 60 °C overnight. Calcination at 400, 600, 800 °C for 2h

was conducted for the dried powder in a muffle furnace. The ramping rate was set to be 1 °C min^{-1}. The samples calcinated at 400, 600, 800 °C are denoted as Au/Al_2O_3-400, Au/Al_2O_3-600 and Au/Al_2O_3-800, respectively.

2.4 General physical characterizations of photocatalysts

The general physical characterizations of photocatalyst are presented in this section. Chapter-dependent characterizations will be described in detail in each chapter.

The crystal structure of catalyst was characterized with an XRD (Bruker D2 Phaser). The surface chemical states and valence band maximum (VBM) positions of prepared samples were measured by the XPS er (, ThermoFisher K-Alpha) with the monochromatic Al Kα source. All XPS data have been calibrated referring to the C1s peak (284.8 eV) derived from the adventitious carbon source to rule out the influence of surface charging.[42] The C, H, N elemental ratio measurements were conducted on an organic elemental analyser (Carlo Erba NA 2500). The optical absorption was measured with a DRS method on a UV-Vis-NIR spectrometer (Shimadzu, UV-3600Plus) equipped with a praying mantis accessory (Harrick Scientific). The IR transmission spectra were measured on a FITR (Shimadzu IRTracer-100) using a standard KBr pellet protocol with a DLATGS detector. PL spectra was measured on a fluorescence spectrometer (RF6000, Shimadzu) with the excitation wavelength of 320 nm. The time-resolved fluorescence spectroscopy was conducted on the fluorescence spectrometer (FLS980, Edinburgh Instrument) with a pulsed excitation source and monitoring the fluorescence intensity decay at the corresponding PL peak wavelength. The samples were protected by the Ar inert atmosphere. The SSA was determined via the N_2 physical adsorption-desorption experiments at 77K (Quantachrome, Autosorb-iQ). Accurate Au loading was determined using the ICP-OES (Varian Vista Pro). The morphology of prepared catalysts was observed using an AC-TEM,, (JEOL ARM200F/FEI Titan). HAADF-STEM mode was used to

investigate the structure and morphology with the help of atomic number contrast. EPR spectroscopy analyses were conducted on an EPR spectrometer (Brucker A3000) at ambient temperature/77 K and ambient atmosphere/Ar with a microwave frequency of 9.857 ± 0.002 GHz.

2.5 References

1. Happel, J., *Chem. Eng. Sci.* **1978,** 33 (11), 1567.
2. Biloen, P., *J. Mol. Catal.* **1983,** 21 (1-3), 17-24.
3. Shannon, S. L.; Goodwin, J. G., *Chem. Rev.* **2002,** 95 (3), 677-695.
4. Dalziel, K.; O'Brien, J. R., *Biochem. J* **1957,** 67 (1), 124-136.
5. Tamaru, K. *Adv. Catal.*, Academic Press: 1965.
6. Ueno, A.; Onishi, T.; Tamaru, K., *Trans. Faraday Society* **1970,** 66, 756-763.
7. Jabłońska, M., *ChemCatChem* **2020,** 13 (3), 818-827.
8. Ledesma, C.; Yang, J.; Chen, D.; Holmen, A., *ACS Catal.* **2014,** 4 (12), 4527-4547.
9. Song, H.; Zhang, L.; Watson, R.; Braden, D.; Ozkan, U., *Catal. Today* **2007,** 129 (3-4), 346-354.
10. Bodenhöfer, K.; Hierlemann, A.; Schlunk, R.; Göpel, W., *Sens. Actuators, B* **1997,** 45 (3), 259-264.
11. Love, A.; Middleman, S.; Hochberg, A. K., *J. Cryst. Growth* **1993,** 129 (1-2), 119-133.
12. Bridgeman, O. C.; Aldrich, E. W., *J. Heat Transfer* **1964,** 86 (2), 279-286.
13. Koch, W.; Holthausen, M. C., *A Chemist's Guide to Density Functional Theory*. 2 ed.; John Wiley & Sons: 2001.
14. Kohn, W.; Sham, L. J., *Phys. Rev.* **1965,** 140 (4A), A1133-A1138.
15. Hohenberg, P.; Kohn, W., *Phys. Rev.* **1964,** 136 (3B), B864-B871.
16. Sholl, D. S.; Steckel, J. A., *Density Functional Theory*. John Wiley & Sons, Inc.: 2009.
17. Kohn, W., *Rev. Mod. Phys.* **1999,** 71 (5), 1253-1266.
18. Wang, L.; Maxisch, T.; Ceder, G., *Phys. Rev. B* **2006,** 73 (19), 195107.
19. Martínez, J. I.; Hansen, H. A.; Rossmeisl, J.; Nørskov, J. K., *Phys. Rev. B* **2009,** 79 (4), 045120.
20. Pacchioni, G., *Catal. Lett.* **2014,** 145 (1), 80-94.
21. Fabris, S.; de Gironcoli, S.; Baroni, S.; Vicario, G.; Balducci, G., *Phys. Rev. B* **2005,** 71 (4), 041102(R).
22. Finazzi, E.; Di Valentin, C.; Pacchioni, G.; Selloni, A., *J. Chem. Phys.* **2008,** 129 (15), 154113.
23. Dudarev, S. L.; Botton, G. A.; Savrasov, S. Y.; Humphreys, C. J.; Sutton, A. P., *Phys. Rev. B* **1998,** 57 (3), 1505-1509.
24. Himmetoglu, B.; Wentzcovitch, R. M.; Cococcioni, M., *Phys. Rev. B* **2011,** 84 (11), 115108.
25. Sun, J.; Ruzsinszky, A.; Perdew, J. P., *Phys. Rev. Lett.* **2015,** 115 (3), 036402.
26. Krukau, A. V.; Vydrov, O. A.; Izmaylov, A. F.; Scuseria, G. E., *J. Chem. Phys.* **2006,** 125 (22), 224106.
27. Heyd, J.; Scuseria, G. E.; Ernzerhof, M., *J. Chem. Phys.* **2003,** 118 (18), 8207-8215.
28. Cococcioni, M.; de Gironcoli, S., *Phys. Rev. B* **2005,** 71 (3), 035105.
29. Timrov, I.; Marzari, N.; Cococcioni, M., *Phys. Rev. B* **2018,** 98 (8), 085127.
30. Ricca, C.; Timrov, I.; Cococcioni, M.; Marzari, N.; Aschauer, U., *Phys. Rev. B* **2019,** 99 (9), 094102.

31. Lutfalla, S.; Shapovalov, V.; Bell, A. T., *J. Chem. Theory Comput.* **2011,** 7 (7), 2218-2223.
32. Hu, Z.; Metiu, H., *J. Phys. Chem. C* **2011,** 115 (13), 5841-5845.
33. Grimme, S., *WIREs Computational Molecular Science* **2011,** 1 (2), 211-228.
34. Berland, K.; Cooper, V. R.; Lee, K.; Schroder, E.; Thonhauser, T.; Hyldgaard, P.; Lundqvist, B. I., *Rep. Prog. Phys.* **2015,** 78 (6), 066501.
35. Lee, K.; Murray, É. D.; Kong, L.; Lundqvist, B. I.; Langreth, D. C., *Phys. Rev. B* **2010,** 82 (8), 081101.
36. Klimes, J.; Bowler, D. R.; Michaelides, A., *J. Phys.: Condens. Matter* **2010,** 22 (2), 022201.
37. Grimme, S.; Ehrlich, S.; Goerigk, L., *J. Comput. Chem.* **2011,** 32 (7), 1456-1465.
38. Grimme, S.; Antony, J.; Ehrlich, S.; Krieg, H., *J. Chem. Phys.* **2010,** 132 (15), 154104.
39. Johnson, E. R.; Becke, A. D., *J. Chem. Phys.* **2006,** 124 (17), 174104.
40. Caldeweyher, E.; Ehlert, S.; Hansen, A.; Neugebauer, H.; Spicher, S.; Bannwarth, C.; Grimme, S., *J. Chem. Phys.* **2019,** 150 (15), 154122.
41. Zanella, R.; Giorgio, S.; Henry, C. R.; Louis, C., *J. Phys. Chem. B* **2002,** 106 (31), 7634-7642.
42. Niu, P.; Yin, L. C.; Yang, Y. Q.; Liu, G.; Cheng, H. M., *Adv. Mater.* **2014,** 26 (47), 8046-8052.

Chapter 3. Photocatalytic CO_2 Reduction on g-C_3N_4 with B, K co-Doping and N Vacancies

This work has been published as *Applied Catalysis, B: Environmental* **2019,** 254, 270-282.[1] It was written by the author of present thesis. This chapter is reproduced from original paper with some modifications.

3.1 Introduction

As it is reviewed in Chapter 1, g-C_3N_4 has been reported as a semiconductor showing promising applications in photocatalysis research field. It has attracted significant attentions from researchers working on developing low-cost and high-performance catalysts for renewable fuel production.[2-3] Although tri-s-triazine (heptazine) based g-C_3N_4 as photocatalyst shows attractive properties such as good stability, low cost and negligible toxicity, the pristine g-C_3N_4 fails to perform satisfactory catalytic activity comparing with other photocatalysts. Its weak performance is mainly attributed to the low efficiency in interlayer charge transfer, high recombination rate and unoptimized electronic structure.[4-5]

In this chapter, I developed a new strategy that integrates co-dopants K and B with controllable N_v. And the mechanism of enhanced photocatalytic CO_2 reduction performance was elucidated. Homogeneous distribution of K, B dopants and N_v with the same molar concentration could only be achieved by using this one-step strategy modifying by single-molecule compound: thermal polymerization of DCDA with KBH_4. The advantage of this strategy relies on

the rational choice of co-dopants and largely cancelled individual drawbacks of each modification factor. To be more specific, K is frequently doped at the interstitial site (also called vacancy site) to enhance CO_2 and g-C_3N_4 interlayer electron transfer; B, a substitutional dopant, helps to remain the high reduction potential for CO_2 by compensating the drawback of K. N_v narrows the bandgap and significantly enhances the CO_2 adsorption.[6-7] The K and B co-dopants and N_v can act synergistically in promoting the photocatalytic CO_2 reduction on g-C_3N_4. Additionally, N_v with controllable quantity was introduced by the self-limited generation of H_2 due to the decomposition of KBH_4. The modification strategy achieves 161% and 527% increases for CH_4 and CO respectively comparing with pristine g-C_3N_4. The achieved electron-rich catalyst surface and optimised electronic structure are proven to be attributed to the enhanced photocatalytic performance by both experimental and theoretical evidence. The CO_2 photocatalytic reduction pathway is further elucidated by *in-situ* DRIFTS.

3.2 Experimental

3.2.1 Catalysts characterization

The CO_2 TPD were conducted on the same equipment with following procedures: 0.1 g samples are placed into a U-shape reactor and further treated under He flow (50 sccm) at 300 °C for 30 min. CO_2 was introduced and adsorbed on the samples for 45 min at room temperature. During the desorption process, the cell was heated to 400 °C with a ramping rate of 10 °C min^{-1} under flowing He (50 sccm). An MS, (HAL 201, Hiden Analytical) was used to monitor the evolution of CO_2 by signalling m/z = 44. SEM (JEOL JSM-6390A) equipped with EDS (JEOL) was used to analyse the spatial distribution of K and B dopants. To determine the concentrations of K and B elements in the g-C_3N_4, the TGA were conducted for both pristine g-C_3N_4 and KBH modified g-C_3N_4 with different concentrations. The samples (i. pristine g-C_3N_4; ii. 1%-KBH C_3N_4; iii. 2%-KBH C_3N_4; iv. 3%-KBH C_3N_4; v. 5%-KBH C_3N_4;) powders were placed into an alumina crucible in a TGA (Mettler Toledo

TGA/DSC 3+). The samples were heated up in flowing air (80 sccm) with the ramping rate of 10 °C min^{-1} to 900 °C to burn all the C and N elements into gaseous products. The residual weight consists of the stable oxides of K and B elements: K_2O and B_2O_3

3.2.2 *In-situ* DRIFTS measurements

In-situ DRIFTS was conducted using a commercial reactor (Praying Mantis HVC-DRP-5, Harrick) placed inside the infrared spectrometer (Shimadzu IRTracer-100) with a liquid nitrogen cooled MCT (Mercury Cadmium Telluride) detector. A Xenon lamp (SLS400, Thorlabs) coupled with a collimator and liquid light guide was used to provide the UV-Vis light to drive the in-situ photocatalytic reaction. A KG-1 IR cut-off filter (Schott AG) is used to eliminate the thermal effects brought by the light source. The power of the light is measured via the pyroelectric optical power meter (PM16-401, Thorlabs) and reaches ~40.3 mW cm^{-2} on the surface of photocatalysts. Around 20 mg of sample is placed into the sample cup and the reaction temperature is fixed at 30 ºC controlled by the chilled-water circulation and a PID controlled cartridge heater underneath the sample cup. The chamber was firstly purged with 20 sccm Ar flow and the samples were heated up to 300 °C with 30 min soaking time to get a clean surface. The baseline for the DRIFT spectra was recorded after the samples cooling down to 30 °C. The spectra for mechanism investigations were conducted using the following procedure: 5% CO_2/Ar was flowing through a water bubbler in a flow rate of 10 sccm for 20 min under darkness. Then the reactor valves are shut off to simulate the batch reaction for 60 min under UV-Vis light irradiation. 116 scans with the resolution of 4 cm^{-1} were averaged for one spectrum to ensure a high signal to noise ratio and the time interval of obtained curves was 1 minute.

3.2.3 Catalytic performance evaluation

Photocatalytic performance on CO_2 reduction with water was evaluated with a stainless-steel batch reactor with quartz window (diameter of 50 mm) under UV-Vis light irradiation (**Figure 3.1**). 0.1 g photocatalysts were loaded on

borosilicate fibre filter (Fisher scientific) by vacuum filtration and drying at 100 °C in an oven. After loading the photocatalysts into reactor, the UV-Vis light was irradiated on the photocatalysts under flowing Ar for 20 min to remove possible surface contamination. Then 0.8 mL water was added to the reactor and purged with CO_2 for 10 times before reaction. CO_2 is introduced in the reactor with the pressure of 2 bar after the last time of purge and the pressure is monitored by a digital compound gauge (DPGM8001-1V6, Omega engineering). A 300 W Xenon lamp (PE300, Excalitas Technologies) is used to mimic the solar light with UV-Vis light output and ~430 mW cm^{-2} light power density is achieved at the surface of the photocatalysts. All the reactions are conducted at room temperature by forced air cooling the reactor with strong convection. The products were analysed with a GC (GC-2010PLUS, Shimadzu) equipped with a TCD and an FID serially connected. A Shincarbon ST micropacked column (Restek Corporation) was used to separate the CO, CO_2, CH_4 from permanent gases.

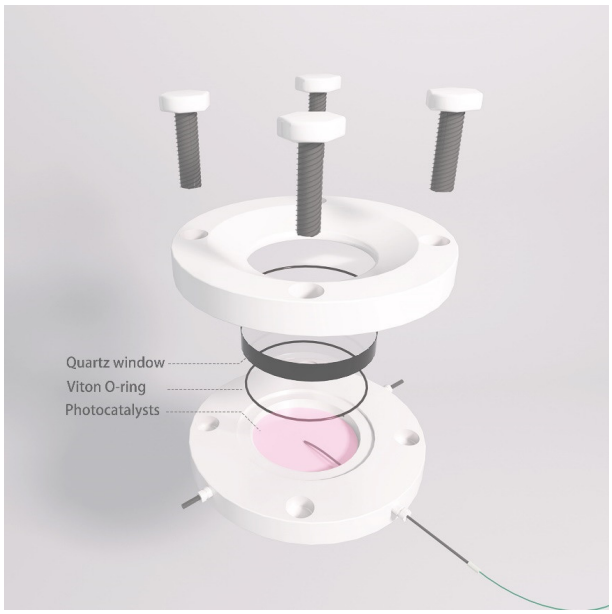

Figure 3.1. Illustration of the batch reactor for photocatalytic CO_2 reduction by water.

3.2.4 Computational details

First-principle calculations based on DFT theory were conducted with the Quantum Espresso package.[8-9] The PAW pseudopotentials[10-12] and plane-wave basis were used. The kinetic energy cut-offs for plane-wave basis sets and charge density and potential were set to be 60 and 540 Ry, respectively. The GGA in form of the Perdew-Burke-Ernzerhof (PBE) functional[13] was used as the treatment of electron exchange and correlation for the geometry relaxation. Heyd-Scuseria-Ernzerhof (HSE06) hybrid functional[14-15] with 25% Fock exchange was used in the electronic structure calculations based on the optimized structure. And long-range vdW force was introduced to the system by using the Grimme-D3 dispersion correction for all calculations.[16] A gaussian smearing of 0.01 Ry was exerted on the orbital occupation during all calculations. The self-consistency convergence threshold for each electronic step was 1×10^{-6} Ry. Geometry relaxations were conducted for all the structures until the force reached less than the criteria of 2×10^{-3} Ry Bohr^{-1}. A 1×1×4 supercell of g-C_3N_4 with the repeated heptazine unit structure and 56 atoms in total was used to represent the pristine g-C_3N_4 before doping. B, K atoms were introduced into the supercell as substitutional or interstitial dopants for comparison. Slab models were built up by cleaving the (001) facet of optimized bulk structure and adding a vacuum layer of 15 Å to prevent the intervention. The bottom layer atoms were fixed and surface 3 layers were free to relax. The 4×4×4 Monkhorst-Pack *k*-points grids were chosen to sample the Brillouin zone for bulk and 4×4×1 mesh for slab models. All the plots related to the calculations were produced with the VESTA.[17]

3.3 Results and Discussion

3.3.1 Photocatalyst characterization

3.3.1.1 Molecular structure characterization

XRD was used to characterize the crystal structure of our photocatalysts synthesized via thermal polymerization of DCDA with different amounts of

KBH_4 powders. The XRD patterns can reflect the effects of doping on the crystal lattice constants and interstitial doping between layers (as illustrated in **Figure 3.2**). As shown in **Figure 3.3**(a), all KBH-C_3N_4 with different modification degrees present similar prominent peaks at around 27°. These peaks are assigned to the (002) facets of g-C_3N_4 derived from the stacking of layers interacting each other via vdW forces. The other smaller peaks centred at ~13° represent in-plane repetition of heptazine motifs. **Figure 3.3**(b) shows the magnified (002) peaks of all the prepared samples. There is a trend of slight shift towards lower angles observed in the XRD patterns, which indicate the interlayer distance of g-C_3N_4 is enlarged after modifications. The increase of the layer distance is likely attributed to the layer distortion and K doping. While the latter is still under debate. K dopants have been claimed to have increased [18-19], decreased [20-21] or no effect [7] on the interlayer distance of g-C_3N_4 in the literature. It is also worth mentioning that the intensities of the peaks shown in the diffraction patterns drop with the higher modification degree. The gradual decrease in crystallinity suggests the distortions of g-C_3N_4 lattice brought by the N_v to the g-C_3N_4.

FTIR spectra were used to elucidate the evolution of molecular structure. As shown in **Figure 3.3**(c), the strong bands ranging from 1200 to 1600 cm^{-1} are attributed to the heterocycles built up with C-N and C=N bonds [22]. The skeletal stretching model remains unchanged through the evolution, which confirms the molecular structure of heptazine unit is well maintained. The peaks centred at 2177 cm^{-1} in curves **ii**, **iii**, **iv**, **v** are derived from the asymmetric vibration of the –C≡N, the cyano groups. When the modification degree increases from 1% to 5%, the peak intensity grows correspondingly. On the contrary, at the same wavenumber, the curve **i** (pristine g-C_3N_4) shows no obvious peak. The peaks located at 887 cm^{-1} and the broad adsorption within the range from 3000 to 3700 cm^{-1} are brought by the N-H bonds [23]. Though insignificantly, the intensity reduction can still be seen from peak **i** to **v**. In order to differentiate the roles of different elements in modifying the structure of g-C_3N_4, the FTIR spectra were acquired with the three control groups: K doped g-C_3N_4 (3% K-C_3N_4), B doped g-C_3N_4 (3% B-C_3N_4), and B, K co-doped g-C_3N_4 (3% KB-C_3N_4). The

corresponding data are presented in **Figure 3.3**(d). Compared with pristine g-C_3N_4 (curve **i**), only curve **vi** (3% K-C_3N_4) shows a sharp increase in the intensity of the peak centred at 2177 cm^{-1}, which is assigned to the -C≡N group. It leads to a conclusion that doping of K can facilitate the generation of the cyano group while B does not show the same function. It could be explained by the fact that potassium oxides react with the amine groups during the thermal polymerization process.[21]. Increasing the amount of KBH_4 will result in more *in-situ* generated H_2, which in turn reacts with –NH_x to form gaseous NH_3. As a result, more N_v was introduced. The phenomenon is supported by the fact that the -NH_x peak intensity decreases with the rise of modification degrees.[24] The nearly unchanged -N-H peak intensities further confirmed that the *in-situ* H_2 treatment doesn't cause H doping to the molecular structure, which will be further verified by the organic elemental analyses in the following discussion (**Table 3.2**). The doping of H is less desirable since the H intends to saturate the N basic sites, which retards the CO_2 adsorption.

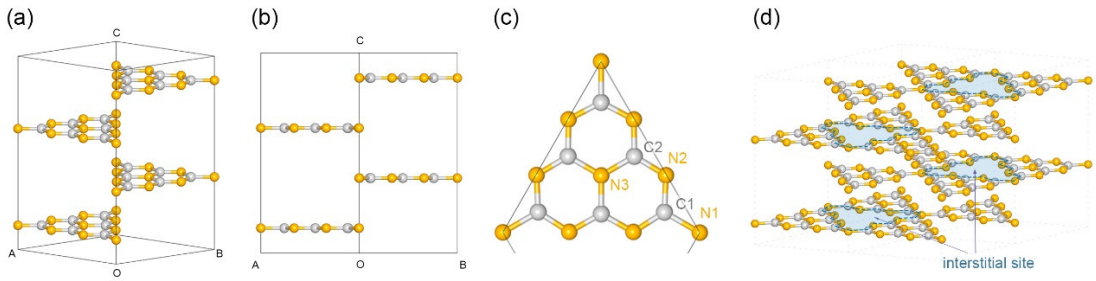

Figure 3.2. The (a) isometric and (b) side views of crystal structure of g-C_3N_4 1×1×4 supercell. (c) Scheme of heptazine unit and notations of inequivalent C, N positions. (d) Scheme shows the interstitial doping site between layers. The balls in amber and grey represent N and C atoms respectively.

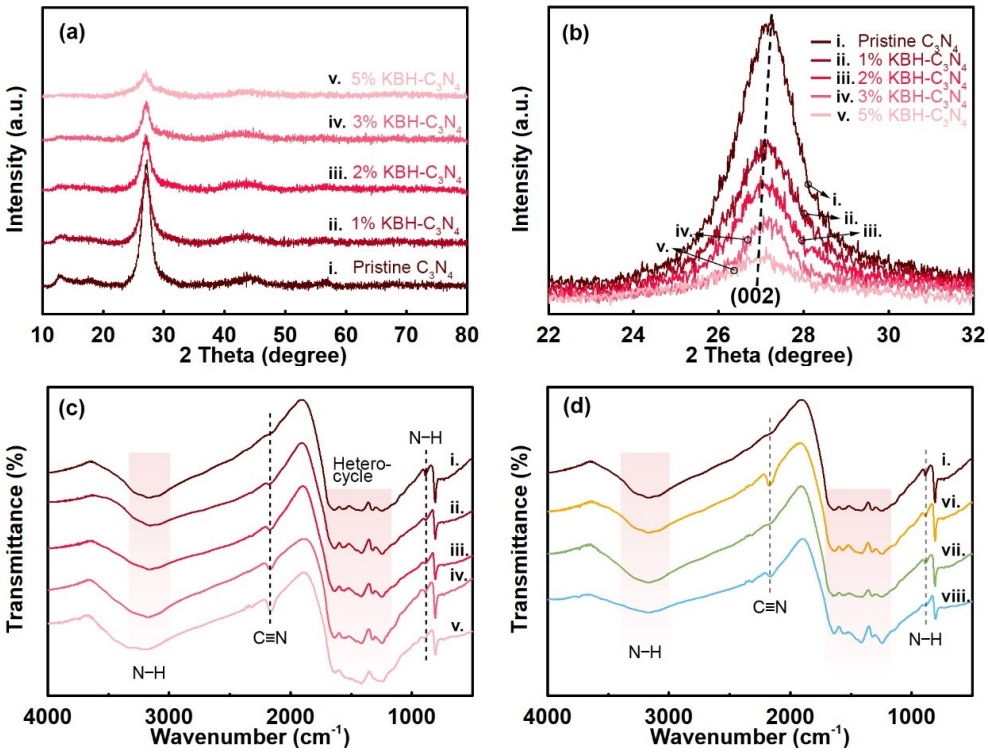

Figure 3.3. (a) XRD patterns of KBH-C_3N_4 with different modification degrees and (b) magnification of the peaks attributed to (002) facet. The FTIR transmission spectra of (c) KBH-C_3N_4 with different modification degrees (**i.** pristine, **ii.** 1%, **iii.** 2%, **iv.** 3%, **v.** 5%) and (d) pristine-C_3N_4 (curve **i.**), 3% K-C_3N_4 (curve **vi.**), 3% B-C_3N_4 (curve **vii.**), 3% KB-C_3N_4 (curve **viii.**).

XPS is a semi-quantitative tool to determine the site of the dopants by identifying their chemical environments. **Figure 3.4**(a) shows the K2p spectra of the pristine g-C_3N_4 and modified KBH-C_3N_4. The pristine g-C_3N_4 shows no peak in the region and the peaks of K $2p_{1/2}$ and $2p_{3/2}$ are positioned at 295.7-295.5 eV and 293.0-292.8 eV, respectively. The K2p peaks correspond to K-N bonds, which agrees with the reported potassium azide.[19-20] The evidence strongly suggests that K dopants locate at the interstitial sites between the layers. Peaks of K $2p_{1/2}$ and $2p_{3/2}$ exhibit a shift of 0.2 eV to lower energy when the percentage of KBH_4 increases from 1% to 5%. A similar shift is also observed in B 1s spectra in **Figure 3.4**(b). The B 1s peaks are centred at the binding energy from 191.8 eV to 191.5 eV in modified g-C_3N_4 samples. It indicates the B-N bonds formed in the heptazine unit and B prefers to replace carbon at C1 position (bay position) in the heptazine structure (as illustrated in **Figure 3.2**(c)) [25-26]. C 1s spectra are given in **Figure 3.4**(c). The peaks

positioned at 288.0-288.2 eV are assigned to C in hetero-cycles, N-C=N [20-21]. A small binding-energy shift towards lower energy is also observed. The peaks at the binding energy of 284.8 eV are caused by the adventitious C (used as charging effects reference).[21] The peaks corresponding to C-NH_x (~286.4 eV) do not show an obvious increase, although more H_2 is generated when higher amount of KBH_4 is used. The N 1s spectra shown in **Figure 3.4**(d) offer more information on molecular structure. In order to elucidate all the bonds formed with N, the dashed lines are plotted in the figure: peaks at 404.1 and 401.0 eV associating with the NH_x groups, the peaks at 400.0 eV being attributed to the N3C (N bonding with 3 C atoms), the peaks at 398.7 eV referring to the N2C (N bonding with 2 C atoms), peaks at 398.0 eV to N-B bonds and peaks at 398.6 eV to the N-K bonds.[20-21, 27-28] The changes in peak intensity suggests how the structure of gC_3N_4 evolves with different degrees of modifications. The significant drop in the N2C intensity, shown in **Figure 3.4**(d), confirms that H_2 is the source creating N_v and the N2C is the most energy favourable N to lose. The peaks corresponding to the N-K and N-B groups rise, which further testifies the bond formation between dopants and g-C_3N_4. The downshift of binding energies of B 1s and N 1s with increasing modification degree can be explained by the same reason: replacement of C by B (the least electronegative element in our structure) and the loss of N (the atom with the highest electronegativity) in the heptazine unit. The modification largely increases the electron density for the remaining atoms in the doped system, which can enhance the screening effects of the core-level electrons. In addition, the concentrations of each atom were also determined using XPS based on the C 1s, N 1s, B 1s and K 2p spectra peak areas with relative sensitivity factors.[29] As presented in **Table 3.1**, for all KBH-C_3N_4 with different concentrations, the C/N atomic ratios show small fluctuations and B/K atomic ratios are close to 1:1. It indicates the molar concentrations of B, K and N_v are nearly equal to each other in KBH-C_3N_4.

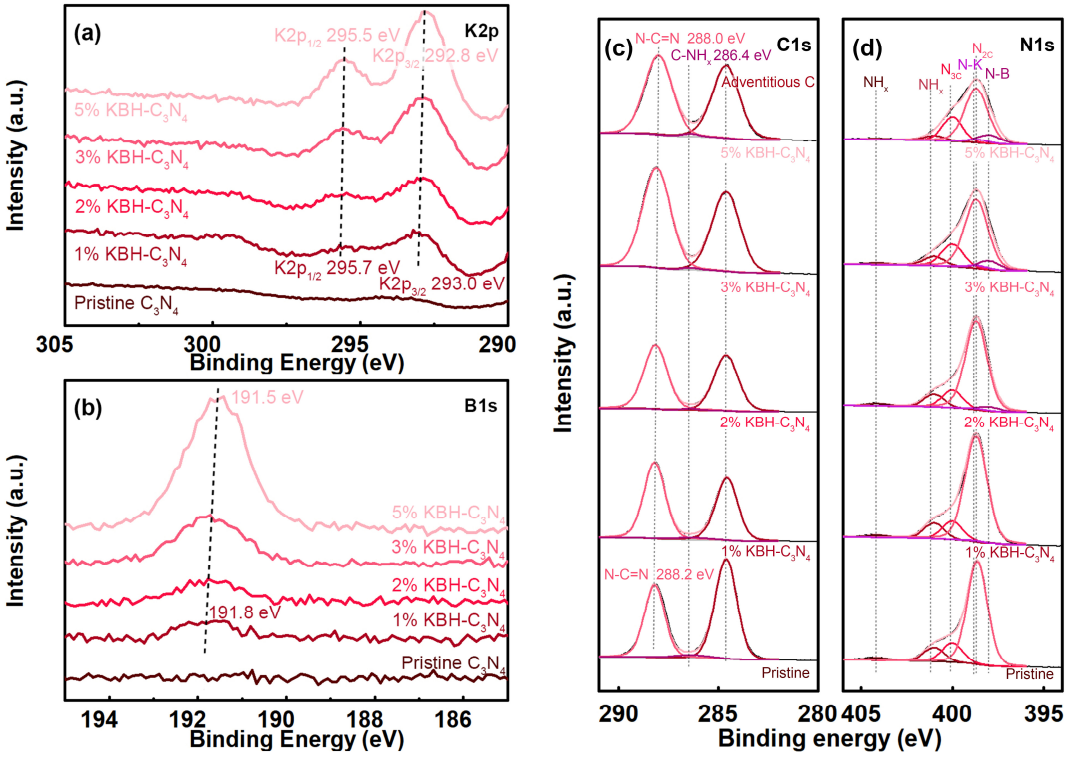

Figure 3.4. XPS profiles of (a) K2p, (b) B1s, (c) C1s and (d) N1s spectra of pristine and KBH modified C_3N_4 (1%-5%).

Table 3.2 shows the organic elemental analysis results for KBH-C_3N_4 with different modification degrees and control groups including 3%K-C_3N_4, 3%B-C_3N_4 and 3%KB-C_3N_4. Comparing with pristine g-C_3N_4, the C/N ratios in modified g-C_3N_4 samples remain similar with only a small fluctuation could be observed. This result again confirms that B is in favour of replacing C and *in-situ* generated H_2 causes the loss of N in g-C_3N_4. Moreover, it quantitatively proves that the B substituting C and N_V shows approximately 1:1 molar ratio. The N loss due to *in-situ* H_2 treatment can also be confirmed by the higher C/N ratio of 3% KBH-C_3N_4 than 3%KB-C_3N_4. A significantly lower C/N atomic ratio of 3%B-C_3N_4 demonstrates the main doping form of B is the substitution of C atoms inside the heptazine structure. K doping causes the loss of N but only slightly. The reason is attributed to the formation of KOH during the synthesis process at ambient atmosphere and the KOH further reacts with g-C_3N_4 resulting the N_V.[21, 30] Additionally, the H wt% shows small difference between all samples, which rules out the possible doping of H into the heptazine unit.

All these quantitative results are in agreement with former FTIR and XPS analyses.

As a complementary method to XPS and organic elemental analyses in quantitative determination of doping concentration, the TGA was used and the results are presented in **Figure 3.5** and **Table 3.3**. The concentrations of K+B in KBH-C_3N_4 are very close to the values determined by XPS (**Table 3.1**), which indicates the homogeneous distribution of the dopants both on the surface and in the bulk. It is in agreement with expectation, since the modification happens during the synthesis process of g-C_3N_4 rather than a post-treatment. To further prove the homogeneous distribution of B, K dopants, an EDS elemental mapping was conducted with a SEM (**Figure 3.6**). The corresponding EDS spectrum further confirms the existences of the C, N, B, K elements without other contaminants.

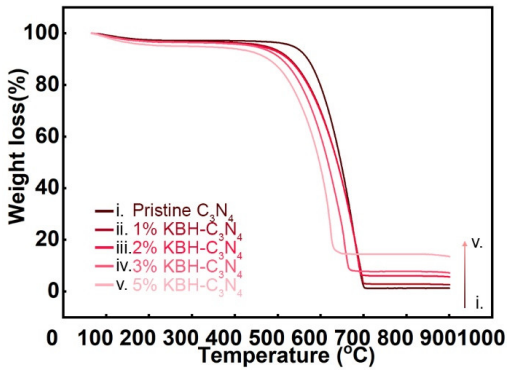

Figure 3.5. TGA profiles of **i.** pristine g-C_3N_4, **ii.** 1% KBH-C_3N_4, **iii.** 2% KBH-C_3N_4, **iv.** 3% KBH-C_3N_4 and **v.** 5% KBH-C_3N_4.

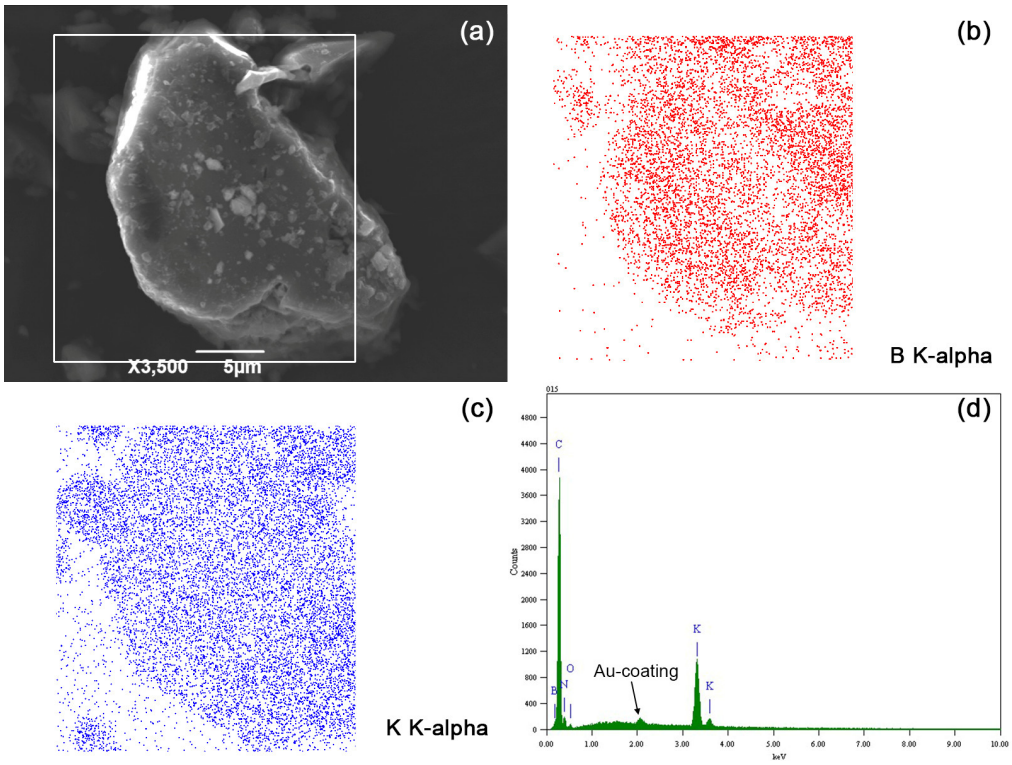

Figure 3.6. (a) SEM image of 3% KBH-C_3N_4 and corresponding EDS elemental mapping of (b) B K-alpha and (c) K K-alpha signals. (d) The EDS spectrum of the selected area.

Table 3.1. XPS spectra-derived atomic percentages of C, N, B, K in pristine and KBH C_3N_4 with different modification degrees.

Sample	C (at%)	N (at%)	B (at%)	K (at%)	C/N atomic ratio	B/K atomic ratio
Pristine g-C_3N_4	40.25	56.29	0	0	0.72	N/A
1% KBH-C_3N_4	41.03	53.5	0.27	0.3	0.76	0.9
2% KBH-C_3N_4	42.6	52.44	1.13	1.06	0.81	1.06
3% KBH-C_3N_4	41.13	51.49	1.55	1.65	0.79	0.94
5% KBH-C_3N_4	40.01	50.47	2.39	2.71	0.79	0.88

Table 3.2. Organic element analysis results: C/N atomic ratios and hydrogen concentration (wt%) of KBH-C_3N_4 with different doping concentrations and 3%K-C_3N_4, 3% B-C_3N_4, 3% KB-C_3N_4 respectively.

Sample	C/N atomic ratio	Hydrogen (wt%)
Pristine g-C_3N_4	0.643	1.69
1% KBH-C_3N_4	0.640	1.69
2% KBH-C_3N_4	0.631	1.67
3% KBH-C_3N_4	0.640	1.55
5% KBH-C_3N_4	0.639	1.54
3%K- C_3N_4	0.653	1.52
3%B- C_3N_4	0.616	1.68
3%KB-C_3N_4	0.623	1.80

Table 3.3. TGA results on K, B contents of (**i.** pristine g-C_3N_4; **ii.** 1%-KBH C_3N_4; **iii.** 2%-KBH C_3N_4; **iv.** 3%-KBH C_3N_4; **v.** 5%-KBH C_3N_4)

sample	B + K (at%)
Pristine C_3N_4	0%
1% KBH C_3N_4	0.8%
2% KBH C_3N_4	1.9%
3% KBH C_3N_4	2.4%
5% KBH C_3N_4	4.9%

3.3.1.2 Electronic structure characterization

The electronic structure including bandgap and band edge positions directly determines the light utilization ability, reduction/oxidation potential and excited carrier recombination rate of the photocatalysts. Therefore, it is more important to figure out how the KBH-modification changes the electronic structure of the g-C_3N_4 after identification of the molecular structure evolution. The band positions of prepared samples were determined via the combination of VBM positions calculated from the XPS VB spectra and bandgap derived from the UV-Vis DRS spectra.

The light absorption is demonstrated via the UV-Vis DRS spectra. The optical bandgaps of the samples could be derived from the Tauc plots and Kubelka-Monk theory, as shown in **Figure 3.7**(a, b). The calculated optical bandgap for pristine g-C_3N_4 is 2.74 eV, which is very close to reported values in literature.[31-32] And the bandgaps for KBH-C_3N_4 with 1-5% concentrations are determined to be 2.66, 2.55, 2.35 and 1.74 eV, respectively. The monotonic narrowing of bandgap is due to the increasing modification degree. Comparing the optical bandgaps of control groups (**Figure 3.7**(b)) with pristine g-C_3N_4 and 3% KBH-C_3N_4, the K, B co-doping only narrows the bandgap by 0.13 eV while *in-situ* H_2 treatment decreases another 0.39 eV than K, B co-doping. The 3% K-C_3N_4 and 3% B-C_3N_4 have similar optical bandgaps of 2.65 and 2.64 eV. The corresponding UV-Vis absorption curves are presented in **Figure 3.8**(a, b) with Kubelka-Monk units. In summary, the N_V caused by *in-situ* H_2 treatment contributes the most to the bandgap narrowing.

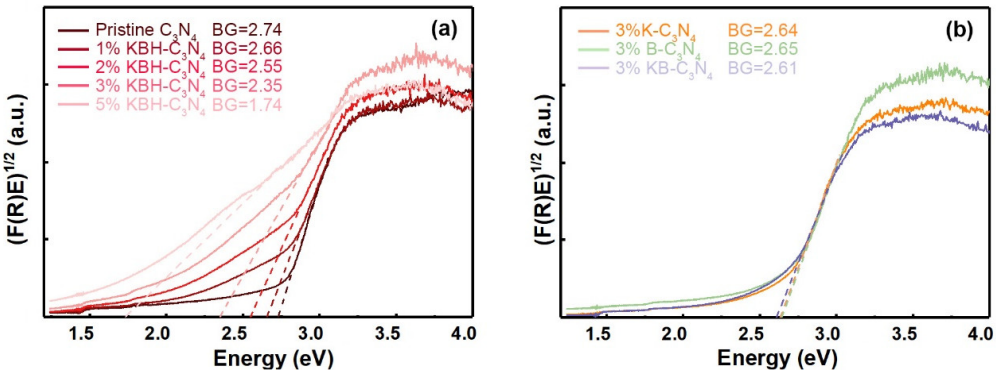

Figure 3.7. Tauc plots for bandgap determination of (a) KBH-C_3N_4 with different modification degree (pristine, 1%, 2%, 3%, 5%) and (b) 3% K-C_3N_4, 3% B-C_3N_4 and 3% KB-C_3N_4.

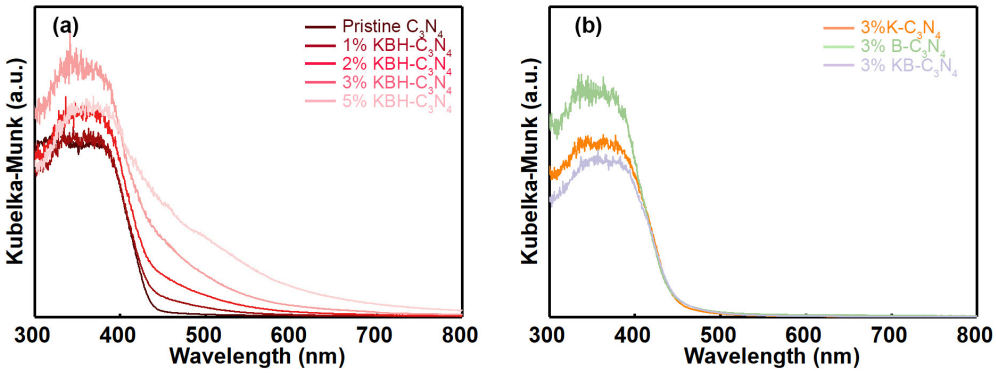

Figure 3.8. UV-Vis DRS of (a) KBH-C_3N_4 with different modification degree (pristine, 1%, 2%, 3%, 5%) and 3% K-C_3N_4, 3% B-C_3N_4 and 3% KB-C_3N_4.

The energy of VBM is the key parameter to know the oxidation capability of the photocatalyst. Characterised by XPS method, the binding energy of the VBM for pristine g-C_3N_4 and 1%, 2% 3% 5% KBH-C_3N_4 is 2.18, 2.18, 2.13, 2.01 and 1.94 eV respectively, as shown in **Figure 3.9**(a). The VBM positions show a slight decrease when KBH modification degree rises, while the discrepancies between each other are quite small (within 0.24 eV). In order to shed light on the role of individual modification factors, control groups of 3% K-C_3N_4, 3% B-C_3N_4 and 3% KB-C_3N_4 have been characterized at the same condition and the XPS VB spectra are presented in **Figure 3.9**(b). It is exhibited that the K holds the capability to shift the VBM more positive when doped into C_3N_4, which is in agreement with previously published reports [19, 33]. On the contrary, B doping shows the opposite effects on VBM by shifting the

VBM upwards, which agrees with the theoretic calculation and experimental results [34-35]. The N_v generated by H_2 treatments also bring the upshift to VBM, while the influence is not significant [24]. From determination of the VBM results, it clearly testifies the derivation of the synergistic effect between B and K: B dopants can compensate the detrimental effect of K doping, decrease of the reduction ability of CO_2, by upshifting the VBM.

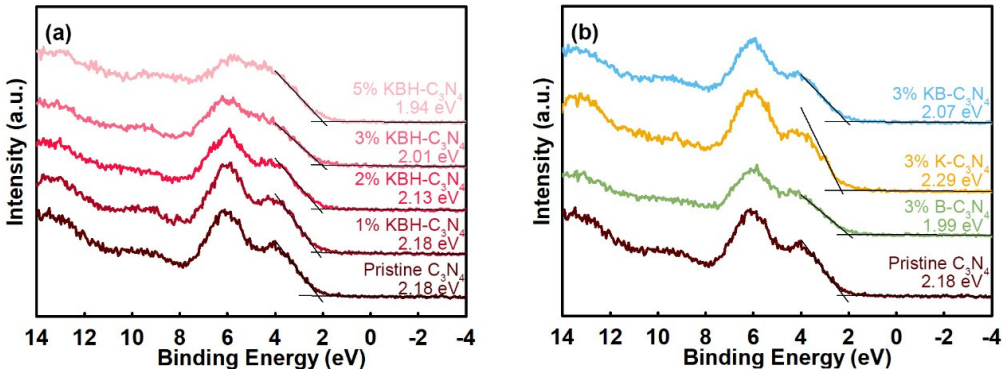

Figure 3.9. XPS VB spectra of (a) pristine and KBH-C_3N_4 with different modification degrees, and (b) control groups of 3% K-C_3N_4, 3% B-C_3N_4 and 3% KB-C_3N_4.

In order to get a full understanding of the band alignments and relative potentials towards different benchmark reactions, the VBM versus SHE is calculated with following equation by estimating the work function Φ of the XPS analyser to be 4.37 eV and vacuum level of -4.44 eV (*vs.* SHE):[21, 36-37]

$$\mathrm{VBM\ (vs.\ SHE)} = \Phi + E_{binding} - 4.44 \tag{3.1}$$

As the result, the VBM potentials (vs. SHE) of the pristine g-C_3N_4 and 1%, 2%, 3%, 5% KBH-C_3N_4 are determined to be 1.62, 1.62, 1.57, 1.45 and 1.38 eV. Combining with the measured bandgap values, the band alignments of different samples are calculated and the results are presented in **Figure 3.10** and the control group in **Figure 3.11**.

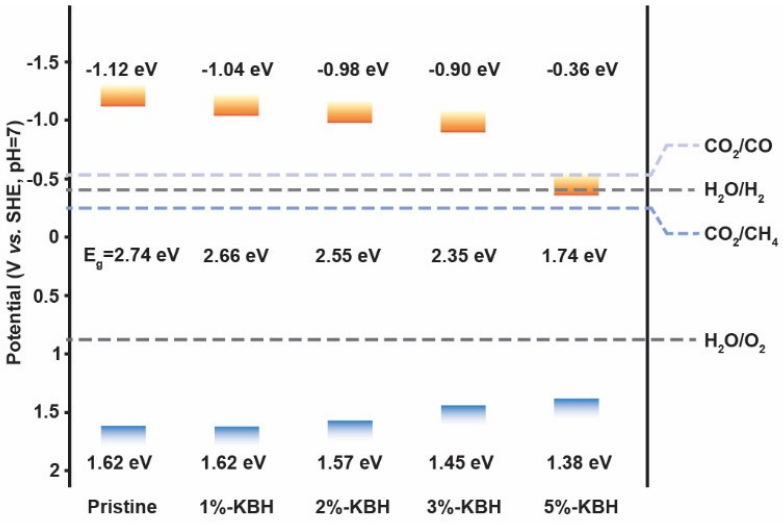

Figure 3.10. Band alignment of the pristine g-C_3N_4 and KBH-C_3N_4 with modification degrees of 1%, 2%, 3% and 5%.

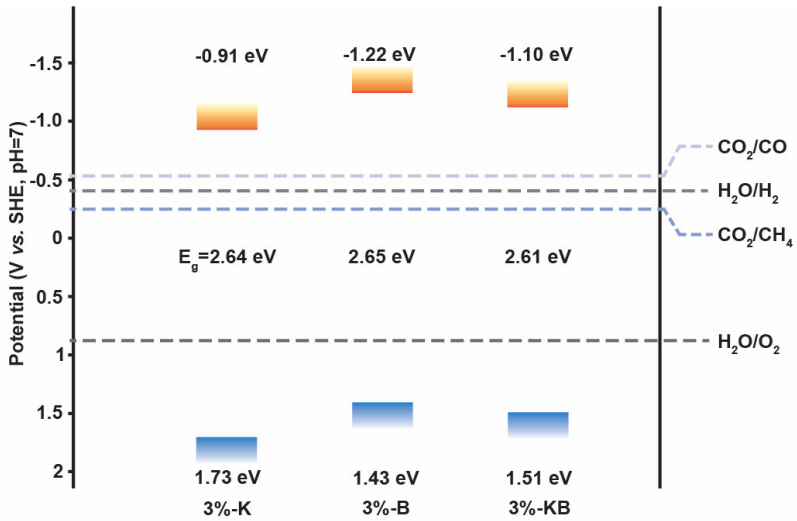

Figure 3.11. Band alignment scheme of control group samples: 3%-K, 3%-B and 3%-KB g-C_3N_4.

The PL spectroscopy and time-resolved fluorescence spectroscopy are often used to evaluate the possibility of recombination and lifetime of the photo-excited carriers in photocatalysts. In **Figure 3.12**(a), the fluorescence peak intensity of KBH-C_3N_4 shows significant and continual decrease with rising modification degrees. This result supports the argument that the KBH-modification is able to limit the recombination of photo-excited electrons and holes in g-C_3N_4. Moreover, the extended lifetime of the charge carriers in

modified KBH-C_3N_4 is further confirmed by conducting the time-resolved fluorescence spectroscopy characterized by monitoring the static PL peak wavelength. The fluorescence decay profiles and the corresponding exponential fittings were presented in **Figure 3.12**(b, c). The average carrier lifetime of 3% KBH-C_3N_4 (**Figure 3.12**(c)) is calculated to be 14.61 ns which is almost twice as long as the pristine g-C_3N_4 of 7.56 ns (**Figure 3.12**(b)). The trapping effects of the dopants, N_v and the interlayer connection achieved by K dopants are supposed to be attributed to the longer carrier lifetime.[5, 19] And atomic scale understandings including nearly no mid-gap state formed by K, B and non-coplanar existence of HOMO and LUMO are proven by the electronic structure calculation, which is discussed in later section.

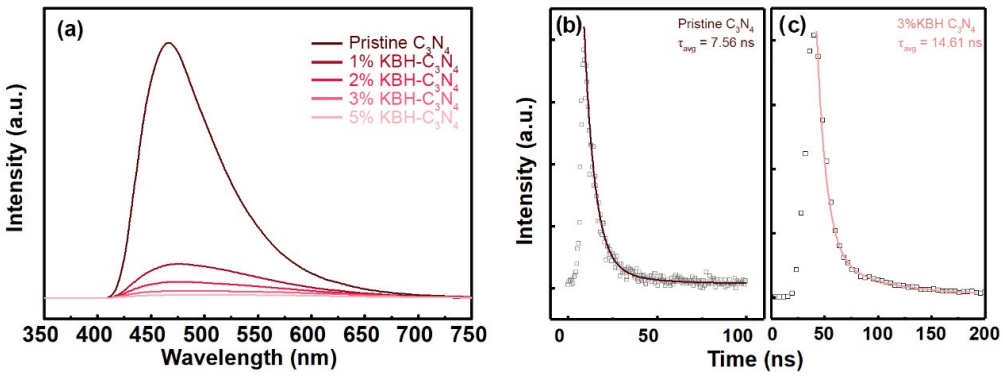

Figure 3.12. (a) PL emission spectra of KBH-C_3N_4 with different concentrations (pristine, 1%, 2%, 3%, 5%). Time-resolved fluorescence decays and fitted lines of (b) pristine g-C_3N_4 and (c) 3% KBH-C_3N_4.

3.3.1.3 Surface area characterization and CO_2 uptake capability

N_2 adsorption was conducted at 77 K to determine the SSA of prepared samples. The corresponding isotherms and calculated gravimetric surface areas based on multi-points BET theory are shown in **Figure 3.13**(a, b). The BET surface area for pristine g-C_3N_4 is 10.83 m^2 g^{-1}, which is quite similar to previous reports.[38-39] The 1%, 2%, 3%, 5% KBH-C_3N_4 exhibit the surface area of 8.46, 5.88, 5.32 and 4.47 m^2 g^{-1} respectively, which clearly shows a decreasing trend. The BET surface area of control groups of 3% K-C_3N_4, 3% B-C_3N_4 and 3% KB-C_3N_4 are tested to be 7.26, 9.42, 7.45 m^2 g^{-1} respectively. Based on these results, it is shown that the doping of B, K and N_v will cause

the drop in SSA. The N_v shows the strongest ability in reducing the SSA, which is believed due to its prominent capability in modifying the molecular structure. The high SSA does not always guarantee a high CO_2 conversion rate and CO_2 uptake ability is a more reliable criterion correlating directly with the CO_2 conversion performance.[40] The CO_2-TPD is a powerful tool to elucidate this important capability. **Figure 3.14** presents the CO_2-TPD profiles of KBH-C_3N_4 with different modification degrees. It is shown clearly that the pristine g-C_3N_4 has weak CO_2 adsorption ability with small desorption peak. The CO_2 uptake increases monotonically with the rise of modification degree and the highest value reaches at 3%-KBH C_3N_4. It drops afterwards to 5% KBH-C_3N_4. The desorption peak positions also shift to higher temperature for 3% KBH-C_3N_4. The significant increase on CO_2 adsorption and shift of desorption peak to higher temperature suggests that both the number and strength of basic sites of the photocatalyst prominently increase.[40] It is due to the synergistic effects of K, B, N_v modifications. It is worth mentioning, the relatively low desorption temperature of CO_2 on pristine and KBH-C_3N_4 is ascribed to the weak Lewis basic sites that has also been observed in previous researches.[25, 41-44] Being a Lewis acid, the CO_2 intends to adsorb on basic sites of catalysts and the electrons transfer from the electron-rich sites on catalyst surface to the $2\pi^*$ antibonding orbital of CO_2. The electron back-donation largely facilitates the activation and dissociation of CO_2.[6-7, 45] The K dopant has been proven as a kind of electron donors, which donate the electrons to the host and thus enhance the basicity of the catalysts. The role of N_v and B dopant in CO_2 adsorption and conversion have been less investigated than K.[46] Theoretically speaking, B is anticipated to increase the electron density of basic site (adjacent N) as it has less electronegativity than C and N. Moreover, the N_v will induce the electron abundance at the adjacent atoms.[25] Therefore, dopants B and K as well as N_v all play positive roles in promoting CO_2 adsorption. To differentiate their roles in modifying g-C_3N_4, control groups are carefully tested following the same CO_2-TPD procedure and the results are shown **in Figure 3.14**(b). The experimental results confirm the CO_2 uptake enhancements caused by B, K dopants and N_v together. Their promoting effects are in the

order of N_v > B > K, which is in the same sequence of their ability of donating electrons. K in this study shows less prominent effects than expected is due to its special interstitial doping sites in the layered g-C_3N_4 structure. In the conventional catalysts using transition metal oxides as supports, the alkali metal atoms stay on the surface of the catalysts, which will result in a direct contact with CO_2 and even form alkali carbonates. However, K in multi-layer g-C_3N_4 dopes at the interstitial sites between layers without direct interaction with CO_2 on the surface. Its promotion effect is only the result of the electron donation. A fundamental understanding with the help of calculated CDD plot and charge density analysis are presented in the next section. The last point needs to emphasize is the unexpected degradation in 5% KBH-C_3N_4. As presented in **Figure 3.15**, the 5% KBH-C_3N_4 fails to show an increase in CO_2 uptake comparing with 5% KB-C_3N_4, while in 3% KBH-C_3N_4 the significant enhancement is unambiguous (**Figure 3.14**(b)). It might be possibly explained by the following reason: N acts as basic sites in the heptazine unit for CO_2 adsorption[47] and the massive loss of N atoms will neutralize the benefits of the localized electron accumulation derived from N_v. Therefore, our synthesis strategy with controllable H_2 generation will prevent the over-generation of N_v and ensure an optimal performance. In summary, the experimental results confirm the synergistic effects of K, B doping to g-C_3N_4 in enhancing the CO_2 adsorption and the N_v brought by the *in-situ* H_2 treatment contributes the most.

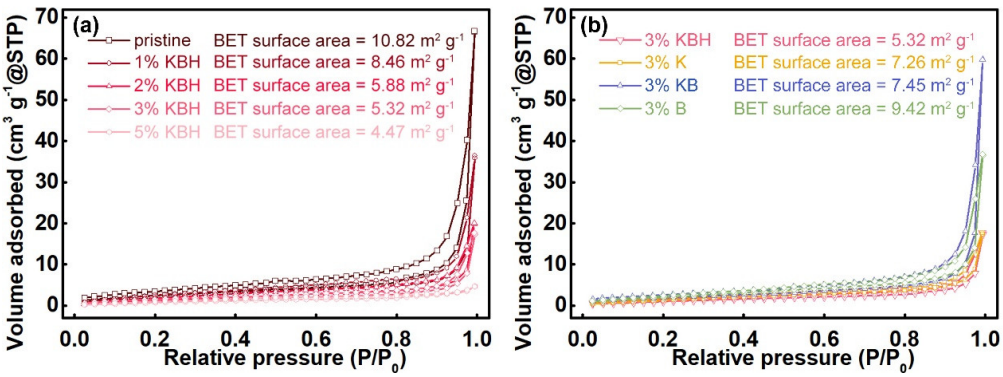

Figure 3.13. N_2 adsorption/desorption isotherms at 77 K for (a) pristine and KBH-C_3N_4 with different degrees and (b) control group of 3% K, B, KB-C_3N_4.

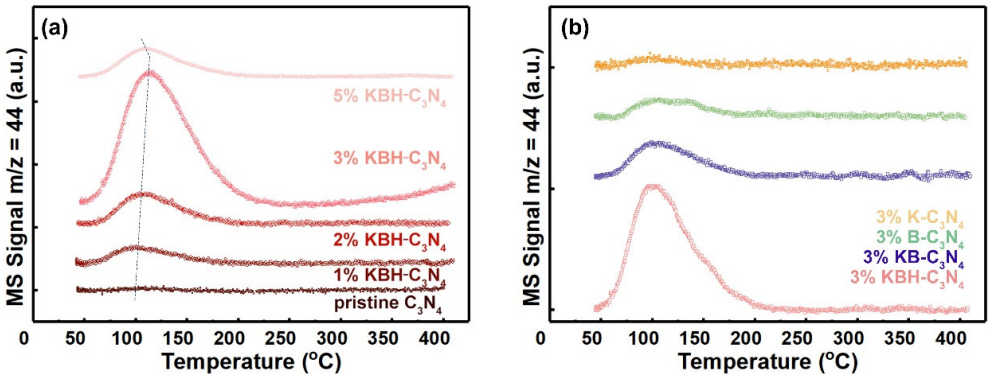

Figure 3.14. The CO_2-TPD profiles of (a) pristine and KBH modified C_3N_4 and (b) control group of 3% K, B, KB modified g-C_3N_4.

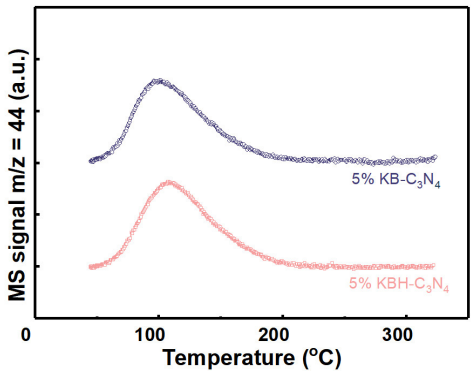

Figure 3.15. CO_2-TPD profiles of 5%KBH-C_3N_4 and 5% KB-C_3N_4.

3.3.2 Theoretical calculations

3.3.2.1 Molecular and electronic structure calculation

First-principle calculation based on DFT is used to help achieving the atom-scale understanding of modification. As discussed in the molecular structure section, K, B and N_V show molar ratios close to 1 in KBH-C_3N_4. Therefore, single K, B and N_V were introduced to the supercell to model the KBH-C_3N_4. In order to figure out the energy-favourable positions for K, B dopants, the formation energy of different doping sites were calculated based on DFT method. The g-C_3N_4 bulk model was built up with the 4 layers of heptazine structure (1×1×4 supercell) with ABAB stacking, as shown in **Figure 3.2**(a, b), which has been widely used to represent the g-C_3N_4 catalysts synthesized via

the thermal condensation process.[19, 30] The optimized structure shows a typical layered crystalline structure and each layer is constituted by the in-planar connection of heptazine unit containing 8 N atoms and 6 C atoms. To calculate the most energy-favourable position for substitutional B doping, the inequivalent positions of the C and N atoms are marked in **Figure 3.2**(c) with corresponding annotations. There are 2 inequivalent C positions and 3 inequivalent N positions in one heptazine structure unit. For interstitial doping, 4 inequivalent doping sites were considered, as presented in **Figure 3.16**(a, b). To prove the optimal doping sites for boron, we conducted the calculations for both the substitutional doping in heptazine unit and interstitial doping between layers. The formation energy is calculated via following equations:

$$E_{Bsub} = E(\mathrm{C_3N_4\text{-}B}) - E(\mathrm{C_3\,N_4}) - \mu(\mathrm{B}) + \mu(\mathrm{C}) \tag{3.2}$$

$$E_{Binter} = E(\mathrm{C_3N_4\text{-}B}) - E(\mathrm{C_3N_4}) - \mu(\mathrm{B}) \tag{3.3}$$

$$E_{\mathrm{Nv}} = E(\mathrm{C_3N_4\text{-}N_v}) - E(\mathrm{C_3N_4}) + \mu(\mathrm{N}) \tag{3.4}$$

The graphite (4 atoms in unit cell), N_2 gas and metal K (2 atoms in unit cell) are used to determine the chemical potentials:

$$\mu(\mathrm{C}) = \frac{1}{4}\mu(\mathrm{graphite}) \tag{3.5}$$

$$\mu(N) = \frac{1}{2}\mu(\mathrm{N_2}) \tag{3.6}$$

Since boron is more stable in the crystalline BN compound at ambient condition than boron bulk phase and likely to form B-N bonds in g-C_3N_4, we use following equation to determine the chemical potential of B, μ(B):

$$\mu(\mathrm{B}) = \mu(\mathrm{BN}) - \frac{1}{2}\mu(\mathrm{N_2}) \tag{3.7}$$

The formation energy of B substitutional doping at C1, C2, N1, N2, N3 is -0.115, -0.104, 0.108, -0.006, 0.121 Ry, respectively. In the case of interstitial doping, the B doped at i1, i2, i3, i4 sites exhibit the formation energy of 0.291, 0.084, 0.113 and 0.261 Ry, respectively. The above results clearly indicate the B intends to replace the C at C1 position as the substitutional dopant. For N vacancy formation, since the H_2 *in-situ* treatment happens on the surface, we

only considered the N_v formation on the top layer of g-C_3N_4. Formation energy is calculated to be 0.456, 0.162 and 0.224 Ry respectively for the N1, N2 and N3 sites respectively. The formation of N_v is an unspontaneous process and the optimal position for N_v is N2. The K doping optimal site has been comprehensively investigated via DFT calculation by Xiong et al.[19] with similar configuration, therefore interstitial doping as the initial position was directly adopted in our work. The optimized KBH-C_3N_4 after geometry optimisation are presented in **Figure 3.17**.

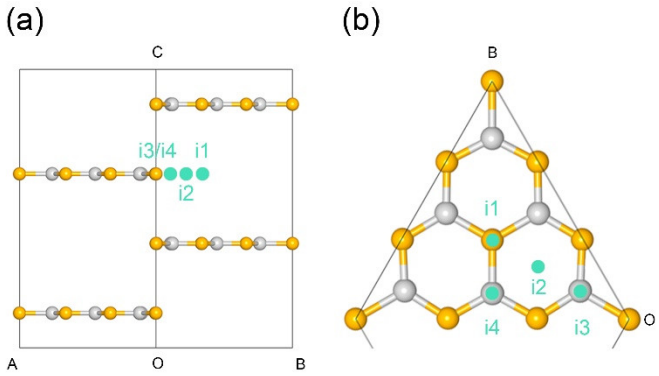

Figure 3.16. Scheme of interstitial inequivalent doping sites in (a) side and (b) top views.

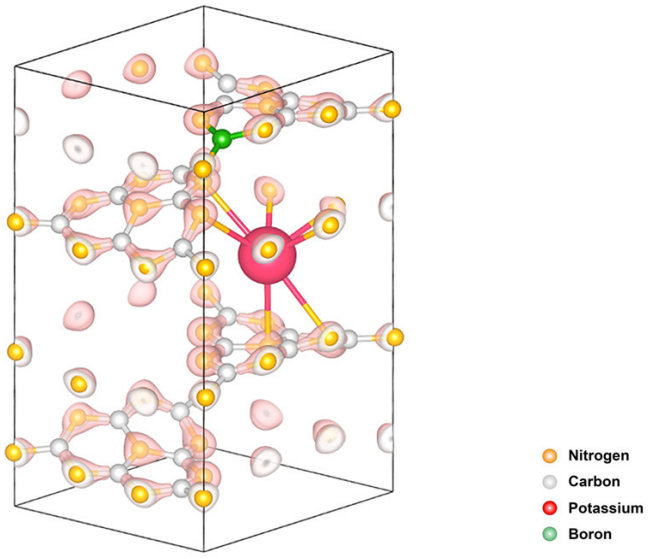

Figure 3.17. The configuration of optimized KBH-C_3N_4 configuration and partial charge density spatial distribution of KBH-C_3N_4. The density of isosurface is 0.3 e Borh^{-3}.

The HSE06 functional[14-15] has been reported to provide more accurate description of the defective g-C_3N_4 geometries by partially cancelling the self-interaction error.[48-49] It is adopted for the electronic structure calculation for g-C_3N_4 and KBH-C_3N_4 here. To elucidate the electronic structure, TDOS and PDOS of pristine g-C_3N_4 and KBH-C_3N_4 have been plotted in **Figure 3.18**(a, b). The contributions from the B s+p orbitals and K s+p orbitals are presented in **Figure 3.19** with the state population enlarged by 20 times. It demonstrates that K, B dopants do not significantly participate in forming the mid-gap states which are deemed as the recombination centre contributing to the carrier recombination.[34] The LUMO and HOMO of KBH-C_3N_4 are mainly constituted by N2p and C2p orbitals respectively, which is also elucidated in isosurface plot (**Figure 3.20**(d)).

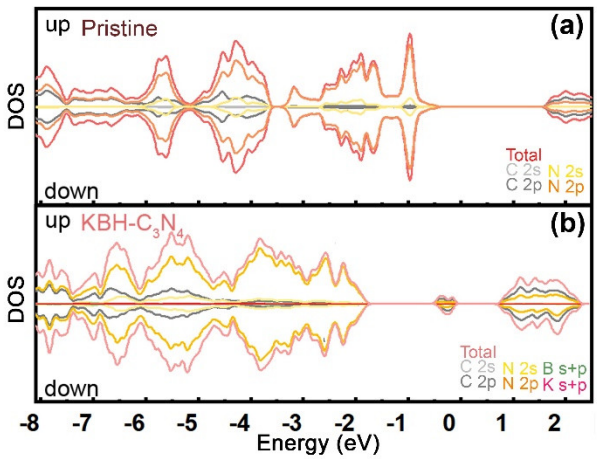

Figure 3.18. Total and projected density of states (TDOS and PDOS) of (a) pristine g-C_3N_4 and (b) KBH-C_3N_4.

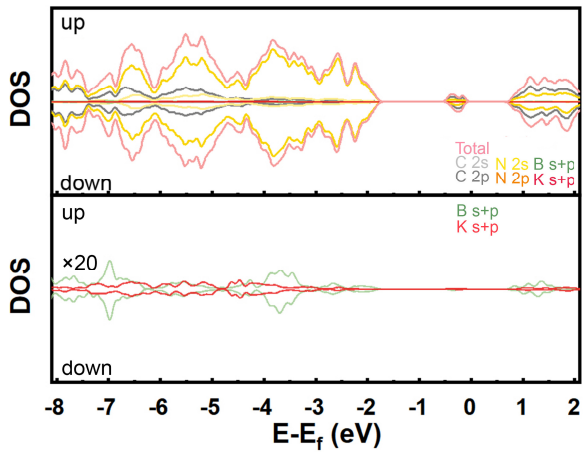

Figure 3.19. The original DOS and PDOS plot for KBH-C_3N_4 and the B s+p and K s+p orbitals enlarged by 20 times.

The CDD plots of KBH-C_3N_4 are presented here for illustrating spatial electron density changes originated from KBH modification. The difference was calculated using the pristine g-C_3N_4 and K atom alone as the references.[7, 50-52] As presented in **Figure 3.20**(a-c), light pink and pale green represent accumulation and depletion of electrons, respectively. **Figure 3.20**(b) shows a top view of CDD to gain an unambiguous view of the roles of N_v and B dopants. Both N_v and B will cause the electron-rich environment at their adjacent atoms. It is also worth mentioning the electron accumulation caused by N_v is stronger than B doping. This explains why N_v exhibits superior enhancement on CO_2 uptake than B doping. **Figure 3.20**(c) presents the side view and places a clear illustration of the electronic role of K dopant. The existence of K will alternate the electron spatial distribution significantly, especially for the adjacent layers. The surface layer of the supercell is relatively less affected (**Figure 3.20**(a)). When N atoms get close to K dopant, they exhibit an accumulation on the electron density, which agrees the formation of K-N chemical bonds as well as the electron donor role of K dopants. The electronic interaction between the K and adjacent layers could also make the electron transfer between layers possible. The calculation results further support our explanations on the emerging of K-N peaks in N 1s XPS spectra and the corresponding shifts due to chemical environment changes.

The AIM charge analyses (Bader analyses[53]) were calculated based on the charge density distribution and results of the surface layer are presented in **Figure 3.21**(a, b). It is worth mentioning that the extra electrons caused by N_v are only partially localized at the adjacent C atoms, which is likely due to the π-conjugated electronic structure and covalent bonds in layered g-C_3N_4. The B dopant shows a Δq (electron transfer) of -2.10 which donates ~0.8 more electron than the C atom in the pristine g-C_3N_4. And N atoms as the Lewis basic sites showing Δq of 1.37, which gains ~0.3 more electron than the N at the same site in pristine g-C_3N_4. As the confirmation of the electrons donating role, the K atom shows a Δq of -1.55. Orbital plots could be used to understand the electron transfer under the excitation. It has been reported that in pristine g-C_3N_4, the HOMO and LUMO are quite localized and in coplanar relation, which is responsible for the high recombination rate.[54] Different from the pristine g-C_3N_4, the HOMO and LUMO in KBH-C_3N_4 are not adjacent but localized mainly at N and C atoms of different layers of g-C_3N_4, as shown in **Figure 3.20**(d). It is in consistence with the PDOS plots (**Figure 3.19**(b)). The non-coplanar spatial relationship between the HOMO and LUMO could significantly benefit the electron/hole separation and ensure a relatively long carrier lifetime.[55] In summary, K acts to bridge the electron transfer between layers and B, N_v rearrange the electron and molecular orbitals spatial distributions. The multiple modifications all contribute to electron-rich sites and enhancement of the charge separation.[56]

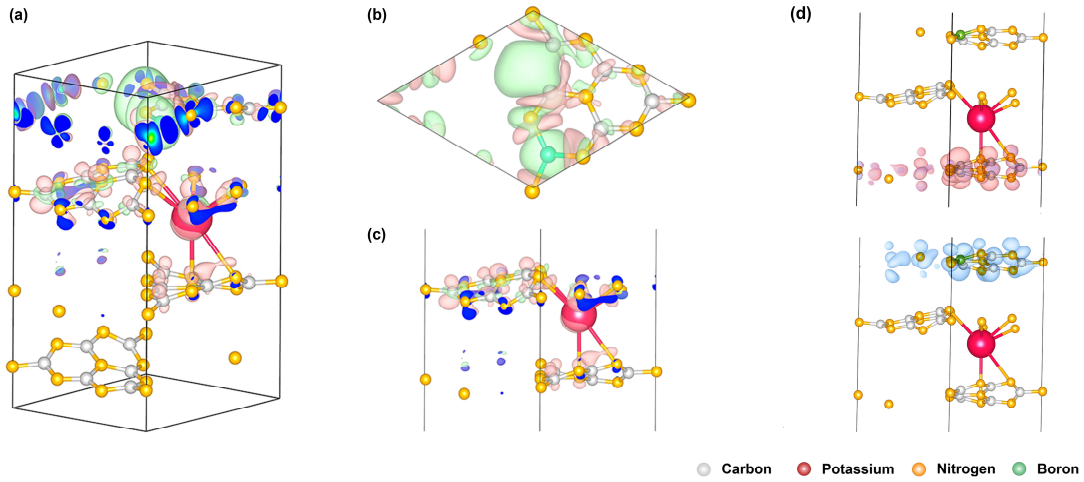

Figure 3.20. (a) Full, (b) top and (c) side views of charge density difference (CDD) plots of optimized KBH-C_3N_4. The pale pink represents the accumulation of electrons and the pale green the electron depletion. (d) The HOMO and LUMO for the KBH-C_3N_4. The pale pink indicates the HOMO and navy blue the LUMO. The density isosurface is set to 0.015 and 0.005 e Bohr^{-3} for CDD plot and molecular orbital plot respectively.

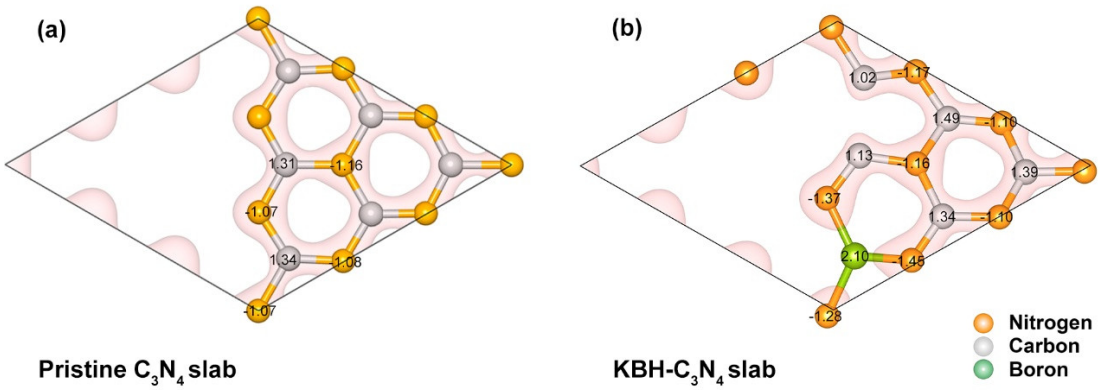

Figure 3.21. The scheme of (a) pristine C_3N_4 and (b) KBH-C_3N_4 slab surface layer with Bader charge analysis results. The isosurface density value is 0.2 e Bohr^{-3}.

3.3.2.2 CO_2 adsorption calculation

To rationalize the CO_2-TPD experimental results, the adsorption of CO_2 was calculated based on the slab models of both pristine g-C_3N_4 and KBH-C_3N_4. The optimal CO_2 adsorption site on pristine g-C_3N_4 has been comprehensively investigated in the literature[57] and CO_2 is believed to adsorb on N2 site of pristine g-C_3N_4, as shown in **Figure 3.22** (left side). The energy-favourable

CO_2 adsorption site on KBH-C_3N_4 is found to be above the interstitial site and the optimized configuration is presented in **Figure 3.22** (right side). It has been reported that the CO_2 adsorption on pristine g-C_3N_4 is only slightly thermodynamically favourable[7, 58] or even not spontaneous[59] based on the DFT calculations. Similarly, our CO_2 adsorption experiments also suggest a weak interaction between CO_2 and pristine g-C_3N_4 (**Figure 3.14**).[31, 60] The CO_2 adsorption energy is calculated with the following equation at different possible sites:

$$E_{ad} = E(\text{slab - } CO_2) - E(\text{slab}) - E(CO_2) \quad (3.8)$$

And a negative value suggests that the CO_2 adsorption is thermodynamically spontaneous. The calculated CO_2 adsorption energy on the most energy favourable site of pristine g-C_3N_4 is only -0.093 eV. However, the CO_2 adsorption on optimal site of KBH-C_3N_4 is a much more spontaneous process with the adsorption energy of -0.361 eV, which is 4 times as much as the pristine one. The Bader charge analyses further elucidate that 0.23 e^- is transferred from the KBH-C_3N_4 surface to the CO_2, which is much more remarkable than the neglectable electron transfer from the pristine slab (0.02 e^-). The accumulation of the electrons on the CO_2 will significantly enhance the activation and following conversion reactions.

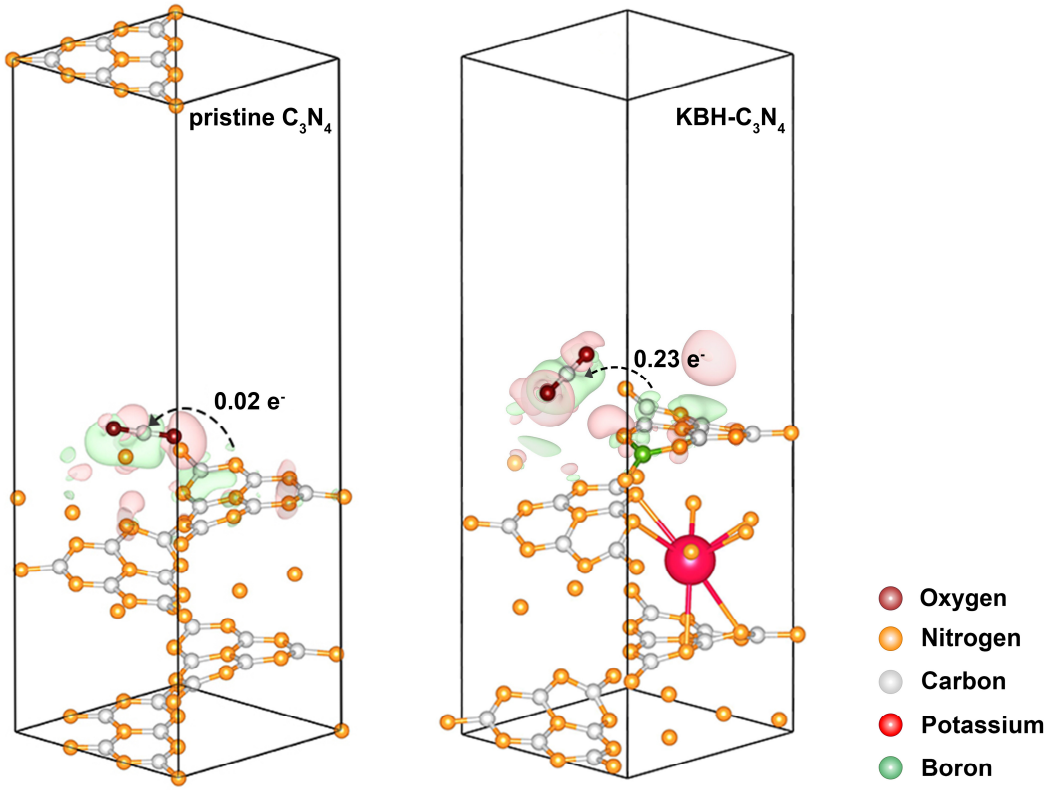

Figure 3.22. Configurations of CO_2 adsorption on pristine (left) and KBH-C_3N_4 (right) after optimization. Charge difference distribution of the optimized CO_2 adsorption on KBH-C_3N_4 slab (pink colour indicating the electron accumulation, green the depletion. Isosurface: 0.0003 e $Bohr^{-3}$). The number of electron transfer from absorbent to CO_2 are based on grid-based Bader calculation results.

3.3.3 Photocatalytic CO_2 reduction

Photocatalytic CO_2 reduction with H_2O was conducted over various modified samples under UV-Vis irradiation generated by a 300 W Xenon Arc lamp in a batch reactor. Controlled experiment in dark generated zero detectable products converted from CO_2. The finding suggests that CO_2 can be converted only under light irradiation. The products after 5-hour reaction time under UV-Vis light irradiation over pristine g-C_3N_4 and 1%, 3% 5% KBH-C_3N_4, respectively, are presented in **Figure 3.23**(a). As shown in the figure, CH_4 and CO are the main products over pristine and KBH modified g-C_3N_4. None of CH_3OH, HCOOH or HCHO is detected in the headspace. The pristine g-C_3N_4 shows a relatively low activity and only 3.69 and 0.6 μmol g^{-1} were produced for CH_4 and CO, respectively. All KBH modified samples exhibit higher

production rates than pristine g-C_3N_4. It is also worth noting that modification degree has an important effect on the catalyst performance. The 3% KBH-C_3N_4 is the best catalyst among the tested catalysts. It produces 5.93 and 3.16 μmol g^{-1} CH_4 and CO respectively after 5 h, which are 1.61 and 5.27 times of pristine g-C_3N_4 respectively. The other two samples produce 4.4 μmol g^{-1} CH_4, 1.25 μmol g^{-1} CO (1% KBH-C_3N_4) and 4.42 μmol g^{-1} CH_4, 1.08 μmol g^{-1} CO (5% KBH-C_3N_4) respectively after 5 h. It is noted that more CH_4 was produced comparing with CO for all catalysts. This is due to the fact that CO requires a higher reduction potential than CH_4, as described by the following equations (also illustrated in **Figure 3.10** and **Figure 3.11**) [61]:

$$CO_2+8H^++8e^-\rightarrow CH_4+2H_2O \text{ (E0 = -0.24 V vs. SHE, pH = 7)} \quad (3.9)$$

$$CO_2+2H^++2e^-\rightarrow CO+H_2O \text{ (E0 = -0.51 V vs. SHE, pH = 7)} \quad (3.10)$$

To further elucidate the correlation of different modification factors on catalytic performances, 3%K and 3%KB modified g-C_3N_4 were evaluated at the same reaction condition. As shown in **Figure 3.24**, the 3% K-C_3N_4 produced 4.61 μmol g^{-1} CH_4 after 5 h, while CO was not detected in the products. And 3% KB-C_3N_4 produces 0.93 μmol g^{-1} CO and 5.53 μmol g^{-1} CH_4. The better performance of 3% KB-C_3N_4 than 3% K-C_3N_4 could elucidate the role of B dopant in KBH-C_3N_4: facilitating the CO_2 activation. Since the CO production requires higher reduction potential as indicated by Equations (3.9) and (3.10), the higher CBM achieved by B dopants could compensate the side effects of K dopant and reach a better CO_2 conversion. The further improvement of both the CO and CH_4 production over 3% KBH-C_3N_4 than 3% KB-C_3N_4 testifies the enhancement brought by N_v.

To verify the stability of the catalysts, the 3%KBH-C_3N_4 was tested at the identical condition for 3 cycles and the CO and CH_4 production results are presented in **Figure 3.23**(b). After 3 cycles, the photocatalysts show only insignificant degradation in terms of the 5-h production, which only drops 9.3% and 8.5% in CH_4 and CO respectively. The experimental results exhibit a good stability for the 3%KBH-C_3N_4 in the CO_2 photocatalytic conversion reaction. To

figure out the reason of catalytic performance decrease after 15 h reaction. The powder after 15-h reaction was extracted from the reactor and dehydrated at 80 °C, vacuum overnight. Then FTIR transmission spectra for fresh and recycled ones are compared in **Figure 3.25**. As could be interpreted in **Figure 3.25**, the peaks centred at 1622, 3423 and 3122 cm^{-1} slightly increase in intensity. All these 3 peaks could be attributed to -NH groups.[62-63] It could be possibly due to the H chemisorbed on the N sites forming N-H bonds during the H_2O splitting. Considering the surface defects and dangling bonds on the surface of KBH-C_3N_4 are also the active sites, the H intends to saturate the dangling bonds and block the Lewis basic sites. Moreover, this specific chemical environment makes the combination of two adsorbed H^* generating H_2 suffer from a high energy barrier. Therefore, the photocatalytic performances exhibit a slight decrease due to partial blocking of the active sites. The rise of H concentration has also been found in defective C_3N_{4-x} prepared via H_2 treatment in the literature.[30, 64]

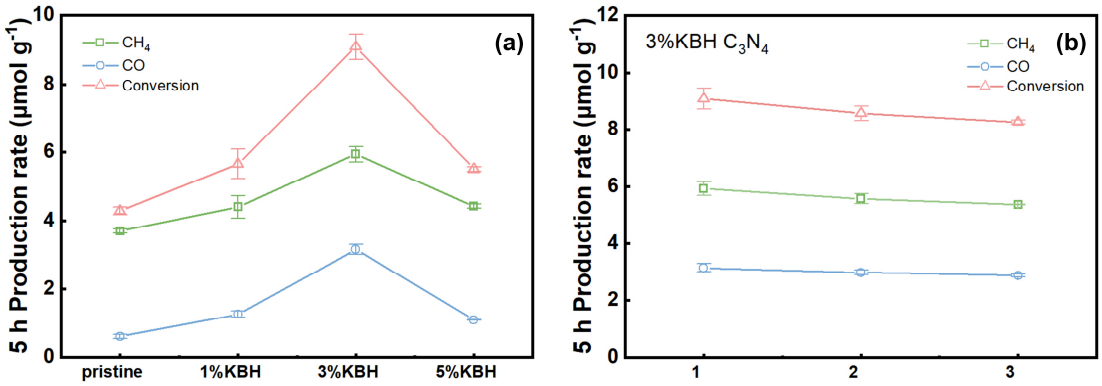

Figure 3.23. (a) 5-h production of CO, CH_4 and total conversion of CO_2 on pristine C_3N_4, 1% KBH-C_3N_4, 3% KBH-C_3N_4 and 5% KBH-C_3N_4 using CO_2 and H_2O as feedstock under the irradiation of UV-Vis light. (b) 5h production of CO and CH_4 and total conversion of CO_2 in the stability tests of 3%KBH-C_3N_4 in 3 cycles.

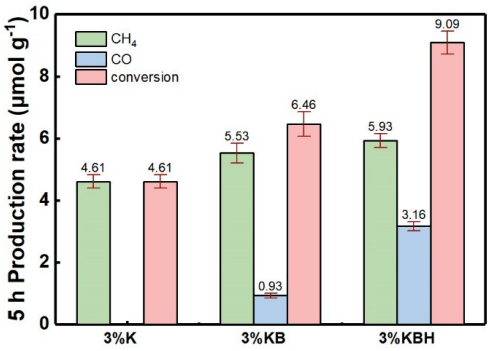

Figure 3.24. 5-h production of photocatalytic CO_2 conversion with water over the control group photocatalysts.

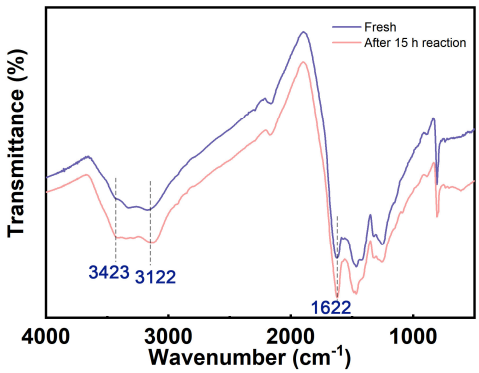

Figure 3.25. The FTIR spectra of as-prepared fresh 3% KBH-C_3N_4 and after 15 h photocatalytic CO_2 reduction with water.

3.3.4 Mechanism investigation via *in-situ* DRIFTS

In-situ DRIFTS is used to elucidate the reaction intermediate species and reaction mechanism. The spectra recorded under both dark and UV-Vis light irradiation are presented in **Figure 3.26**(a, b) for pristine g-C_3N_4 and 3%KBH-C_3N_4 respectively. To ensure the intensity of the peaks rationally comparable between these two spectra, the absorbances are normalized based on the peak intensity of gaseous CO_2 (2350 cm^{-1}). Thus, it rules out the influences of experimental setups. Before the reaction, all the sample surfaces were cleaned with flowing Ar at the temperature of 300 °C for 30 min. After cooling down to room temperature, CO_2/H_2O was introduced with Ar as the balance gas into the reactor. CO_2 are generally adsorbed on the surface in the form of

carbonate and bicarbonate with the presence of moisture. After exposing the CO_2/H_2O vapour to pristine g-C_3N_4 and KBH-C_3N_4 under dark for 20 min, the following species are observed on the surface: monodentate carbonate (m-CO_3^{2-}, 1546-1547, 1464-1466),[65-66] bidentate carbonate (b-CO_3^{2-}, 1701, 1688, 1352 cm^{-1}),[7, 65-69] polydentate carbonate (p-CO_3^{2-} 1601 cm^{-1})[70-71] and bicarbonate (HCO_3^- 1397, 1304 cm^{-1}).[66] The 1650 cm^{-1} peak is assigned to water adsorbed on the surface.[7] It is noted that all these carbonate peaks are much higher on the surface of 3% KBH-C_3N_4 than the pristine one. It is due to the fact that 3% KBH-C_3N_4 has stronger CO_2 adsorption ability than pristine g-C_3N_4, which is in agreement with the CO_2-TPD experiments and DFT calculation results discussed earlier.

When reaching equilibrium in dark, UV-Vis light was then irradiated on the catalysts with a power density of ~40.3 mW cm^{-2} using an optical liquid light guide coupled Xenon lamp. After irradiation for 60 min, new peaks centred at 1521, 1670 and 1755 cm^{-1} emerged significantly, which are assigned to formate, CO_2^- and carbonyl species on both pristine and 3% KBH-C_3N_4.[31, 65, 72] Along with the appearance of these new peaks, the CO_3^{2-} adsorption, centred at 1701, 1688, 1546-1547 cm^{-1}, significantly increase over both catalysts. The rise of carbonate adsorption peak under UV-Vis irradiation suggests the carbonate species could be the primary reaction intermediates. More importantly, it is worth pointing out that the 3% KBH-C_3N_4 is capable to generate more anionic CO_2^- than the pristine g-C_3N_4 under UV-Vis light irradiation. Being an intermediate species generated via direct CO_2 photocatalytic activation, CO_2^- is very active and tends to react, via self-reaction or a proton-coupled electron, to CO, CO_3^{2-} and HCOOH. The generation of CO_2^- is usually believed as the RDS due to its high reduction potential required (-1.90 eV vs SHE).[61] More importantly, electron-rich catalysts surface is usually indispensable for its generation.[73] A correlation between the concentration of CO_2^- and photocatalytic CO_2 conversion rate of TiO_2 was reported in the literature.[73-74] In our case, a positive correlation (correlation coefficient = 0.988) has been found between the CO_2^- band intensity increments of *in-situ* DRIFT spectra after 60 min UV-Vis irradiation

and total CO_2 conversion after 5 h (**Figure 3.28**). It suggests the CO_2^- is the key intermediate determining photocatalytic CO_2 reduction rate on pristine and KBH-C_3N_4. The DRIFT spectra of 1%-KBH and 5%-KBH C_3N_4 are presented in **Figure 3.27**(a, b). It is worth emphasizing that the larger amount of CO_2^- generated on the surface of KBH-C_3N_4 should be attributed to the higher basicity of the surface. And the excess electron brought by N_V is believed to make the greatest contribution. Above discussion is also supported by the theoretical calculation results that the KBH-C_3N_4 contains electron-rich surface sites and more electron could transfer from KBH-C_3N_4 to CO_2 (**Figure 3.22**).

In summary, the major reaction intermediates observed in this work are CO_2^-, HCO_3^-, CO_3^{2-} and $HCOO^*$ on both pristine g-C_3N_4 and 3% KBH-C_3N_4 catalysts. A higher photocatalytic CO_2 conversion rate should be ascribed to the higher efficiency of CO_2^- species generation on 3% KBH-C_3N_4 than the pristine counterpart.

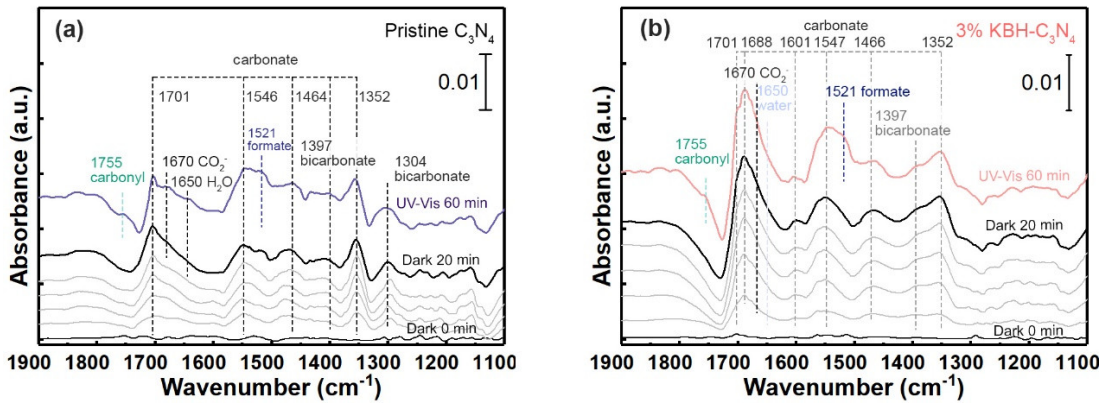

Figure 3.26. DRIFT spectra of (a) pristine g-C_3N_4 and (b) 3% KBH-C_3N_4 with CO_2/H_2O under dark for 20 min and UV-Vis irradiation for another 60 min.

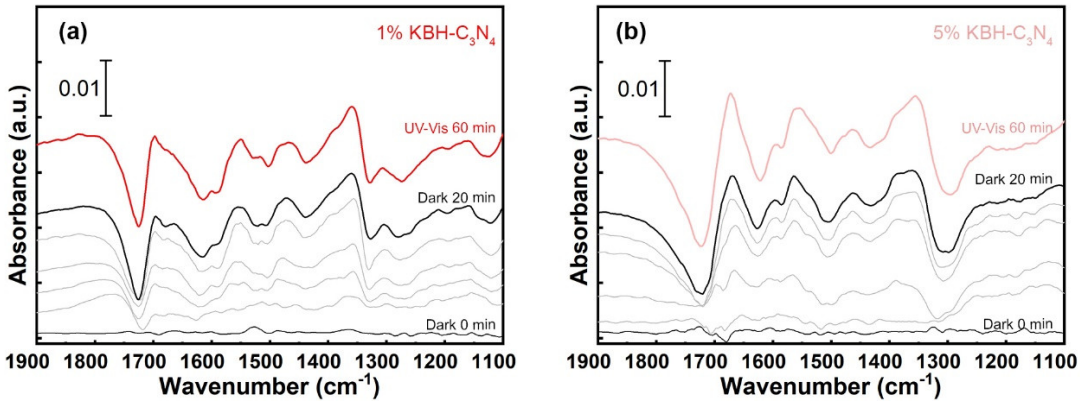

Figure 3.27. DRIFT spectra of (a) 1% and (b) 5% KBH-C_3N_4 with CO_2/H_2O under dark for 20 min and UV-Vis irradiation for another 60 min.

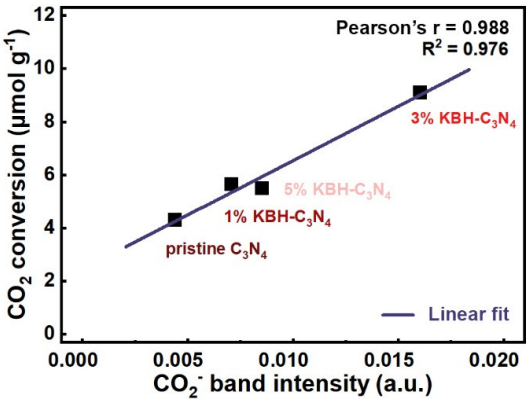

Figure 3.28. Correlation between 5-h photocatalytic CO_2 conversion and the CO_2^- band increments in DRIFT spectra.

To support the argument that formate is an intermediate for CO and CH_4 production, additional control experiment of photocatalytic reduction of 5%v/v formic acid aqueous solution on the 3% KBH-C_3N_4 has been conducted in the absence of CO_2 atmosphere. 0.1 g catalysts were loaded on a borosilicate glass filter and placed inside the reactor. Then 0.8 mL 5%v/v formic acid aqueous solution was added into the reactor. Flowing He (20 sccm) was used to purge the reactor for 30 min to get rid of air. Then the UV-Vis light was turned on for 30 min. 500 μL gaseous mixture was withdrawn with a gastight syringe for GC analyses after reaction and the corresponding chromatograph was presented as **Figure 3.29**. The main products of HCOOH photocatalytic

reduction with water are CO_2 and H_2, which is known in the dehydrogenation of formic acid process.[75-76] Meanwhile, the CO and CH_4 were also detected which could support the argument that formic acid/formate is the possible reaction intermediate for CO and CH_4 production. And the CO generated from formate decomposition could also act as the intermediate for CH_4 production via the carbene pathway (equations (3.19) to (3.23)).[77-78] Finally, the possible mechanism of CO_2 photocatalytic conversion with H_2O on 3% KBH-C_3N_4 could be expressed by the following equations:

$$H_2O + h^+ \rightarrow H^+ + {}^*OH \tag{3.11}$$

$$CO_2 + H_2O \rightarrow 2H^+ + CO_3^{2-} \tag{3.12}$$

$$CO_2 + e^- \rightarrow CO_2^- \tag{3.13}$$

$$CO_2^- + {}^*OH \rightarrow HCO_3^- \tag{3.14}$$

$$CO_2^- + CO_2^- \rightarrow CO + CO_3^{2-} \tag{3.15}$$

$$CO_2^- + 2H^+ + e^- \rightarrow HCOOH \tag{3.16}$$

$$CO_2^- + H^+ + e^- \rightarrow CO + OH^- \tag{3.17}$$

$$HCOO^* \rightarrow CO + {}^*OH \tag{3.18}$$

$${}^*CO + H^+ + e^- \rightarrow {}^*C + {}^*OH \tag{3.19}$$

$${}^*C + H^+ + e^- \rightarrow {}^*CH \tag{3.20}$$

$${}^*CH + H^+ + e^- \rightarrow {}^*CH_2 \tag{3.21}$$

$${}^*CH_2 + H^+ + e^- \rightarrow {}^*CH_3 \tag{3.22}$$

$${}^*CH_3 + H^+ + e^- \rightarrow CH_4 \tag{3.23}$$

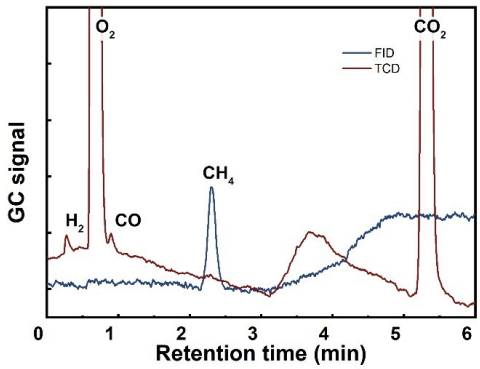

Figure 3.29. The gas chromatograph of products in HCOOH decomposition control experiment.

3.4 Summary

In this chapter, a new g-C_3N_4 optimization strategy combining B, K co-doping and N_V has been developed. An electron-rich surface that remarkably enhances the CO_2 adsorption and activation has been achieved. In addition, K, B co-doping and N_V introduction in g-C_3N_4 is prepared by a facile one-step method. The specific role of each modification element has been carefully investigated and the synergistic effects are observed. K acts as the electron donor and facilitates the electron transfers between the layers; N_V contributes the most to the CO_2 adsorption enhancement and basicity; B helps to maintain a high reduction potential and compensates the drawbacks of the K; N_V acts in lowering the CBM as well as in promoting CO_2 adsorption. The synergistic effects of multiple modifications synergistically achieve a 5-h production of 5.93 μmol g^{-1} CH_4 and 3.16 μmol g^{-1} CO, respectively, using CO_2 and H_2O without organic hole scavengers. It is 161% and 527% of the production over pristine g-C_3N_4 at the identical condition. The significantly improved CO_2 photocatalytic conversion performance of the catalysts approve the validity of the proposed new strategy: combination of doping and N_V introduction with careful consideration of the synergistic effects between the modification elements. More importantly, the selection of co-modification factors is rationalized. The prepared transition metal-free KBH-C_3N_4 shows great performance as a candidate for photocatalytic solar fuel production and CO_2 control.

3.5 References

1. Wang, K.; Fu, J.; Zheng, Y., *Appl. Catal., B* **2019,** 254, 270-282.
2. Wang, X.; Maeda, K.; Thomas, A.; Takanabe, K.; Xin, G.; Carlsson, J. M.; Domen, K.; Antonietti, M., *Nat. Mater.* **2009,** 8 (1), 76-80.
3. Ong, W. J.; Tan, L. L.; Ng, Y. H.; Yong, S. T.; Chai, S. P., *Chem. Rev.* **2016,** 116 (12), 7159-7329.
4. Wang, X.; Blechert, S.; Antonietti, M., *ACS Catal.* **2012,** 2 (8), 1596-1606.
5. Cao, S.; Li, H.; Tong, T.; Chen, H.-C.; Yu, A.; Yu, J.; Chen, H. M., *Adv. Funct. Mater.* **2018,** 28 (32), 1802169.
6. Sun, Z.; Wang, S.; Li, Q.; Lyu, M.; Butburee, T.; Luo, B.; Wang, H.; Fischer, J. M. T. A.; Zhang, C.; Wu, Z.; Wang, L., *Adv. Sustainable Syst.* **2017,** 1 (3-4), 1700003.
7. Sun, Z.; Fischer, J. M. T. A.; Li, Q.; Hu, J.; Tang, Q.; Wang, H.; Wu, Z.; Hankel, M.; Searles, D. J.; Wang, L., *Appl. Catal., B* **2017,** 216, 146-155.
8. Giannozzi, P.; Baroni, S.; Bonini, N.; Calandra, M.; Car, R.; Cavazzoni, C.; Ceresoli, D.; Chiarotti, G. L.; Cococcioni, M.; Dabo, I.; Dal Corso, A.; de Gironcoli, S.; Fabris, S.; Fratesi, G.; Gebauer, R.; Gerstmann, U.; Gougoussis, C.; Kokalj, A.; Lazzeri, M.; Martin-Samos, L.; Marzari, N.; Mauri, F.; Mazzarello, R.; Paolini, S.; Pasquarello, A.; Paulatto, L.; Sbraccia, C.; Scandolo, S.; Sclauzero, G.; Seitsonen, A. P.; Smogunov, A.; Umari, P.; Wentzcovitch, R. M., *J. Phys.: Condens. Matter* **2009,** 21 (39), 395502.
9. Giannozzi, P.; Andreussi, O.; Brumme, T.; Bunau, O.; Buongiorno Nardelli, M.; Calandra, M.; Car, R.; Cavazzoni, C.; Ceresoli, D.; Cococcioni, M.; Colonna, N.; Carnimeo, I.; Dal Corso, A.; de Gironcoli, S.; Delugas, P.; DiStasio, R. A.; Ferretti, A.; Floris, A.; Fratesi, G.; Fugallo, G.; Gebauer, R.; Gerstmann, U.; Giustino, F.; Gorni, T.; Jia, J.; Kawamura, M.; Ko, H. Y.; Kokalj, A.; Kucukbenli, E.; Lazzeri, M.; Marsili, M.; Marzari, N.; Mauri, F.; Nguyen, N. L.; Nguyen, H. V.; Otero-de-la-Roza, A.; Paulatto, L.; Ponce, S.; Rocca, D.; Sabatini, R.; Santra, B.; Schlipf, M.; Seitsonen, A. P.; Smogunov, A.; Timrov, I.; Thonhauser, T.; Umari, P.; Vast, N.; Wu, X.; Baroni, S., *J. Phys.: Condens. Matter* **2017,** 29 (46), 465901.
10. Dal Corso, A., *Comput. Mater. Sci.* **2014,** 95, 337-350.
11. Kresse, G.; Joubert, D., *Phys. Rev. B* **1999,** 59 (3), 1758-1775.
12. Blochl, P. E., *Phys Rev B* **1994,** 50 (24), 17953-17979.
13. Perdew, J. P.; Burke, K.; Ernzerhof, M., *Phys. Rev. Lett.* **1996,** 77 (18), 3865-3868.
14. Heyd, J.; Scuseria, G. E.; Ernzerhof, M., *J. Chem. Phys.* **2003,** 118 (18), 8207-8215.
15. Krukau, A. V.; Vydrov, O. A.; Izmaylov, A. F.; Scuseria, G. E., *J. Chem. Phys.* **2006,** 125 (22), 224106.
16. Grimme, S.; Antony, J.; Ehrlich, S.; Krieg, H., *J. Chem. Phys.* **2010,** 132 (15), 154104.
17. Momma, K.; Izumi, F., *J. Appl. Crystallogr.* **2011,** 44 (6), 1272-1276.
18. Cui, W.; Li, J.; Cen, W.; Sun, Y.; Lee, S. C.; Dong, F., *J. Catal.* **2017,** 352, 351-360.
19. Xiong, T.; Cen, W.; Zhang, Y.; Dong, F., *ACS Catal.* **2016,** 6 (4), 2462-2472.
20. Li, Y.; Xu, H.; Ouyang, S.; Lu, D.; Wang, X.; Wang, D.; Ye, J., *J. Mater. Chem. A* **2016,** 4 (8), 2943-2950.
21. Yu, H.; Shi, R.; Zhao, Y.; Bian, T.; Zhao, Y.; Zhou, C.; Waterhouse, G. I. N.; Wu, L. Z.; Tung, C. H.; Zhang, T., *Adv. Mater.* **2017,** 29 (16), 1605148.
22. Ong, W.-J.; Putri, L. K.; Tan, Y.-C.; Tan, L.-L.; Li, N.; Ng, Y. H.; Wen, X.; Chai, S.-P., *Nano Res.* **2017,** 10 (5), 1673-1696.
23. Samanta, S.; Martha, S.; Parida, K., *ChemCatChem* **2014,** 6, 1453-1462.
24. Niu, P.; Yin, L. C.; Yang, Y. Q.; Liu, G.; Cheng, H. M., *Adv. Mater.* **2014,** 26 (47), 8046-8052.

25. Zhu, J.; Diao, T.; Wang, W.; Xu, X.; Sun, X.; Carabineiro, S. A. C.; Zhao, Z., *Appl. Catal., B* **2017,** 219, 92-100.
26. Wang, Y.; Li, H.; Yao, J.; Wang, X.; Antonietti, M., *Chem. Sci.* **2011,** 2 (3), 446-450.
27. Li, P.; Li, H.; Pan, X.; Tie, K.; Cui, T.; Ding, M.; Bao, X., *ACS Catal.* **2017,** 7 (12), 8572-8577.
28. Sharma, J.; Gora, T.; Rimstidt, J. D.; Staley, R., *Chem. Phys. Lett.* **1972,** 15 (2), 232-235.
29. Wang, K.; Zhou, C.; Xi, D.; Shi, Z.; He, C.; Xia, H.; Liu, G.; Qiao, G., *Nano Energy* **2015,** 18, 1-11.
30. Tay, Q.; Kanhere, P.; Ng, C. F.; Chen, S.; Chakraborty, S.; Huan, A. C. H.; Sum, T. C.; Ahuja, R.; Chen, Z., *Chem. Mater.* **2015,** 27 (14), 4930-4933.
31. Xia, P.; Zhu, B.; Yu, J.; Cao, S.; Jaroniec, M., *J. Mater. Chem. A* **2017,** 5 (7), 3230-3238.
32. Fang, W.; Liu, J.; Yu, L.; Jiang, Z.; Shangguan, W., *Appl. Catal., B* **2017,** 209, 631-636.
33. Hu, S.; Li, F.; Fan, Z.; Wang, F.; Zhao, Y.; Lv, Z., *Dalton Trans.* **2015,** 44 (3), 1084-1092.
34. Ding, K.; Wen, L.; Huang, M.; Zhang, Y.; Lu, Y.; Chen, Z., *Phys. Chem. Chem. Phys.* **2016,** 18 (28), 19217-19226.
35. Ruan, Q.; Luo, W.; Xie, J.; Wang, Y.; Liu, X.; Bai, Z.; Carmalt, C. J.; Tang, J., *Angew. Chem., Int. Ed.* **2017,** 56 (28), 8221-8225.
36. Trasatti, S., *Pure Appl. Chem.* **1986,** 58 (7), 955-966.
37. Hong, Z.; Shen, B.; Chen, Y.; Lin, B.; Gao, B., *J. Mater. Chem. A* **2013,** 1 (38), 11754-11761.
38. Jorge, A. B.; Martin, D. J.; Dhanoa, M. T. S.; Rahman, A. S.; Makwana, N.; Tang, J.; Sella, A.; Corà, F.; Firth, S.; Darr, J. A.; McMillan, P. F., *J. Phys. Chem. C* **2013,** 117 (14), 7178-7185.
39. Walsh, J. J.; Jiang, C.; Tang, J.; Cowan, A. J., *Phys. Chem. Chem. Phys.* **2016,** 18 (36), 24825-24829.
40. Hattori, H., *Chem. Rev.* **2002,** 95 (3), 537-558.
41. Park, H.; Lee, J. H.; Kim, E. H.; Kim, K. Y.; Choi, Y. H.; Youn, D. H.; Lee, J. S., *Chem. Commun.* **2016,** 52 (99), 14302-14305.
42. Song, S.; Lu, C.; Wu, X.; Jiang, S.; Sun, C.; Le, Z., *Appl. Catal., B* **2018,** 227, 145-152.
43. Tian, J.; Zhang, L.; Fan, X.; Zhou, Y.; Wang, M.; Cheng, R.; Li, M.; Kan, X.; Jin, X.; Liu, Z.; Gao, Y.; Shi, J., *J. Mater. Chem. A* **2016,** 4 (36), 13814-13821.
44. Wei, J.; Shen, W.; Zhao, J.; Zhang, C.; Zhou, Y.; Liu, H., *Catal. Today* **2018,** 316, 199-205.
45. Li, D.; Ichikuni, N.; Shimazu, S.; Uematsu, T., *Appl. Catal., A* **1998,** 172 (2), 351-358.
46. Guo, Y.; Liu, Q.; Li, Z.; Zhang, Z.; Fang, X., *Appl. Catal., B* **2018,** 221, 362-370.
47. Thomas, A.; Fischer, A.; Goettmann, F.; Antonietti, M.; Müller, J.-O.; Schlögl, R.; Carlsson, J. M., *J. Mater. Chem.* **2008,** 18 (41), 4893-4908.
48. Zhu, B.; Zhang, L.; Cheng, B.; Yu, J., *Appl. Catal., B* **2018,** 224, 983-999.
49. Tan, D.; Zhang, X.; Li, J.; Tan, H.; Fu, Q., *Appl. Surf. Sci.* **2012,** 258 (7), 2697-2706.
50. Genisel, M. F.; Uddin, M. N.; Say, Z.; Kulakci, M.; Turan, R.; Gulseren, O.; Bengu, E., *J. Appl. Phys.* **2011,** 110 (7).
51. Huang, Z.-F.; Song, J.; Pan, L.; Wang, Z.; Zhang, X.; Zou, J.-J.; Mi, W.; Zhang, X.; Wang, L., *Nano Energy* **2015,** 12, 646-656.
52. Maiti, D.; Daza, Y. A.; Yung, M. M.; Kuhn, J. N.; Bhethanabotla, V. R., *J. Mater. Chem. A* **2016,** 4 (14), 5137-5148.
53. Henkelman, G.; Arnaldsson, A.; Jónsson, H., *Comput. Mater. Sci.* **2006,** 36 (3), 354-360.
54. Ma, X.; Lv, Y.; Xu, J.; Liu, Y.; Zhang, R.; Zhu, Y., *J. Phys. Chem. C* **2012,** 116 (44), 23485-23493.
55. Fukuzumi, S.; Kotani, H.; Ohkubo, K.; Ogo, S.; Tkachenko, N. V.; Lemmetyinen, H., *J. Am. Chem. Soc.* **2004,** 126 (6), 1600-1601.
56. Liu, C.; Huang, H.; Cui, W.; Dong, F.; Zhang, Y., *Appl. Catal., B* **2018,** 230, 115-124.
57. Zhu, B.; Zhang, L.; Xu, D.; Cheng, B.; Yu, J., *J. CO2 Util.* **2017,** 21, 327-335.

58. Ji, Y.; Dong, H.; Lin, H.; Zhang, L.; Hou, T.; Li, Y., *RSC Adv.* **2016,** 6 (57), 52377-52383.
59. Azofra, L. M.; MacFarlane, D. R.; Sun, C., *Phys. Chem. Chem. Phys.* **2016,** 18 (27), 18507-18514.
60. Fu, J.; Zhu, B.; Jiang, C.; Cheng, B.; You, W.; Yu, J., *Small* **2017,** 13 (15), 1603938.
61. Chang, X.; Wang, T.; Gong, J., *Energy Environ. Sci.* **2016,** 9 (7), 2177-2196.
62. Wei, X.; Qiu, Y.; Duan, W.; Liu, Z., *RSC Adv.* **2015,** 5 (34), 26675-26679.
63. Marchewka, M. K., *Mater. Sci. Eng., B* **2002,** 95 (3), 214-221.
64. Ho, W.; Zhang, Z.; Xu, M.; Zhang, X.; Wang, X.; Huang, Y., *Appl. Catal., B* **2015,** 179, 106-112.
65. Cao, S.; Li, Y.; Zhu, B.; Jaroniec, M.; Yu, J., *J. Catal.* **2017,** 349, 208-217.
66. Di, T.; Zhu, B.; Cheng, B.; Yu, J.; Xu, J., *J. Catal.* **2017,** 352, 532-541.
67. Liu, Q.; Mace, A.; Bacsik, Z.; Sun, J.; Laaksonen, A.; Hedin, N., *Chem. Commun.* **2010,** 46 (25), 4502-4504.
68. Schwertmann, L.; Grünert, A.; Pougin, A.; Sun, C.; Wark, M.; Marschall, R., *Adv. Funct. Mater.* **2015,** 25 (6), 905-912.
69. Liu, S.; Chen, F.; Li, S.; Peng, X.; Xiong, Y., *Appl. Catal., B* **2017,** 211, 1-10.
70. Ricca, C.; Grishin, A.; Ringuedé, A.; Cassir, M.; Adamo, C.; Labat, F., *J. Mater. Chem. A* **2016,** 4 (44), 17473-17482.
71. Dai, Y.; Wu, X. P.; Tang, Y.; Yang, Y.; Gong, X. Q.; Fan, J., *Chem. Commun.* **2016,** 52 (13), 2827-2830.
72. Wilfong, W. C.; Srikanth, C. S.; Chuang, S. S., *ACS Appl. Mater. Interfaces* **2014,** 6 (16), 13617-13626.
73. Liu, L.; Zhao, H.; Andino, J. M.; Li, Y., *ACS Catal.* **2012,** 2 (8), 1817-1828.
74. Yin, G.; Huang, X.; Chen, T.; Zhao, W.; Bi, Q.; Xu, J.; Han, Y.; Huang, F., *ACS Catal.* **2018,** 8 (2), 1009-1017.
75. Enthaler, S.; von Langermann, J.; Schmidt, T., *Energy Environ. Sci.* **2010,** 3 (9), 1207-1217.
76. Wang, X.; Meng, Q.; Gao, L.; Jin, Z.; Ge, J.; Liu, C.; Xing, W., *Int. J. Hydrogen Energy* **2018,** 43 (14), 7055-7071.
77. Anpo, M.; Yamashita, H.; Ichihashi, Y.; Ehara, S., *J. Electroanal. Chem.* **1995,** 396 (1), 21-26.
78. Tan, S. S.; Zou, L.; Hu, E., *Catal. Today* **2008,** 131 (1-4), 125-129.

Chapter 4. Photocatalytic CO_2 Reduction with H_2O over Au/TiO_{2-x}: Mechanism for Higher Hydrocarbon Production

This work has been published as *Applied Catalysis, B: Environmental* **2021,** 292, 120147.[1] It was written by the author of present thesis. This chapter is reproduced from the original paper with some modifications.

4.1 Introduction

As mentioned in previous chapters, documented researches have been primarily focused on the development of new photocatalysts with high efficiency in CO_2 photocatalytic conversion with H_2O. However, most of the works in the literature on photocatalytic CO_2 reduction with H_2O can only produce less valuable products including CO, CH_4, HCOOH etc. Increasing the selectivity to higher value-added products is one of the main challenges. The CO_2 photocatalytic conversion mechanism is less investigated and still ambiguous.[2] The lack of mechanism understanding significantly hinders the further development of photocatalysts with both high activity and controllable product selectivity.[3]

In this chapter, the CO_2 photocatalytic reduction with H_2O is investigated on oxygen-deficient Au/TiO_{2-x} catalyst under continuous flow condition. The reaction rate and product selectivity have been compared over Au/TiO_{2-x} with different Au NP sizes and UV or visible light excitation mechanisms. With the involvement of V_O and plasmonic excitation under green light irradiation, a maximum 20% selectivity to C_2H_6 is achieved over 2.76wt% Au/TiO_{2-x}.

Moreover, the mechanism of CO_2 photocatalytic reduction with water on Au/TiO_{2-x} is investigated via the *in-situ* DRIFTS technique. The plausible key C-C coupling mechanism is proposed based on the experimental observation of *in-situ* DRIFTS, *in-situ* determined electronic property of Au at excitation state and the important role of V_O. The reason for higher selectivity towards C_2H_6 is rationalized. In addition, the correlation between V_O and CO_2 conversion rate is further elucidated via *in-situ* UV-Vis spectroscopy.

4.2 Experimental

4.2.1 *In-situ* DRIFTS and UV-Vis DRS experiments

The setup for the *in-situ* DRIFTS/UV-Vis DRS analyses is described in Section 2.1.2. The commercial praying mantis mirror set and high temperature reaction chamber (Harrick Scientific) were used as the *in-situ* reactor. The FTIR, (Shimadzu, IRTracer-100) and UV-Vis spectrophotometer (Shimazu, UV-3600plus) were used to provide the spectroscopic analyses. The Ar purging and reactive gas lines were connected to a 4-way switching valve to ensure a fast switch between purging and reactive gases. All the gases used in the experiments are controlled by the independent mass flow controllers. The gas flow rate is regularly calibrated with an electronic flow meter (Agilent ADM1000). Pretreatment of the Au/TiO_2 was conducted every time before the experiments. Firstly, the powders were calcinated under flowing Air (20 sccm) for 30 min at 300 °C to remove any residual C on the surface of the catalysts. Then the reactor was purged with Ar (20 sccm) and treated at 300 °C for another 60 min. This series of pretreatments have been reported capable of removing the surface contaminants/carbon residuals as much as possible.[4] The similar pretreatments were also conducted with 20% H_2 (balanced with Ar) or O_2 for control group samples. The corresponding samples after pretreatments under flowing Ar, H_2 or O_2 atmosphere are named as Au/TiO_2(Ar), Au/TiO_2(H), and Au/TiO_2(O), respectively. The samples were directly used after calcination at 400 ^oC in air without any pretreatment are marked as Au/TiO_2(UP).

The photocatalytic CO_2 reduction with H_2O reaction at 30 °C was simulated by introducing 1 v/v% CO_2 balanced by Ar into reactor. The moisture was introduced into the DRIFTS reactor with the independent gas line with Ar (0.5 sccm) as the carrier gas flowing through the water bubbler at 25 °C. The total flow rate under all circumstances was controlled to 20 sccm by adjusting the balance Ar flow rate. The partial pressure of H_2O vapour (P_{H_2O}) inside the bubbler can be calculated via the Antoine equation (Equation (2.5)). The composition of the feed gas into the DRIFTS reactor is calculated to be ~1 v/v% CO_2, ~0.078 v/v% $H_2O_{(g)}$ balanced in Ar. The UV (365nm) or green (530 nm) light was provided by the LED lamps coupled with an optical liquid guide (Thorlabs) and shed onto the catalysts surface through the quartz window. For DRIFTS experiments, the background was collected after the Ar treated sample cooling down to room temperature. 64 scans were averaged to achieve a good signal to noise ratio. In UV-Vis DRS experiments, the background was collected using $BaSO_4$ powders. Since the external light interferes with UV-Vis DRS analyses, the *in-situ* UV-Vis absorbance curves were recorded every 0.5 h with external light blocked temporally.

4.2.2 Evaluation of photocatalytic CO_2 reduction performance

The photocatalytic CO_2 reduction with H_2O performance was evaluated using the flow reactor illustrated in **Figure 4.1**. 50 mg photocatalysts were homogeneously dispersed on the glass fibre filter (47mm, Fisher Scientific, UK) using vacuum filtration method. The actual loading of catalysts is determined by calculating the weight difference before and after loading 50 mg catalysts onto the glass fibre filter. The average actual loading is 47.39±0.58 mg with a small deviation of 1.2%. The whole piece of filter was transferred to the bottom of the reactor and the reactor was sealed with a UV-grade fused silica window. Before the reaction, the reactor was firstly purged by flowing Ar (30sccm) for 1 h with the mass flow controller to completely remove air from the reactor. Then a band heater (Omega Engineering, UK) was used to heat the whole reactor to 300 °C and soaked for 30 min under the control of a PID temperature controller. After cooling down to 30 °C, the inlet gas was switched to the CO_2

(3 sccm) flowing through the water bubbler under controlled temperature (25 °C). According to Antoine equation, the feed gas mixture is composed by ~3.1 v/v% $H_2O_{(g)}$ and ~96.9 v/v% CO_2. The UV or visible light was provided by a 365 nm or 530 nm LED light module (50W, EPILED Ltd.), respectively. The power outputs at the plane of the catalysts were tested to be ~49.5 and 64.9 mW cm^{-2} using a thermopile optical power meter (PM16-401, Thorlabs). The products of the reaction were collected every 0.5 hours and analysed by a GC (Shimadzu GC-2010) equipped with a Shincarbon-ST micropacked column using TCD-FID detectors. Products in isotopic labelling experiment with $^{13}CO_2$ as feedstock were analysed with a GC-MS (Shimadzu, GCMS-QP2010SE).

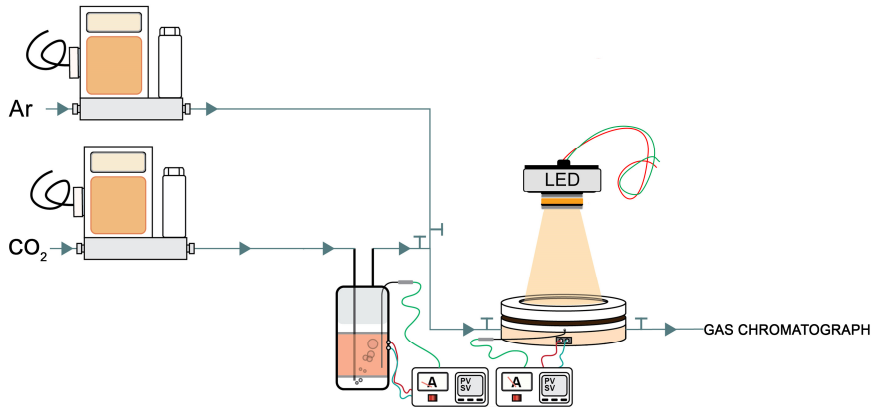

Figure 4.1. Scheme of reaction setup for photocatalytic CO_2 reduction with H_2O.

4.2.3 Theoretical calculation

The calculation is conducted at GGA-PBE+U level with Grimm-D3 correction using Quantum Espresso package.[5-6] Effective Hubbard U_{eff}= 4.2 eV[7-9] is added to Ti 3d electrons to correctly describe the electronic structure of TiO_2. The nuclei and core-electrons are represented with ultrasoft pseudopotentials in "GBRV" library.[10] 45 and 450 Ry for kinetic energy and wavefunction cutoff can achieve converged results. The energy and force convergence criteria for the structure relaxation are set to be 1×10^{-4} Ry and 1×10^{-3} Ry $Bohr^{-1}$, respectively. Bulk anatase TiO_2 and Au are calculated with their primitive cells with 6 × 6 × 6 and 16 × 16 × 16 k-points meshes, respectively. The anatase

(101) surface model is built with 2×3 supercell with 3 O-Ti-O layers. An Au nanorod along [010] direction loading onto anatase (101) surface is used to represent the Au/TiO_2 catalyst. The mismatch between Au nanorod and anatase (101) surface leaving a small residual compressive strain of 5.1% on Au nanorod. A vacuum layer of 17 Å is added for Au/TiO_2 slab model along Z-direction. Due to the supercell of Au/TiO_2 (TiO_2) showing the dimension of 20.8, 11.4 and 26.5 Å, Gamma point calculation generates converged results. VESTA is used for the visualization of computational results.[11] The V_O formation energy (E_{form}) for the most energy-favourable site is calculated with following equation:

$$E_{\text{form}} = E_{TiO_2-V_o} + \frac{1}{2}\mu_{O_2} - E_{TiO_2} \quad (4.1)$$

where, the $E_{TiO_2-V_o}$, μ_{O_2} and E_{TiO_2} represent the DFT energy of slab model with V_O, the energy of O_2 molecule and the energy of slab model without V_O, respectively.

4.3 Results

4.3.1 Physical characterizations of the catalysts

ICP-OES is used to determine the actual loadings of Au on TiO_2. The Au loadings of the two samples in this chapter are tested to be 0.74wt% and 2.76wt%, respectively. XRD is used to characterize the crystal structure of prepared sample. As presented in **Figure 4.2**(a), the P25 TiO_2 support is a mixture of anatase and rutile with anatase as the major component. The small peaks at 2θ of ~38° are assigned to crystalline Au (111) facet. A peak with lower intensity at the same position is observed for 0.74wt% Au/TiO_2(Ar) comparing with 2.76wt% Au/TiO_2, due to the smaller Au nanocluster size and lower loading. As presented in **Figure 4.2**(b), the optical absorption of TiO_2 and Au/TiO_2(Ar) powders are characterized by the UV-Vis DRS spectroscopy inside the praying mantis accessory. In the cases of 0.74wt% Au/TiO_2 and 2.76wt% Au/TiO_2, the UV region absorbances are almost identical to the TiO_2. While in the visible light region, both the 0.74wt% and 2.76wt% Au/TiO_2

samples exhibit a broad absorption peak in 500-650 nm range, which is attributed to the effect of the LSPR of Au NPs. In addition, it is noted that the visible light absorption of 2.74wt% Au/TiO_2 sample is much stronger than 0.76wt% Au/TiO_2. This is due to their different loadings and Au nanocrystal size distributions.[12-15] SSA of Au/TiO_2 catalysts are characterized using N_2 sorption method at 77K. As presented in **Figure 4.3**(a-c), the SSAs determined based on the BET theory are 56.9, 52.6 and 53.5 $m^2\ g^{-1}$ for TiO_2, 0.74wt% and 2.76 wt% Au/TiO_2, respectively.

The determination of Cl concentration followed a modified protocol reported in literature.[16] TPR experiments were performed with a series of anhydrous $CuCl_2$ powder with known weights (**Figure 4.4**(a)) and the calibration curve was created by plotting the MS peak area against Cl concentration (**Figure 4.4**(b)). This method achieves a detection limit of 162 ppm residual Cl when using 100 mg catalyst. The similar TPR experiments of 100 mg catalysts were conducted under 20% H_2 balanced in N_2. The residual Cl in catalyst formed effluent HCl, which was analysed online with a mass spectrometer (**Figure 4.4**(c)). By using this method, the residual Cl concentrations are determined to be 184 and 223 ppm for 0.74%wt and 2.76%wt Au/TiO_2, respectively.

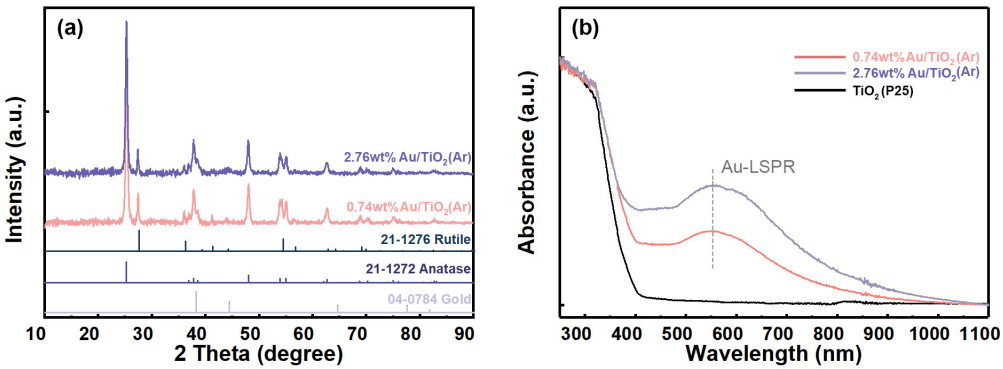

Figure 4.2. (a) XRD patterns and (b) UV-vis diffuse reflectance spectra of 0.74wt% Au/TiO_2(Ar) and 2.76wt% Au/TiO_2(Ar).

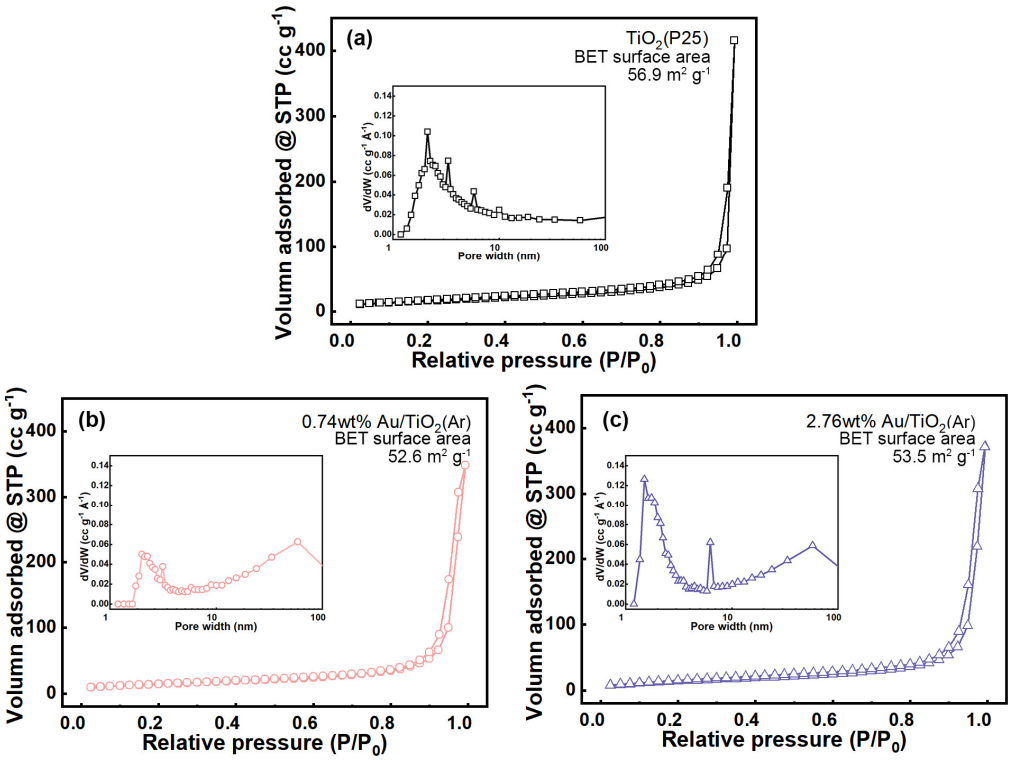

Figure 4.3. N_2 adsorption-desorption isotherms for (a) TiO_2 (P25), (b) 0.74wt% Au/TiO_2(Ar) and (c) 2.76wt%Au/TiO_2(Ar). The insets for each graph exhibit the corresponding pore size distribution curve derived from the isotherms using Barrett-Joyner-Halenda (BJH) method.

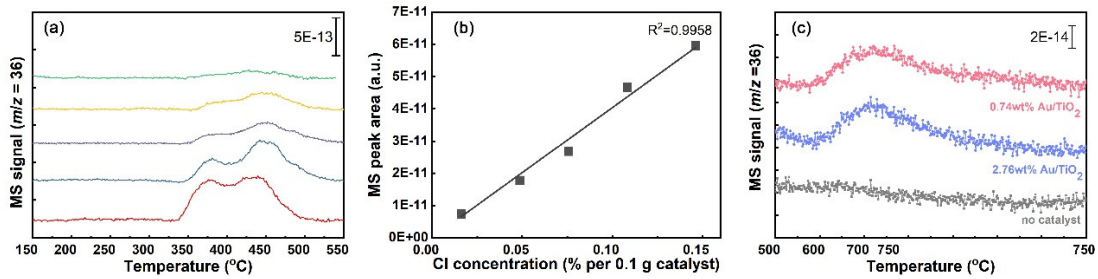

Figure 4.4. (a) MS signal of HCl during the $CuCl_2$ TPR process under 20% H_2 (balanced in N_2, 20 sccm). (b) The calibration curve of MS peak area as a function of Cl concentration. (c) The MS spectra of Au/TiO_2 TPR under 20% H_2 (balanced in N_2, 20 sccm).

The Au NP size distributions of 0.74wt% and 2.76wt% Au/TiO_2(Ar) are characterized using an aberration-corrected TEM under HAADF-STEM mode. The intensity of HAADF-STEM image is proportional to ~Z^2 (square of the atomic number) and the brighter pixels represent the Au atoms in the images (**Figure 4.5**). In all the images, the larger NPs with an average diameter of ~20

nm are TiO_2 (P25). The smaller nanoclusters with higher brightness are Au clusters, and homogeneously distributed on the surface of the TiO_2. As expected, much more Au clusters can be observed on the 2.76wt% Au/TiO_2(Ar), and the average size of the Au NPs is larger than that of 0.74wt% Au/TiO_2(Ar). Based on counting of 144 and 160 NPs, the average Au NP diameters are 1.65 ± 1.1 nm and 4.79 ± 2.0 nm for 0.74wt% and 2.76wt% Au/TiO_2(Ar) samples, respectively (**Figure 4.6**). Note that the STEM characterizations were conducted for Au/TiO_2(Ar), which had been further treated under flowing Ar at 300 °C for 0.5 h after the calcination in muffle furnace. Therefore, the Au NPs sizes reported here are their actual sizes during the photocatalytic reaction.

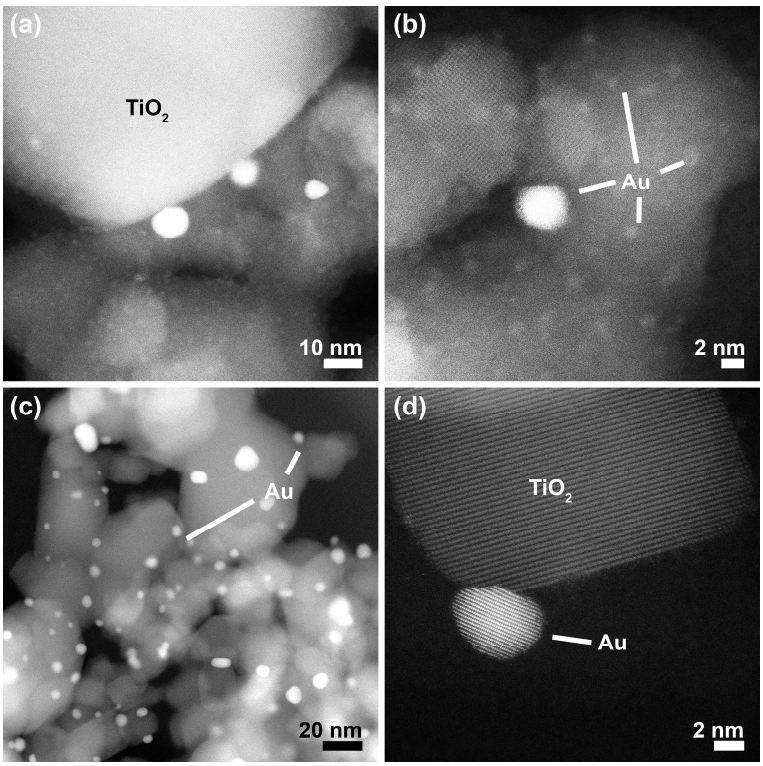

Figure 4.5. Aberration corrected HAADF-STEM images in low and high magnifications of (a, b) 0.74wt% Au/TiO_2(Ar) and (c, d) 2.76wt% Au/TiO_2(Ar).

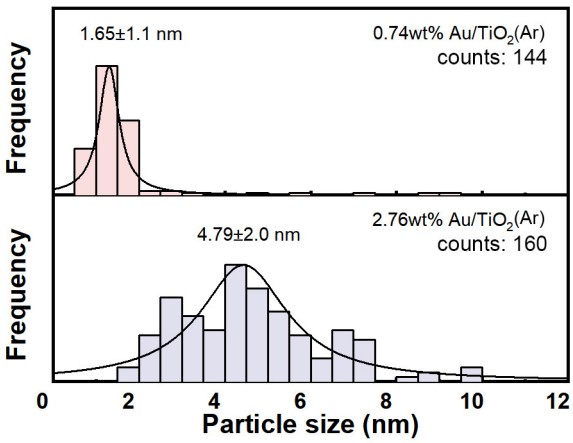

Figure 4.6. The Au particle size distribution curves of 0.74wt% Au/TiO_2(Ar) and 2.76wt% Au/TiO_2(Ar).

4.3.2 V_O and Ti^{3+} generation due to calcination in flowing Ar

4.3.2.1 EPR experimental results

Thermal treatment of Au/TiO_2 in oxygen-deficient atmosphere will result in the formation of V_O. In order to quantitively analyse the formation of V_O during the thermal treatment in flowing Ar, the EPR experiments were conducted for 0.74wt% and 2.76wt% Au/TiO_2, which were treated at 300 °C for 30 min under either flowing Ar or Air (Au/TiO_2(Ar) and Au/TiO_2(Air)), respectively. V_O concentrations created by Ar treatment are determined to be 158% and 255% of the Air treatment at the same temperature for 0.74wt% and 2.76wt% Au/TiO_2, respectively (**Figure 4.7**). The high V_O concentration achieved by 2.76wt% Au/TiO_2 is attributed to the high loading of Au NPs.

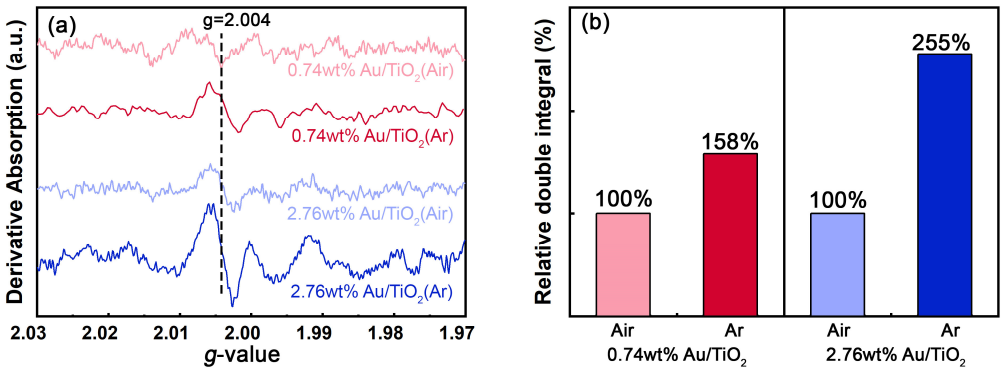

Figure 4.7. (a) EPR spectra of Au/TiO_2 treated at 300 °C for 30 min under flowing Ar and Air. (b) The relative EPR signal double-integral of the V_O peaks.

4.3.2.2 Theoretical analyses

Annealing TiO_2 in O_2-deficinet atmosphere will induce the generation of V_O. It is because the O atom in TiO_2 needs to achieve equilibrium with chemical potential of the O_2 in gas atmosphere thermodynamically, which is a function of its partial pressure (P_{O_2}). If considering O_2 as ideal gas, the chemical potential of O_2 at fixed temperature ($\mu_{O_2,T}(P)$) is expressed with the following equation:

$$\mu_{O_2,T}(P) = \mu^0_{O_2,T}(P^0) + k_B T\, ln(\frac{P_{O_2}}{P^0_{O_2}}) \tag{4.2}$$

If we approximate the reaction of V_O generation using following equation:

$$O_{TiO_2} \leftrightharpoons V_O + 0.5O_2 + 2e^-, \Delta G(T,P) \tag{4.3}$$

at equilibrium, the concentration of O in TiO_2 lattice ($[O]_{TiO_2}$), V_O concentration ($[V_O]$) and O_2 partial pressure (P_{O_2}) show the following relation:

$$[V_O] = \exp\left(-\frac{\Delta G^0}{RT}\right)[O]_{TiO_2}\, {P_{O_2}}^{-\frac{1}{2}} \tag{4.4}$$

Therefore, a higher concentration of V_O is achieved under higher temperature (T) and lower O_2 partial pressure. Another important parameter is the V_O formation energy, ΔG^0 in equation (4.3) & (4.4). With larger ΔG^0, the V_O is more difficult to form and its corresponding equilibrium concentration is lower.

DFT calculation is used to approximately determine the V_O formation energy (Equation (4.1)) and most energy-favourable site. After screening all the possible V_O site on the surface, the formation energy of the most stable V_O on TiO_2 and Au/TiO_2 are summarized in **Table 4.1**. The unpaired extra electron(s) locate(s) at the nearest Ti atoms is reflected by the total Bohr magneton value, which is consistent with the spin density plot in **Figure 4.8**. The localized extra electron induces the generation of Ti^{3+} directly. The V_O formation energy on Au/TiO_2 is calculated to be 0.15 eV smaller than on pristine TiO_2, which proves that Au can facilitate the V_O generation by interacting electronically with the surface Ti atoms.

From equation (4.4), the V_O concentration ratio between Au/TiO_2 and TiO_2 ($\frac{[V_{O\text{-}Au/TiO_2}]}{[V_{O\text{-}TiO_2}]}$) can be further written as:

$$\frac{[V_{O\text{-}Au/TiO_2}]}{[V_{O\text{-}TiO_2}]} = \exp\left(-\frac{\Delta G^0_{Au/TiO_2} - \Delta G^0_{TiO_2}}{RT}\right) \quad (4.5)$$

The thermodynamic Gibbs free energy can be calculated via *ab-initio* method.[17] The contributions from electron, magnetism, lattice vibration and gaseous O_2 to total Gibbs free energy at standard condition roughly cancel each other out during calculating the difference.[18-19] Therefore, the equation (4.5) can be reasonably approximated to:

$$\frac{[V_{O\text{-}Au/TiO_2}]}{[V_{O\text{-}TiO_2}]} \approx \exp\left(-\frac{E_{\text{form-Au/TiO}_2} - E_{\text{form-TiO}_2}}{k_B T}\right) \quad (4.6)$$

where k_B represents the Boltzmann constant (≈ 8.617×10^{-5} eV K^{-1}). The difference between V_O formation energy in Au/TiO_2 and TiO_2 ($E_{\text{form-Au/TiO}_2} - E_{\text{form-TiO}_2}$) is calculated to be -0.15 eV (**Table 4.1**). Therefore, the V_O concentration ratio between Au/TiO_2 and TiO_2 ($\frac{[V_{O\text{-}Au/TiO_2}]}{[V_{O\text{-}TiO_2}]}$) at 573 K is calculated to be 20.86. This theoretical derivation suggests a much higher concentration of V_O is created due to the presence of Au NP during the Ar treatment.

Table 4.1. Calculated formation energy for most energy-favourable VO at anatase (101) surface and Au/anatase (101) interface.

Sample	E_{form} (eV)	Total Bohr magneton
Anatase (101)	3.77	2.00
Au/Anatase (101)	3.62	1.00

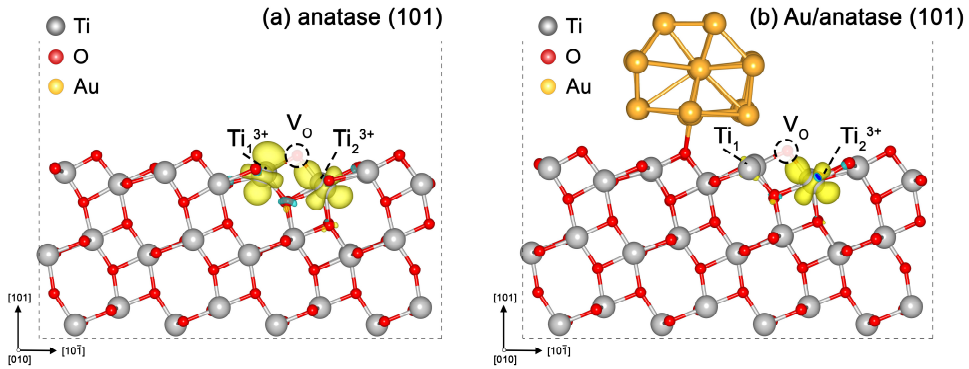

Figure 4.8. Spin-density plots for (a) anatase (101) surface and (b) Au/anatase (101) with most energy-favorable V_O on the surface.

4.3.3 The electronic properties of Au/TiO_2(Ar) in dark

The electronic states of the catalyst are important to its catalytic performance. *Ex-situ* XPS was used to characterize the oxidation states of Au and Ti in Au/TiO_2 pretreated under different atmospheres at the temperature of 300 °C for 0.5h. All the spectra are calibrated to adventitious carbon C 1s of 284.8 eV as reference.[20] As presented in **Figure 4.9**(a), for 2.76wt% Au/TiO_2(Ar) samples, the peaks centred at 83.3 eV and 87.0 eV are assigned to the metallic Au $4f_{7/2}$ and $4f_{5/2}$ spectra, which is in agreement with typical Au(0) supported by TiO_2. A 0.3 eV shift to lower binding energy is observed on 0.74wt% Au/TiO_2(Ar) Au 4f peaks, which suggests the Au NPs are still in metallic state but more negatively charged than 2.76wt% Au/TiO_2(Ar). The Ti 2p peaks of 2.76wt% Au/TiO_2(Ar) located at 458.7 and 464.4 eV are assigned to the $2p_{3/2}$ and $2p_{1/2}$ peaks of Ti^{4+} in TiO_2, as shown in **Figure 4.9**(b).[21-22] Similarly, the Ti $2p_{3/2}$ and $2p_{1/2}$ peaks for 0.74wt% Au/TiO_2(Ar) samples are positioned at 458.3 and 464.0 eV corresponding to Ti^{4+} in TiO_2 too. **Figure 4.9**(c) presents O 1s

spectra of the 0.74wt% and 2.76wt% Au/TiO_2(Ar). The peaks of these two samples can be further deconvoluted into the major lattice O in bulk TiO_2 (529.9 eV), surface O at bridging site (bridging-O 531.2 eV), surface O at top site (532.2 eV) and O in adsorbed H_2O (533.5 eV). Therefore, the electronic property of the Au NP is size- and loading- dependent. The Au 4f binding energy shift for 0.74wt% Au/TiO_2(Ar) can be explained by more negatively charged Au due to electron transfer from the reduced TiO_2,[23-24] which is supported by the downshift of Ti 2p peaks for 0.74wt% Au/TiO_2 (**Figure 4.9**(b, c)) in our case. To verify that the Ar treatment can create V_O on the surface and a more reduced TiO_2 surface is achieved on 0.74wt% Au/TiO_2 than 2.76wt% Au/TiO_2(Ar), the control groups of Au/TiO_2 with two different loadings were treated with flowing H_2 and O_2 respectively. And the corresponding XPS Ti 2p spectra were plotted in **Figure 4.10**. First of all, both the Ti 2p peaks after Ar treatment show a shift to smaller binding energy comparing with the O_2-treated sample. The result confirms that the V_O can be introduced by Ar treatment. Secondly, the 2.76wt% Au/TiO_2 exhibits a smaller shift in Ti $2p_{3/2}$ peak position from 458.8 eV (O_2 treated) to 458.7 eV (H_2 treated). By contrast, the Ti $2p_{3/2}$ peak of 0.74wt% Au/TiO_2 remarkably shifts from 458.5 eV (O_2 treated) to 458.2 eV (H_2 treated). The more significant Ti 2p binding energy red-shift on 0.74wt% Au/TiO_2 is attributed to its stronger V_O production ability. In summary, the Au supported by TiO_2 with two different loadings are all in metallic state, while it is more negatively charged in 0.74wt% than the 2.76wt% Au/TiO_2(Ar). Because the 0.74wt%Au/TiO_2 with smaller Au NPs shows higher V_O generation capability. These phenomena were further confirmed by *in-situ* DRIFTS CO adsorption experiments described in the following paragraph.

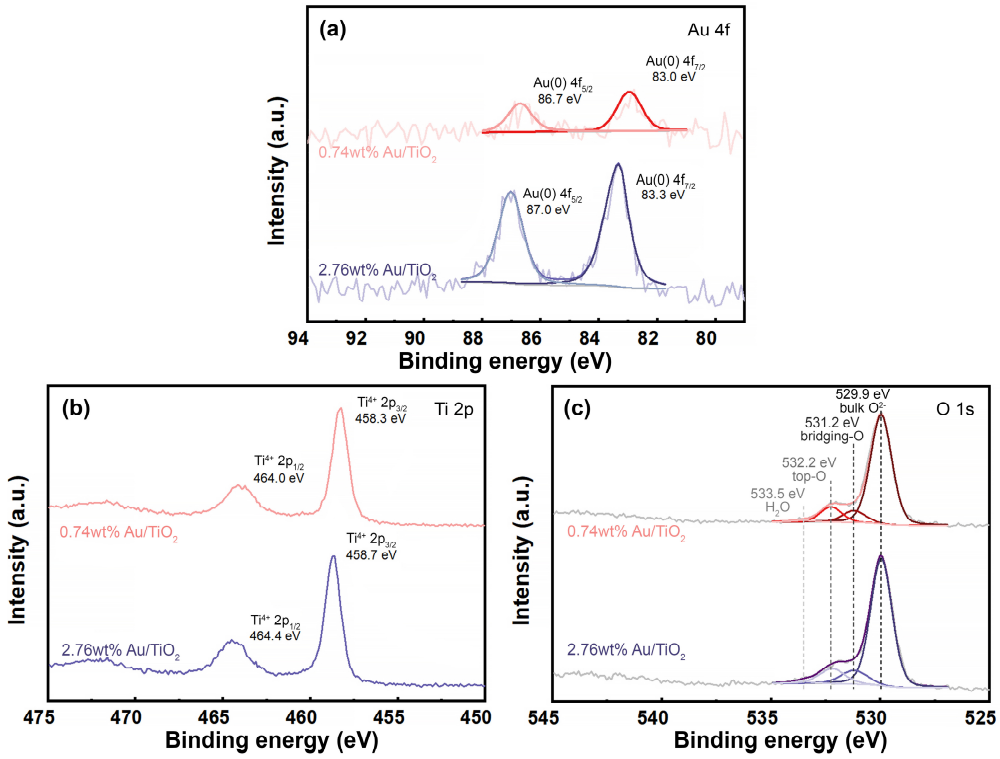

Figure 4.9. XPS core-level spectra of 0.74wt% Au/TiO_2(Ar) and 2.76wt% Au/TiO_2(Ar): (a) Au 4f, (b) Ti 2p and (c) O 1s regions.

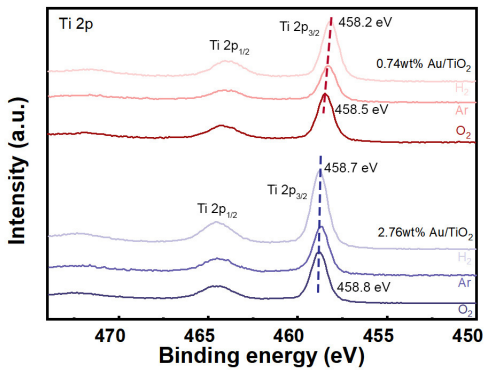

Figure 4.10. XPS Ti 2p spectra of 0.74wt% and 2.76wt% Au/TiO_2 treated under H_2, Ar, O_2 atmosphere respectively at 300 °C for 0.5 h.

In-situ DRIFTS for CO molecule probe adsorption experiment is used to *in-situ* determine the ground-state electronic property of Au/TiO_2(Ar) in dark. As presented in **Figure 4.11**(a, b), both Au/TiO_2(UP) present 3 peaks, 2108, 2119 and 2171 cm^{-1} in the carbonyl region (2300 to 2000 cm^{-1}). The latter two peaks

are ascribed to the gaseous CO. The peak at 2108 cm^{-1} is assigned to the CO adsorbed to Au(0).[25-26]

The spectra of CO adsorption on Ar-pretreated Au/TiO_2(Ar) are also presented in **Figure 4.11**(a, b). For 0.74wt% Au/TiO_2(Ar), the peak corresponding to the CO* adsorbed on Au becomes extremely weak. The suppression of CO adsorption on 0.74wt% Au/TiO_2(Ar) is ascribed to the electron-rich state of Au cluster, which is the direct evidence of V_O formation. Along with the disappearance of CO-Au(0) peak, a new peak is observed at 2185 cm^{-1}, which is due to the enhanced CO adsorption on coordinatively-unsaturated or electron-rich Ti site ($Ti^{(4-\delta)+}$) of TiO_2.[26-29] The generation of $Ti^{(4-\delta)+}$ is also attributed to the V_O generated during the Ar treatment. On the other hand, the 2.76wt% Au/TiO_2 before and after the flowing Ar treatment at 300 °C doesn't induce the disappearance of CO adsorption. The peak at 2185 cm^{-1} (CO-$Ti^{(4-\delta)+}$) becomes more prominent too. The control experiments are conducted for pristine TiO_2 in dark. As shown in **Figure 4.11**(a, b) and **Figure 4.13**(a), the CO doesn't evidently adsorb on the TiO_2 with and without pretreatment in Ar. It is because the Au NPs can facilitate the V_O generation, which is described in Section 4.3.2.

In summary, the *in-situ* CO adsorption IR spectroscopy results in dark suggest that V_O are created on both 0.74wt% and 2.76wt% Au/TiO_2(Ar) by Ar treatment at 300 °C. CO preferentially adsorbs onto Au and $Ti^{(4-\delta)+}$ site. While the 0.74wt% Au/TiO_2(Ar) exhibits a more negatively charged Au with suppressed CO-Au adsorption. Since the CO-Au adsorption suppression is derived from the localised electron transfer from V_O to Au, the Au NPs size rather than loading is the critical factor. These *in-situ* CO adsorption IR spectroscopy results are consistent with *ex-situ* XPS analyses described in the former paragraph.

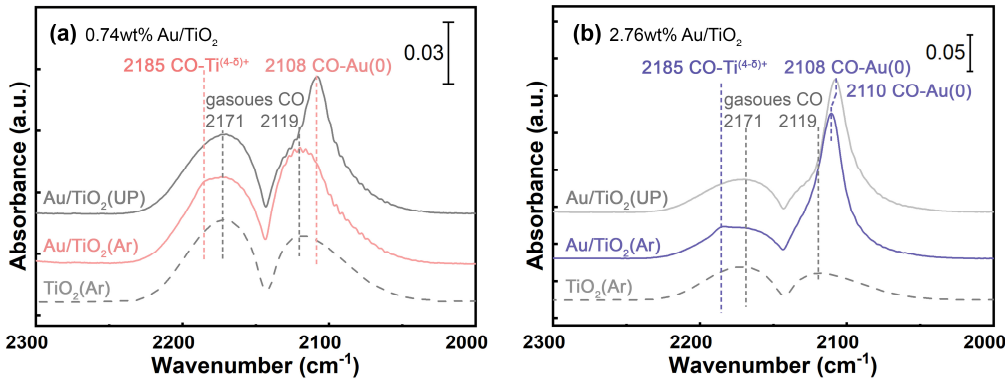

Figure 4.11. *In-situ* DRIFT spectra for CO molecule probe adsorption experiments at 30 °C on (a) 0.74wt% Au/TiO_2 and (b) 2.76wt% Au/TiO_2 before and after treatment under flowing Ar (20 sccm) at 300 °C for 0.5 h. The spectrum of CO adsorption on Ar treated pristine TiO_2 is also presented from comparison. UP represents unpretreated samples after calcination in muffle furnace in ambient atmosphere at 400 °C, 2h.

4.3.4 Electronic properties of Au/TiO_2(Ar) under UV or visible light irradiation

To elucidate the electronic property of Au/TiO_2(Ar) under UV or visible light irradiation, *in-situ* DRIFTS of CO adsorption experiments are conducted under external light irradiation. The stability of the key reaction intermediate *CO can also be demonstrated. As illustrated in **Figure 4.12**(a), 0.74wt% Au/TiO_2(Ar) under UV light shows a significant higher CO-$Ti^{(4-\delta)+}$ peak at 2184 cm^{-1} and even more suppressed CO-Au peak comparing with the control group under darkness or visible light irradiation. By comparison, the spectrum of the 0.74wt% Au/TiO_2(Ar) under visible light irradiation shows less strong CO-$Ti^{(4-\delta)+}$ peak comparing with the one under UV. The peak centred at 2116 cm^{-1} emerges, which is ascribed to CO adsorption on slightly positively charged Au (CO-$Au^{\delta+}$).[30]

In the case of 2.76wt% Au/TiO_2(Ar) (**Figure 4.12**(b)), the CO-Au(0) adsorption peak under UV irradiation is also positioned at 2110 cm^{-1}. It suggests the electronic property of Au doesn't change significantly under UV excitation. When the 2.76wt% Au/TiO_2(Ar) is irradiated by visible light, the main peak

attributed to CO-$Au^{\delta+}$ exhibits a blue shift to 2116 cm^{-1}. A new peak emerges at the wavenumber of 2178 cm^{-1}, which is assigned to CO-Au^{+}.[26]

The control experiments are conducted for pristine TiO_2 pretreated in flowing Ar (TiO_2(Ar)) under UV or green light irradiation. As shown in **Figure 4.13**(b), TiO_2(Ar) doesn't show any CO adsorption peak under green light irradiation is within expectation. However, under UV light, TiO_2(Ar) doesn't show the CO-$Ti^{(4-\delta)+}$ peak observed in the case of 0.74wt% Au/TiO_2(Ar) irradiated under UV light either. The plausible explanation could be the less efficient photo-excited electron-hole separation without the Au co-catalysts and insufficient Au-induced V_O to trap the photo-excited electrons.

In summary, the electronic property of Au/TiO_2(Ar) under UV and plasmonic excitations are determined from the *in-situ* DRIFTS of CO molecule probe adsorption experiments: (1) UV and visible light irradiation bring negatively and positively charged Au, respectively. (2) Visible light irradiation enhances CO adsorption on Au and suppresses the adsorption on TiO_2; on the contrary, the UV light irradiation suppresses the CO adsorption on Au but enhances the adsorption on TiO_2. (3) Smaller Au NPs are more strongly influenced by UV light excitation, while larger Au NPs are more significantly affected by visible light excitation.

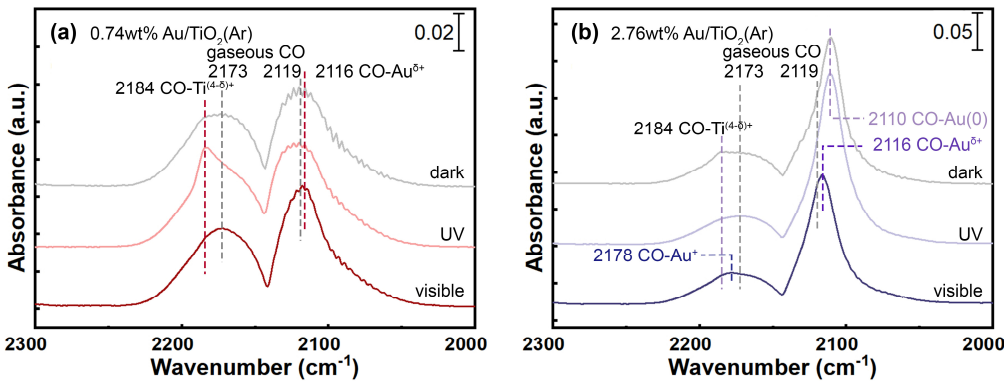

Figure 4.12. *In situ* DRIFT spectra of CO molecule probe adsorption at 30 °C on (a) 0.74wt% and (b) 2.76wt% Au/TiO_2(Ar) under dark, UV and visible light irradiation.

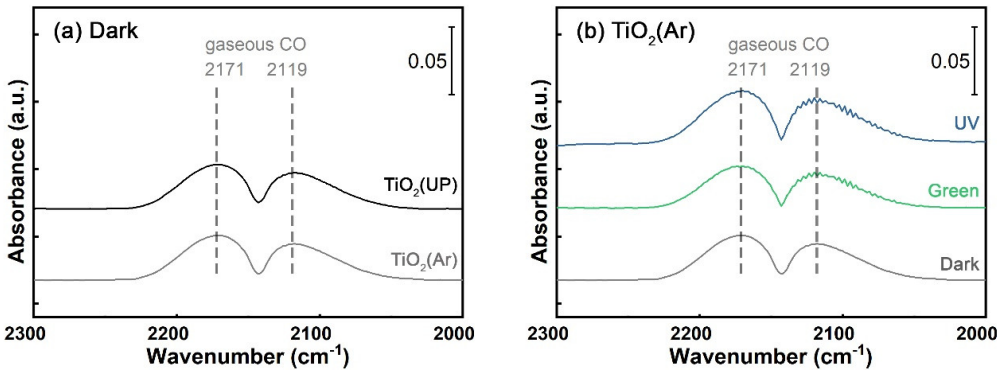

Figure 4.13. *In-situ* DRIFTS spectra for CO molecule probe adsorption experiments at 30 °C on (a) pristine TiO_2 with (TiO_2(Ar)) and without (TiO_2(UP)) treatment under flowing Ar (20 sccm) at 300 °C for 0.5 h and (b) TiO_2(Ar) under dark, green and UV irradiation conditions. UP represents unpretreated samples.

4.3.5 Photocatalytic activity

The photocatalytic CO_2 conversion with water is conducted over both the 0.74 wt% and the 2.76 wt% Au/TiO_2 samples under UV (centred at 365 nm) or green light (centred at 530 nm) irradiation, respectively. The pretreatment at 300 °C under Air and Ar flow for 30 min in sequence can remove carbon pool and generate V_O.[4] The reaction products in continuous flow condition are collected and analysed every 0.5 h. As presented in **Figure 4.14**(a, b), the 0.74wt% Au/TiO_2(Ar) produces CO, CH_4 and C_2H_6 of 8.77, 3.92 and 0.87 μmol g^{-1}_{cat} h^{-1} in the first 0.5 h, respectively. The corresponding product selectivities are 65%, 29% and 6%, respectively. The 2.76wt% Au/TiO_2(Ar) produces the same products of CO, CH_4 and C_2H_6 but at slower rates of 7.52, 3.57 and 0.59 μmol g^{-1}_{cat} h^{-1} at the first 0.5 h, respectively. The corresponding product selectivities are 64%, 31% and 5%, respectively. Although the product selectivity is similar for these two samples, the higher activity of 0.74wt% Au/TiO_2(Ar) under UV light irradiation is attributed to the smaller Au nanocluster size: (1) the under-coordinated Au ensures the more efficient H* production from H_2O splitting; (2) the stronger electronic metal support interaction after the Ar treatment (section 4.3.3). The lower loading is another plausible reason.[31-32] The situation is inversed when comparing their reactivities under visible light irradiation (**Figure 4.15**(a, b)). In the first 0.5 h, the 2.76wt% Au/TiO_2(Ar) produces 0.66

μmol g^{-1}_{cat} h^{-1} C_2H_6, which is ~2.4 times as much as 0.74wt% Au/TiO_2(Ar) produces. The selectivity towards C_2H_6 reaches ~20% for 2.76wt% Au/TiO_2(Ar) under green light irradiation; Comparatively, the C_2H_6 selectivity is only ~9% over 0.74wt% Au/TiO_2(Ar) under the same irradiation condition. The CH_4 production rates over both catalysts are similar.

Based on the comparisons of the reaction rates under different conditions, three results are worth noting: (1) the total CO_2 conversion rate is dependent on Au particle size and excitation light wavelength. The small Au NP show the advantages under UV light irradiation. On the contrary, the larger Au NPs outperform under plasmonic excitation mechanism. Note that although the larger particles generally show stronger plasmonic effects, the larger size of Au NPs don't always guarantee a fast plasmonic reaction rate. Because the small metal NPs provide stronger electronic interaction with support and exhibit more active sites along the perimeter at the Au/TiO_2 interface.[33-34] (2) C_2H_6 production rate on 2.76wt% Au/TiO_2(Ar) under green light irradiation is higher than the same catalyst under UV light irritation, though the UV light contains much more energy than the green light. The selectivity to C_2H_6 reaches ~20% on the 2.76wt% Au/TiO_2(Ar) under green light irradiation, comparing with 5% selectivity to C_2H_6 achieved under UV light irradiation. (3) The reaction rate decreases gradually within 3 hours in all the cases, which indicates the deactivation of the catalysts. Similar phenomenon has been found for CO_2 photocatalytic reduction with water on other catalyst surfaces too. However, no consensus on the reason has been achieved to date.[28, 35-36]

The photocatalytic CO_2 reduction performance of pristine TiO_2 is also evaluated under UV or green light irradiation. Under 365 nm UV light irradiation, CO is the only product detected. As shown in **Figure 4.16**, at first 0.5 h, the pristine TiO_2 produces CO in the production rate of 5.07 μmol g_{cat}^{-1} h^{-1}, which is significantly slower than Au/TiO_2. It is because the Au NPs as co-catalyst can enhance the photo-excited electron-hole separation at the interface. With longer reaction time, the CO production rate shows a small gradual decrease, which is possibly due to the consumption of V_O. CO production rate of 3.95

μmol g_{cat}^{-1} h^{-1} is determined at 3 h. No product can be detected for reaction under green light irradiation. Control experiment is conducted for the glass fibre filter without catalysts too. No product can be detected by GC, which indicates the catalysts are critical for the CO_2 photocatalytic reduction.

One of the possible reasons for the gradual deactivation is the consumption of surface C contamination. To rule out this possibility and confirm that the CO, CH_4 and C_2H_6 are produced from CO_2 reduction, the isotopic labelling experiments are conducted using the same setup but replacing $^{12}CO_2$ with $^{13}CO_2$. The products are analysed in a GC-MS. The achieved mass spectra of $^{13}CH_4$ and $^{13}C_2H_6$ are presented in **Figure 4.17**(a, b). The retention time of C_2H_6 is determined to be ~9.36 min by using standard mixture. At the same retention time, **Figure 4.17**(c) shows a peak at m/z=30 corresponding to $^{13}C_2H_6$. The predominant presence of ^{13}C-based products confirms that they are from the photocatalytic reduction of CO_2.

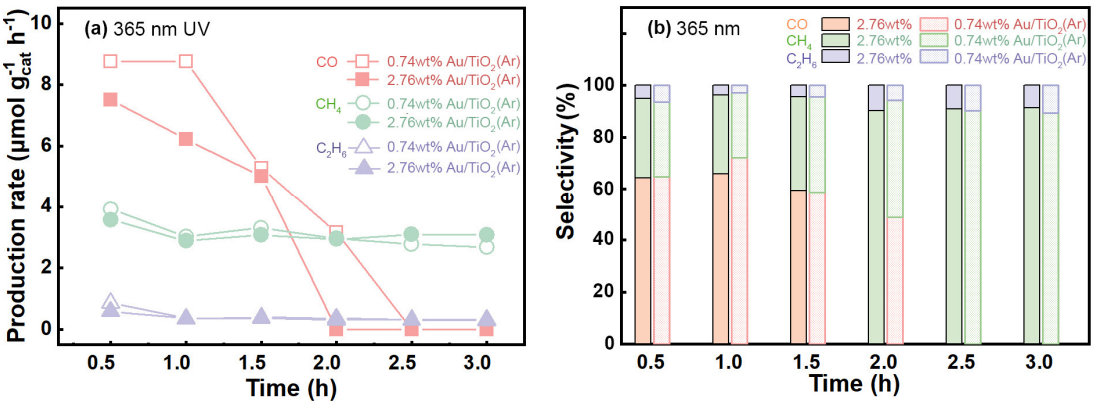

Figure 4.14. (a) Production rate and (b) selectivity on 0.74wt% and 2.76wt% Au/TiO_2(Ar) under the 365 nm UV light irradiation at 30 °C.

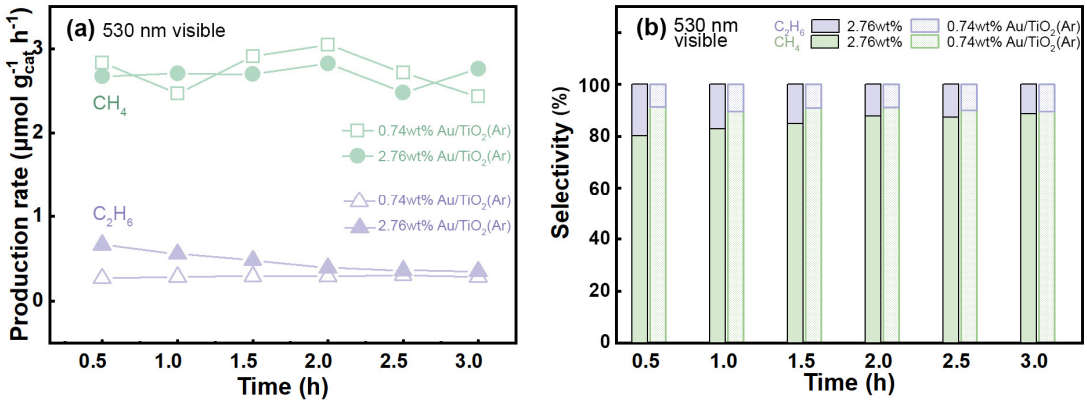

Figure 4.15. (a) Production rate and (b) selectivity on 0.74wt% and 2.76wt% $Au/TiO_2(Ar)$ under the 530 nm visible light irradiation at 30 °C.

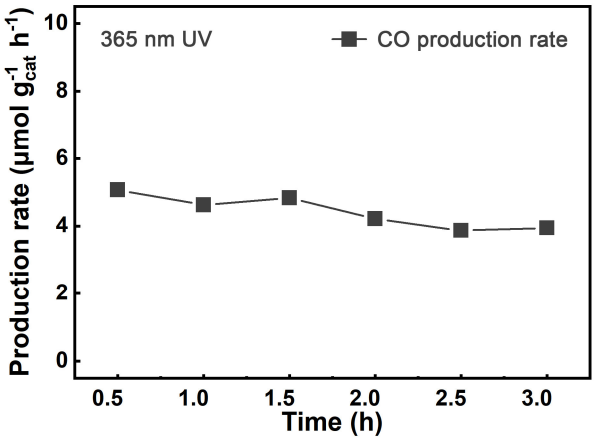

Figure 4.16. CO production rate on pristine $TiO_2(Ar)$ under 365 nm UV light irradiation at 30 °C.

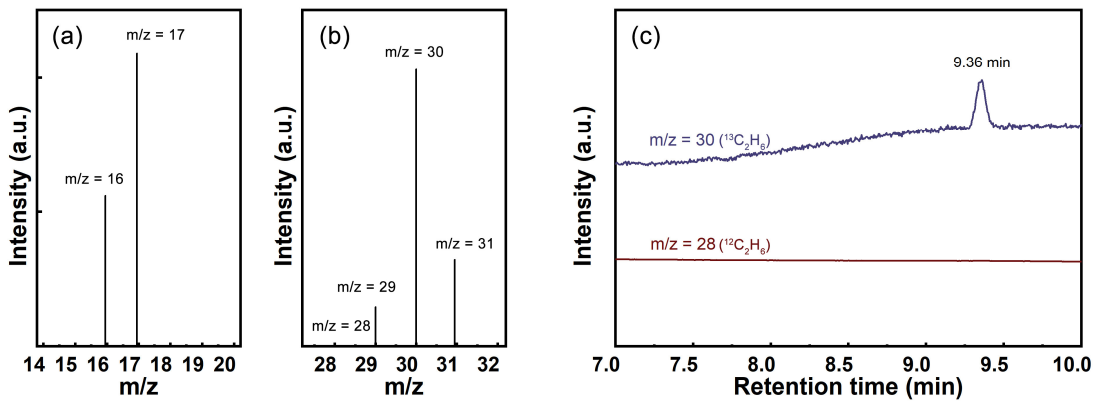

Figure 4.17. Mass spectra of (a) $^{13}CH_4$, (b) $^{13}C_2H_6$ and (c) Chromatogram of $^{13}C_2H_6$ as products in the isotopic labelled photocatalytic experiments.

4.3.6 *In-situ* DRIFTS investigations on CO_2 photocatalytic reduction mechanism

4.3.6.1 IR peak assignment of plausible C1-C2 chemical species adsorbed on Au/TiO_2

The most important part to achieve a reliable mechanism understanding from *in-situ* DRIFTS experiments is the correct assignments of observed IR peaks. To achieve correct IR peak assignments for possible species as the reaction intermediates in our work, the adsorptions of possible intermediate candidates (C1 species: formate, methanol, formaldehyde; C2 species: oxalate, acetate, glyoxal, glyoxylic acid, acetaldehyde) were performed on exactly the same Au/TiO_2 catalyst and analysed in the identical *in-situ* DRIFTS reactor at 30 °C. The detailed procedure is described as follows:

Involatile compounds: firstly, 50 ml water is bubbling with N_2 under vigorous stirring for 1 h to get rid of dissolved oxygen. Then 10 mg oxalic acid was added into the solution with the protection of flowing N_2. 30 mg 2.76wt% Au/TiO_2 was added into the O_2-free aqueous solution and stirred for another 30 min. The catalyst powder with adsorbed chemical species was separated from the solution using vacuum filtration method with a Nylon-66 filtering membrane (Waterman). The catalysts were instantly transferred to a vacuum oven to dry at room temperature under vacuum for 5 h. After completely drying, the powder was packed into the DRIFTS reactor for analysis. The adsorption spectra of the sodium oxalate, sodium formate, glyoxylic acid, glyoxal were conducted under the same procedure except replacing oxalic acid with different adsorbates.

Volatile compounds: the DRIFT spectra of volatile compounds including methanol, acetic acid, acetaldehyde, formaldehyde was achieved by injecting 500 µL headspace vapour into the DRIFTS reactor packed with the Au/TiO_2(Ar) powder using a gas-tight syringe. All the compounds were bubbled with He in the vials before headspace vapour withdraw. Ar carrier gas (20 sccm) was flowing through the DRIFTS reactor during the whole injection process. The IR

spectra of formic acid/formate, methanol and formaldehyde on 2.76wt% Au/TiO_2 at 30 °C are shown in **Figure 4.18** and the corresponding peak assignments are presented in **Table 4.2** to **Table 4.4**. In the case of C2 species, the IR spectra of oxalate, acetate, glyoxal, glyoxylic acid, acetaldehyde adsorbed on Au/TiO_2 surface are shown in **Figure 4.19** and the corresponding peak assignments are summarized in **Table 4.5** to **Table 4.9**.

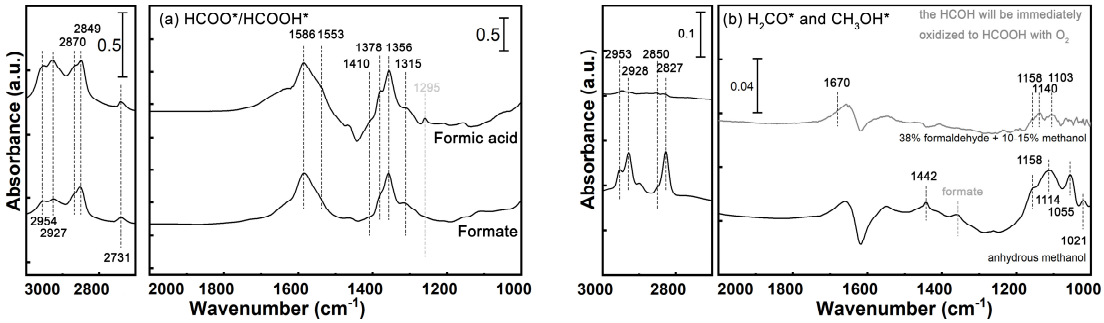

Figure 4.18. Adsorption of (a) formic acid/formate and (b) methanol/formaldehyde on 2.76wt% Au/TiO_2 at 30 °C and their corresponding DRIFT spectra.

Table 4.2. Vibration modes assignments for adsorbed formic acid/formate ($HCOOH_{(a)}$/$HCOO_{(a)}$) on 2.76wt% Au/TiO_2.

Assignment	Formic acid$_{(a)}$				Formate$_{(a)}$					Present work 2.76wt% Au/TiO_2
	TiO_2 [37]	Au/TiO_2 [38]	TiO_2 [39]	TiO_2 [40]	Au/TiO_2 [38]	TiO_2 [40]	TiO_2 [39]	TiO_2 [41]	Au/TiO_2 [42]	
δ(OCO) + δ(C-H)					2955 2764		2945	2957	2954	2954
ν(C-H)	2923	2928	2921		2868		2867	2873	2867 2731	2927$_{(formic acid)}$ 2870 2849
ν(C=O)	1725$_{(p)}$ 1675$_{(c)}$	1658	1787$_{(p)}$ 1675$_{(c)}$	1682						2742 1680
ν_{as}(OCO)					1550	1557	1565$_{(m)}$ 1550$_{(bd)}$	1575	1550 1570 1690$_{(m)}$	1586$_{(bd)}$ 1560$_{(bd)}$ 1535$_{(m)}$
ν_s(OCO)					1367	1371	1378$_{(bd)}$ 1360$_{(m)}$	1358	1382 1367 1315$_{(m)}$	1378$_{(bd)}$ 1356$_{(bd)}$ 1315$_{(m)}$
δ(CH) δ(OCO)		1081	1323$_{(c)}$	1325		1414 1385	1323	1323		1410
ν(CO) or ν(CH)	1252$_{(c)}$ 1208$_{(p)}$		1263$_{(c)}$ 1105$_{(p)}$	1277						1259

Note: subscript (a) represented adsorbed; (c) and (p) denotes chemisorbed and physiosorbed respectively; (s) represents solvated chemical species, which means formate or formic acid co-adsorbed with H_2O; (bd) and (md) denote bidentate and monodentate, respectively.

Table 4.3. Vibration modes assignments for adsorbed formaldehyde on 2.76wt% Au/TiO_2.

Assignment	formaldehyde				Present work
	FTIR transmission Au/TiO_2 [43]	FTIR TiO_2 [44]	FTIR TiO_2 [45]	FTIR reflectance TiO_2 [46]	2.76wt% Au/TiO_2
$\nu_{as}(CH_2)$	2804		2977 2913	2956 2913	
$\nu_{as}(CH_2)$				2863 2759	
ν(C=O)	1706–1710	1670	1650	1547	1670
$\delta(CH_2)$			1428	1413 1357 1303	
ω(CH2)	1251	1252		1254	1158
$\rho(CH_2)$	1155-1164		1106 1059		1140

Table 4.4. Vibration modes assignments for adsorbed methanol on 2.76wt% Au/TiO_2.

Assignment	Methanol/Methoxyl						Present work
	FTIR transmission P25-TiO_2 [47]	DRIFTS Au/TiO_2 [48]	FTIR transmission Au/TiO_2 [49]	DRIFTS Au/TiO_2 [50]	DRIFTS TiO_2 [51]	FTIR transmission rutile [52]	2.76wt% Au/TiO_2
ν_{as}(CH)	2929	2946	2923 2915	2948 2922	2940- 2938 2920	$2951_{(mo)}$ 2927	2953 2928
ν_s(CH)	2828	2844	2815-2814	2841 2818	2838 2819	$2849_{(mo)}$ 2827	
$\delta_a(CH_3)$ in CH_3O^*	1441			$1438_{(bended)}$	1437 1262 1235	1440, 1460	1442
δ(C−H) $\rho(CH_3)$ CH_3O^* at Au or Ti^{3+}		1436	1156	$1142_{(m)}$	1155	1153	1158
ν(C−O) in CH_3O^*	$1126_{(m)}$, $1045_{(b)}$		1125-1128 (at Ti^{4+} site); $1055_{(br)}$	$1119_{(m)}$	1125	1109	1114, 1055
ν(C−O) in $CH_3OH_{(ad)}$					1057	1050	
ν(C−O) in CH_3O^*				$1037_{(b\text{-}br)}$,	$1036_{(b\text{-}br)}$, $1012_{(triple\text{-}br)}$	$1020_{(triple\text{-}br)}$	1021

Note: subscript (mo) represented molecular adsorption; (ad) represents adsorption (b) denotes bidentate; (m) denotes monodentate; (br) denotes bridged adsorption

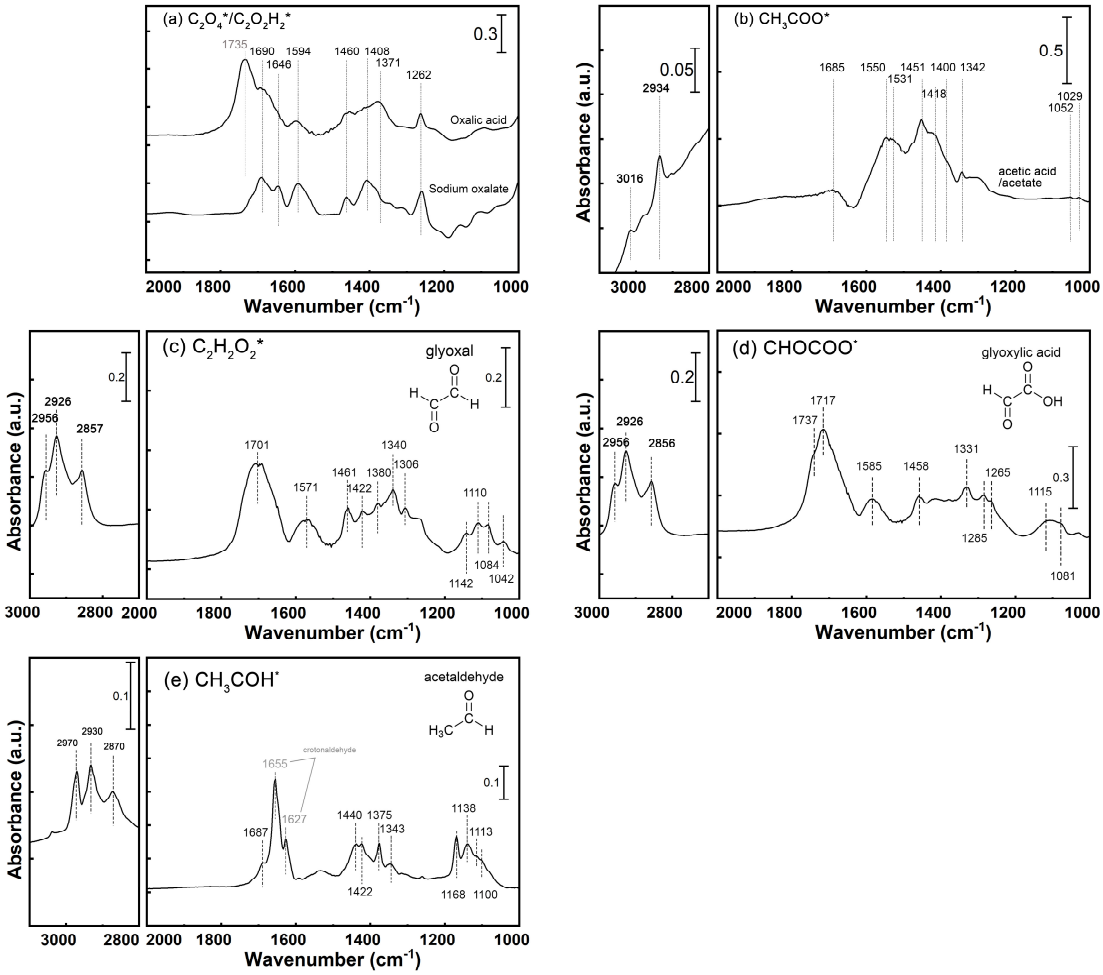

Figure 4.19. DRIFT spectra of C_2 compounds as possible reaction intermediate on the surface of 2.76wt% Au/TiO_2 at 30 °C: (a) oxalic acid/oxalate, (b) acetic acid/acetate, (c) glyoxal, (d) glyoxylic acid and (e) acetaldehyde.

Table 4.5. Vibration mode assignments for adsorbed glyoxylic acid/glyoxylate on 2.76wt% Au/TiO_2.

Assignment	glyoxylic acid (HCO-COOH)/glyoxylate			Present work
	FTIR (transmission) TiO_2 (P25) [53-54]	ATR TiO_2 [55]	ATR TiO_2 [56] (pH=2.3)	Au/TiO_2
ν(OH)	2928			2926
ν(CH)	2857			2856
ν(C=O)	1742			1737, 1717
ν_{as}(COO)	1563	1643	1668	1585
ν_{s}(COO)	1431	1431	1353	1458
δ(CCH) + δ(COH)	1334			1331
ν(CO) + ν(CC) + δ(COH)	1313, 1270	1315		1285, 1265
δ(COH) + ν(CO) + ν(CC)	1208			
ν(CC) and ν(CO) in HCOH	1147, 1115,1083	1092	1098	1115, 1081

Table 4.6. Vibration mode assignments for adsorbed glyoxal on 2.76wt% Au/TiO_2.

Assignment	glyoxal (CHOCHO)					Present work 2.76wt% Au/TiO_2
	FTIR Al_2O_3 [57]	FTIR SiO_2 [58]	FTIR Al_2O_3 [58]	FTIR vapour [59-60]	FTIR Pd [61]	
C-H stretch		2936		3023		
C-H stretch				2979		2956, 2926
C-H stretch		2867		2945		257
C-H stretch				1731-1732		1701
C=O	1661	1745, 1717	1738/1742	1616		
ν_{as}(COO)					1577	1571
						1380
C-H rocking				1338		1340
C-H bend				1312-1313		1306
						1142
						1110
C-C stretching				1065	1076	1084
C-H wagging		$996_{(O)}$, $927_{(O)}$	$1087_{(O)}$, $1017_{(O)}$	1048		1042

Note: subscript (o) represents the oligomer derived from the glyoxal

Table 4.7. Vibration mode assignments for adsorbed oxalic acid/oxalate on 2.76wt% Au/TiO_2.

Assignment	oxalic acid/oxalate									Present work
	FTIR TiO_2 [62]	FTIR TiO_2 [63-64]	FTIR Au/TiO_2 [65]	ATR TiO_2 [66]	ATR Au/TiO_2 [67]	ATR TiO_2 [68]	ATR TiO_2 [69]	ATR anatase [70]	ATR TiO_2 [71-72]	2.76wt% Au/TiO_2
v1(C=O)	1731 (bd)	1715	1736	1718	1710	1717	1712 (bd) 1719 (bbd) 1726 (m)	1719	1716-1713	1735
v2(C=O)	1697 (bd)	1690	1680	1698	1690	1697	1692(bd) 1680(m)	1701-1692	1696-1679	1690
v_s(C-O)+ v_s(C-C)			1363		1408		1415 (bd) 1405 (bbd) 1409 (m)	1420	1424-1412	1460
v_{as}(C-O)+ v_{as}(C-C)			1213	1268				1270	1279-1264	1262
v_s(C-O)+ δ(O-C=O)						1270	1268 (bd) 1252 (bbd) 1254 (m)			
v_s(C-O) +v_s(O-C=O)					1263					
v_s(C-O)+ v_s(C-C)+ v_s(O-C=O)				1417		1420				
v_s(C-O)+ v_s(C-C)+ v_s(O-C=O)+ δ(O-C=O)										
v_{as}(O-C=O)			1630	1630		1635-1625				1646 1594
Outer-sphere O_x^{2-} (charged system)				1310		1310		1600 1306		1371 1408
not assigned		1445 1379							1679 1424	

Note: subscript (a) represents adsorbed, (cbd), (bbd) and (md) denote chelating bidentate, bridged bidentate and monodentate respectively.

Table 4.8. Vibration mode assignments for adsorbed acetic acid/acetate on 2.76wt% Au/TiO_2.

Assignment	Acetic acid$_{(a)}$			Acetate$_{(a)}$						Present work 2.76wt % Au/TiO_2
	TiO_2 [73]	TiO_2 [74]	TiO_2 [75]	Au/TiO_2 [76-77]	TiO_2 [74]	TiO_2 [73]	TiO_2 [75]	TiO_2 [78]	Pt/TiO_2 [79]	
$\nu_s(CH_3)$				2936						
$\nu(CH_3)$			3016 2988 2938			2935	2938		3016 2986 2936	3016 2934
$\nu_{as}(COO)$				$1532_{(bd)}$	1542 1537	1535 (cb)	1540	1509	1540	1550 1531
$\nu_s(COO)$				$1454_{(bd)}$	1446 1443 1438 1421	1445 (cb)	1454 1420	1419	1450	1451 1418
$\delta(CH_3)$				1400 1338 1324		1324 1338		1346	1400	1400
$\delta_{as}(CH_3)$					1469					
$\delta_s(CH_3)$					1340					1342
$\delta(C=O)$		1684								
$\rho(CH_3)$						1027			1050 1030	1029
$\nu(C=O)$	1675 1736		1684							1685
$\nu(C-C)$						1049				1052
Not assigned	1296 1415		1304							

Note: subscript (a) represents adsorbed, (cbd), (bbd) and (md) denote chelating bidentate, bridged bidentate and monodentate respectively.

Table 4.9. Vibration mode assignments for adsorbed acetaldehyde on 2.76wt% Au/TiO_2.

Assignment	acetaldehyde (CH_3CHO)					Present work
	FTIR (transmission) TiO_2(anatase) [80-81]	FTIR (transmission) TiO_2 [82]	FTIR TiO_2 [44]	FTIR (transmission) anatase [83]	FTIR (transmission) rutile [83]	2.76wt% Au/TiO_2
$\nu_{as}(CH_3)$		2960		2969	2963	2970
$\nu_s(CH_3)$		2923		2914	2915	2930
$2\nu_s(A')$ resonance				2846	2848	2870
ν(CH)		2723		2759	2759	
ν(C=O)	1693 (Ti site), 1677 (V_O site)	1729-1686	1714, 1693	1718	1703, 1725	1687
ν(C=O)(*)	1653					1655
ν(C=C)(*)	1630					1627
acetate	1444					1440
$\delta_{as}(CH_3)$	1421 (d-deformation)	1440-1434				1422
δ(CH)	1376 (bending)		1377			1375
$\delta_s(CH_3)$	1355 (s-deformation)	1334	1352	1355	1348	1343
ν(C−C)	1168					1168
$\gamma(CH_3)$, ν(C−C)		1139-1110				
ν(C−C)	1129					1138
$\rho(CH_3)$	1099					1100,1113

Note: (*) assigned to crotonaldehyde ($CH_3CH=CHCHO$) due to the condensation reaction of acetaldehyde. It is reported that the acetaldehyde will undergo condensation reaction formation as soon as it adsorbed on the catalysts surface.[80]

4.3.6.2 Au/TiO_2(Ar) interaction with CO_2 and H_2O in dark

To understand how the CO_2 and H_2O interact with Au/TiO_2(Ar) in dark, the time-resolved DRIFT spectra were recorded every minute once Au/TiO_2(Ar) was exposed to CO_2/H_2O reactants. As presented in **Figure 4.20**(a, b), the peaks at 1670 and 1247 cm^{-1} are attributed to the CO_2^-,[28, 84-85] which is deemed as the product between the CO_2 and Ti^{3+} derived from V_O. These two strong peaks appear immediately after exposing the clean surface to CO_2/H_2O and soon vanish after 2 min. The peak at ~1650 cm^{-1} attributed to the adsorbed H_2O molecules predominates in the following curves. Supported by the higher binding energy of H_2O than CO_2 on V_O, the competitive adsorption of H_2O to CO_2 is believed as the reason for the loss of CO_2^- peaks.[84] CO_2 adsorbs on the surface of Au/TiO_2 mainly in the form of carbonate and bicarbonate with the presence of moisture. b-HCO_3^- adsorption peak shifts to higher wavenumber in the range of 1385-1423 cm^{-1}, when its coverage increases on the surface. There is no agreement in the literature about the assignment for the peaks at 1596 cm^{-1} and it could be assigned to either carbonate or bicarbonate on the surface. The detailed peak assignments and peak deconvolution results are presented in **Figure 4.21** & **Figure 4.22** and **Table 4.10** & **Table 4.11**. In summary, the CO_2/H_2O interacts with the Au/TiO_2(Ar) under dark can be described by the following equations:

$$Ti^{3+} + CO_2 \rightarrow Ti^{4+}\text{-}CO_2^- \quad (4.7)$$

$$OH^- + CO_2 \rightarrow HCO_3^- \quad (4.8)$$

$$Ti^{4+}\text{-}O^{2-} + CO_2 \rightarrow Ti^{4+}\text{-}CO_3^{2-} \quad (4.9)$$

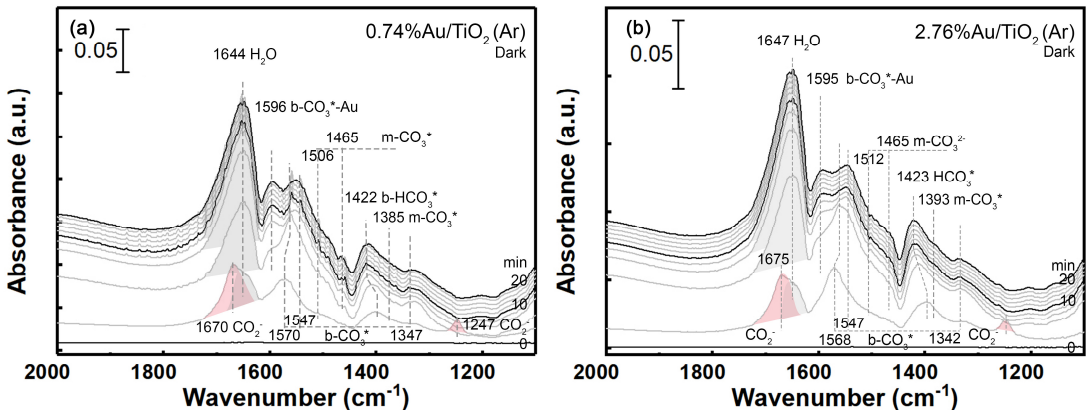

Figure 4.20. The time-resolved DRIFT spectra of (a) 0.74wt% Au/TiO_2(Ar) and (b) 2.76wt% Au/TiO_2(Ar) on adsorbing CO_2/H_2O at 30 °C under dark.

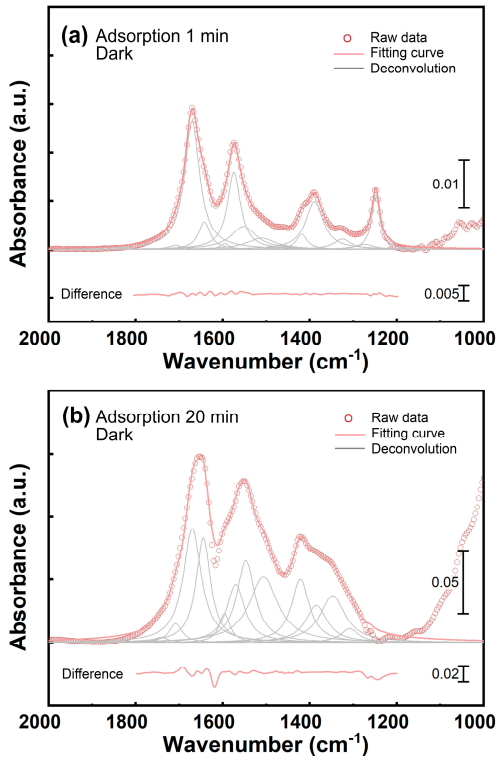

Figure 4.21. Deconvolution of IR spectra of CO_2 and H_2O adsorption on 0.74wt% Au/TiO_2(Ar) after (a) 1 min and (b) 20 min in dark at 30 °C.

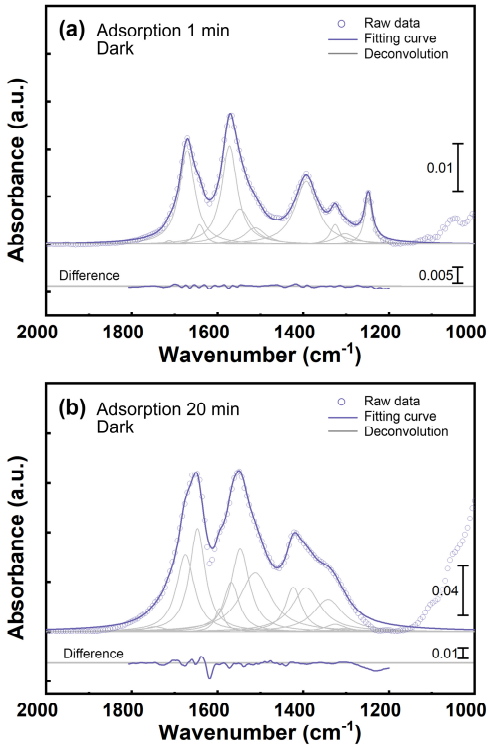

Figure 4.22. Deconvolution of IR spectra of CO_2 and H_2O adsorption on 2.76wt% Au/TiO_2(Ar) after (a) 1 min and (b) 20 min in dark at 30 °C.

Table 4.10. Peak assignments for CO_2/H_2O adsorption on 0.74wt% Au/TiO_2(Ar)

Assignments	1 min (dark)	20 min (dark, saturated adsorption)
c-CO_3[85-86]	1708	1708
CO_2^-[28, 84, 87]	1670	1670
H_2O[84, 86]	1642	1644
b-carbonate-Au[28, 88]	1595	1595
b-HCO_3^--Au or b-CO_3^{2-}-TiO_2[4, 28, 89-91]	1574	1570
b-carbonate[4, 28, 92]	1552	1547
m-carbonate[28, 85, 87, 90]	1510	1510
m-carbonate[28, 85, 93]	1465	1465
bicarbonate[28, 91]	1418	1422
(m-or b-carbonate)[85, 89-90, 92]	1389	1385
b-carbonate[4, 28]		1347
s-carbonate[92]	1325	
b-carbonate[92]		1308
CO_2^- [28, 84-85, 87]	1247	
bicarbonate[85, 88]	1217	

Table 4.11. Peak assignments for CO_2/H_2O adsorption on 2.76wt% Au/TiO_2(Ar)

Assignment	1 min (dark)	20 min (dark, saturated adsorption)
c-CO_3[85-86]	1712	1712
CO_2^-[28, 84, 87]	1671	1675
H_2O[84, 86]	1642	1647
b-carbonate[88]-Au		1595
b-HCO_3^--Au or b-CO_3^{2-}-TiO_2[4, 28, 89-91]	1568	1568
b-carbonate[4, 28, 92]	1548	1547
m-carbonate[28, 85, 87, 90]	1512	1512
m-carbonate[28, 85, 93]	1465	1465
bicarbonate[28, 91]		1423
(m-or b-carbonate)[85, 89-90]	1393	1393
b-carbonate[4, 28]		1342
s-carbonate[92]	1325	1325
b-carbonate[92]	1302	1302
CO_2^- [28, 84, 87]	1248	

To further support the claim that the Ti^{3+} is created during the thermal treatment in Ar, the control experiment monitoring the surface species evolution via DRIFTS is conducted for the interaction between TiO_2(Ar) and TiO_2(UP) with CO_2/H_2O following the same procedure. For TiO_2(Ar) (**Figure 4.23**(a)), the peaks of CO_2^- (1670, 1247 cm^{-1}) also emerge at the beginning of the interaction. It is because annealing pure TiO_2 at oxygen-deficient atmosphere also induces the generation of V_O. To prove that the CO_2^- is derived from the Ti^{3+}, control experiment is also conducted on the interaction between unpretreated TiO_2 (TiO_2(UP)) with CO_2/H_2O and the corresponding time-resolved DRIFT spectra are shown in **Figure 4.23**(b). In **Figure 4.23**(b), the TiO_2(UP) interaction with CO_2 and H_2O in dark does not show the emerging

peaks at 1670 and 1247 cm^{-1}. Therefore, it is rational to claim the CO_2^- is derived by interaction between CO_2 and Ti^{3+}.

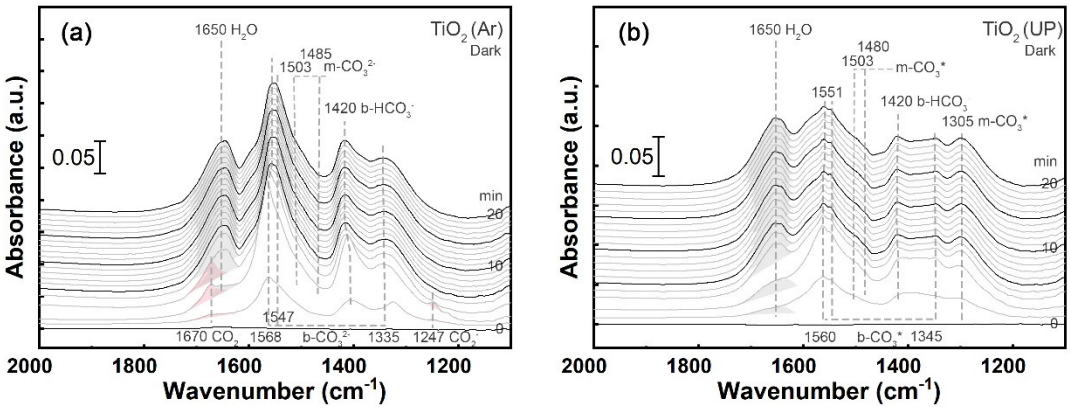

Figure 4.23. Time-resolved DRIFT spectra of (a) TiO_2(Ar) and (b) TiO_2(UP) with CO_2 and H_2O in dark. TiO_2(Ar) represents pristine TiO_2 treated at 300 ºC for 30 min under flowing Ar; TiO_2(UP) denotes pristine TiO_2 without pretreatment.

4.3.6.3 *In-situ* DRIFTS investigations on photocatalytic reaction mechanism

From the catalytic activity results (**Figure 4.14** and **Figure 4.15**), it can conclude that the 0.74wt% Au/TiO_2(Ar) possesses a higher CO_2 conversion rate under UV light, while the 2.76wt% Au/TiO_2(Ar) performs favourably under green light. Therefore, these two reaction conditions were further investigated using time-resolved *in-situ* DRIFTS technique. The following special experimental procedures were designed: (i) CO_2 and H_2O are flowed through the Au/TiO_2(Ar) for 20 min to achieve an adsorption equilibrium; (ii) the inlet gas is then switched to Ar purging the reactor for 10 min to remove free gaseous CO_2/H_2O; (iii) the inlet/outlet valves are closed and UV or green light is switched on for 60 min. Three main objectives can be achieved through this procedure. Firstly, it can demonstrate the reaction intermediates generated immediately after the incident light switch-on. The Ar purge procedure rules out the light-induced gaseous CO_2 re-adsorption, which will result in the (bi)carbonate IR peak rise. Therefore, when light is irradiated onto the catalyst surface, all the increased peaks can be ascribed to the generated reaction intermediates. Secondly, the static environment after Ar purge ensures a

relatively low coverage of reactants on the surface. It will make the newly formed intermediates show more prominent peaks with less overlap. Lastly, the static environment can help to maintain a higher intermediates concentration on the surface. Since the adsorption of CO_2 and H_2O under dark has been described in Section 4.3.6.2 and **Figure 4.20**, this section only focuses on the IR spectra evolution after light switch-on. To ensure the peaks evolution is not due to this special experimental procedure, the control group performed under dark following the entire procedure was conducted. As shown in **Figure 4.24**, there is no peak evolution after adsorption equilibrium.

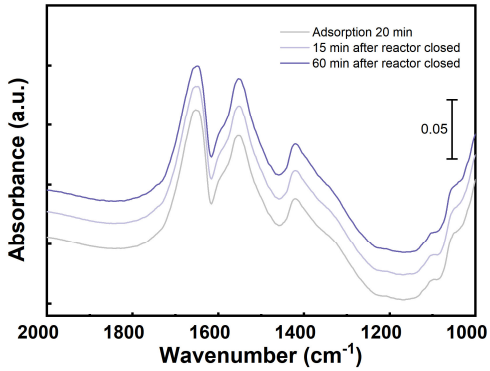

Figure 4.24. *In situ* DRIFT spectra of Au/TiO_2(Ar) after saturated CO_2/H_2O adsorption for 20 min and another 15, 60 min of reaction under static atmosphere. The whole process was conducted in dark at 30 °C.

4.3.6.3.1 0.74wt% Au/TiO_2(Ar) under UV light irradiation

Figure 4.25(a) presents the *in-situ* DRIFT spectra during the first 10 min under UV light irradiation. The UV light induced desorption is the main feature at this period of time. The first significant intensity drop is observed for the peak centred at ~1650 cm^{-1}, which represents the H_2O desorption. Besides, the adsorbed CO_3^{2-} (1595, 1547, 1510, 1390, 1340 cm^{-1}) and HCO_3^- (1416 cm^{-1}) also exhibit reduced intensities. On the contrary, the peaks at 1281 and 1265 cm^{-1} show the trend of increasing, which is due to the fast formation of reaction intermediates under UV light irradiation. Additionally, these two peaks can be reasonably assigned to glyoxylic acid/glyoxylate species according to the adsorption experiments results of possible C2 intermediates on the same

Au/TiO_2 catalysts used in this work (as shown in **Figure 4.19**(d), **Table 4.5**). The details of the IR peak assignments based on the control experiments have been described in section 4.3.6.1. The ν_{as}(C-O) and ν_s(C-O) of carboxylate group in glyoxylate species is hardly observed because their frequencies overlap with the carbonate species. And the relatively small increases ascribed to glyoxylate formation are concealed by the larger decrease trend brought by carbonate/bicarbonate desorption. In addition, the peak at 1340 cm^{-1} emerges as well, which is assigned to the glyoxal species on the surface (as shown in **Figure 4.19**(c), **Table 4.6** and **Table 4.5**).

After the UV light induced desorption reaches equilibrium after ~10 min, the peak evolution reaches the next stage. The spectra of 10 min and 60 min under UV irradiation was compared in **Figure 4.25**(b). In this 50 min reaction under UV irradiation, the following peaks increase: 1683, 1635, 1586, 1557, 1538, 1459, 1413, 1396, 1361 and 1340 cm^{-1}. Among them, the peaks of 1557, 1538 and 1413, 1459 cm^{-1} are assigned to the ν_{as}(COO) and ν_s(COO) of CH_3COO*, respectively. And the peaks at 1683 cm^{-1} correspond to the ν(C=O) of CH_3COO*. The 1396 and 1340 cm^{-1} peaks are ascribed to the asymmetric and symmetric bending vibration of the CH_3 group ($\delta_{as}(CH_3)$ and $\delta_s(CH_3)$) of CH_3COO*. The peak located at 1635, 1586 and 1361 cm^{-1} can be assigned to formate species. The 1586 and 1361 cm^{-1} are derived from the asymmetric and symmetric stretching of carboxylate group, ν_{as}(OCO) and ν_s(OCO) of formate. It is noted that the other featured peaks of formate at ~1560 and ~1410 cm^{-1} (seen in **Figure 4.18**(a)) overlap with the carboxylate group of CH_3COO*. The sum of the formate and acetate peaks makes these two peaks exhibit a more significant increase than others. In the C-H range, a broad peak including the 3018, 2934 cm^{-1} and 2950, 2872 cm^{-1} can be assigned to CH_3COO^* and $HCOO^*$, respectively.

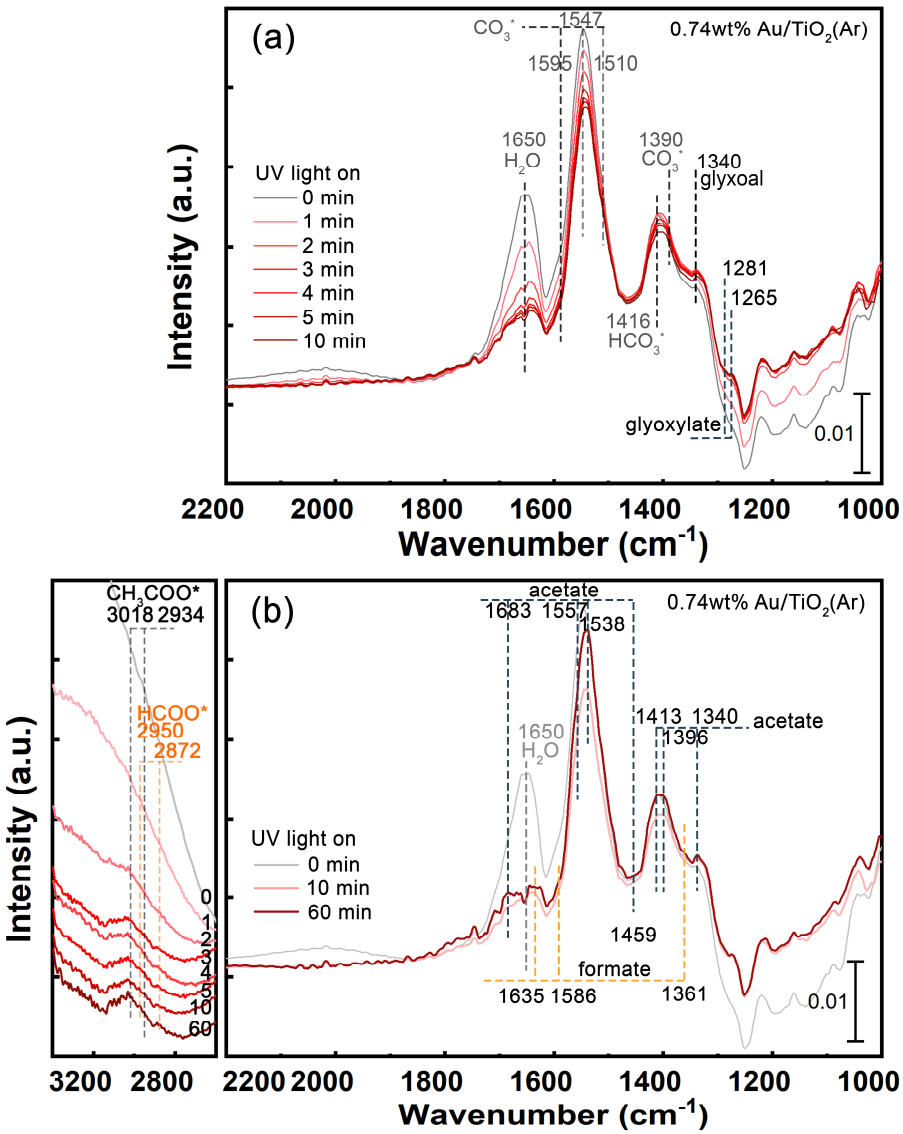

Figure 4.25. *In-situ* DRIFT spectra of 0.74wt% Au/TiO_2(Ar) at 30 °C after UV light-on: (a) evolution within the first 10 min and (b) comparison between 10 min and 60 min.

4.3.6.3.2 2.76wt% Au/TiO_2(Ar) under green light irradiation

The DRIFTS experiment was conducted on 2.76wt% Au/TiO_2(Ar) with green light irradiation following the same experimental procedure as 0.74wt% Au/TiO_2(Ar) under UV light irradiation. Similar to 0.74wt% Au/TiO_2(Ar), the peak evolution after green light switch-on can be divided into 2 parts: desorption-predominated 0-10 min and reaction-predominated 10-60 min. As shown in **Figure 4.26**(a), the green light induces the desorption of H_2O^*, HCO_3^* and CO_3^* species on the surface, which corresponds to the reduced peaks at

1650, 1410, 1595, 1546, 1510, 1392, 1356, 1326 cm^{-1}, respectively. It is noted that the peaks at 1279 and 1270 cm^{-1} emerge at the first 10 min after green light switch-on. The increase of these two peaks can only be explained by the formation of the reaction intermediate, $CHOCOO^*$ (glyoxylate) by referring to the DRIFT spectra of possible intermediate candidates on the same Au/TiO_2 catalysts (**Figure 4.19**(d) & **Table 4.5**). In addition, the 1340 cm^{-1} peak is assigned to glyoxal, while the intensity of glyoxal peak is weaker than the case under UV irradiation condition (**Figure 4.19**(c) & **Table 4.6**). It could be possibly due to the fact that the glyoxal is easily oxidised by the hot holes generated by Au plasmonic excitation.[94] The DRIFT spectra comparison between 10 min and 60 min after green light switch-on is presented in **Figure 4.26**(b). The increase of peaks at 1687, 1550, 1531, 1454, 1415 and 1396 cm^{-1} are assigned to the formation of CH_3COO^* on the surface. The 1632, 1356 cm^{-1} are assigned to the formation of $HCOO^*$ on the surface. In the C-H range, a similar broad peak shows up. The 3018, 2938 cm^{-1} and 2955, 2873 cm^{-1} can be assigned to CH_3COO^* and $HCOO^*$, respectively.

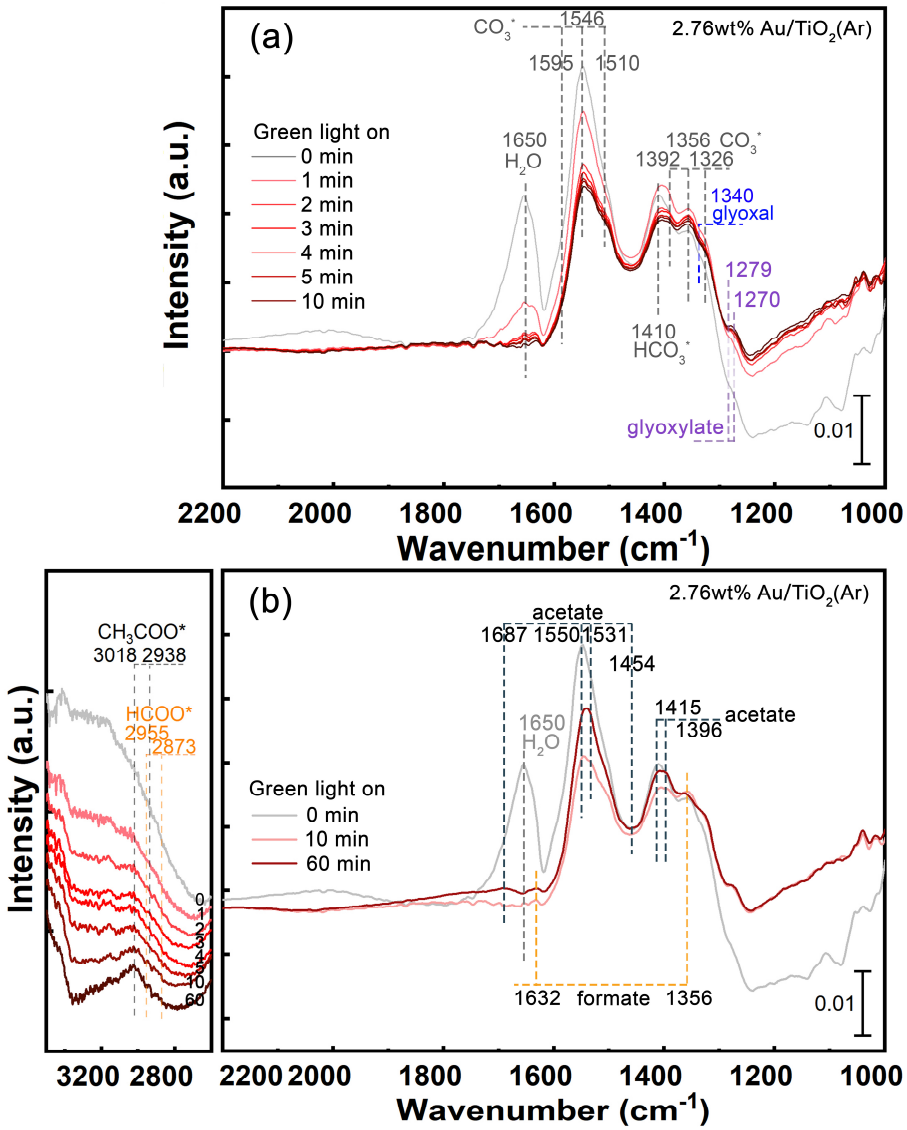

Figure 4.26. *In-situ* DRIFT spectra of 2.76wt% Au/TiO_2(Ar) at 30 °C after green light-on: (a) evolution within the first 10 min and (b) comparison between 10 min and 60 min.

4.3.7 *In-situ* UV-Vis spectroscopy experiments to unravel the role of V_O

The *in-situ* UV-Vis spectroscopy has been reported useful to qualitatively characterize the concentration of V_O.[95-96] Since the light used to drive the reaction also falls in the UV-Vis light range, the UV-Vis spectra are only collected at the interval of 0.5 h with the incident light being blocked temporally.

The *in-situ* UV-Vis DRS experiments were firstly conducted during the Ar treatment of the samples. As shown in **Figure 4.27**(a, b), the broadband (400-500 nm) intensity increase confirms the generation of V_O after treatment in flowing Ar.[95] It is consistent with XPS (**Figure 4.9**) and *in-situ* CO adsorption IR spectroscopy (**Figure 4.11**) experimental results. Therefore, the adsorption band from 400-500 nm is suitable to work as a descriptor of the V_O concentration on the surface.[95] The *in-situ* UV-Vis spectra of 0.74wt% and 2.76wt% Au/TiO_2(Ar) under UV and green light irradiation after different reaction time are plotted in **Figure 4.28**(a-d). To further elucidate the V_O concentration evolution, the absorbances at 450 nm are extracted from the UV-Vis spectra and plotted as a function of time on stream (**Figure 4.29**(a-d)). It can be concluded that the Vo concentration does increase after calcination under Ar flow at 300 °C. However, after the calcinated catalyst surface exposed to the reactants of H_2O and CO_2, the V_O concentration sharply decreases in the first 0.5 h, which is consistent with the highest production rate at the first 0.5 h. The absorbance values at 450 nm reaches stable after 2 h of reaction for all 4 different combinations of catalysts and light irradiation conditions.

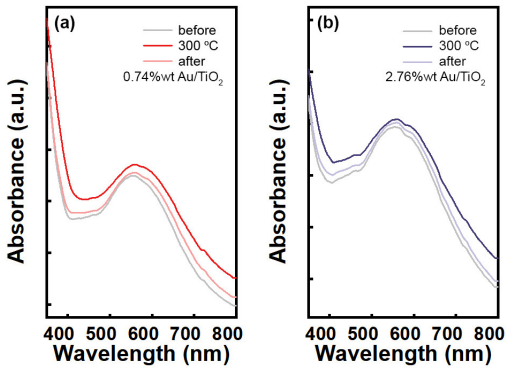

Figure 4.27. The *in-situ* UV-Vis spectra of (a) 0.74wt% Au/TiO_2 and (b) 2.76wt% Au/TiO_2 before, after calcination in flowing Ar at 30 °C and during the treatment at 300 °C.

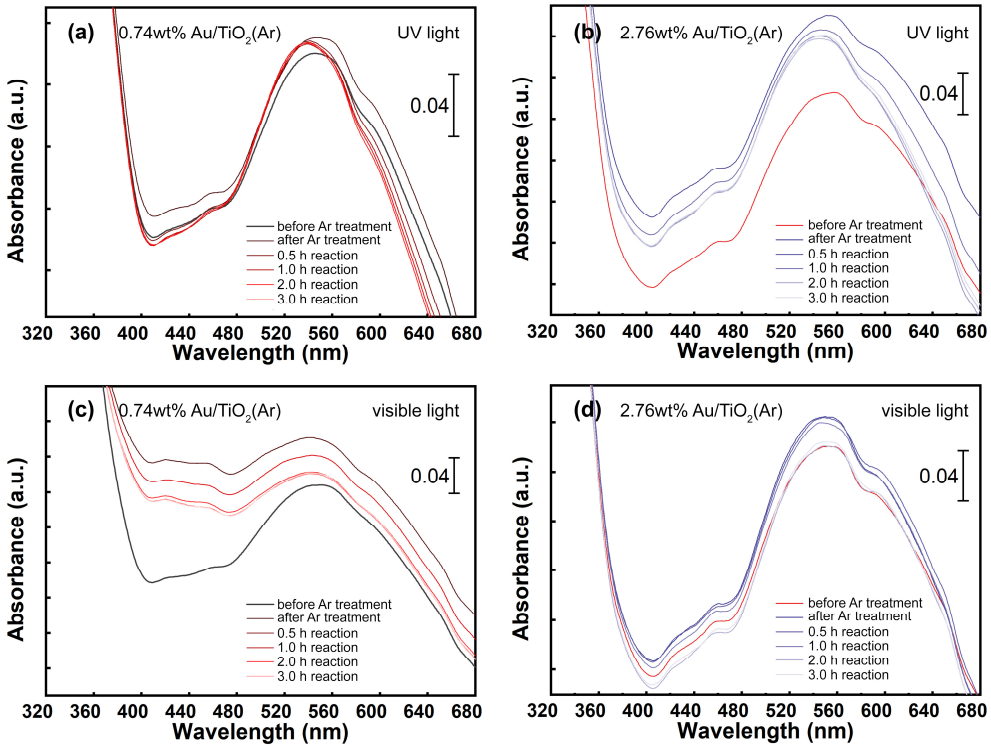

Figure 4.28. The *in-situ* UV-Vis spectra of (a, c) 0.74wt% and (b, d) 2.76wt% $Au/TiO_2(Ar)$ right after activation and following CO_2/H_2O reaction at 30 °C under the irradiation of (a, b) UV and (c, d) visible light.

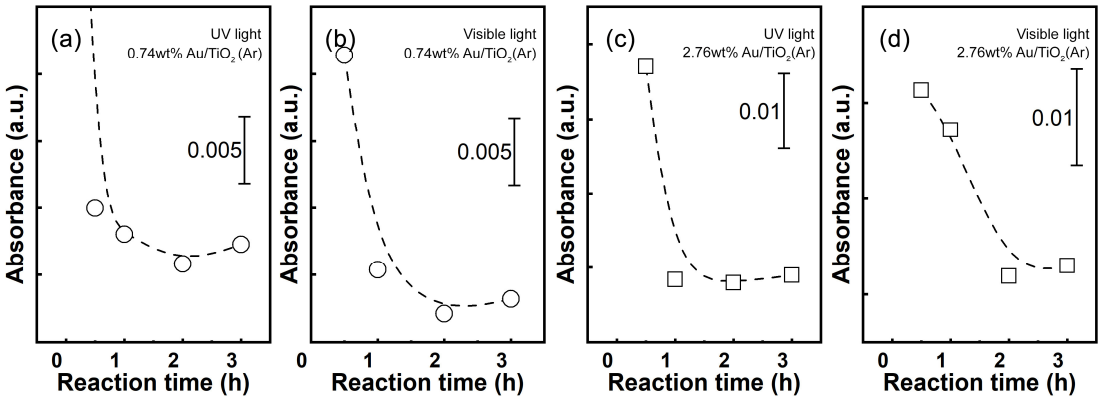

Figure 4.29. The absorbance at 450 nm in *in-situ* UV-Vis spectra versus reaction time of 0.74wt% $Au/TiO_2(Ar)$ under (a) UV, (b) visible light irradiation and 2.76wt% $Au/TiO_2(Ar)$ under (c) UV and (d) visible light irradiation.

4.4 Discussion

4.4.1 The electronic property of Au/TiO_2(Ar) and *CO stability at excitation state.

The CO is a good molecule probe to determine the electronic state of Au/TiO_2, since its characteristic vibration frequency is strongly affected by the electronic properties of the adsorption sites. Known as the Blyholder model,[97] when adsorbed at an electron-rich site, the *CO vibration frequency shows a red-shift due to the back-donation of electrons from the adsorbent to the 2π* antibonding orbital of *CO. Whereas, when adsorbed at an electron-deficient site, the 5σ-donation of electrons from *CO to the binding site causes the blue-shift of the vibration frequency.[29, 98]

In dark, the EMSI on ground state is the critical factor determining the electronic property of the catalysts and further affecting its catalytic performance. Both theoretical and experimental investigations suggest the Au NPs interact weakly with stoichiometric TiO_2 surface.[23] Only with the presence of V_O, the resulting extra electrons will transfer from the Ti^{3+} to the Au and generate negatively charged $Au^{\delta-}$ NPs. In our case, the experimental results confirm the negatively charged Au and existence of V_O after Ar treatment (**Figure 4.9** and **Figure 4.10**). And the negatively charged Au NPs suppress the CO adsorption as suggested by the *in-situ* DRIFTS results (**Figure 4.11**(a)). The 0.74wt% Au/TiO_2(Ar) shows the strongly suppressed CO-Au peak at 30 °C. The similar phenomenon has been observed by Wang et al.[27] that the reduced Au/TiO_{2-x} shows inferior CO oxidation performance than the stoichiometric counterpart due to the suppressed CO adsorption. Therefore, under dark, the retarded CO adsorption is caused by the negatively charged Au, which is derived from the introduction of V_O. It is also noted that the ground-state Au/TiO_2(Ar) electronic property and CO adsorption exhibit size-dependence. Comparing with 0.74wt% Au/TiO_2(Ar), the 2.76wt% Au/TiO_2(Ar) (**Figure 4.11**(a, b)) doesn't show significantly retarded CO adsorption. And the *CO vibration frequency stays less changed indicating the electronic property of Au is less

affected. It can be explained by the dilution effects with larger Au NPs and higher Au loadings. Another reason is the weaker V_O generation enhancement of larger Au NPs comparing with smaller Au nanoclusters.

Based on the understanding of ground-state electronic property, it is more important to unravel the electronic property of Au/TiO_2(Ar) and the stability of *CO under excitation state and the difference between UV and plasmonic excitations. The electronic property of Au NPs determines the *CO stability, which further affects the product selectivity. Because the *CO is the key intermediate for producing CO, CH_4, C_2H_6 and other possible products. As shown in **Figure 4.12**(a, b), the UV and visible light exert opposite effects on the electronic property of Au/TiO_2(Ar) and corresponding CO adsorption. Under UV light irradiation, the 0.74wt%(Ar) shows completely suppressed CO adsorption on Au but enhanced adsorption on TiO_2 at 30 °C. It is because the UV light excited electrons inside TiO_2, which results in the electron-rich $Ti^{(4-\delta)+}$ and $Au^{\delta-}$. The effects of UV irradiation are not significant on 2.76wt% Au/TiO_2(Ar). On the contrary, the green light irradiation causes a completely different result. The excited electrons due to plasmonic excitation in Au NP undergo a back-transfer to the TiO_2 support. The Au NPs, therefore, show positively charged electronic property under continuous irradiation, which is confirmed by the blue shift of the *CO vibration frequency on both 0.74wt% and 2.76wt% Au/TiO_2(Ar). The positive charge state of Au NPs can also enhance the *CO stability at Au site. It is consistent to the theoretical calculation results that the CO shows larger adsorption energy on positively charged Au clusters than neutral or negatively charged clusters in the same size.[99-102] It is also in agreement with the Blyholder model that the positively charged Au will cause less occupied $2\pi^*$ antibonding orbitals which stabilises the *CO.

4.4.2 The essential role of V_O: positive correlation between V_O concentration with reaction rate

As presented in Section 4.3.7 (**Figure 4.28** & **Figure 4.29**), the V_O concentration determined by *in-situ* UV-Vis absorption band intensity clearly shows a positive correlation between reaction rates (**Figure 4.14** & **Figure 4.15**). It suggests the deactivation after 2 h can be attributed to the replenishment of V_O at the perimeter site of Au/TiO_2(Ar). This conclusion is valid for all reaction conditions with small/large Au NPs and UV/green light irradiations. Based on the experimental results, following two critical roles of V_O can be proposed. Firstly, the V_O activates the CO_2 and ensures the breaking of a C=O bond forming *CO. Secondly, the V_O also helps to break the H-O bonds in H_2O providing *H for CO_2 hydrogenation. It is in consistency with the recent work reported by Dilla et al.[103] that the O_2 was not detected in the effluent gases during photosynthesis reaction over TiO_2. In order to further verify the argument that catalyst deactivation is caused by the consumption of V_O on TiO_2 surface. The 2.76wt% Au/TiO_2(Ar) is firstly conducted plasmonic photocatalytic reaction under green light irradiation for 3 h. Then the catalyst is *in-situ* regenerated by calcination at 300 °C under the flowing Ar for 0.5 h. And another 3-h photocatalytic CO_2 reduction reaction is performed again. This regeneration-reaction process is repeated for 3 times and the reaction yields are plotted in **Figure 4.30**. It can be seen that after *in-situ* regeneration, the catalysts can be very well recovered, presenting a similar performance as the fresh catalysts. Since no carbon contamination is introduced during the regeneration, the possibility that deactivation is due to the consumption of active carbon contamination can be rationally ruled out. The regeneration of V_O is the reason for the recovery of the activity of photocatalytic CO_2 reduction with H_2O. In summary, it is confirmed that the V_O in the TiO_2 is responsible for the fast reaction rate at the first 0.5 h. Additionally, the V_O is used up during the photocatalytic CO_2 reduction with H_2O within 3 h, which is the reason for the deactivation of Au/TiO_2(Ar). The generally believed V_O generation driven by either UV or plasmon-induced hot electrons/holes is a rather slow process comparing to V_O consumption.

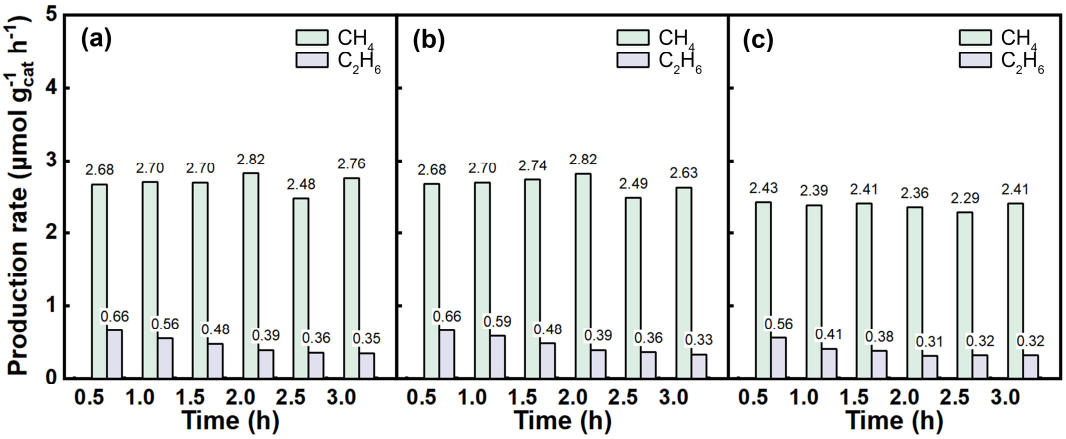

Figure 4.30. The repetition of green light driven plasmonic photocatalytic CO_2 reduction with water at 30 °C on 2.76wt% Au/TiO_2(Ar) for 3 times. Between each time the catalysts are regenerated by calcinating at 300 °C under flowing Ar for 30 min.

4.4.3 Discussion on plausible reaction mechanism for photocatalytic CO_2 reduction with H_2O.

Firstly, CO_2, which is a Lewis acid, intends to adsorb on the V_O sites at the Au/TiO_2 perimeter site. With the replenishment of V_O site of Au/TiO_2 interface, *CO is formed at the same site. The *CO is the initial intermediate indispensable for the following products (CO, CH_4, C_2H_6) generation. It is supported by the following two experimental evidence: under UV irradiation, the CO is the preferred product on both 0.74wt% and 2.76wt% Au/TiO_2(Ar) due to the suppressed CO adsorption (discussed in Section 4.4.1); more importantly, a direct correlation exists between the reaction rate and V_O concentration on both 0.74 and 2.76wt% Au/TiO_2(Ar) (discussed in Section 4.4.2). Another competing first step of CO_2 conversion is the addition of H forming COOH*. However, at the V_O site, it is less likely due to the high activation energy barrier for the hydrogenation comparing with the direct C-O bond dissociation according to the DFT calculation results.[104-105] In the case of formate species, the CO_2 adsorbed on the V_O at the perimeter site of Au/TiO_2(Ar) can be easily hydrogenated to the HCOO* with low activation barrier calculated to be 0.35 eV.[104] While adding the second H to HCOO* becomes energy unfavourable.[106] The formate is likely to be the spectator

rather than the reaction intermediate. The second step of CO_2 photocatalytic reduction is believed to be the hydrogenation of CO* to HCO*. The alternative pathway of further deoxygenation from CO* to C*, the carbene pathway, is less plausible due to the high activation energy of this process on either stoichiometric or defective TiO_2 surface.[105] The further hydrogenation of HCO* results in the production of CH_4, which has been observed on supported Ru via DRIFTS technique.[107] While it is also noted that the CH_4 production rate is less affected by the V_O concentration, it probably indicates there is a parallel reaction pathway for CH_4 formation.[84-85]

The C-C bond formation mechanism is the most important part of the reaction pathway, since a ~20% C_2H_6 selectivity is reached during the plasmonic photocatalytic CO_2 conversion. The mechanisms of CO_2 related C-C coupling in literature are briefly reviewed here. In literature, the C-C coupling mechanism investigations mainly focus on the following research fields: (1) the Fischer-Tropsch reaction for higher hydrocarbon production; (2) the electrochemical CO_2 reduction on Cu surface. For Fischer-Tropsch reaction, the prevailing mechanisms for C-C bond formation in literature include insertion of *CO to *CH_x or *CH_xO_y, and coupling between *CH_x and *CH_y (carbide mechanism). Alternatively, the coupling of oxygenates responsible for C-C bond formation has also been proposed. For example, the coupling between *CHO and *CH_x on Rh and Co was proposed based on DFT calculations.[108-109] For electrochemical C-C coupling mechanism, more complicated pathways have been raised. For example, direct dimerization of *CO as the C-C formation step was proposed based on both the DFT calculation and experimental evidence.[110-112] Dimerization of *CHO was another plausible mechanism.[113-114] Montoya et al.[115] claimed that the dimerization of *CH_2O on Cu exhibited a lower activation energy than *CO dimerization. Additionally, the coupling between more than one type of oxygenate species has also been claimed. For instance, the coupling between *CHO and *CO was proposed under higher overpotential on Cu surface.[113, 116] Besides the Cu surface, Liu et al.[117] reported the acetate electrochemical synthesis on N-doped diamond. A direct dimerization of CO_2^- was believed as

the C-C coupling step. Focusing on the specific topic of photocatalytic CO_2 reduction, C-C bond formation are even more tentative. Firstly, the glyoxal mechanism[118-119] was proposed based on the EPR spectroscopy evidence on TiO_2. The C-C coupling process happened through dimerization of HCO* forming glyoxal (HOC-COH) on TiO_2 surface. The mechanism of direct coupling between two activated CO_2^- was proposed by Yu et al.[120] on Au NPs dispersed in isopropanol solution. CO_2 insertion into $*CH_3$ on Zn doped ZrO_2 was raised to explain the formation of acetate on the surface.[121] CO_2 insertion into HOCO* forming the $HOCOCO_2$* was proposed as the mechanism on the surface of $WO_3 \cdot 0.33H_2O$.[122]

In our case, the C-C coupling mechanism based on the DRIFTS evidence and critical role of V_O is proposed and illustrated in **Figure 4.31**. First of all, the DRIFTS results (**Figure 4.25** and **Figure 4.26**) prove the formation of glyoxylate species (*CHOCOO) on the surface immediately after light switch-on. It suggests the direct coupling between *CHO and $*CO_2$ on the surface. The observed glyoxal species indicate the C-C coupling happens via dimerization of *CHO. As discussed at the beginning of this section, the *HCO formation should be more energy-favourable than *COOH at the V_O site. Therefore, the possible glyoxylate formation pathway through the coupling between *CHO and *COOH is not considered as the main mechanism. Besides the direct indication of possible reaction pathway, the species on the surface observed via *in-situ* DRIFTS can also help to rule out two possible C-C coupling mechanisms on Au/TiO_2 surface: (1) The carbene pathway similar to that in the Fischer-Tropsch reaction. As suggested by the observation of *CHOCOO, the C-C coupling happens before the formation of *C on the surface with breaking both C=O bonds of CO_2; (2) The direct dimerization of CO_2^- radicals. The oxalate species formed due to direct dimerization of CO_2^- are not observed via DRIFTS. After the C-C coupling step, the further hydrogenation of the *CHOCOO can form the other key intermediate observed on the surface, CH_3COO*. However, it is reported that only ~5-10 % of CH_3COO* forms C_2H_6 during the decomposition.[123] It suggests that there could be another reaction pathway responsible for the C_2H_6 production in addition to

CH_3COO^* conversion. A plausible mechanism is the coupling between the alkyl species on the surface, as proposed in Fischer-Tropsch reaction and C-C coupling on Cu surface.

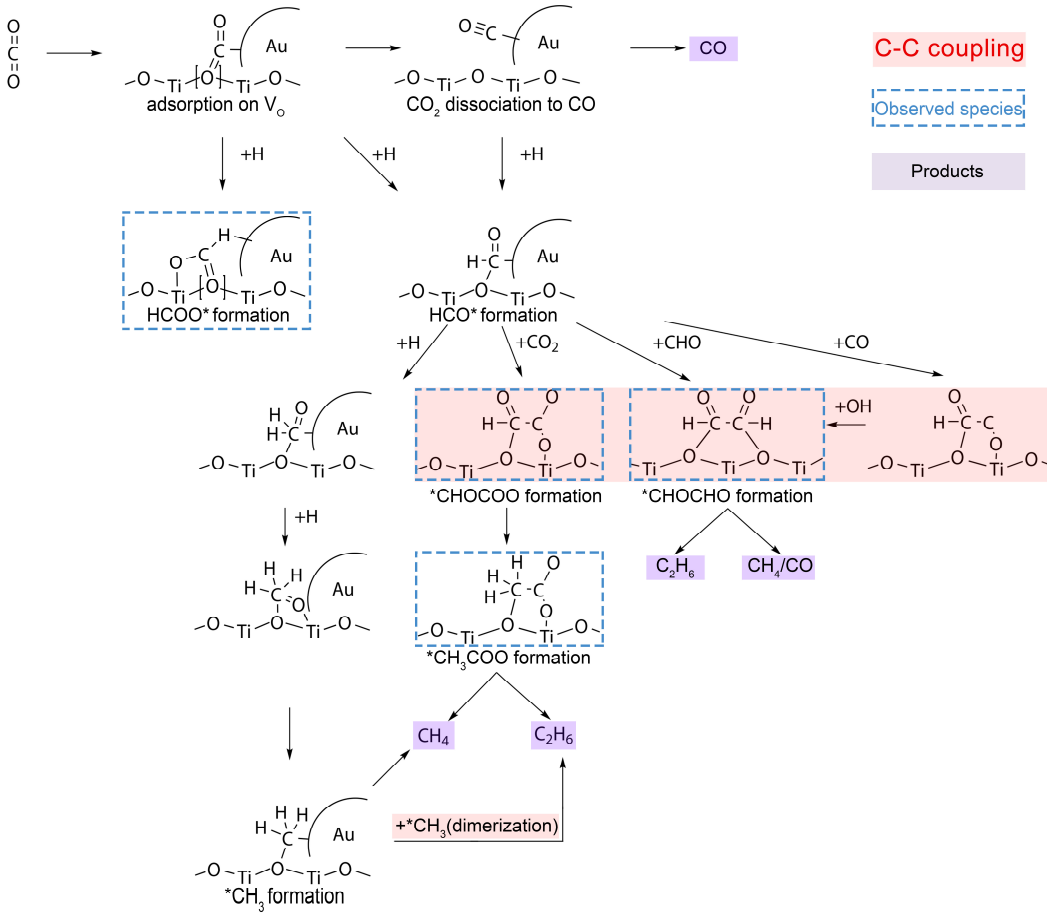

Figure 4.31. The scheme of plausible reaction pathways for C-C coupling and CO, CH_4, C_2H_6 production.

4.4.4 The origin of the product selectivity difference under UV and green light irradiation.

Generally, the product selectivity in photocatalytic CO_2 reduction can be explained from two aspects: (i) thermodynamics and (ii) kinetics. Firstly, the UV light centred at 365 nm corresponds to ~3.4 eV photon energy, which is much higher than the 530 nm green light with ~ 2.4 eV photon energy. Following equations present the potential required to generate the CO, CH_4 and C_2H_6 versus normal hydrogen electrode (NHE, pH =7, 25 °C, 1 atm) [124]:

$$CO_2 + 2H^+ + 2e^- \rightarrow CO + H_2O \quad E^0 = -0.51\ V \tag{4.10}$$

$$CO_2 + 8H^+ + 8e^- \rightarrow CH_4 + 2H_2O \quad E^0 = -0.24\ V \tag{4.11}$$

$$2CO_2 + 14H^+ + 14e^- \rightarrow C_2H_6 + 4H_2O \quad E^0 = -0.27\ V \tag{4.12}$$

It is noted that the CO production requires the highest potential of -0.51 V vs NHE, which is much higher than CH_4 and C_2H_6. Therefore, the CO production is thermodynamically favourable under UV than visible light irradiation. Secondly, the CO, CH_4 and C_2H_6 require 2, 8 and 14 proton-electron coupled transfers, respectively. From the kinetics perspective, the difficulty of CO, CH_4 and C_2H_6 production increases in sequence.

However, in this chapter, these two explanations are insufficient to explain the faster C_2H_6 production and higher C_2H_6 selectivity over 2.76wt% Au/TiO_2(Ar) under plasmonic excitation. As shown in **Figure 4.14** and **Figure 4.15**, under green light irradiation, the C_2H_6 production rate over 2.76wt% Au/TiO_2(Ar) is ~2.4 times as much as the 0.74wt% Au/TiO_2(Ar); and the C_2H_6 selectivity is more than twice as much as 0.74wt% Au/TiO_2(Ar). Moreover, for the same catalyst 2.76wt% Au/TiO_2(Ar), the plasmonic photocatalytic C_2H_6 production rate (0.66 μmol g^{-1}_{cat} h^{-1}) is much larger than the UV light-driven reaction (0.59 μmol g^{-1}_{cat} h^{-1}). The trend to produce more C_2H_6 under plasmonic catalytic condition is unusual because the UV light contains much higher energy than the green light. Considering the *CO is an important reaction intermediate for the formation of C_2H_6 (discussed in Section 4.4.3), it is reasonable to believe *CO stability strongly correlates with C_2H_6 selectivity. As proposed in **Figure 4.31**, the *CO derived from the CO_2 adsorbed at V_O can either desorb from the surface or further converted to *HCO, which is the key intermediate for C-C coupling for C_2H_6 production. As discussed in Section 4.4.1, the plasmonic excitation-induced positively charged Au can stabilize *CO adsorbed on the surface; in comparison, the UV excitation mechanism suppresses the adsorption of *CO. It is the additional important mechanism for the higher C_2H_6 production under plasmonic excitation.

4.5 Summary

The photocatalytic CO_2 reduction with H_2O is investigated over oxygen-deficient Au/TiO_{2-x} driven by UV or visible light under continuous flow condition. The CO_2 conversion rate and product selectivity are found depending on the Au NP size and excitation mechanism. By combining the V_O with plasmonic excitation, the 2.76wt% Au/TiO_{2-x} achieves a 20% selectivity towards C_2H_6. The C-C coupling mechanism for C_2H_6 production is investigated via the *in-situ* DRIFTS experiments. The glyoxal and glyoxylate are observed as the key intermediates after C-C coupling for C_2H_6 production. The high selectivity towards C_2H_6 is rationalized by the *in-situ* determined positively charged Au NPs in Au/TiO_{2-x} under plasmonic excitation and the enhanced stability of the key intermediate *CO. The critical role of V_O in photocatalytic CO_2 reduction with H_2O is also demonstrated. This work provides more insights on the factors promoting the C_2 hydrocarbon production via photocatalytic CO_2 reduction with H_2O, which can inspire future works on photocatalysts design for high value-added products.

4.6 References

1. Wang, K.; Lu, J.; Lu, Y.; Lau, C. H.; Zheng, Y.; Fan, X., *Appl. Catal., B* **2021,** 292, 120147.
2. Zhao, J.; Liu, B.; Meng, L.; He, S.; Yuan, R.; Hou, Y.; Ding, Z.; Lin, H.; Zhang, Z.; Wang, X.; Long, J., *Appl. Catal., B* **2019,** 256, 117823.
3. Li, P.; Liu, L.; An, W.; Wang, H.; Guo, H.; Liang, Y.; Cui, W., *Appl. Catal., B* **2020,** 266, 118618.
4. Yang, C. C.; Yu, Y. H.; van der Linden, B.; Wu, J. C.; Mul, G., *J. Am. Chem. Soc.* **2010,** 132 (24), 8398-8406.
5. Giannozzi, P.; Baroni, S.; Bonini, N.; Calandra, M.; Car, R.; Cavazzoni, C.; Ceresoli, D.; Chiarotti, G. L.; Cococcioni, M.; Dabo, I.; Dal Corso, A.; de Gironcoli, S.; Fabris, S.; Fratesi, G.; Gebauer, R.; Gerstmann, U.; Gougoussis, C.; Kokalj, A.; Lazzeri, M.; Martin-Samos, L.; Marzari, N.; Mauri, F.; Mazzarello, R.; Paolini, S.; Pasquarello, A.; Paulatto, L.; Sbraccia, C.; Scandolo, S.; Sclauzero, G.; Seitsonen, A. P.; Smogunov, A.; Umari, P.; Wentzcovitch, R. M., *J. Phys.: Condens. Matter* **2009,** 21 (39), 395502.
6. Giannozzi, P.; Andreussi, O.; Brumme, T.; Bunau, O.; Buongiorno Nardelli, M.; Calandra, M.; Car, R.; Cavazzoni, C.; Ceresoli, D.; Cococcioni, M.; Colonna, N.; Carnimeo, I.; Dal Corso, A.; de Gironcoli, S.; Delugas, P.; DiStasio, R. A.; Ferretti, A.; Floris, A.; Fratesi, G.; Fugallo, G.; Gebauer, R.; Gerstmann, U.; Giustino, F.; Gorni, T.; Jia, J.; Kawamura, M.; Ko, H. Y.; Kokalj, A.; Kucukbenli, E.; Lazzeri, M.; Marsili, M.; Marzari, N.; Mauri, F.; Nguyen, N. L.; Nguyen, H. V.; Otero-de-la-Roza, A.; Paulatto, L.; Ponce, S.; Rocca, D.; Sabatini, R.; Santra, B.; Schlipf, M.; Seitsonen, A. P.; Smogunov, A.; Timrov, I.;

Thonhauser, T.; Umari, P.; Vast, N.; Wu, X.; Baroni, S., *J. Phys.: Condens. Matter* **2017,** 29 (46), 465901.
7. Ma, X.; Dai, Y.; Guo, M.; Huang, B., *Langmuir* **2013,** 29 (44), 13647-13654.
8. Farnesi Camellone, M.; Zhao, J.; Jin, L.; Wang, Y.; Muhler, M.; Marx, D., *Angew. Chem., Int. Ed.* **2013,** 52 (22), 5780-5784.
9. Morgan, B. J.; Watson, G. W., *J. Phys. Chem. C* **2010,** 114 (5), 2321-2328.
10. Garrity, K. F.; Bennett, J. W.; Rabe, K. M.; Vanderbilt, D., *Comput. Mater. Sci.* **2014,** 81, 446-452.
11. Momma, K.; Izumi, F., *J. Appl. Crystallogr.* **2011,** 44 (6), 1272-1276.
12. Pelton, M.; Aizpurua, J.; Bryant, G., *Laser Photonics Rev.* **2008,** 2 (3), 136-159.
13. Yu, K.; Tian, Y.; Tatsuma, T., *Phys. Chem. Chem. Phys.* **2006,** 8 (46), 5417-5420.
14. Govorov, A. O.; Richardson, H. H., *Nano Today* **2007,** 2 (1), 30-38.
15. Govorov, A. O.; Zhang, H.; Demir, H. V.; Gun'ko, Y. K., *Nano Today* **2014,** 9 (1), 85-101.
16. Oh, H., *J. Catal.* **2002,** 210 (2), 375-386.
17. Li, Z.; Wang, K.; Ge, B.; Zhang, Z.; Wei, Z.; Shi, Z.; Qiao, G., *Chem. Eng. J.* **2020,** 400, 125924.
18. Liu, Z.-K.; Wang, Y., *Computational Thermodynamics of Materials*. Cambridge University Press: 2016.
19. Stoffel, R. P.; Wessel, C.; Lumey, M. W.; Dronskowski, R., *Angew. Chem., Int. Ed.* **2010,** 49 (31), 5242-5266.
20. Wang, K.; Fu, J.; Zheng, Y., *Appl. Catal., B* **2019,** 254, 270-282.
21. Sanjinés, R.; Tang, H.; Berger, H.; Gozzo, F.; Margaritondo, G.; Lévy, F., *J. Appl. Phys.* **1994,** 75 (6), 2945-2951.
22. Chen, W.-T.; Chan, A.; Al-Azri, Z. H. N.; Dosado, A. G.; Nadeem, M. A.; Sun-Waterhouse, D.; Idriss, H.; Waterhouse, G. I. N., *J. Catal.* **2015,** 329, 499-513.
23. Jiang, Z.; Zhang, W.; Jin, L.; Yang, X.; Xu, F.; Zhu, J.; Huang, W., *J. Phys. Chem. C* **2007,** 111 (33), 12434-12439.
24. Worz, A. S.; Heiz, U.; Cinquini, F.; Pacchioni, G., *J. Phys. Chem. B* **2005,** 109 (39), 18418-18426.
25. Boccuzzi, F.; Chiorino, A.; Manzoli, M.; Andreeva, D.; Tabakova, T., *J. Catal.* **1999,** 188 (1), 176-185.
26. Boccuzzi, F.; Chiorino, A.; Manzoli, M.; Lu, P.; Akita, T.; Ichikawa, S.; Haruta, M., *J. Catal.* **2001,** 202 (2), 256-267.
27. Wang, Y.; Widmann, D.; Behm, R. J., *ACS Catal.* **2017,** 7 (4), 2339-2345.
28. Liu, L.; Zhao, C.; Li, Y., *J. Phys. Chem. C* **2012,** 116 (14), 7904-7912.
29. Panayotov, D. A.; Burrows, S. P.; Yates, J. T.; Morris, J. R., *J. Phys. Chem. C* **2011,** 115 (45), 22400-22408.
30. Green, I. X.; Tang, W.; McEntee, M.; Neurock, M.; Yates, J. T., Jr., *J. Am. Chem. Soc.* **2012,** 134 (30), 12717-12723.
31. Bahadori, E.; Tripodi, A.; Villa, A.; Pirola, C.; Prati, L.; Ramis, G.; Dimitratos, N.; Wang, D.; Rossetti, I., *Catal. Sci. Technol.* **2019,** 9 (9), 2253-2265.
32. Murdoch, M.; Waterhouse, G. I.; Nadeem, M. A.; Metson, J. B.; Keane, M. A.; Howe, R. F.; Llorca, J.; Idriss, H., *Nat. Chem.* **2011,** 3 (6), 489-492.
33. Lee, J. E.; Bera, S.; Choi, Y. S.; Lee, W. I., *Appl. Catal., B* **2017,** 214, 15-22.
34. Yoo, S. M.; Rawal, S. B.; Lee, J. E.; Kim, J.; Ryu, H.-Y.; Park, D.-W.; Lee, W. I., *Appl. Catal., A* **2015,** 499, 47-54.
35. Bazzo, A.; Urakawa, A., *ChemSusChem* **2013,** 6 (11), 2095-2102.
36. Poudyal, S.; Laursen, S., *J. Phys. Chem. C* **2018,** 122 (15), 8045-8057.
37. Nanayakkara, C. E.; Dillon, J. K.; Grassian, V. H., *J. Phys. Chem. C* **2014,** 118 (44), 25487-25495.

38. Kecskes, T., *Appl. Catal., A* **2004,** 268 (1-2), 9-16.
39. Miller, K. L.; Lee, C. W.; Falconer, J. L.; Medlin, J. W., *J. Catal.* **2010,** 275 (2), 294-299.
40. Liao, L.-F.; Wu, W.-C.; Chen, C.-Y.; Lin, J.-L., *J. Phys. Chem. B* **2001,** 105 (32), 7678-7685.
41. El-Maazawi, M.; Finken, A. N.; Nair, A. B.; Grassian, V. H., *J. Catal.* **2000,** 191 (1), 138-146.
42. Sridhar, M.; Ferri, D.; Elsener, M.; van Bokhoven, J. A.; Kröcher, O., *ACS Catal.* **2015,** 5 (8), 4772-4782.
43. Kecskés, T.; Raskó, J.; Kiss, J., *Appl. Catal., A* **2004,** 273 (1-2), 55-62.
44. Hauchecorne, B.; Terrens, D.; Verbruggen, S.; Martens, J. A.; Van Langenhove, H.; Demeestere, K.; Lenaerts, S., *Appl. Catal., B* **2011,** 106 (3-4), 630-638.
45. Araña, J.; Doña-Rodríguez, J. M.; Cabo, C. G. i.; González-Díaz, O.; Herrera-Melián, J. A.; Pérez-Peña, J., *Appl. Catal., B* **2004,** 53 (4), 221-232.
46. Sun, S.; Ding, J.; Bao, J.; Gao, C.; Qi, Z.; Li, C., *Catal. Lett.* **2010,** 137 (3-4), 239-246.
47. Wu, W.-C.; Chuang, C.-C.; Lin, J.-L., *J. Phys. Chem. B* **2000,** 104 (36), 8719-8724.
48. Kähler, K.; Holz, M. C.; Rohe, M.; van Veen, A. C.; Muhler, M., *J. Catal.* **2013,** 299, 162-170.
49. Manzoli, M.; Chiorino, A.; Boccuzzi, F., *Appl. Catal., B* **2005,** 57 (3), 201-209.
50. Martinez-Ramirez, Z.; Flores-Escamilla, G. A.; Berumen-España, G. S.; Jimenez-Lam, S. A.; Handy, B. E.; Cardenas-Galindo, M. G.; Sarmiento-Lopez, A. G.; Fierro-Gonzalez, J. C., *Appl. Catal., A* **2015,** 502, 254-261.
51. Flores-Escamilla, G. A.; Fierro-Gonzalez, J. C., *J. Mol. Catal. A: Chem.* **2012,** 359, 49-56.
52. Panayotov, D. A.; Burrows, S.; Mihaylov, M.; Hadjiivanov, K.; Tissue, B. M.; Morris, J. R., *Langmuir* **2010,** 26 (11), 8106-8112.
53. Ho, C.-H.; Shieh, C.-Y.; Tseng, C.-L.; Lin, J.-L., *J. Phys. Chem. C* **2008,** 112 (46), 18134-18140.
54. Ho, C.; Shieh, C.; Tseng, C.; Chen, Y.; Lin, J., *J. Catal.* **2009,** 261 (2), 150-157.
55. Zhao, F.; Yan, F.; Qian, Y.; Xu, Y.; Ma, C. a., *J. Electroanal. Chem.* **2013,** 698, 31-38.
56. Ekström, G. N.; McQuillan, A. J., *J. Phys. Chem. B* **1999,** 103 (48), 10562-10565.
57. Sun, Z.; Kong, L.; Ding, X.; Du, C.; Zhao, X.; Chen, J.; Fu, H.; Yang, X.; Cheng, T., *Phys. Chem. Chem. Phys.* **2016,** 18 (14), 9367-9376.
58. Shen, X.; Wu, H.; Zhao, Y.; Huang, D.; Huang, L.; Chen, Z., *Atmos. Environ.* **2016,** 131, 133-140.
59. Profeta, L. T.; Sams, R. L.; Johnson, T. J.; Williams, S. D., *J. Phys. Chem. A* **2011,** 115 (35), 9886-9900.
60. Cole, A. R. H.; Osborne, G. A., *Spectrochim. Acta, Part A* **1971,** 27 (12), 2461-2490.
61. Wang, L.; Meng, H.; Shen, P. K.; Bianchini, C.; Vizza, F.; Wei, Z., *Phys. Chem. Chem. Phys.* **2011,** 13 (7), 2667-2673.
62. Singh, J.; Gusain, A.; Saxena, V.; Chauhan, A. K.; Veerender, P.; Koiry, S. P.; Jha, P.; Jain, A.; Aswal, D. K.; Gupta, S. K., *J. Phys. Chem. C* **2013,** 117 (41), 21096-21104.
63. Mino, L.; Zecchina, A.; Martra, G.; Rossi, A. M.; Spoto, G., *Appl. Catal., B* **2016,** 196, 135-141.
64. Mino, L.; Negri, C.; Zecchina, A.; Spoto, G., *Z. Phys. Chem.* **2016,** 230 (9), 1441-1451.
65. Tan, T. H.; Wong, R. J.; Scott, J.; Ng, Y. H.; Taylor, R. A.; Aguey-Zinsou, K.-F.; Amal, R., *ACS Catal.* **2018,** 8 (8), 7158-7163.
66. Park, J.; Moon, G.-h.; Shin, K.-O.; Kim, J., *Chem. Eng. J.* **2018,** 343, 689-698.
67. Hu, X.; Bürgi, T., *Appl. Catal., A* **2012,** 449, 139-144.
68. Mendive, C. B.; Bredow, T.; Blesa, M. A.; Bahnemann, D. W., *Phys. Chem. Chem. Phys.* **2006,** 8 (27), 3232-3247.
69. Weisz, A. D.; García Rodenas, L.; Morando, P. J.; Regazzoni, A. E.; Blesa, M. A., *Catal. Today* **2002,** 76 (2-4), 103-112.

70. Young, A. G.; McQuillan, A. J., *Langmuir* **2009,** 25 (6), 3538-3548.
71. Hug, S. J.; Bahnemann, D., *J. Electron. Spectrosc. Relat. Phenom.* **2006,** 150 (2-3), 208-219.
72. Hug, S. J.; Sulzberger, B., *Langmuir* **2002,** 10 (10), 3587-3597.
73. Liao, L.-F.; Lien, C.-F.; Lin, J.-L., *Phys. Chem. Chem. Phys.* **2001,** 3 (17), 3831-3837.
74. Yu, Z.; Chuang, S., *J. Catal.* **2007,** 246 (1), 118-126.
75. Backes, M. J.; Lukaski, A. C.; Muggli, D. S., *Appl. Catal., B* **2005,** 61 (1-2), 21-35.
76. Green, I. X.; Tang, W.; Neurock, M.; Yates, J. T., Jr., *Faraday Discuss.* **2013,** 162 (0), 247-265.
77. Green, I. X.; Tang, W.; Neurock, M.; Yates, J. T., Jr., *J. Am. Chem. Soc.* **2012,** 134 (33), 13569-13572.
78. Ojamae, L.; Aulin, C.; Pedersen, H.; Kall, P. O., *J. Colloid. Interface Sci.* **2006,** 296 (1), 71-78.
79. Rachmady, W.; Vannice, M. A., *J. Catal.* **2002,** 207 (2), 317-330.
80. Topalian, Z.; Stefanov, B. I.; Granqvist, C. G.; Österlund, L., *J. Catal.* **2013,** 307, 265-274.
81. Stefanov, B. I.; Topalian, Z.; Granqvist, C. G.; Österlund, L., *J. Mol. Catal. A: Chem.* **2014,** 381, 77-88.
82. Raskó, J.; Kiss, J., *Appl. Catal., A* **2005,** 287 (2), 252-260.
83. Rekoske, J. E.; Barteau, M. A., *Langmuir* **1999,** 15 (6), 2061-2070.
84. Liu, L.; Zhao, H.; Andino, J. M.; Li, Y., *ACS Catal.* **2012,** 2 (8), 1817-1828.
85. Liu, L.; Jiang, Y.; Zhao, H.; Chen, J.; Cheng, J.; Yang, K.; Li, Y., *ACS Catal.* **2016,** 6 (2), 1097-1108.
86. Yin, G.; Huang, X.; Chen, T.; Zhao, W.; Bi, Q.; Xu, J.; Han, Y.; Huang, F., *ACS Catal.* **2018,** 8 (2), 1009-1017.
87. Liu, L.; Zhao, C.; Miller, J. T.; Li, Y., *J. Phys. Chem. C* **2016,** 121 (1), 490-499.
88. Haruta, M.; Tsubota, S.; Kobayashi, T.; Kageyama, H.; Genet, M. J.; Delmon, B., *J. Catal.* **1993,** 144 (1), 175-192.
89. Gaur, S.; Wu, H.; Stanley, G. G.; More, K.; Kumar, C. S. S. R.; Spivey, J. J., *Catal. Today* **2013,** 208, 72-81.
90. Baltrusaitis, J.; Schuttlefield, J.; Zeitler, E.; Grassian, V. H., *Chem. Eng. J.* **2011,** 170 (2-3), 471-481.
91. Su, W.; Zhang, J.; Feng, Z.; Chen, T.; Ying, P.; Li, C., *J. Phys. Chem. C* **2008,** 112 (20), 7710-7716.
92. Liu, L.; Gu, X.; Cao, Y.; Yao, X.; Zhang, L.; Tang, C.; Gao, F.; Dong, L., *ACS Catal.* **2013,** 3 (12), 2768-2775.
93. Liao, L. F.; Lien, C. F.; Shieh, D. L.; Chen, M. T.; Lin, J. L., *J. Phys. Chem. B* **2002,** 106 (43), 11240-11245.
94. Aslam, U.; Rao, V. G.; Chavez, S.; Linic, S., *Nat. Catal.* **2018,** 1 (9), 656-665.
95. Bobadilla, L. F.; Santos, J. L.; Ivanova, S.; Odriozola, J. A.; Urakawa, A., *ACS Catal.* **2018,** 8 (8), 7455-7467.
96. Nakamura, I.; Negishi, N.; Kutsuna, S.; Ihara, T.; Sugihara, S.; Takeuchi, K., *J. Mol. Catal. A: Chem.* **2000,** 161 (1-2), 205-212.
97. Blyholder, G., *J. Phys. Chem.* **2002,** 68 (10), 2772-2777.
98. Lin, X.; Yang, B.; Benia, H. M.; Myrach, P.; Yulikov, M.; Aumer, A.; Brown, M. A.; Sterrer, M.; Bondarchuk, O.; Kieseritzky, E.; Rocker, J.; Risse, T.; Gao, H. J.; Nilius, N.; Freund, H. J., *J. Am. Chem. Soc.* **2010,** 132 (22), 7745-7749.
99. Wang, F.; Zhang, D.; Xu, X.; Ding, Y., *J. Phys. Chem. C* **2009,** 113 (42), 18032-18039.
100. Xu, H.; Cheng, D.; Gao, Y.; Zeng, X. C., *ACS Catal.* **2018,** 8 (10), 9702-9710.
101. Wu, X.; Senapati, L.; Nayak, S. K.; Selloni, A.; Hajaligol, M., *J. Chem. Phys.* **2002,** 117 (8), 4010-4015.

102. Prestianni, A.; Martorana, A.; Labat, F.; Ciofini, I.; Adamo, C., *J. Phys. Chem. B* **2006,** 110 (25), 12240-12248.
103. Dilla, M.; Jakubowski, A.; Ristig, S.; Strunk, J.; Schlogl, R., *Phys. Chem. Chem. Phys.* **2019,** 21 (29), 15949-15957.
104. Sun, K.; Kohyama, M.; Tanaka, S.; Takeda, S., *J. Phys. Chem. C* **2017,** 121 (22), 12178-12187.
105. Ji, Y.; Luo, Y., *J. Am. Chem. Soc.* **2016,** 138 (49), 15896-15902.
106. Ji, Y.; Luo, Y., *ACS Catal.* **2016,** 6 (3), 2018-2025.
107. Eckle, S.; Anfang, H.-G.; Behm, R. J., *J. Phys. Chem. C* **2010,** 115 (4), 1361-1367.
108. Zhao, Y. H.; Sun, K.; Ma, X.; Liu, J.; Sun, D.; Su, H. Y.; Li, W. X., *Angew. Chem., Int. Ed.* **2011,** 50 (23), 5335-5338.
109. Chen, C.; Wang, Q.; Wang, G.; Hou, B.; Jia, L.; Li, D., *J. Phys. Chem. C* **2016,** 120 (17), 9132-9147.
110. Calle-Vallejo, F.; Koper, M. T., *Angew. Chem., Int. Ed.* **2013,** 52 (28), 7282-7285.
111. Cheng, T.; Xiao, H.; Goddard, W. A., 3rd, *Proc. Natl. Acad. Sci. U. S. A.* **2017,** 114 (8), 1795-1800.
112. Schouten, K. J. P.; Kwon, Y.; van der Ham, C. J. M.; Qin, Z.; Koper, M. T. M., *Chem. Sci.* **2011,** 2 (10), 1902.
113. Garza, A. J.; Bell, A. T.; Head-Gordon, M., *ACS Catal.* **2018,** 8 (2), 1490-1499.
114. Luo, W.; Nie, X.; Janik, M. J.; Asthagiri, A., *ACS Catal.* **2015,** 6 (1), 219-229.
115. Montoya, J. H.; Peterson, A. A.; Nørskov, J. K., *ChemCatChem* **2013,** 5 (3), 737-742.
116. Goodpaster, J. D.; Bell, A. T.; Head-Gordon, M., *J. Phys. Chem. Lett.* **2016,** 7 (8), 1471-1477.
117. Liu, Y.; Chen, S.; Quan, X.; Yu, H., *J. Am. Chem. Soc.* **2015,** 137 (36), 11631-11636.
118. Shkrob, I. A.; Dimitrijevic, N. M.; Marin, T. W.; He, H.; Zapol, P., *J. Phys. Chem. C* **2012,** 116 (17), 9461-9471.
119. Shkrob, I. A.; Marin, T. W.; He, H.; Zapol, P., *J. Phys. Chem. C* **2012,** 116 (17), 9450-9460.
120. Yu, S.; Wilson, A. J.; Heo, J.; Jain, P. K., *Nano Lett.* **2018,** 18 (4), 2189-2194.
121. Zhao, Y.; Cui, C.; Han, J.; Wang, H.; Zhu, X.; Ge, Q., *J. Am. Chem. Soc.* **2016,** 138 (32), 10191-10198.
122. Sun, S.; Watanabe, M.; Wu, J.; An, Q.; Ishihara, T., *J. Am. Chem. Soc.* **2018,** 140 (20), 6474-6482.
123. Kraeutler, B.; Bard, A. J., *J. Am. Chem. Soc.* **2002,** 100 (19), 5985-5992.
124. Chang, X.; Wang, T.; Gong, J., *Energy Environ. Sci.* **2016,** 9 (7), 2177-2196.

Chapter 5. *Operando* DRIFTS-MS Investigation on CO_2 Hydrogenation over Au/TiO_2 under Photo-Thermo Coupled Reaction Condition

This work has been published as *Applied Catalysis, B: Environmental* **2021,** 296, 120341.[1] It was written by the author of present thesis. This chapter is reproduced from the original paper with modifications.

5.1 Introduction

As presented in last two chapters, the photocatalytic CO_2 reduction with H_2O is indeed a green and promising process. The reaction rate and product selectivity can be improved by further optimisation of catalysts. However, pure photocatalysis still shows rather slow reaction rate and fails to meet the requirements of practical implementation. H_2O performs poorly as proton donors for CO_2 conversion. Therefore, it is promising to combine the photocatalysis and thermocatalysis together for a synergistic effect on boosting the CO_2 conversion.[2-5]

In this chapter, the reaction mechanisms of RWGS on Au/TiO_2 under thermocatalytic and plasmon-enhanced thermocatalytic reaction conditions are investigated via *operando* DRIFTS-MS, *ex-situ* EPR spectroscopy, SSITKA and KIE measurements. The CO_2 directly dissociates at the V_O site, the redox pathway, is proven as the main reaction mechanism of CO_2 conversion over Au/TiO_2 under both thermal and photo-thermo coupled reaction condition. Both experimental and theoretical evidence indicate that

the plasmon-excited hot electrons in Au inject into TiO_2 and facilitate the V_O generation, which is the plasmonic enhancement mechanism.

5.2 Experimental

5.2.1 Catalytic performance evaluation

The commercial praying mantis high temperature reactor was used as the reactor to ensure the consistent condition with the *in-situ* spectroscopy analyses. Au/TiO_2 catalyst powder was first pelletised and sieved into the size between 63-125 microns according to the standard palletisation procedure. 10 mg powder was packed into the reactor every time. The temperature of the reactor was calibrated for the whole reaction temperature range with an external thermocouple (0.5 mm in diameter) immersed inside the powder and a thermometer (RS Pro) was used to read the real temperature. CO_2 (1 sccm), H_2 (4 sccm) and Ar (25 sccm) were controlled by mass flow controllers (Omega engineering) and mixed before being introduced into the reactor. The inlet and outlet gas line of the reactor was kept at 130 °C to prevent condensation. The products of reaction were analysed with a GC (Shimadzu 2010 Plus) equipped with a TCD and an FID. A carbon molecular sieve micro-packed column (Restek ShinCarbon ST Column) was used to separate the gaseous analytes for quantitative analyses. The gas flows are regularly calibrated with an electronic gas flowmeter (Agilent). External green (520 nm) and blue (445 nm) LED lights were introduced into the reactor from the front quartz window via an optical liquid guide. The power intensities of green and blue light are measured to be 250.1 and 320 mW cm^{-2} respectively using a thermopile optical power meter (Thorlabs, PM601).

5.2.2 *Operando* DRIFTS-MS analyses

The operando DRIFTS-MS was used to *in-situ* analyse the chemical species on the surface during the reaction. The praying mantis (Harrick) mirror set with the reactor was installed inside an FTIR (Shimadzu, IRTracer-100) with the gas supplying system described in the catalytic performance evaluation

section. Buffering gas lines with Ar (30 sccm) or Air (30 sccm) are also included and controlled with mass flow controllers. The buffering gas lines and the reaction gas lines are switchable with a four-way valve to ensure a fast and reliable exchange. A liquid nitrogen cooled MCT detector was used to detect the IR signal from 1000 to 4000 cm^{-1} with the resolution of 4 cm^{-1}. All the effluent gases during the *operando* experiments were monitored with an online MS (QGA Hiden Analytical).

5.2.3 SSITKA-MS and KIE analyses

SSITKA were conducted using the same setup with *operando* DRIFTS-MS. The stable isotope-labelled $^{13}CO_2$ was used during the SSITKA-MS experiments. The flow of $^{13}CO_2$ was controlled with a mass flow controller and checked regularly to keep it the same to the unlabelled $^{12}CO_2$ flow with an electronic gas flowmeter. The switch between $^{12}CO_2$ and $^{13}CO_2$ gas flow was achieved by a four-way valve. The surface intermediates were observed with the IR spectrophotometer and gaseous effluent from the reactor was monitored by an MS.

The kinetic isotope effects were measured using the same setup with the catalytic performance evaluation. Deuterium gas (D_2) was used to replace the H_2 during the reaction and the gas flow of 4 sccm was calibrated using the electronic gas flowmeter to ensure the same flow with H_2 used in the catalytic performance evaluation. The products were quantitatively measured by a GC.

5.2.4 Theoretical calculation

The theoretical calculation based on DFT was conducted using the Quantum Espresso package.[6-7] The exchange-correlation energy and potential are described at GGA level with PBE functional.[8] The potentials of nuclei and core electrons are approximated with USPP in “GBRV” library.[9] The kinetic energy cutoff for plane-waves and charge density/potential were 45 and 450 Ry respectively according to convergence test results. A gaussian smearing with 0.01 Ry width was used in the calculation to accelerate the convergence. The

energy and force convergence criteria for the structure relaxation were set to be 1×10^{-4} Ry and 1×10^{-3} Ry $Bohr^{-1}$ respectively. Spin-polarization was considered for all the calculation in this work. Bulk anatase TiO_2 and Au were calculated with their primitive cells with 6 × 6 × 6 and 16 × 16 × 16 k-points meshes, respectively. A Hubbard U_{eff} = 4.2 eV[10-12] correction was added to Ti 3d orbitals in a simplified form[13] to have a better description of on-site Coulomb interaction. For small molecule adsorption calculation, the unphysical dipole potential due to periodic boundary condition was corrected along Z-direction. The vdW interaction is corrected using the empirical Grimme-D3 method.[14] The transition states were searched with the CI-NEB method[15] with the convergence threshold of 0.03 eV $Å^{-1}$. All the plots related to DFT calculation were generated with the VESTA.[16] The COHP bonding analyses were conducted with the Lobster code[17] with the structure optimised with PAW pseudopotentials from PSLibrary.[18]

5.3 Results and discussion

5.3.1 Catalysts characterization

The catalysts used in this work is Au/TiO_2 with Au loading of 2.76 wt%, which is determined by ICP-OES. The Au particles size is measured with HAADF-STEM images with typical images, which has been shown in **Figure 4.5**(c, d), Chapter 4. In the HAADF-STEM images, the TiO_2 supports (P25) exhibit darker contrast comparing with Au NP due to its lower atomic weights. The size of the TiO_2 powder is ~20 nm. The Au NPs, showing brighter contrast, homogeneously distribute on the TiO_2 surface. The mean Au particle diameter is calculated to be 4.79±2.0 nm based on the measurement of 160 Au NPs in total (**Figure 4.6**). Additional physical characterizations and discussions including XRD, XPS, N_2 sorption and UV-Vis DRS analyses have already been presented and discussed in Chapter 4. In summary, the 2.76wt% Au/TiO_2 catalysts used in this work is a typical Au/TiO_2 catalyst similar to those reported in many former works for either photo- or thermo- catalytic applications [19-24]. The characterization results prove the Au/TiO_2 is a suitable catalyst for

plasmon-enhanced thermocatalytic CO_2 hydrogenation. It also ensures the mechanism investigation results of this work of general interests to the catalysis research community.

5.3.2 The plasmon-enhanced CO_2 hydrogenation performance at different temperatures

The CO is the only product detected and the production rates (r_{CO}) under different reaction conditions are plotted in **Figure 5.1**(a). It shows that both green and blue light-induced plasmonic hot carriers do enhance the reaction rate for faster CO production at all temperatures investigated. At 200 °C, the CO production rates reach 0.22, 0.70 and 0.30 μmol g_{cat}^{-1} s^{-1} at dark, green and blue light irradiation conditions. The reaction rate at 200 °C under dark is similar to the reported value of typical Au/TiO_2 catalyst.[19, 25] The green-light induced plasmon significantly enhances the reaction rate to ~318% of the dark reaction. Different from the green-light enhancement, the blue-light is less effective in promoting the reaction rate, which shows only 136% promotion comparing with dark reaction condition. It is noted that the net plasmon-induced CO production rate ($r_{CO\text{-}green} - r_{CO\text{-}dark}$ or $r_{CO\text{-}blue} - r_{CO\text{-}dark}$) shows a monoclinic increase with temperature rise. However, the plasmonic enhancement ratios decline. The apparent E_a of reaction on Au/TiO_2 under dark is calculated to be 46±4.7 kJ mol^{-1}, which is similar to literature.[19, 24] The blue and green light induced plasmon-enhanced RWGS reaction exhibit a lower E_a of 44.0±2.9 and 37.0±0.9 kJ mol^{-1}, respectively (**Figure 5.2**), which suggests the plasmonic hot electrons help to lower the kinetic energy barrier of the RDS. Additionally, the correlation between light intensity and plasmon-enhancement is also investigated. The CO production rates are plotted as a function of green light intensity at different reaction temperatures in **Figure 5.1**(b). Note that the CO production rate increases linearly with the light intensity. The high linearity suggests the hot-electrons rather than simple light induced thermal effects are likely to be responsible for the reaction rate enhancement.[26]

Further discussions on the QE and the hot electron enhancement are presented as follows. Amount of net CO generation due to plasmon induced reaction per second can be calculated as the product of reaction rate $r_{CO}(T)$ times loading of catalysts (W_{cat}) 10 mg and the Avogadro' constant N_A:

$$n_{CO}(T) = r_{CO}(T) * W_{\text{cat}} * N_A \tag{5.1}$$

The amount of incident photon and absorbed photon can be calculated from:

$$q_{\text{int photon}} = \frac{P\lambda a}{hc} \tag{5.2}$$

$$q_{\text{abs photon}} = q_{\text{int photon}} \times (1 - 10^{-A}) \tag{5.3}$$

where *a* is the area of catalyst loading, *A* represents the optical absorbance at a specific wavelength. From **Figure 4.2**(b), the absorbances at 445 and 520 nm are 0.576 and 0.702 respectively. Apparent and internal quantum efficiency (AQY and IQY) can be calculated with equ. (5.4) & (5.5). The calculated results are presented in **Table 5.1**.

$$AQY(T) = \frac{2n_{CO}(T)}{q_{\text{int photon}}} \times 100\% \tag{5.4}$$

$$IQY(T) = \frac{2n_{CO}(T)}{q_{\text{abs photon}}} \times 100\% \tag{5.5}$$

In this work, a much higher promotion effects are observed on green light (centred at 520 nm) than the blue (centred at 445 nm) control light group (**Figure 5.1**(a, b)). The power of green and blue light is measured to be 250.1 and 320 mW cm^{-2} respectively. Therefore, quantity of the photon absorbed ($q_{\text{abs photon}}$) can be calculated from the quantity of incident photon ($q_{\text{int photon}}$) and absorbance (*A*) at specific wavelength.[27] At 200 °C, the AQY and IQY under green light irradiation is 3.15% and 3.91% respectively, which is ~640% and ~590% of the corresponding values under blue light irradiation. The much higher quantum efficiency of green-light induced plasmon is observed in every temperature within range from 150 to 500 °C. The intraband excitation by green light showing higher efficiency is commonly observed at the systems that plasmonic metal NPs are loaded onto a support or acting as an antenna.

For instance, Zhou et al.[3] observed the largest enhancement achieved by incident light with wavelength matching the Cu SPR adsorption peak. The Cu is used as the antenna that transfer the LSPR induced hot electrons to the active centre on Ru nanocrystals for ammonia decomposition reaction. A more fundamental work on Au/TiO_2 reported by Tatsuma et al.[28] suggests the correlation between photon to current conversion efficiency (IPCE) and incident light wavelength perfectly matches the light absorption spectrum of the Au/TiO_2. It means the maximum plasmon-induced hot electron injection is achieved when incident light wavelength matches the intraband plasmonic excitation peak. In this work, the Au/TiO_2 catalysts also follow the plasmonic hot electrons injection model. The *in-situ* CO molecule probe adsorption experiments on Au/TiO_2 can provide support for this model. The results in Chapter 4 (**Figure 4.12**) confirm the Au NPs under green light irradiation exhibit slightly positive charge and the hot electrons inject into the TiO_2 at the interface. The extra electron is the main reason for the enhanced V_O formation.[29-31]

Table 5.1. The calculated external and internal quantum efficiency of plasmon-enhanced CO production from CO_2 hydrogenation. The CO production rate is calculated from the rate difference between plasmon-enhanced and dark reaction condition.

	Green			Blue		
	power (mW cm^{-2})	$q_{int\ photon}$	$q_{abs\ photon}$	power (mW cm^{-2})	$q_{int\ photon\ (s^{-1})}$	$q_{abs\ photon\ (s^{-1})}$
	250.1	1.84891×10^{17}	$1.4817E\times10^{17}$	320	2.02446×10^{17}	1.48705×10^{17}
Temperature	$r_{CO\ (\mu mol\ g_{cat}\ s^{-1})}$	AQY	IQY	$r_{CO\ (\mu mol\ g_{cat}\ s^{-1})}$	AQY	IQY
150	0.16277	1.06%	1.32%	0.0167	0.10%	0.14%
200	0.48332	3.15%	3.91%	0.08182	0.49%	0.66%
250	0.85867	5.59%	6.95%	0.14867	0.88%	1.20%
300	1.32759	8.65%	10.75%	0.01374	0.08%	0.11%
350	1.48313	9.66%	12.01%	0.23667	1.41%	1.92%
400	1.85047	12.05%	14.98%	0.07059	0.42%	0.57%
450	2.49846	16.27%	20.23%	0.73699	4.38%	5.97%
500	3.51608	22.90%	28.47%	1.08645	6.46%	8.80%

In summary, these experimental results demonstrate that the light-induced plasmonic enhancement positively correlates with both temperature and light intensity. The apparent activation energy can be significantly reduced by coupling light to thermocatalytic RWGS reaction.

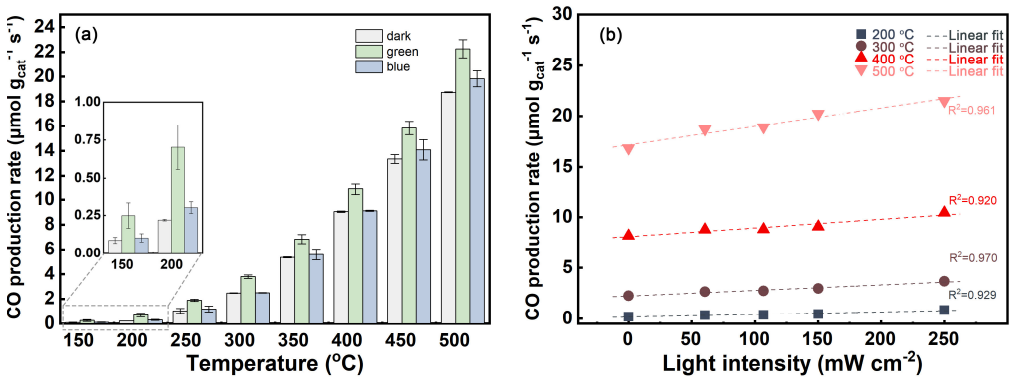

Figure 5.1. (a) The CO production rates of Au/TiO_2 at temperatures ranging from 150 to 500 °C under dark, green light and blue light irradiation. The inset is the magnification of columns at 150 and 200 °C. (b) CO production rates at different green light power densities and the corresponding linear regression analyses.

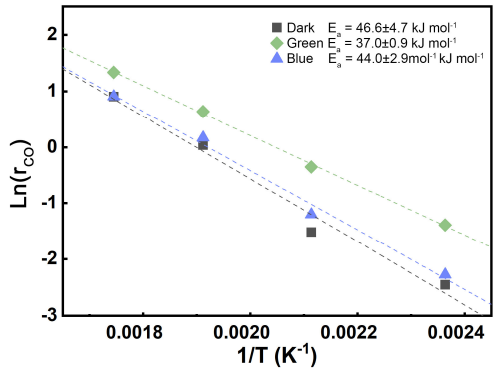

Figure 5.2. The Arrhenius plot and apparent activation energy (E_a) of RWGS reaction over Au/TiO_2 under dark, blue and green-light irradiation.

It is also of interest to investigate the catalytic activity as a function of time. As shown in **Figure 5.3**, the Au/TiO_2 shows an activation process within the first 20 min of time on stream and becomes stable after 120 min. The activation process is likely derived from the V_O accumulation at first 20 min and reaching equilibrium concentration after 120 min. The catalytic performance of pristine TiO_2 support under dark and green light irradiation is also evaluated as control experiments. The corresponding results are shown in **Figure 5.3**. The pristine TiO_2 shows negligible activity at all temperatures under dark. The green light shows small enhancements on CO production rate only at temperature higher than 300 °C. This result is rationalized by the weak absorption of green light when V_O energy level is created within the bandgap of H_2-reduced TiO_2.[32-34]

The net light-induced CO production rate ($r_{CO\text{-}green} - r_{CO\text{-}dark}$) over pristine TiO_2 at 500 °C is measured to be 0.51 μmol g_{cat}^{-1} s^{-1}, which is only 14.5% of the net light-induced CO production rate of 3.52 μmol g_{cat}^{-1} s^{-1} over Au/TiO_2. The more pronounced light-enhancement is attributed to the plasmonic effects of Au NPs. The roles of Au NPs in the thermo-photo coupled CO_2 hydrogenation reaction can be summarized to three aspects: (1) facilitating H_2 dissociation; (2) facilitating V_O generation and (3) producing plasmonic hot electrons.[35-37]

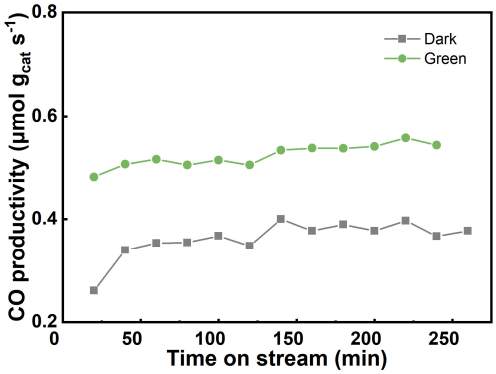

Figure 5.3. The CO productivity as a function of time on stream at 250 °C over Au/TiO_2

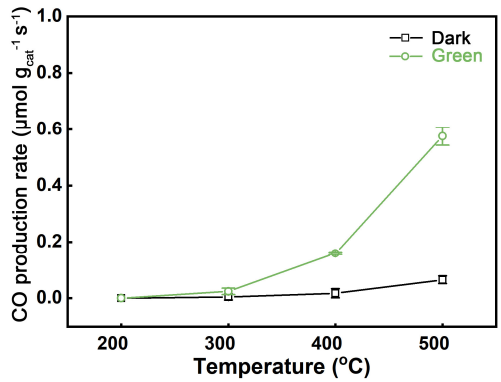

Figure 5.4. The CO production rate of pristine TiO_2 at temperatures of 200-500 °C under dark or green light irradiation.

5.3.3 Enhanced V_O formation elucidated by *ex-situ* EPR analyses

The *ex-situ* EPR measurements providing a direct understanding of V_O concentration in Au/TiO_2 are used to elucidate the effects of light irradiation on V_O creation. The 4 groups of catalysts are treated at 200 °C for 1 h to reach

the equilibrium at the different light irradiation conditions and atmospheres: (i) dark/air, (ii) dark/reaction atmosphere, (iii) green light/reaction atmosphere and (iv) blue light/reaction atmosphere, respectively. As shown in **Figure 5.5**(a), the peaks at g = 2.004 in EPR spectra are assigned to V_O in Au/TiO_2.[38-40] To achieve a quantitative comparison of V_O concentration,[41] the microwave absorbances peaks at 2.004 are double-integrated and the normalised peak areas are plotted in **Figure 5.5**(b). Note that the Au/TiO_2 under green light irradiation and reaction atmosphere shows the highest V_O concentration. Comparatively, the V_O concentration of Au/TiO_2 under dark condition with reaction atmosphere is only 48.6% of the counterpart under green light irradiation. The control group of Au/TiO_2 treated under flowing air in dark at the same temperature exhibits the lowest V_O concentration of 34.0%. The non-zero V_O concentration is because the TiO_2 is an n-type semiconductor possessing intrinsic V_O in the lattice even annealed in air.[42] The EPR analyses results prove that more V_O is generated under plasmonic enhancement comparing with pure thermocatalytic reaction condition.

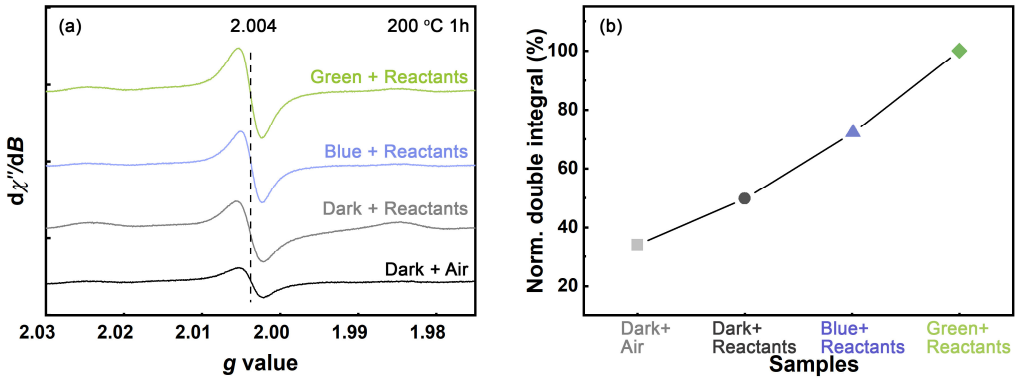

Figure 5.5. (a) EPR spectra of samples treated at different light irradiation conditions and atmospheres at 200 °C for 1h. (b) The corresponding double-integrals of ESR peak at g=2.004 at different atmosphere and light irradiation conditions; the integrals are normalized to the maximum value. The dark, blue and green represent the no irradiation, green light and blue light irradiation conditions, respectively. The reactants atmosphere is the same to the atmosphere during the catalytic performance evaluation.

5.3.4 *In-situ* spectroscopy analysis of reaction mechanism

5.3.4.1 IR peak assignment

To ensure a reliable IR assignment for peaks in our work, $^{12}CO_2/^{13}CO_2$ and formic acid adsorption control experiments were conducted on this specific Au/TiO_2 catalyst.

Control groups were carefully prepared and analysed with DRIFTS technique under identical condition to the reaction but exclusively containing interested chemical structures. For formic acid/formate peak assignment control group, 10 μL formic acid was added into ultrapure water (resistance ≥ 18 MΩ cm), which has been bubbled with N_2 for 30 min in advance to remove the dissolved O_2. Then 30 mg Au/TiO_2 powder was added in to the solution under the protection of N_2 and stirred for another 30 min. The catalysts were further vacuum filtrated and dried in a vacuum oven at room temperature for 5 h. The dried sample was then loaded into the sample cup of the DRIFTS cell. After purging with flowing Ar for 30 min, the cell was heated up to 200 °C and corresponding spectrum was recorded (**Figure 5.6**). The background was chosen as the Au/TiO_2 without surface adsorption at the same atmosphere and temperature. To achieve a reliable peak assignment, the careful comparison with reported data in literature are conducted. The summary of HCOO* assignments is presented in **Table 5.2**.

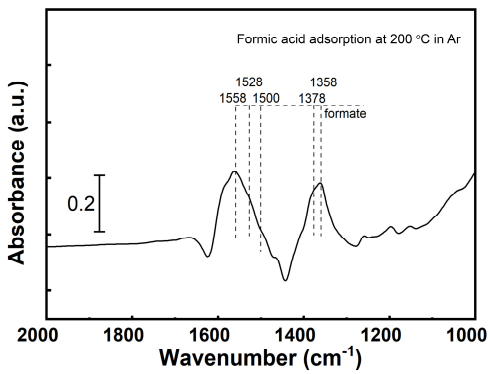

Figure 5.6. DRIFT spectra of formic acid adsorption on Au/TiO_2 at 200 °C under flowing Ar.

Table 5.2. Peak assignments of formic acid adsorption on Au/TiO_2 at 200 °C.

Assignment	Au/TiO_2[43]	TiO_2[44]	TiO_2[45]	Anatase (101)[46]	TiO_2 (110)[47]	Au/TiO_2[48]	This work
ν(C=O)	1658						1680
ν_{as}(OCO)	1550	$1565_{(m)}$ $1550_{(bd)}$	1575	$1598_{(bd)}$ $1647_{(md)}$	1566 1535	1550 1570 $1690_{(m)}$	$1586_{(bd)}$ $1558_{(bd)}$ $1528_{(m)}$
ν_{s}(OCO)	1367	$1378_{(bd)}$ $1360_{(m)}$	1358	$1362_{(bd)}$ $1315_{(md)}$	1363 1393	1382 1367 $1315_{(m)}$	$1378_{(bd)}$ $1358_{(bd)}$ $1315_{(m)}$
δ(CH)	1081	1323	1323	1386			1410
ν(CO) or ν(CH)							1259

Note: m denotes monodentate; bd denotes bridged.

The control group with only carbonate and bicarbonate group was prepared by loading the Au/TiO_2 sample to the DRIFTS cell and introducing either $^{12}CO_2$ or $^{13}CO_2$. In detail, the Au/TiO_2 was firstly treated with flowing Air (20 sccm) at 400 °C for 30 min and followed by flowing Ar (20 sccm) for the same duration time. H_2-free atmosphere is indispensable to achieve the intervention-free carbonate, bicarbonate spectra, since the H^* derived from heterolytic H_2 dissociation interacts with the adsorbed CO_2*. The recorded spectra with corresponding peak deconvolution are presented in **Figure 5.7**.

Based on the harmonic oscillation approximation, the isotope induced vibration peak shift can be theoretically calculated by the following equation:

$$\frac{N_1}{N_2} = \frac{\omega_1}{\omega_2} = \frac{\sqrt{\frac{k}{m_1}}}{\sqrt{\frac{k}{m_2}}} = \sqrt{\frac{m_2}{m_1}} \tag{5.6}$$

where the *N* refers the wavenumber, *ω* the vibration frequency and *k* the force constant. The reduced mass *m* is defined as:

$$m = \frac{m_a m_b}{m_a + m_b} \tag{5.7}$$

Therefore, the O-^{13}C-O peak in ^{13}C-labelled HCO_3* is theoretically shifted to the lower wavenumber by a coefficient of 0.9778. The 1520 and 1324 cm^{-1} are assigned to ν_{as}(O–^{13}C–O) and ν_{s}(O–^{13}C–O) of b-$^{13}CO_3$*. In addition, the 1488, 1456 and 1361 cm^{-1} are assigned to ν_{as}(O–C–O) and ν_{s}(O–C–O) of m-$^{13}CO_3$* respectively. The peaks at 1428 and 1383 are attributed to the H$^{13}CO_3$* groups on the surface. The wavenumber ratios of ^{12}C and ^{13}C species on the surface

is close to the theoretical value. The summary of CO_3*/HCO_3* peak assignments and comparison with literature values is presented in **Table 5.3**.

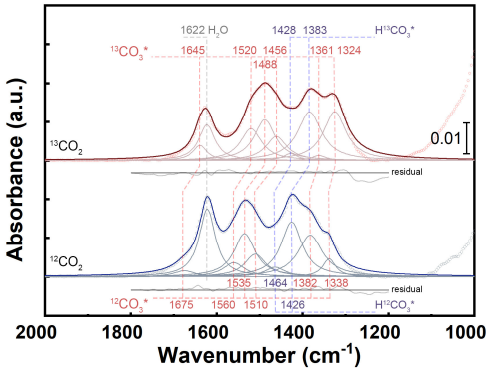

Figure 5.7. DRIFT spectra of Au/TiO_2 with 5% $^{12}CO_2$ or $^{13}CO_2$ balanced in Ar adsorption at 200 °C respectively. The peaks deconvolutions and assignments of carbonate and bicarbonate groups are also presented.

Table 5.3. The assignments of carbonate/bicarbonate peaks in CO_2 adsorption on Au/TiO_2 at 200 °C.

Assignment	Au/TiO_2[49]	$Au\text{-}Cu/TiO_2$[50]	Au/TiO_2[51]	Au/TiO_2[52]	Au/TiO_2[53]	Au/TiO_2 [$^{12}CO_2$ This work]	Au/TiO_2 [$^{13}CO_2$ This work]	freq(^{13}C-O)/ freq(^{12}C-O)
b-carbonate			1670		1670	1675	1645	0.9821
water						1622	1622	
bicarbonate								
carbonate		1589						
b-carbonate ν_{as}(O–C–O)		1555	1564			1560	1520	0.9743
Bi-bicarbonate					1492-1490			
ν(C=O) b-carbonate				1527				
m-carbonate ν_{as}(O–C–O)	1512			1430-1530		1535 1510	1488 1456	0.9694 0.9642
m-bicarbonate					1465	1464	1428	0.9754
Bicarbonate ν_s(O–C–O)	1405-1425	1434			1424	1426	1383	0.9698
bridged-carbonate			1403					
b-carbonate					1396			
m-carbonate ν_{as}(O–C–O)	1364-1384	1378				1382	1361	0.9848
m-carbonate ν_s(O–C–O)				1359				
b-carbonate ν_s(O–C–O)	1308	1323	1323			1338	1324	0.9895
b-bicarbonate on Au					1358-1356, 1337			
bicarbonate		1221	1249					

5.3.4.2 Steady-state operando DRIFTS-MS analysis

In order to elucidate and compare the RWGS reaction pathways under dark and plasmon-enhanced reaction conditions, the *operando* DRIFTS-MS

measurements are conducted at reaction temperature of 200 °C in dark for 30 min, which is followed by an instant switch-on of green light for another 30 min (**Figure 5.8**).

As shown in **Figure 5.8**(a), the time-resolved DRIFT spectra of Au/TiO_2 under dark at 200 °C show that the steady state is reached within 30 min. 4 different species are observed on the surface: H_2O, carbonate, bicarbonate and formate. The peaks at 1620 cm^{-1} are assigned to adsorbed H_2O*[54] due to the consistent peak position in $^{12}CO_2$ and $^{13}CO_2$ adsorption spectra (**Figure 5.7**). The peaks centred at 1560, 1338 cm^{-1} are assigned to the asymmetric and symmetric stretching of O-C-O (ν_{as}(O–C–O) and ν_s(O–C–O)) respectively in bidentate carbonate (b-CO_3*) group. Similarly, the ν_{as}(O–C–O) and ν_s(O–C–O) of monodentate carbonate (m-CO_3*) group exhibit the corresponding peaks at 1535, 1510 and 1382 cm^{-1}.[51-53, 55-56] In the case of bicarbonate, the peaks emerged at 1455, 1440 and 1424 cm^{-1} are assigned to either monodentate or bidentate bicarbonate (m-HCO_3* or b-HCO_3*) on the surface.[49, 53, 55-56] Formate is featured by its C-H vibration peaks at 2955 and 2887 cm^{-1}.[43-45, 48] Additionally, the peaks at 1553, 1360 cm^{-1} are assigned to the asymmetric and symmetric stretching of O-C-O (ν_{as}(O–C–O) and ν_s(O–C–O)) in formate species ($HCOO^*$). After achieving the steady state of surface species under dark reaction condition, the green light is switched on to provide a plasmon-enhanced reaction condition. It can be seen from **Figure 5.8**(b) that the CO production rate indicated by MS signal increases as soon as the green light is turned on, which confirms the existence of plasmon-enhancement. After green light switch-on, the evolution of characteristic peaks for each species are normalized and plotted as a function of time (**Figure 5.8**(c)). The most significant difference after the green light switch-on is the peak intensity drop of H_2O* (1620 cm^{-1}) and HCO_3* (1455, 1440, 1424 cm^{-1}). The peaks corresponding to HCOO* and CO_3* remain stable under light irradiation. In summary, HCOO*, CO_3* and HCO_3* surface species are observed during the reaction. The green light irradiation doesn't introduce extra adsorbed species on the surface, while the adsorbed H_2O* are strongly depressed by light irradiation. Note that the peak at 3412 cm^{-1} is relatively stable, which is very

different from molecular H_2O* at 1620 cm^{-1}. In literature, the 3412 cm^{-1} peak assignment is an unresolved question, which is either assigned to OH* or H_2O*. A very recent combined experiment and simulation work by Mino et al.[57] suggested the peak at around ~3420 cm^{-1} was derived from H-bonded OH* group. Considering the different behaviours of peaks at 3412 and 1620 cm^{-1}, the 3412 cm^{-1} peak might be either OH* or H_2O* adsorbed at site far away from Au/TiO_2 interface, which is less affected by plasmonic effects.

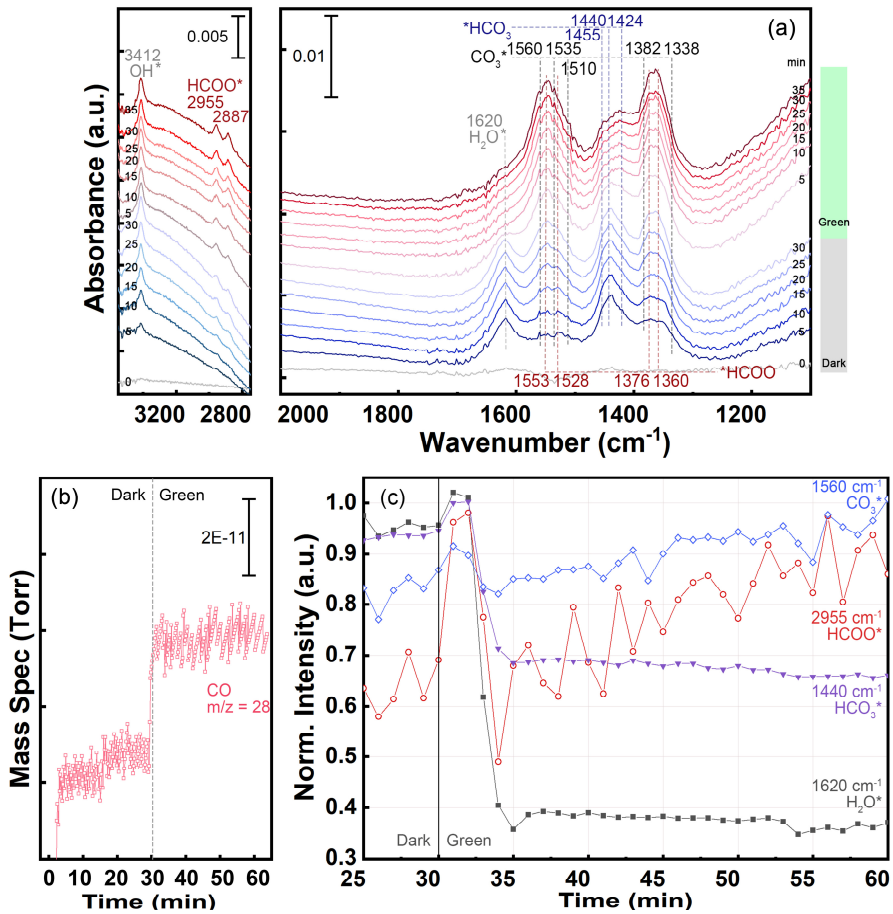

Figure 5.8. (a) Time-resolved operando-DRIFT spectra and corresponding (b) CO MS signal (m/z =28) of Au/TiO_2 interaction with reaction gas mixture (CO_2 1 sccm, H_2 4 sccm, balanced with 25 sccm Ar) at 200 °C. The green light is switched on at 30 min after reaction reaches steady state under dark. (c) The time-resolved IR peak intensity changes representing surface species of CO_3*, HCOO*, HCO_3* and H_2O*. The IR peak intensities are normalized to their individual maximum.

5.3.4.3 Reaction intermediate analysis by SSITKA-MS

To distinguish the observed species in *in-situ* DRIFTS-MS experiments as reaction intermediates or spectators, the SSITKA-MS experiments can provide

more convincible evidence. As shown in **Figure 5.9**(a, b), the IR spectra of Au/TiO_2 under dark reaction condition at 200 °C reach steady-state within 60 min. The peaks stabilized on the surface are assigned to HCOO*, HCO_3*, CO_3* respectively, which are consistent to **Figure 5.8**(a). At 60 min, the $^{12}CO_2$ is instantly switched to $^{13}CO_2$ and the IR peaks of CO_3* and HCO_3* exhibit a gradual decrease. It is noticed that the $H^{12}COO$* at 2955 and 2887 cm^{-1} shows no shift or decrease after switching from $^{12}CO_2$ to $^{13}CO_2$ within 0.5 h. The effluent $^{12}CO/^{13}CO$ is monitored via an MS and the results are shown in **Figure 5.9**(c). The SSITKA-MS experiment for plasmon-enhanced reaction condition is conducted following the same procedure with the dark counterpart except that green light irradiation is implemented throughout the experiment. The time-resolved DRIFT spectra and corresponding IR peak intensity evolutions are presented in **Figure 5.9**(g, h). Similar phenomena are observed in plasmon-enhanced reaction that the IR peaks of HCO_3*, CO_3* shift to lower wavenumbers and the $H^{12}COO$* peak stays stable under plasmon-enhanced reaction condition. In MS plot (**Figure 5.9**(i)), it is noted that the decrease of ^{12}CO MS signal is faster in plasmon-enhanced reaction condition than the dark counterpart. To further verify the correlation between the light induced plasmonic enhancement with the surface lifetime of adsorbed species, a control group with green light power density of ~150 mW (60% of the full power used in **Figure 5.9**(g, h)) is conducted following the same SSITKA-MS protocol. The recorded DRIFT spectra and CO-MS signal evolution are presented in **Figure 5.9**(d, e) and (f). The corresponding mean surface lifetime of $H^{12}CO_3$*, $^{12}CO_3$* and ^{12}CO* ($\tau_{HCO_3^*}$, $\tau_{CO_3^*}$ and τ_{CO^*}) are calculated and summarized in **Table 5.4**. The MS-CO decay profiles are plotted together for a clear comparison as shown in **Figure 5.10**.

The SSITKA-MS experimental results can provide following insights. Firstly, the HCOO* can be identified as the spectator in both the thermo- and plasmon-enhanced thermocatalytic reactions, because IR peak of HCOO* shows no shift after switching from $^{12}CO_2$ to $^{13}CO_2$ in SSITKA-MS experiments conducted in dark or green light irradiation (**Figure 5.9**). Secondly, the CO_3*

and HCO_3* can be ruled out as the main reaction intermediates. As demonstrated in **Table 5.4**, the surface residual time $\tau_{CO_3^*}$ and $\tau_{HCO_3^*}$ shows no correlation to the τ_{CO}.[58] Additionally, the $\tau_{CO_3^*}$ and $\tau_{HCO_3^*}$ are not sensitive to the power density of incident light.

$^{12}CO_2$-$^{13}CO_2$ isotope exchange without H_2 is an important control group to further support the claim that HCO_3* and CO_3* are spectators. The catalysts are loaded into the reactor in the same condition to SSITKA experiments under dark condition. The catalysts are firstly treated with flowing Ar (30 sccm) at 400 °C for 30 min, then cooling down to 200 °C. Then 1 sccm $^{12}CO_2$ balanced by Ar in 30 sccm is introduced into the reactor without H_2 for 60 min to reach the equilibrium on the surface. Then the $^{12}CO_2$/Ar is switched to $^{13}CO_2$/Ar in the same concentration and flow rate. The achieved time-resolved DRIFT spectra are shown in **Figure 5.11**(a) and the IR peak intensity evolution of corresponding chemical species is presented in **Figure 5.11**(b). It is demonstrated that the CO_3* and HCO_3* also show the isotope exchange phenomenon on the surface within 5 min even without the presence of H_2.

In summary, the HCOO*, HCO_3* and CO_3* are all identified as the spectators and the redox reaction pathway is strongly suggested.

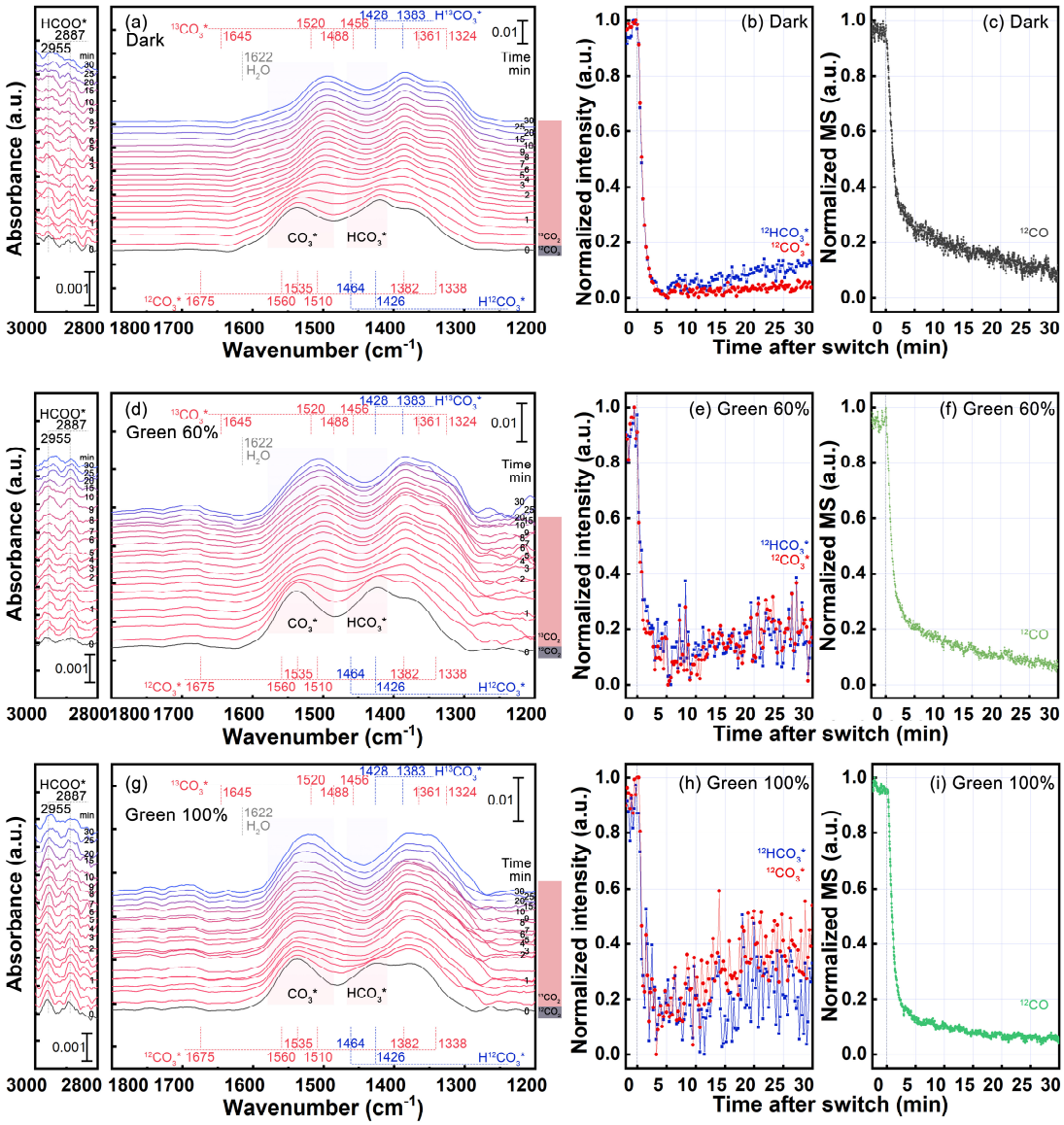

Figure 5.9. The operando-DRIFT spectra of Au/TiO_2 during SSITKA experiments under (a) dark, (d) green light with 60% power and (g) green light in full output, 200 °C. The corresponding time-resolved IR peak intensity decays of $^{12}HCO_3$, $^{12}CO_3$ in (b) dark, (e) 60% output green light and (h) full power green light. The corresponding ^{12}CO MS signal decays in (c) dark, (f) 60% power green light and (i) full power green light. ^{12}CO MS signal is measured with *m*/*z* =28. 0 min represents the moment $^{12}CO_2$ is switched to $^{13}CO_2$.

Table 5.4. Gas-phase (MS) and surface (IR absorbance band) kinetic mean surface lifetime of CO, CO_3^* and HCO_3^* derived from SSIKTA-MS experiments under different reaction conditions at 200 °C.

	GC	MS	IR	
	CO yield ($\mu mol\ g_{cat}^{-1}\ s^{-1}$)	τ_{CO} (s)	$\tau_{CO_3^*}$ (s)	$\tau_{HCO_3^*}$ (s)
Dark	0.22	307.2±18.6	50.6±2.0	47.4±2.4
Green in 60% output (ND2)	0.45	231.0±7.8	45.1±5.4	44.8±6.6
Green in 100% output	0.70	185.4±27.6	42.0±8.4	45.6±14.4

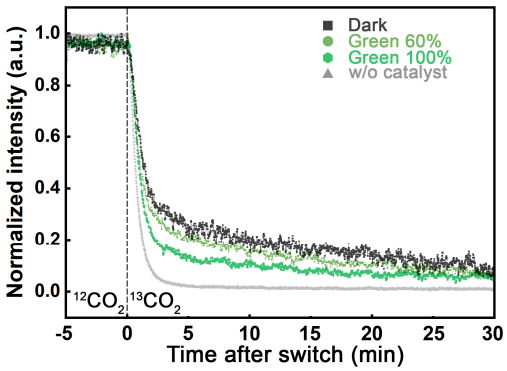

Figure 5.10. The time-resolved normalized MS signal monitoring the ^{12}CO (m/z = 28) within the SSIKTA-MS experiments. The $^{12}CO_2/H_2/Ar$ is switched to $^{13}CO_2/H_2/Ar$ at 0 min. The experiments are conducted at 200 °C, under dark, green light with 100% and 60% output irradiation conditions, respectively. The CO_2 decay curve without catalysts is presented for comparison.

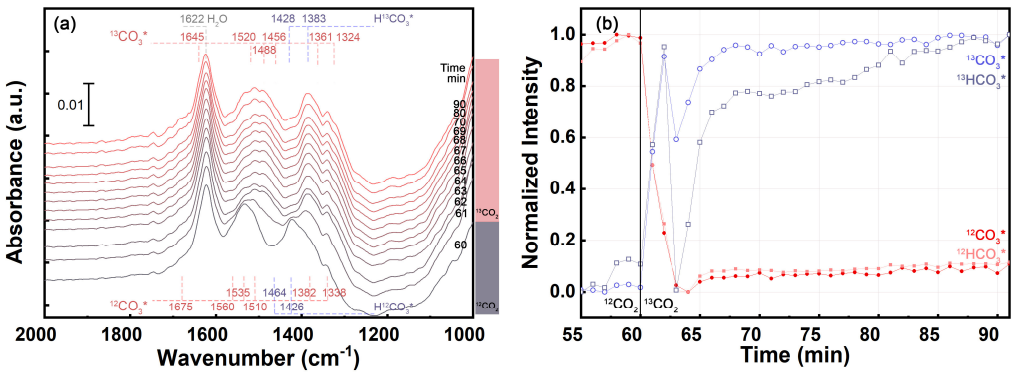

Figure 5.11. (a) The *operando* DRIFT spectra of Au/TiO_2 during SSITKA experiments under dark condition at 200 °C without the presence of H_2. (b) The corresponding selected IR peak intensity evolution as a function of time.

5.3.4.4 Spontaneous dissociation of CO_2 on reduced Au/TiO_{2-x}

Another key evidence to support the redox mechanism of RWGS over Au/TiO_2 is that the CO_2 can be reduced by Au/TiO_{2-x} to CO without the assistance of H* (or H_2). The direct experimental evidence has not been reported before on Au/TiO_2. To provide solid evidence of CO_2 spontaneous dissociation to CO on Au/TiO_{2-x}, the isotope-labelled CO_2 adsorption experiments are conducted at both 30 and 200 °C. The catalysts are firstly *in-situ* treated with flowing air (30 sccm) at 400 °C for 30 min to remove the absorbed H* and carbon species on the surface. Then the Au/TiO_2 catalysts are treated with flowing Ar (30 sccm) at 400 °C for another 30 min to create V_O.[59-60] After cooling down, the $^{12}CO_2$ or $^{13}CO_2$ balanced in Ar is introduced and the surface species evolution is monitored by time-resolved DRIFTS. As shown in **Figure 5.12**(a), the peaks at 2176 and 2077 cm^{-1} emerge immediately after the $^{12}CO_2$ interacts with Au/TiO_{2-x}. These peaks are assigned to the ^{12}CO adsorption on the Ti^{4+} and $Au^{\delta-}$ sites of reduced Au/TiO_{2-x} surface. To rule out possible interventions from residual carbon, isotope labelled $^{13}CO_2$ is used and the corresponding DRIFT spectra are presented in **Figure 5.12**(b). Two peaks at 2138 and 2039 cm^{-1} ascribed to ^{13}CO show up, which match the theoretical frequency shift due to larger reduced mass (Equations (5.6) and (5.7)). More unambiguous spectroscopic evidence of dissociative adsorption of CO_2 on the Au/TiO_{2-x} is achieved at 30 °C with the same experimental procedure (**Figure 5.12**(c, d)). The peaks at the same vibration frequency emerge with a higher intensity.

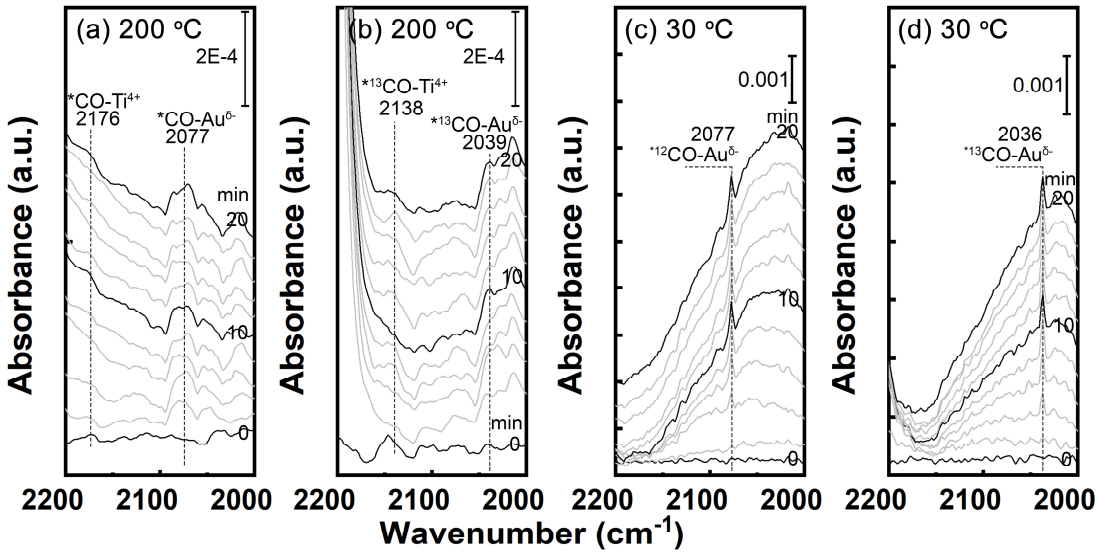

Figure 5.12. Time-resolved DRIFT spectra of CO_2 interaction with reduced Au/TiO_{2-x} in flowing Ar with the absence of H_2: (a) $^{12}CO_2$ (b) $^{13}CO_2$ at 200 °C and (c) $^{12}CO_2$ (d) $^{13}CO_2$ at 30 °C.

Since CO is known as a possible contaminant in CO_2 gas, it is important to rule out the possibility that observed CO* peak in **Figure 5.12** is ascribed to the trace CO in CO_2 gas. An important control group monitoring the CO_2 interaction with irreducible Au/Al_2O_3 catalysts is conducted following the same procedure as Au/TiO_2. $Au/\gamma\text{-}Al_2O_3$ was treated under flowing Air (30 sccm) and Ar (30 sccm) at 400 °C for 30 min in sequence; After cooling down to 30 °C (or 200 °C) under flowing Ar, the IR spectrum background was collected. Then, CO_2/Ar was introduced into the DRIFTS reactor and the collected time-resolved IR spectra were shown in **Figure 5.13**(a, b). As shown in **Figure 5.13**, the absence of CO* peak proves that CO* is not generated from the CO contaminant in CO_2. It also suggests CO* observed in Au/TiO_{2-x} is derived from CO_2 self-dissociation at V_O site.

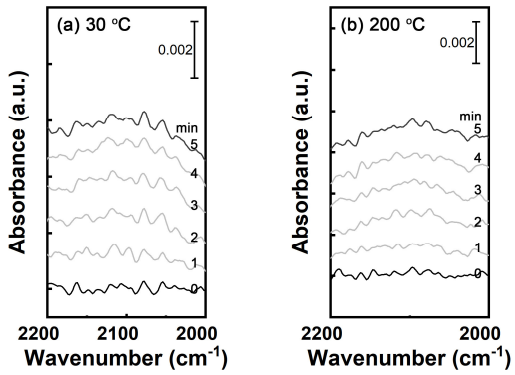

Figure 5.13. Time-resolved DRIFT spectra of $^{12}CO_2$ interaction with pre-treated $Au/\gamma\text{-}Al_2O_3$ in flowing Ar with the absence of H_2 at (a) 30 °C and (b) 200 °C.

Another control experiment is the CO_2 interaction with reduced TiO_{2-x}. P25 was firstly treated in Air (30 sccm) and Ar flow (30 sccm) at 400 °C for 30min in sequence, respectively. After cooling down in Ar to 30 (200) °C, the DRIFT spectra backgrounds were collected. Then CO_2 balanced in Ar was introduced into the reactor, the corresponding spectra were collected and shown in **Figure 5.14**. The CO-Ti peak reported[37, 61-63] to locate at ~2190-2170 cm^{-1} is not observable in **Figure 5.14**. It is attributed to the following three possibilities: (i) too low V_O concentration created during Ar treatment at 400 °C; (ii) CO adsorption on TiO_2 is too weak; (iii) CO_2 cannot dissociate on V_O site of TiO_2. To date, there is no direct experimental evidence supporting the dissociative adsorption of CO_2 on the V_O site of pristine TiO_2;[64] on the contrary, DFT calculation suggests the kinetic energy barrier for the dissociation is very small (~0.04 to 0.15 eV).[65-66] Therefore, though our experiment doesn't support the dissociative adsorption of CO_2 on V_O site of TiO_{2-x}, I believe it is still an unresolved question.

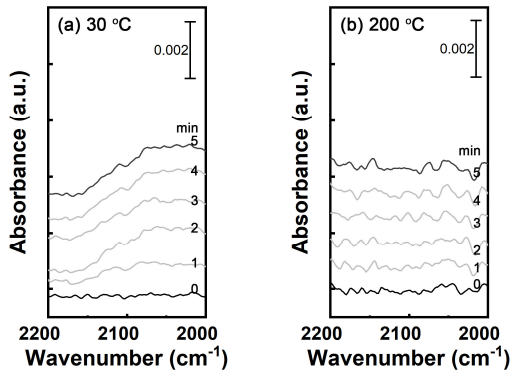

Figure 5.14. Time-resolved DRIFT spectra of $^{12}CO_2$ interaction with pre-treated pure TiO_2 in flowing Ar with the absence of H_2 at (a) 30 °C and (b) 200 °C.

5.3.5 The inverse H/D kinetic isotope effects

To further unravel reaction pathway and the plasmon-enhancement mechanism for CO_2 hydrogenation on Au/TiO_2, H/D kinetic isotope effects are measured at both dark and green-light irradiation conditions at 200 to 400 °C (**Figure 5.15**). The inverse KIE, the ratio between reaction rate using H_2 and D_2 smaller than 1, is observed on both dark and green irritation conditions at all investigated temperature. At reaction temperature of 200, 250, 300, 400 °C, the KIE values are 0.56, 0.59, 0.61, 0.79 under dark and 0.61, 0.64, 0.72, 0.80 under green light irradiation, respectively. Two results are worth notices: first, the KIE of reaction under green-light irradiation condition always shows the higher value (closer to 1) than the counterpart in dark; Secondly, the KIE value differences between reactions under green light irradiation and dark show an abrupt drop to 0.01 at 400 °C.

Since the overall apparent KIE can be a result combining the EIE and KIE, spectrokinetic tests are conducted to determine the EIE of H/D adsorbed on the surface. After annealing the Au/TiO_2 in H_2 (or D_2) balanced by Ar at 200 °C for 30 min, purging with Ar flow for 5 min can remove the gaseous H_2 (or D_2) from the reaction chamber. After the introduction with CO_2, the HCOO* (or DCOO*) formed on the surface is a spectator and stable on the surface (**Figure 5.8**, SSITKA-MS experiments). As shown in **Figure 5.16**(a, b), peak intensity of HCOO* and DCOO* located at 1571, 1568 cm^{-1} are compared.[67] Peaks

located at 1571, 1568 cm^{-1} correspond to C-O asymmetric vibration of HCOO* and DCOO*, respectively. Since this vibration doesn't directly include the isotope atom, the intensity and frequency are less affected. In literature, the calculated intensity ratios for v(C-O) in similar HCOO(H)/DCOO(H) system are very close to 1: ~0.94-1.11.[68-70] Since there is no accurate experimental extinction coefficients available, the EIE calculation here assuming the identical extinction coefficients is a qualitatively correct result. The ratios of their absorbances are summarized in **Figure 5.16**(c), which represents the equilibrium concentration of H*/D* on the surface. It confirms a positive EIE of ~1.5 at 200 and 300 °C, which are not affected by the irradiation condition. In summary, based on the observed inverse apparent H/D KIE and the normal EIE, the inverse KIE of the reaction is proven.

The observed inverse H/D KIE strongly supports the redox mechanism. If the elementary step involving the bond formation/cleavage with H/D is the RDS, a normal KIE is expected, as reported in the literature for Au based catalysts.[71-73] The inverse KIE can be plausibly explained by the steric effects of H_2O* adsorbed at the V_O site.[74-75] The high energy (1.38 eV, **Figure 5.18**(a)) required for H_2O* desorption for V_O generation indicates the H_2O* desorption is another possible rate-limiting step at low temperature. This argument is supported by the evolution of inverse KIE value at higher temperature. At 400 °C when H_2O* is not stable on the surface any more,[76-77] an insignificant inverse KIE is observed, which indicates the RDS is irrelevant to H/D[*]. Under green light irradiation, the KIE values are significantly shifted to 1, comparing with the corresponding dark counterparts. It suggests that the light irradiation can significantly facilitate the desorption of the H_2O* and creation of V_O. The *ex-situ* ESR analyses (**Figure 5.5**) confirm that more V_O is formed during the plasmon-enhanced RWGS reaction under green light irradiation than in dark.

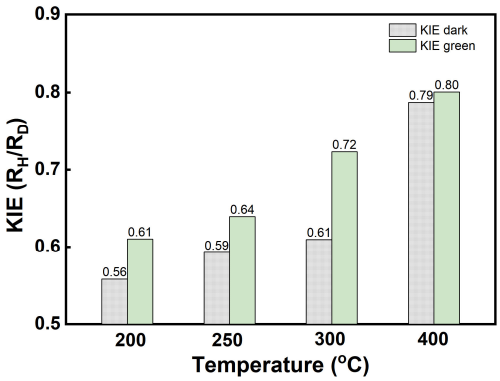

Figure 5.15. H_2/D_2 kinetic isotope effects of RWGS reaction under dark or green-light irradiation condition at different temperatures.

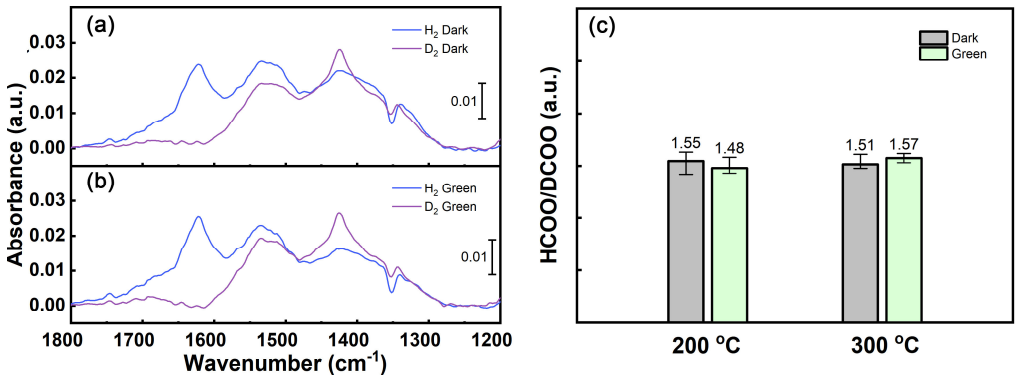

Figure 5.16. DRIFT spectra collected at 200 °C after 30 min H_2 (or D_2) treatment, 5 min Ar purge and 10 min CO_2 reaction in sequence. The H_2 (or D_2) adsorptions are conducted in (a) dark and (b) green light irradiation, respectively. The following CO_2 reactions are kept in dark for both cases. (c) The ratios of $HCOO^*$ and $DCOO^*$ IR absorbances after flowing CO_2 for 10 min.

5.3.6 The theoretical analyses of redox reaction pathway and the plasmonic enhancement mechanism

The redox mechanism is further supported by the DFT calculation results. The Au/TiO_2 catalysts are modelled with an Au nanorod supported by anatase (101) surface, as illustrated in **Figure 5.17**. Unlike the Au nanocluster on rutile (110) facet most commonly used in the literature, the model presented here is more suitable due to the following two considerations: (i) the anatase constitutes ~80% of the commercial P25 TiO_2 used as the support for catalysts in the experiments; (ii) the (101) facet is the most stable surface of anatase.[66] Anatase (101) facet is cleaved based on the relaxed bulk structure and

enlarged to a 2 × 3 supercell with 3 O-Ti-O trilayers. During the calculation, the bottom O-Ti-O layer is fixed to mimic the bulk effects and the top 2 layers are free to relax. The Au nanorod (32 atoms in total) is built in a structure of 3 layers, which are constituted by 3, 3, 2 atoms in cross section, respectively. The Au nanorod axial direction is optimized in a box with 15 Å vacuum space at the rest two directions. Then, the (111) surface of Au nanorod is exposed at the Au/TiO_2 interface leaving a small residual compressive strain of 5.1% on Au nanorod. It is similar to the reported value of 5.53%[78] and 3.7%.[79] A vacuum layer of 17 Å is added for Au/TiO_2 slab model along Z-direction. Due to the supercell of Au/TiO_2 contains 248 atoms in total and possesses 20.8, 11.4 and 26.5 Å lattice constants along X, Y, Z direction respectively, the gamma point sampling provides converged results.

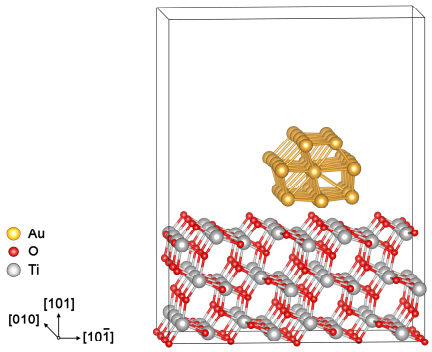

Figure 5.17. Scheme of Au/TiO_2 (anatase (101) surface) slab model for DFT calculations. The arrows indicate the directions in bulk anatase crystal structure.

Because the important role of V_O has been both confirmed by the experimental results in this work as well as in the literature,[19, 80] the redox and carboxyl pathways are compared at the V_O site. As shown in **Figure 5.18**(a, b), the V_O creation is initialised with the heterolytic H_2 dissociation at the perimeter site of Au/TiO_2 [35]. In our case, the adsorption energy of H_2 is calculated to be -0.11 eV and calculated activation energy (E_a) for H_2 dissociation is 0.46 eV, which is close to the reported values determined by calculations [35, 78] and experiment.[81] The generation of H_2O* and V_O through the addition of H* to the HO_{2C} site on the TiO_2 (101) surface exhibits an even smaller E_a of 0.25 eV. In contrast to the two smaller E_a barriers for V_O formation, the desorption of the

H_2O* from the V_O site is an endothermic process requiring a high energy of 1.38 eV. At V_O site, the energy profiles of the two plausible pathways, direct CO_2 dissociation and carboxyl formation, are compared. As shown in **Figure 5.18**(b), the most energy-favourable CO_2 adsorption at the V_O sites is in bended configuration with the adsorption energy of -0.85 eV. The direct dissociation of CO_2* with the formation of CO* on Au and replenishment of V_O exhibits the E_a of 0.65 eV. By contrast, the formation of COOH* at the V_O site requires an E_a of 0.96 eV, which is 1.48 times as large as the E_a of CO_2* dissociation step. The calculation results suggest COOH pathway is less favourable than redox pathway. Although the DFT calculation results, inverse KIE and spontaneous CO_2 dissociation at 30 °C all suggest the redox mechanism is the main pathway, it is also worth mentioning that the COOH pathway is likely to be the minor reaction mechanism at 200 °C. In **Figure 5.10**, the MS-CO signal decays don't follow a perfect exponential function, which suggests a minor reaction pathway exists at 200 °C. Since we have completely ruled out the HCOO pathway, the most plausible candidate is the COOH pathway.

The light-enhanced V_O creation can be explained by the plasmonic hot electron indirect transfer model:[82] plasmonic hot electrons fill into the electron orbitals of adsorbed molecules. For Au/TiO_2, the Schottky barrier smaller than 1 eV[83] is low enough for plasmon-excited hot electrons to overcome and inject into TiO_2 conduction band within a short timescale ~20 fs.[84] This physical model is verified by the *in-situ* IR spectra of CO adsorption on Au/TiO_2 under dark and green light irradiation (**Figure 4.12**). As shown in **Figure 4.12**, the blue-shift of CO-Au peak proves that the Au under green light irradiation is positively charged and the excited electrons inject into the TiO_2 support. Because H_2O* desorption and CO_2* dissociation are the two plausible RDSs, the electronic structure analyses of H_2O* and CO_2* adsorbed at V_O site of Au/TiO_{2-x} are conducted to provide insights on the roles of hot electrons. As shown in **Figure 5.18**(c, e), the COHP bonding analyses are conducted between the O atom in H_2O and two adjacent Ti atoms in TiO_2 slab. It can be seen that the antibonding states are very close to the E_F (0.16 eV above E_F). Especially for O-Ti2, there

are major peaks of anti-bonding states existing above the E_F within 2.34 eV (the photon energy of 530 nm green light). Comparatively, in the COHP analyses of CO_2* at V_O site, the lowest unoccupied C-O1 antibonding state peak locates at 1.94 eV above the E_F (**Figure 5.18**(d, f)). Another possible plasmonic enhancement mechanism is the facilitated H_2 dissociation induced by hot electrons. However, since the molecular orbitals of H_2 only weakly couple with Au/TiO_2, the antibonding orbital is higher than ~2.5 eV above the E_F (**Figure 5.19**). In summary, the COHP analyses indicate the plasmonic hot electrons are more likely to fill into the antibonding orbitals of H_2O* on Au/TiO_2 and significantly enhance its desorption. As the result, the V_O formation is remarkably promoted.

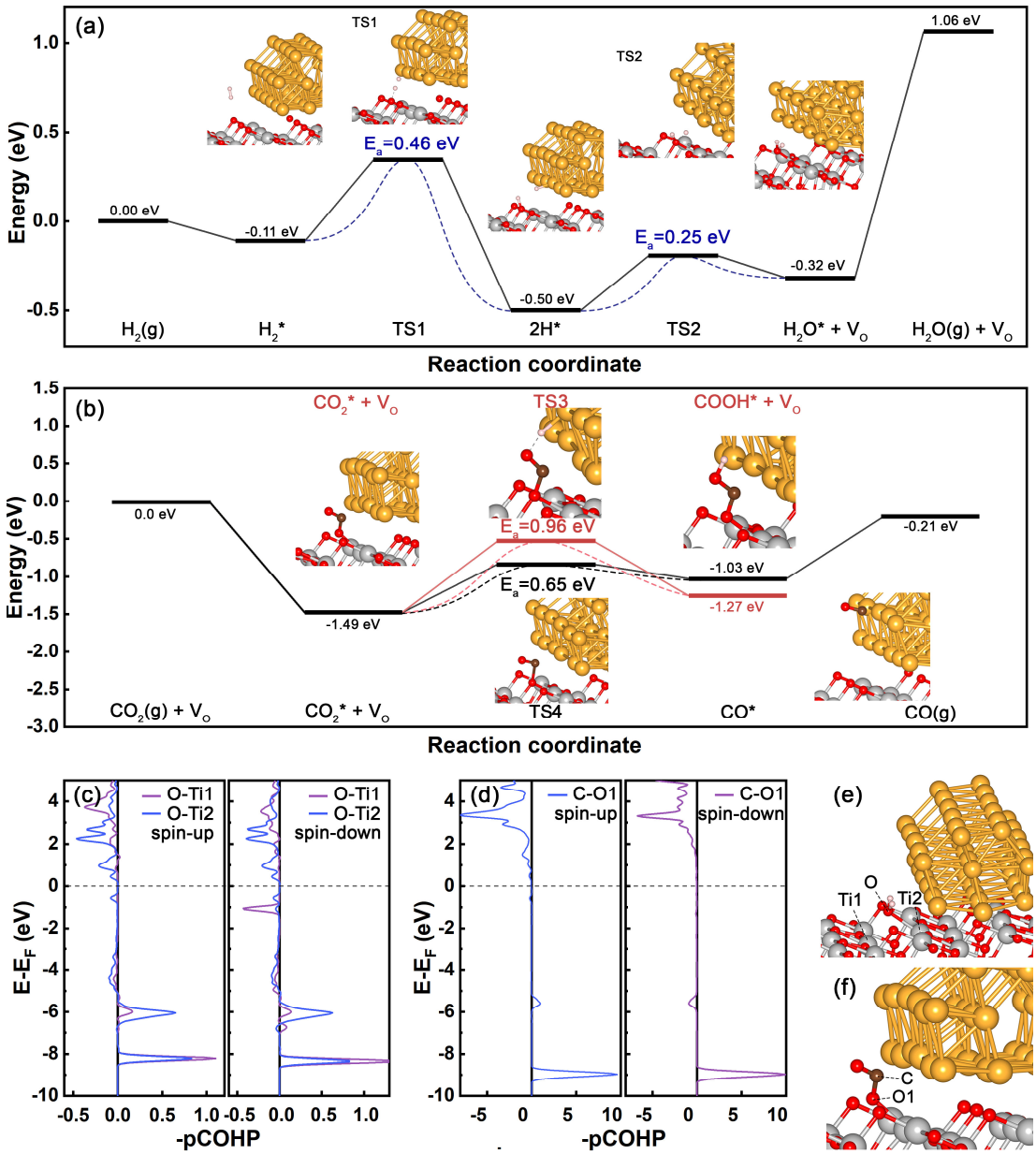

Figure 5.18. DFT calculated reaction profiles of (a) Au/TiO_2 reduction by H_2 with V_O formation and (b) CO_2 conversion to CO via redox or carboxyl pathways. (c) pCOHP bonding analyses between O in H_2O^* at V_O site and two adjacent Ti atoms in TiO_2 slab. The corresponding configuration is shown in (e). (d) pCOHP bonding analyses of C-O in CO_2^* at V_O site of Au/TiO_2. The corresponding configuration is shown in (f). The negative and positive values of pCOHP represent the bonding and antibonding states, respectively. The amber, red, grey, brown and pink spheres represent Au, O, Ti, C and H atoms, respectively.

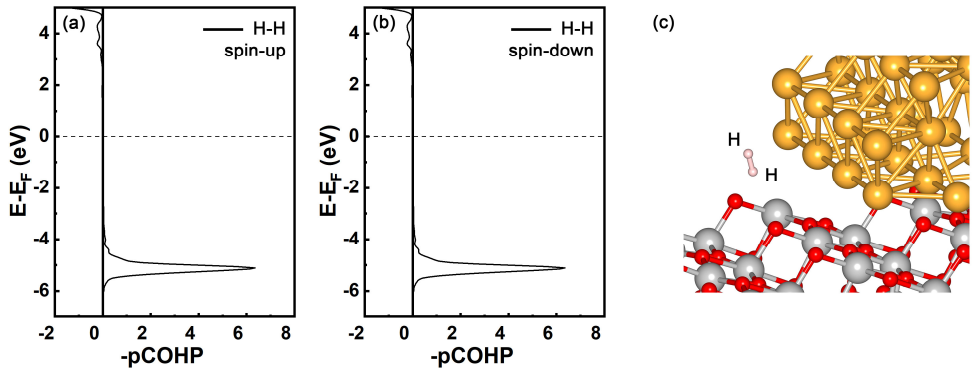

Figure 5.19. (a) Spin-up and (b) spin-down pCOHP bonding analyses between H-H in H_2* at Au/TiO_2 interface. The corresponding configuration is shown in (c). The negative and positive values of pCOHP represent the bonding states and the antibonding states, respectively. The amber, red, grey, brown and pink spheres represent Au, O, Ti, C and H atoms, respectively.

5.4 Summary

The redox mechanism is proven to be the main reaction pathway of CO_2 hydrogenation to CO reaction over Au/TiO_2 under both dark and green light irradiation conditions at 200 °C. The HCOO*, HCO_3* and CO_3* observed in the *operando* DRIFT spectra are identified as the spectators based on SSITKA-MS experimental results. The isotope-labelled DRIFTS experiments demonstrate the dissociative adsorption of CO_2 at the V_O site of Au/TiO_{2-x} in the absence of H_2. Theoretical calculation and inverse H/D KIE further support the redox mechanism and suggest the RDS is likely to be the V_O creation step. Additionally, the facilitation of V_O formation is proven to be the main plasmonic enhancement mechanism by multiple experiments: *ex-situ* EPR spectroscopy analyses confirm a higher V_O concentration is formed during the reaction under green light irradiation; the H_2O IR peak is suppressed by light-irradiation during DRIFTS-MS experiments; the inverse KIE is significantly shifted to 1 under plasmonic enhancement. The COHP bonding analyses suggest the plasmonic hot electrons are most likely to transfer to the antibonding orbitals of H_2O* adsorbed at the V_O site, which promotes the H_2O* desorption and V_O formation. The insights on the mechanism of plasmonic promotion provided by this work can inspire the design of high-performance catalysts specific for photo-thermo coupled catalytic CO_2 conversion in the future.

5.5 References

1. Wang, K.; Cao, M.; Lu, J.; Lu, Y.; Lau, C. H.; Zheng, Y.; Fan, X., *Appl. Catal., B* **2021,** 296, 120341.
2. Wang, Z.-j.; Song, H.; Pang, H.; Ning, Y.; Dao, T. D.; Wang, Z.; Chen, H.; Weng, Y.; Fu, Q.; Nagao, T.; Fang, Y.; Ye, J., *Appl. Catal., B* **2019,** 250, 10-16.
3. Zhou, L.; Swearer, D. F.; Zhang, C.; Robatjazi, H.; Zhao, H.; Henderson, L.; Dong, L.; Christopher, P.; Carter, E. A.; Nordlander, P.; Halas, N. J., *Science* **2018,** 362 (6410), 69-72.
4. Wang, Z. J.; Song, H.; Liu, H.; Ye, J., *Angew. Chem., Int. Ed.* **2020,** 59 (21), 8016-8035.
5. Tan, T. H.; Xie, B.; Ng, Y. H.; Abdullah, S. F. B.; Tang, H. Y. M.; Bedford, N.; Taylor, R. A.; Aguey-Zinsou, K.-F.; Amal, R.; Scott, J., *Nat. Catal.* **2020,** 3 (12), 1034-1043.
6. Giannozzi, P.; Baroni, S.; Bonini, N.; Calandra, M.; Car, R.; Cavazzoni, C.; Ceresoli, D.; Chiarotti, G. L.; Cococcioni, M.; Dabo, I.; Dal Corso, A.; de Gironcoli, S.; Fabris, S.; Fratesi, G.; Gebauer, R.; Gerstmann, U.; Gougoussis, C.; Kokalj, A.; Lazzeri, M.; Martin-Samos, L.; Marzari, N.; Mauri, F.; Mazzarello, R.; Paolini, S.; Pasquarello, A.; Paulatto, L.; Sbraccia, C.; Scandolo, S.; Sclauzero, G.; Seitsonen, A. P.; Smogunov, A.; Umari, P.; Wentzcovitch, R. M., *J. Phys.: Condens. Matter* **2009,** 21 (39), 395502.
7. Giannozzi, P.; Andreussi, O.; Brumme, T.; Bunau, O.; Buongiorno Nardelli, M.; Calandra, M.; Car, R.; Cavazzoni, C.; Ceresoli, D.; Cococcioni, M.; Colonna, N.; Carnimeo, I.; Dal Corso, A.; de Gironcoli, S.; Delugas, P.; DiStasio, R. A.; Ferretti, A.; Floris, A.; Fratesi, G.; Fugallo, G.; Gebauer, R.; Gerstmann, U.; Giustino, F.; Gorni, T.; Jia, J.; Kawamura, M.; Ko, H. Y.; Kokalj, A.; Kucukbenli, E.; Lazzeri, M.; Marsili, M.; Marzari, N.; Mauri, F.; Nguyen, N. L.; Nguyen, H. V.; Otero-de-la-Roza, A.; Paulatto, L.; Ponce, S.; Rocca, D.; Sabatini, R.; Santra, B.; Schlipf, M.; Seitsonen, A. P.; Smogunov, A.; Timrov, I.; Thonhauser, T.; Umari, P.; Vast, N.; Wu, X.; Baroni, S., *J. Phys.: Condens. Matter* **2017,** 29 (46), 465901.
8. Perdew, J. P.; Burke, K.; Ernzerhof, M., *Phys. Rev. Lett.* **1996,** 77 (18), 3865-3868.
9. Garrity, K. F.; Bennett, J. W.; Rabe, K. M.; Vanderbilt, D., *Comput. Mater. Sci.* **2014,** 81, 446-452.
10. Ma, X.; Dai, Y.; Guo, M.; Huang, B., *Langmuir* **2013,** 29 (44), 13647-13654.
11. Farnesi Camellone, M.; Zhao, J.; Jin, L.; Wang, Y.; Muhler, M.; Marx, D., *Angew. Chem., Int. Ed.* **2013,** 52 (22), 5780-5784.
12. Morgan, B. J.; Watson, G. W., *J. Phys. Chem. C* **2010,** 114 (5), 2321-2328.
13. Cococcioni, M.; de Gironcoli, S., *Phys. Rev. B* **2005,** 71 (3), 035105.
14. Grimme, S.; Antony, J.; Ehrlich, S.; Krieg, H., *J. Chem. Phys.* **2010,** 132 (15), 154104.
15. Smidstrup, S.; Pedersen, A.; Stokbro, K.; Jonsson, H., *J. Chem. Phys.* **2014,** 140 (21), 214106.
16. Momma, K.; Izumi, F., *J. Appl. Crystallogr.* **2011,** 44 (6), 1272-1276.
17. Maintz, S.; Deringer, V. L.; Tchougreeff, A. L.; Dronskowski, R., *J. Comput. Chem.* **2016,** 37 (11), 1030-1035.
18. Dal Corso, A., *Comput. Mater. Sci.* **2014,** 95, 337-350.
19. Bobadilla, L. F.; Santos, J. L.; Ivanova, S.; Odriozola, J. A.; Urakawa, A., *ACS Catal.* **2018,** 8 (8), 7455-7467.
20. Priebe, J. B.; Radnik, J.; Lennox, A. J. J.; Pohl, M.-M.; Karnahl, M.; Hollmann, D.; Grabow, K.; Bentrup, U.; Junge, H.; Beller, M.; Brückner, A., *ACS Catal.* **2015,** 5 (4), 2137-2148.
21. Qian, K.; Sweeny, B. C.; Johnston-Peck, A. C.; Niu, W.; Graham, J. O.; DuChene, J. S.; Qiu, J.; Wang, Y. C.; Engelhard, M. H.; Su, D.; Stach, E. A.; Wei, W. D., *J. Am. Chem. Soc.* **2014,** 136 (28), 9842-9845.

22. Jovic, V.; Chen, W.-T.; Sun-Waterhouse, D.; Blackford, M. G.; Idriss, H.; Waterhouse, G. I. N., *J. Catal.* **2013,** 305, 307-317.
23. Kotobuki, M.; Leppelt, R.; Hansgen, D. A.; Widmann, D.; Behm, R. J., *J. Catal.* **2009,** 264 (1), 67-76.
24. Upadhye, A. A.; Ro, I.; Zeng, X.; Kim, H. J.; Tejedor, I.; Anderson, M. A.; Dumesic, J. A.; Huber, G. W., *Catal. Sci. Technol.* **2015,** 5 (5), 2590-2601.
25. Zhang, X.; Li, X.; Zhang, D.; Su, N. Q.; Yang, W.; Everitt, H. O.; Liu, J., *Nat. Commun.* **2017,** 8, 14542.
26. Baffou, G.; Bordacchini, I.; Baldi, A.; Quidant, R., *Light: Sci. Appl.* **2020,** 9, 108.
27. Yu, S.; Fan, X. B.; Wang, X.; Li, J.; Zhang, Q.; Xia, A.; Wei, S.; Wu, L. Z.; Zhou, Y.; Patzke, G. R., *Nat. Commun.* **2018,** 9 (1), 4009.
28. Yu, K.; Tian, Y.; Tatsuma, T., *Phys. Chem. Chem. Phys.* **2006,** 8 (46), 5417-5420.
29. Mochizuki, S.; Fujishiro, F.; Iino, A.; Shibata, K.; Yamamoto, H., *Physica B: Condensed Matter* **2007,** 401-402, 426-429.
30. Mezhenny, S.; Maksymovych, P.; Thompson, T. L.; Diwald, O.; Stahl, D.; Walck, S. D.; Yates, J. T., *Chem. Phys. Lett.* **2003,** 369 (1-2), 152-158.
31. Howe, R. F.; Gratzel, M., *J. Phys. Chem.* **2002,** 91 (14), 3906-3909.
32. Naldoni, A.; Allieta, M.; Santangelo, S.; Marelli, M.; Fabbri, F.; Cappelli, S.; Bianchi, C. L.; Psaro, R.; Dal Santo, V., *J. Am. Chem. Soc.* **2012,** 134 (18), 7600-7603.
33. Zhou, X.; Wierzbicka, E.; Liu, N.; Schmuki, P., *Chem. Commun.* **2019,** 55 (4), 533-536.
34. Shin, J.-Y.; Joo, J. H.; Samuelis, D.; Maier, J., *Chem. Mater.* **2012,** 24 (3), 543-551.
35. Sun, K.; Kohyama, M.; Tanaka, S.; Takeda, S., *J. Phys. Chem. C* **2014,** 118 (3), 1611-1617.
36. Ruiz Puigdollers, A.; Schlexer, P.; Tosoni, S.; Pacchioni, G., *ACS Catal.* **2017,** 7 (10), 6493-6513.
37. Wang, K.; Lu, J.; Lu, Y.; Lau, C. H.; Zheng, Y.; Fan, X., *Appl. Catal., B* **2021,** 292, 120147.
38. Liu, H.; Ma, H. T.; Li, X. Z.; Li, W. Z.; Wu, M.; Bao, X. H., *Chemosphere* **2003,** 50 (1), 39-46.
39. Okumura, M.; Coronado, J. M.; Soria, J.; Haruta, M.; Conesa, J. C., *J. Catal.* **2001,** 203 (1), 168-174.
40. Zou, X.; Liu, J.; Su, J.; Zuo, F.; Chen, J.; Feng, P., *Chem. - Eur. J.* **2013,** 19 (8), 2866-2873.
41. Priebe, J. B.; Karnahl, M.; Junge, H.; Beller, M.; Hollmann, D.; Bruckner, A., *Angew. Chem., Int. Ed.* **2013,** 52 (43), 11420-11424.
42. Choudhury, B.; Choudhury, A., *J. Appl. Phys.* **2013,** 114 (20), 203906.
43. Kecskes, T., *Appl. Catal., A* **2004,** 268 (1-2), 9-16.
44. Miller, K. L.; Lee, C. W.; Falconer, J. L.; Medlin, J. W., *J. Catal.* **2010,** 275 (2), 294-299.
45. El-Maazawi, M.; Finken, A. N.; Nair, A. B.; Grassian, V. H., *J. Catal.* **2000,** 191 (1), 138-146.
46. Xu, M.; Noei, H.; Buchholz, M.; Muhler, M.; Wöll, C.; Wang, Y., *Catal. Today* **2012,** 182 (1), 12-15.
47. Hayden, B. E.; King, A.; Newton, M. A., *J. Phys. Chem. B* **1998,** 103 (1), 203-208.
48. Sridhar, M.; Ferri, D.; Elsener, M.; van Bokhoven, J. A.; Kröcher, O., *ACS Catal.* **2015,** 5 (8), 4772-4782.
49. Liu, L.; Gu, X.; Cao, Y.; Yao, X.; Zhang, L.; Tang, C.; Gao, F.; Dong, L., *ACS Catal.* **2013,** 3 (12), 2768-2775.
50. Neatu, S.; Macia-Agullo, J. A.; Concepcion, P.; Garcia, H., *J. Am. Chem. Soc.* **2014,** 136 (45), 15969-15976.
51. Wei, S.; Wang, W.-W.; Fu, X.-P.; Li, S.-Q.; Jia, C.-J., *J. Catal.* **2019,** 376, 134-145.
52. Denkwitz, Y.; Zhao, Z.; Hormann, U.; Kaiser, U.; Plzak, V.; Behm, R., *J. Catal.* **2007,** 251 (2), 363-373.

53. Gaur, S.; Wu, H.; Stanley, G. G.; More, K.; Kumar, C. S. S. R.; Spivey, J. J., *Catal. Today* **2013,** 208, 72-81.
54. Tanaka, K.; White, J. M., *J. Phys. Chem.* **2002,** 86 (24), 4708-4714.
55. Yin, G.; Huang, X.; Chen, T.; Zhao, W.; Bi, Q.; Xu, J.; Han, Y.; Huang, F., *ACS Catal.* **2018,** 8 (2), 1009-1017.
56. Baltrusaitis, J.; Schuttlefield, J.; Zeitler, E.; Grassian, V. H., *Chem. Eng. J.* **2011,** 170 (2-3), 471-481.
57. Mino, L.; Morales-Garcia, A.; Bromley, S. T.; Illas, F., *Nanoscale* **2021,** 13 (13), 6577-6585.
58. Nelson, N. C.; Nguyen, M.-T.; Glezakou, V.-A.; Rousseau, R.; Szanyi, J., *Nat. Catal.* **2019,** 2 (10), 916-924.
59. Liu, L.; Jiang, Y.; Zhao, H.; Chen, J.; Cheng, J.; Yang, K.; Li, Y., *ACS Catal.* **2016,** 6 (2), 1097-1108.
60. Liu, L.; Zhao, H.; Andino, J. M.; Li, Y., *ACS Catal.* **2012,** 2 (8), 1817-1828.
61. Martra, G., *Appl. Catal., A* **2000,** 200 (1-2), 275-285.
62. Hadjiivanov, K.; Lamotte, J.; Lavalley, J.-C., *Langmuir* **1997,** 13 (13), 3374-3381.
63. Toledo-Antonio, J. A.; Cortés-Jácome, M. A.; Navarrete, J.; Angeles-Chavez, C.; López-Salinas, E.; Rendon-Rivera, A., *Catal. Today* **2010,** 155 (3-4), 247-254.
64. Liu, L.; Zhao, C.; Li, Y., *J. Phys. Chem. C* **2012,** 116 (14), 7904-7912.
65. Ji, Y.; Luo, Y., *J. Am. Chem. Soc.* **2016,** 138 (49), 15896-15902.
66. Liu, J.-Y.; Gong, X.-Q.; Alexandrova, A. N., *J. Phys. Chem. C* **2019,** 123 (6), 3505-3511.
67. El-Roz, M.; Bazin, P.; Daturi, M.; Thibault-Starzyk, F., *Phys. Chem. Chem. Phys.* **2015,** 17 (17), 11277-11283.
68. Jensen, S. K.; Keiding, S. R.; Thogersen, J., *Phys. Chem. Chem. Phys.* **2010,** 12 (31), 8926-8933.
69. Nejad, A.; Suhm, M. A.; Meyer, K. A. E., *Phys. Chem. Chem. Phys.* **2020,** 22 (44), 25492-25501.
70. Yokoyama, I.; Miwa, Y.; Machida, K., *J. Am. Chem. Soc.* **2002,** 113 (17), 6458-6464.
71. Green, I. X.; Tang, W.; Neurock, M.; Yates, J. T., Jr., *Angew. Chem., Int. Ed.* **2011,** 50 (43), 10186-10189.
72. Rezvani, A.; Abdel-Mageed, A. M.; Ishida, T.; Murayama, T.; Parlinska-Wojtan, M.; Behm, R. J., *ACS Catal.* **2020,** 10 (6), 3580-3594.
73. Bai, Y.; Chen, B. W. J.; Peng, G.; Mavrikakis, M., *Catal. Sci. Technol.* **2018,** 8 (13), 3321-3335.
74. Soper, A. K.; Benmore, C. J., *Phys. Rev. Lett.* **2008,** 101 (6), 065502.
75. Tse, E. C. M.; Hoang, T. T. H.; Varnell, J. A.; Gewirth, A. A., *ACS Catal.* **2016,** 6 (9), 5706-5714.
76. Beck, D. D.; White, J. M.; Ratcliffe, C. T., *J. Phys. Chem.* **2002,** 90 (14), 3123-3131.
77. Egashira, M.; Kawasumi, S.; Kagawa, S.; Seiyama, T., *Bull. Chem. Soc. Jpn.* **1978,** 51 (11), 3144-3149.
78. Whittaker, T.; Kumar, K. B. S.; Peterson, C.; Pollock, M. N.; Grabow, L. C.; Chandler, B. D., *J. Am. Chem. Soc.* **2018,** 140 (48), 16469-16487.
79. Duan, Z.; Henkelman, G., *ACS Catal.* **2015,** 5 (3), 1589-1595.
80. Yang, X.; Kattel, S.; Senanayake, S. D.; Boscoboinik, J. A.; Nie, X.; Graciani, J.; Rodriguez, J. A.; Liu, P.; Stacchiola, D. J.; Chen, J. G., *J. Am. Chem. Soc.* **2015,** 137 (32), 10104-10107.
81. Yang, B.; Cao, X. M.; Gong, X. Q.; Hu, P., *Phys. Chem. Chem. Phys.* **2012,** 14 (11), 3741-3745.
82. Mukherjee, S.; Libisch, F.; Large, N.; Neumann, O.; Brown, L. V.; Cheng, J.; Lassiter, J. B.; Carter, E. A.; Nordlander, P.; Halas, N. J., *Nano Lett.* **2013,** 13 (1), 240-247.

83. Arshad, M. S.; Trafela, Š.; Rožman, K. Ž.; Kovač, J.; Djinović, P.; Pintar, A., *J. Mater. Chem. C* **2017,** 5 (40), 10509-10516.
84. Clavero, C., *Nat. Photonics* **2014,** 8 (2), 95-103.

Chapter 6. *In-situ* DRIFTS-MS Investigation on CO_2 Hydrogenation over Au/γ-Al_2O_3 under Photo-Thermo Coupled Reaction Condition

This work has been submitted to *Applied Catalysis, B: Environmental*. It was written by the author of the present thesis. This chapter is reproduced from original manuscript with modifications.

6.1 Introduction

In previous chapter, I have investigated the photo-thermo coupled catalytic CO_2 hydrogenation reaction mechanism over Au/TiO_2. How the external light induced plasmonic hot carriers promote the reaction kinetics are focused. In previous chapter, the TiO_2 support is a typical reducible semiconductor, which is feasible for hot electron injection mechanisms. Besides reducible semiconductor, there is another important group of metal oxides also very commonly used as the catalyst supports: non-reducible metal oxides with wide bandgap including γ-Al_2O_3, SiO_2, MgO etc. Therefore, it is also important to investigate the mechanisms of RGWS reaction and thermo-photo coupling mechanism over Au supported by non-reducible metal oxides. In this chapter, Au/γ-Al_2O_3 is chosen as a typical one for investigation.

In this chapter, I have investigated RWGS reaction over Au/γ-Al_2O_3 with similar loading and Au NPs in different sizes. Since the Au size is the fundamental factor determining the LSPR strength, the mechanism underpinning plasmonic enhancement on reaction kinetics can be elucidated. The catalytic activities

were compared between thermal and photo-thermo coupled condition. The reaction mechanisms both in thermal and photo-thermo coupled condition were analysed by a series of *in-situ* DRIFTS-MS experiments. It is found that both carboxyl and formate pathways contribute to the reaction. While the proportions of their contributions vary with Au size and irradiation conditions. Moreover, the plasmonic resonance can preferentially enhance the kinetics of formate intermediates, which in turn facilitates the overall reaction rate.

6.2 Experimental

6.2.1 Physical characterisation

CO_2-TPD experiment was conducted with automatic sorption analyser (Autosorb-iQ, Quantachrome) equipped with an MS (Hidden, RGA201). 50 mg Au/Al_2O_3 was packed into a quartz U-shape reactor and pretreated at 800 °C in flowing He (50 sccm) for 30 min to achieve a clean surface. Then CO_2 was flowed into the reactor for 30 min at 30 °C to achieve an equilibrium. Then the cell was purged under He flow (50 sccm) for 1 h at 30 °C and ramp to 800 °C at a rate of 10 °C min^{-1}. The installed MS was used to monitor the evolution of CO_2 concentration with m/z = 44.

6.2.2 CO_2 hydrogenation performance evaluation

CO_2 hydrogenation performance evaluation was conducted with the commercial DRIFTS in-situ Reactor, as shown in **Figure 2.4**. The temperature was calibrated with a thermocouple inserted into the powder from the bottom. 1 sccm CO_2 and 4 sccm H_2 balanced with Ar into 30 sccm in total were controlled by mass flow controllers and introduced into the reactor. The inlet and outlet gas lines were kept at 130 °C to prevent any condensation, which was controlled by a PID temperature controller. The effluent gas from the vent of the reactor was analysed by a GC (Shimadzu GC-2010 plus) equipped with a TCD and an FID. A micro-packed carbon molecular sieve column (Restek, ShinCarbon ST column) was used to separate the products from permanent gases. External LED green light was used as the external source to promote

the reaction, which was introduced into the reactor via a liquid light guide. The power intensity of the green light was measured to be 250.1 mW cm^{-2} with a thermopile optical power meter (Thorlabs, PM601).

H/D KIE and EIE were measured using the same setup by replacing H_2 with D_2. The flow of D_2 was maintained the same to the H_2 flow rate by regularly checking with an electronic flow meter. The KIE value was equal to the ratio of reaction rate (r_{CO}) with H_2 over the r_{CO} with D_2.

The H/D EIE, which is derived from the different equilibrium concentrations of H*(D*), can be determined following procedure: (1) the catalyst are treated with flowing Air (30 sccm) at 400 °C for 1 h to remove the adsorbed carbon pool or $H^*(D^*)$; (2) the feed gas is switched to Ar (30 sccm) for 30 min to achieve a clean surface; (3) cooling down to 300 °C for background collection; (4) flowing H_2 or D_2 at 300 °C for 30 min under dark or green light irradiation to achieve an equilibrium concentration of H* or D* on the surface; (5) inlet gas is switched to Ar and flow for 5 min under dark to purge out the undissociated H_2 or D_2 gas; (6) switch the feeding gas to CO_2 balanced in Ar. After switching to CO_2/Ar, there is no $H(D)COO^*$ observed on the surface, which is due to limited $H^*(D^*)$ on the surface. The only observed species are carbonate and bicarbonate due to CO_2 adsorption.

6.2.3 *In-situ* DRIFTS-MS analyses

6.2.3.1 Reaction mechanism investigation with TPSR-DRIFTS-MS

The reaction mechanisms in dark or under green light irradiation were investigated via TPSR. The evolved surface species and effluent gaseous products were in-situ monitored by DRIFTS-MS technique (m/z = 18, 29, 45 for H_2O vapour, ^{13}CO and $^{13}CO_2$, respectively). 10 mg catalysts were packed into the reactor sample cup each time. The catalysts were *in-situ* treated at 400 °C under flowing Air and Ar in sequence for 30 min, respectively, to achieve a clean surface for spectroscopy analyses. After cooling down naturally to 30 °C, 1 sccm $^{13}CO_2$, 4 sccm H_2, 25 sccm Ar were controlled by mass flow controllers and premixed before being introduced into the reactor.

The temperature of the reactor ramped to 480 °C in a rate of 10 °C min^{-1}. Using $^{13}CO_2$ instead of $^{12}CO_2$ can significantly increase the lower detection limit of CO by MS, because the intervention from N_2 is fully ruled out.

6.2.3.2 Br-HCOO* role investigation with TPSR via DRIFTS-MS

Similar TPSR protocol was used to investigate the role of Br-HCOO* during the reaction. The catalysts were pretreated in flowing Air and Ar in sequence, which is identical to the procedure described in last section. To *in-situ* create br-HCOO* species on the surface of Au/γ-Al_2O_3, the reactant gas mixture (1sccm $^{13}CO_2$, 4 sccm H_2, 25 sccm Ar) was introduced into reactor at 300 °C for 20 min. This step is identical to the catalytic performance evaluation. Then the inlet gas mixture was swiftly switched to either H_2/Ar mixture (4 sccm/25 sccm) or pure Ar (30 sccm in the buffering line). Simultaneously, the reactor was cooled down to room 30 °C naturally. Since the temperature of the reactor side wall is controlled by water circulation with a chiller working at 25 °C, the cooling down process always takes ~20 min. After stabilising at 30 °C, the reactor ramped to 480 °C with a rate of 10 °C min^{-1}. The evolution of $H^{13}COO$* on surface and effluent gases were monitored by DRIFTS and MS (m/z = 18, 29, 45 for H_2O vapour, ^{13}CO and $^{13}CO_2$, respectively). The TPSR experiments were conducted under dark and green light irradiation, respectively, to elucidate the plasmonic enhancement mechanism.

6.2.3.3 SSITKA-DRIFTS experiments

SSITKA-DRIFTS experiments were conducted with the setup shown in **Figure 2.3** and **Figure 2.4**. The catalysts were pretreated in Air and Ar at 400 °C for 30 min in sequence to achieve a clean surface. After cooling down to 300 °C, under Ar flowing, the BKG was collected. 1 sccm $^{12}CO_2$, 4 sccm H_2 balanced by Ar to 30 sccm in total was switchable with 1 sccm $^{12}CO_2$, 4 sccm H_2, 0.5 sccm He balanced to 30 sccm by Ar. $^{12}CO_2/H_2$ was introduced into the reactor for at least 30 min at 300 °C until reaching steady state. $^{13}CO_2/H_2$ was switched via a 4-way switching valve. DRIFTS spectra were recorded with a FTIR (Shimadzu IRTracer-100) with a scanning rate of 3 spectra per minute.

6.2.4 Theoretical calculations

Spin-polarized DFT calculations were conducted using the Quantum Espresso package[1] with PBE functional[2] at GGA level. Semi-empirical Grimme-D3 dispersion correction[3] was applied to achieve a better description of long-range dispersion interaction. The nuclei and core electrons were described by ultrasoft pseudopotentials from GBRV library.[4] The wavefunctions and charge density were expanded with kinetic cutoff of 45 and 450 Ry, respectively. The first Brillouin zones of bulk γ-Al_2O_3 and slab model of Au_{13}/γ-Al_2O_3 were sampled with Monkhorst-Pack k-points grids of 14 × 10 × 10 and 2 × 2 × 1, respectively. A gaussian smearing was added with 0.01 Ry width to accelerate the convergence. For optimization, the energy and force convergence criteria were set to be 5 × 10^{-5} Ry and 5 × 10^{-4} Ry $Bohr^{-1}$, respectively. The transition states were searched with the CI-NEB[5] method with a convergence criterium of 0.05 eV $Å^{-1}$. Lobster code[6] was used to perform COHP analyses. The visualization of calculation results was conducted with VESTA[7] code. The CO_2 adsorption energy (E_{ad}) was calculated with following equation:

$$E_{ad} = E\left(\mathrm{CO_2}^{*} + \mathrm{slab}\right) - E\left(\mathrm{CO_{2,gas}}\right) - E(\mathrm{slab}) \tag{6.1}$$

6.3 Results and discussion

6.3.1 Catalysts characterization

The actual loadings of the Au on γ-Al_2O_3 were determined by ICP-OES method. The Au loadings are determined to be 3.62±0.01%, 3.58±0.02% and 3.75±0.02% for Au/Al_2O_3-400, Au/Al_2O_3-600 and Au/Al_2O_3-800, respectively. The Au/γ-Al_2O_3 catalysts were characterized with XRD and the corresponding diffraction patterns are shown in **Figure 6.1**(a). The diffraction peaks are in consistency with standard γ-Al_2O_3 pattern (JCPDS 029-0063) and small peaks corresponding to Au NPs (JCPDS 04-0784) are also observed. The higher calcination temperature brings stronger diffraction peaks due to larger NP sizes. The SSA of γ-Al_2O_3 and Au/γ-Al_2O_3 were measured with N_2 sorption

experiments (**Figure 6.1**(b)). The derived BET-SSAs are 111.5, 116.7 and 111.5 m^2 g^{-1} for Au/Al_2O_3-400, Au/Al_2O_3-600, Au/Al_2O_3-800, respectively. Comparing with the pristine γ-Al_2O_3 with SSA of 99.9 m^2 g^{-1}, the SSAs of Au/Al_2O_3 are not influenced by calcination temperature. From above results, it can be concluded that the calculation temperature within the investigated range in this work shows less influence on the Au loadings and SSAs, which can be treated as insignificant factors in this work.

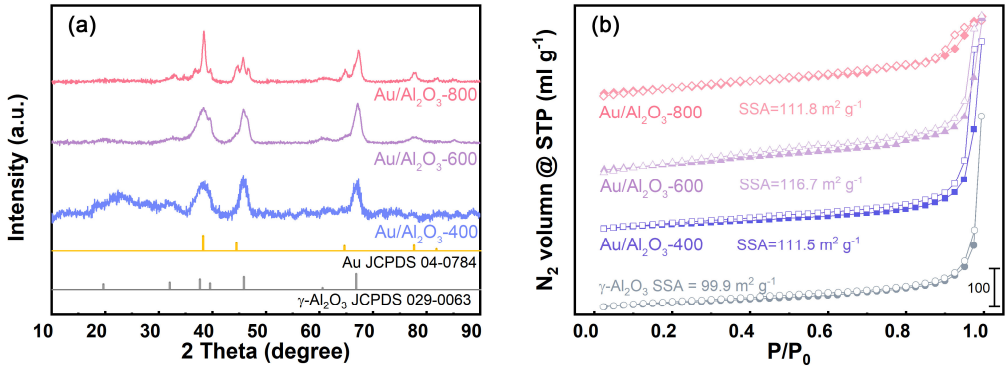

Figure 6.1. (a) XRD pattern and (b) N_2 sorption isotherm of Au/γ-Al_2O_3 calcinated at 400, 600 and 800 °C, respectively.

Au NP size was characterized with HAADF-STEM images (**Figure 6.2**(a, b)). Based on measuring a few hundreds of NPs, the average diameters of Au NP dispersed on γ-Al_2O_3 are calculated to be 4.3, 6.7 and 31.3 nm corresponding to Au/Al_2O_3-400, Au/Al_2O_3-600, Au/Al_2O_3-800, respectively. The size distributions are shown in **Figure 6.3**. The calcination temperature shows significant influences on the size of Au NPs. The different Au NP sizes and the different LSPR effects derived from the Au sizes are the main factors determining the thermal and photo-thermal coupled reaction mechanisms.

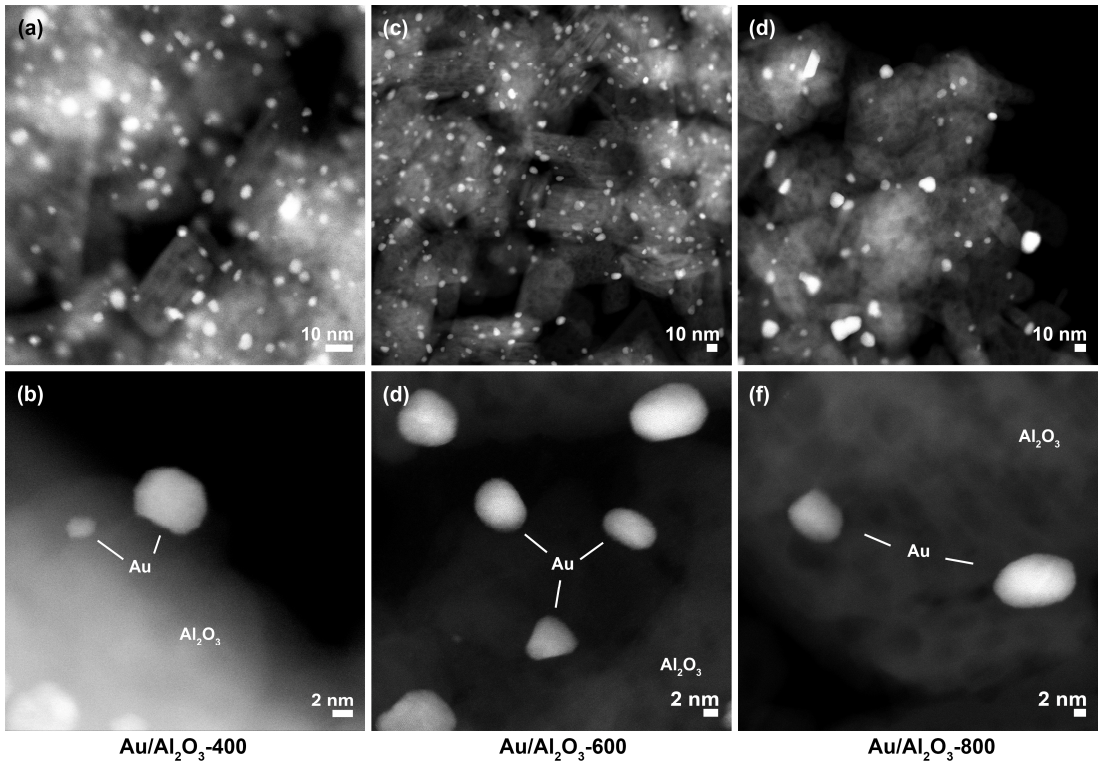

Figure 6.2. HAADF-STEM images of (a, b) Au/Al_2O_3-400, (c, d) Au/Al_2O_3-600, (e, f) Au/Al_2O_3-800.

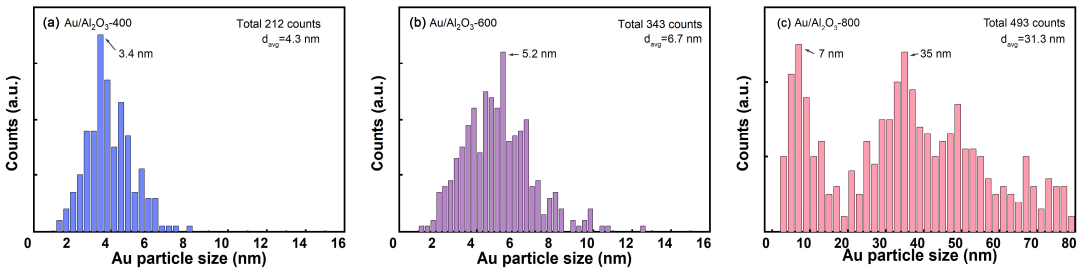

Figure 6.3. Size distributions of (a) Au/Al_2O_3-400, (b) Au/Al_2O_3-600 and (c) Au/Al_2O_3-800.

The XPS is used to elucidate the electronic states of Au NPs of different sizes. As shown in **Figure 6.4**, with different Au NP sizes at the similar loading, Al 2p peaks (the spin-orbital coupling induced peak splitting is not significant) remain constant at 74.4 eV.[8] It suggests that γ-Al_2O_3 is stable and the EMSI is weak in Au/γ-Al_2O_3 catalysts. Comparatively, the Au $4f_{5/2}$ and $4f_{7/2}$ peaks show slight shifts of 0.3 eV to larger binding energy from Au/Al_2O_3-400 to Au/Al_2O_3-800. This phenomenon is related to the effects of increased Au NP size.[9] The UV-Vis DRS give direct evidence of LSPR effects of Au NPs in different sizes. As shown in **Figure 6.5**, the Au LSPR peaks show a significant increase of

intensity and a slight red-shift of wavelength from Au/Al_2O_3-400 to Au/Al_2O_3-800. These results prove the stronger light absorption and stronger LSPR effects of larger Au NPs.

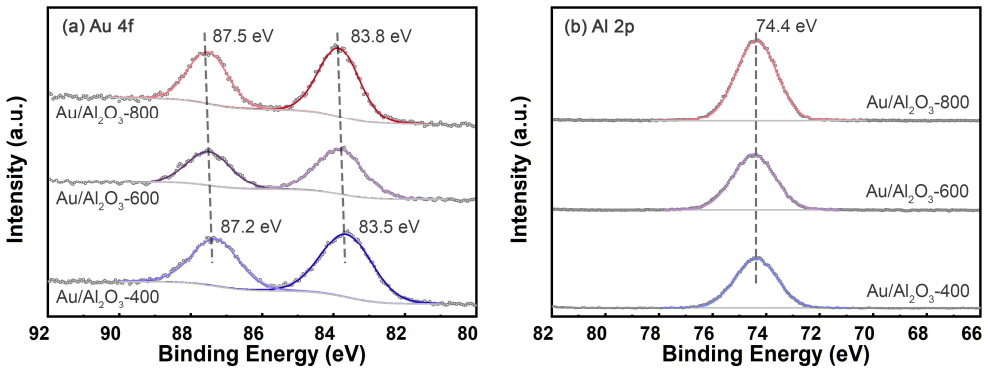

Figure 6.4. XPS core-level spectra of Au/γ-Al_2O_3 calcinated at different temperatures (400, 600, 800 °C): (a) Au 4f, (b) Al 2p.

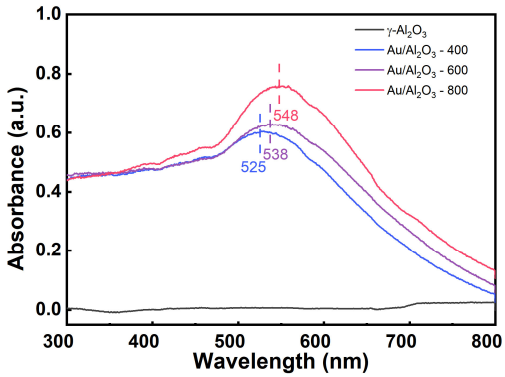

Figure 6.5. UV-Vis DRS of γ-Al_2O_3 and Au/ γ-Al_2O_3 calcinated at different temperatures (400, 600, 800 °C).

6.3.2 Plasmonic enhancement of RWGS

The CO_2 hydrogenation performances were evaluated at temperatures from 285 to 330 °C with a step of 15 °C. The performance results in dark or under green light irradiation are shown in **Figure 6.6**(a-c). In the case of reaction in dark, the Au size effects on CO production rate are significant. At 300 °C, the Au/Al_2O_3-400 with smallest Au NP size produces CO in a rate of 0.47 mmol g_{cat}^{-1} h^{-1}, which is significantly higher than the counterparts of Au/Al_2O_3-600 (0.40 mmol g_{cat}^{-1} h^{-1}) and Au/Al_2O_3-800 (0.17 mmol g_{cat}^{-1} h^{-1}) with larger Au

NPs. The inferior pure thermocatalytic performance of larger Au NPs is attributed to the much less Au/γ-Al_2O_3 perimeter active sites for the CO_2 hydrogenation and H_2 dissociation.[10] The corresponding activation energies in dark show the same sequence as presented in **Figure 6.6**(d-f). Au/Al_2O_3-400 shows an activation energy of 50.6 kJ mol^{-1} in dark, which is only 37.6% of Au/Al_2O_3-800 (134.6 kJ mol^{-1}). By contrast, for reaction under green light irradiation, the plasmonic enhancement of CO production rate ($\boldsymbol{r}_{green}/\boldsymbol{r}_{dark}$) follows an inversed trend. At 300 °C under green light irradiation, the CO production rates are 211.8%, 150.0% and 142.5% of dark reaction rate for Au/Al_2O_3-800, Au/Al_2O_3-600 and Au/Al_2O_3-400, respectively. The more pronounced plasmonic enhancement is directly related to the stronger LSPR effects, since the loading and SSAs are similar across all 3 samples. The most significant plasmonic enhancement is also reflected by the reduction of activation energy comparing with its counterpart in dark. The activation energy reduces by 2.1, 6.7 and 15.3 kJ mol^{-1} for Au/Al_2O_3-400, Au/Al_2O_3-600 and Au/Al_2O_3-800 under green light irradiation, respectively. In summary, the pronounced plasmonic enhancement differences across the 3 samples with different Au NP sizes ensure them as great sample group for thermo-photo coupling mechanism investigations.

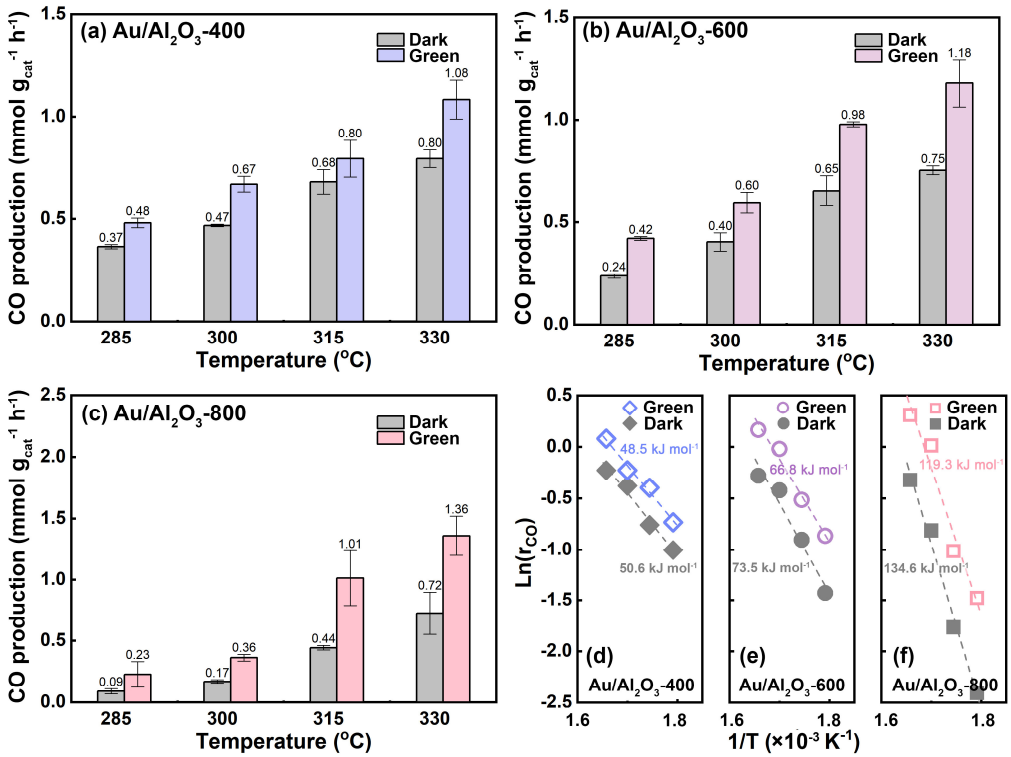

Figure 6.6. CO production rates in dark and under green light irradiation over (a) Au/Al_2O_3-400, (b) Au/Al_2O_3-600 and (c) Au/Al_2O_3-800. The corresponding Arrhenius plots for (d) Au/Al_2O_3-400, (e) Au/Al_2O_3-600 and (f) Au/Al_2O_3-800.

6.3.3 *In-situ* DRIFTS-MS investigations on reaction mechanism and plasmonic enhancement

6.3.3.1 IR peak assignments

To achieve reliable assignments of IR peaks, $^{12}CO_2/^{13}CO_2$ was introduced to interact with clean surface of Au/Al_2O_3. The spectra after achieving equilibrium are shown in **Figure 6.7**. Only HCO_3* and CO_3* are observed on the surface in the absence of H_2. The HCO_3* and CO_3* show multiple adsorption configurations including monodentate, bidentate, bridged and unidentate etc. By comparing with typical literature reported values, the assignments are summarized in **Table 6.1**. The DRIFT spectra of $H^{12}COO$* and $H^{13}COO$* were achieved in a similar procedure by introducing CO_2 and H_2 together. The catalysts were pretreated in flowing Air and Air in sequence at 400 °C. The background was collected under flowing Ar, when the temperature was cooled down to 300 °C. Then, H_2/CO_2/Ar was flowed into the reactor at 300 °C along

with *in-situ* DRIFTS characterization. After achieving equilibrium within 30 min, the typical spectra were extracted and plotted in **Figure 6.8**. There are two main kinds of formate observed on the surface: monodentate and bridged formate (m-HCOO* and br-HCOO*). After comparing with literature, the detailed assignments are summarized in **Table 6.2**.

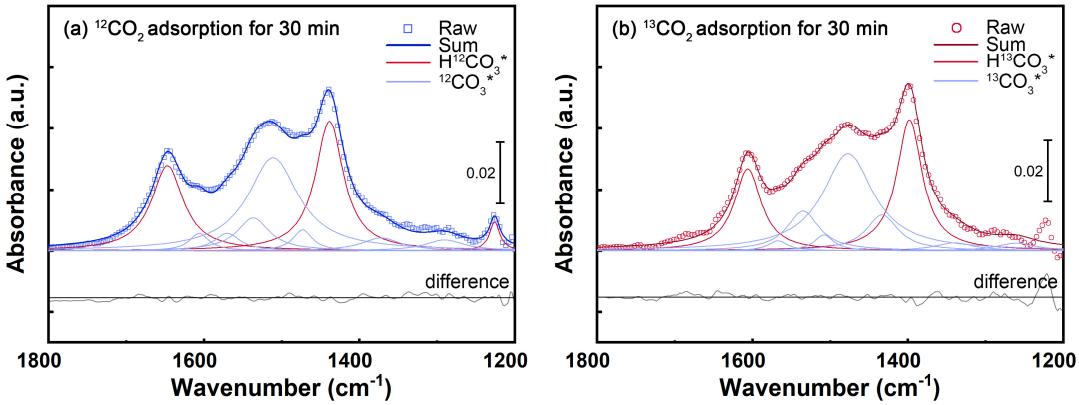

Figure 6.7. The IR peak deconvolution and assignments of carbonate/bicarbonate groups adsorbed on Au/Al_2O_3-400 surface at 300 °C. The Au/Al_2O_3-400 was pretreated in flowing Ar at 400 °C for 1 h.

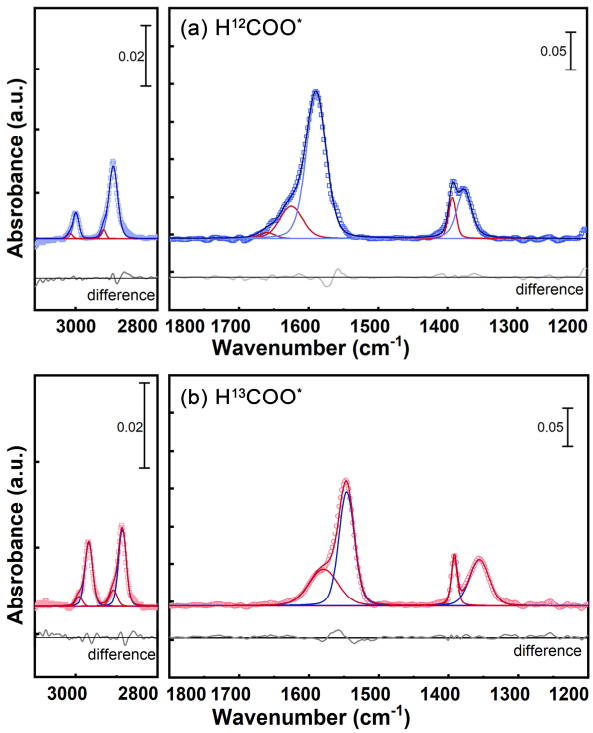

Figure 6.8. DRIFT spectra of (a) $H^{12}COO^*$ and (b) $H^{13}COO^*$ adsorbed on the surface of Au/Al_2O_3-400 at 300 °C. The Au/Al_2O_3 was pretreated in flowing Ar at 400 °C for 1 h.

Table 6.1. The IR peak assignments of CO_3*/HCO_3* on Au/Al_2O_3.

		Au/Al_2O_3[11]	Pd/Al_2O_3[12]	Pd/Al_2O_3[13]	γ-Al_2O_3[14]	γ-Al_2O_3[15]	γ-Al_2O_3[16]	γ-Al_2O_3[17]	This work ^{12}C	This work ^{13}C
	ν(OH)				3621-3607	3612	3601-3605	3623		
	Physisorbed CO_2					2382				
HCO_3*	ν_{as}(OCO)	1647	1648	1646	1644-1650	1647	1650-1639	1648	1647	1606
	ν_s(OCO)	1437	1438	1438	1438, 1469-1486	1455	1490-1440	1438	1438	1398
	δ(COH)	1229	1228	1230	1228-1236	1233	1236-1225	1231	1226	n/a
CO_3*	bidentate						1730-1660		1606	1567
	bridged			1525	1720-1870	1575			1536, 1570,	1508,1535
	unidentate					1517	1530		1511	1480
	unidentate				1409	1455	1370		1473,1372	1433,1340
	bidentate				1206-1191		1270-1230		1290	1260
	bridged						1180			

Table 6.2. The IR peak assignments of $H^{12}COO$* and $H^{13}COO$* on Au/Al_2O_3.

	Au/Al_2O_3[11]	Rh/Al_2O_3[18]	Pd/Al_2O_3[12]	Pd/Al_2O_3[13]	This work ^{12}C	This work ^{13}C
br-ν(C-H)		3060				
m-ν(C-H)					3014	2992
br-ν(C-H)	2996	2986			2998	2968
m-ν(C-H)					2932	2908
br-ν(C-H)		2905			2908	2886
m- ν_{as}(OCO)			1660		1660	1621
m- ν_{as}(OCO)			1625		1625	1579
br- ν_{as}(OCO)	1590	1594	1590	1593	1590	1546
δ(CH)	1392		1393	1393	1391	1391
m- ν_a(OCO)						1371
br- ν_a(OCO)	1372	1375	1377	1376	1376	1356
m- ν_s(OCO)			1321			

6.3.3.2 Ruling out redox pathway

As generally believed non-reducible oxide support, the γ-Al_2O_3 surface is unlikely to reduce CO_2 by itself. Considering oxide of Au is thermodynamically unfeasible to form at reaction temperature investigated, Au NPs can hardly reduce CO_2 to CO either. Experiments were further conducted to rule out the redox pathway over Au/γ-Al_2O_3. The Au/γ-Al_2O_3 was firstly treated under

flowing Ar at 400 °C for 30 min to achieve a clean surface, then cooled down to target temperature (30 °C or 200 °C) naturally. The CO_2/Ar without H_2 was introduced into the reactor in dark or under green light irradiation conditions with surface species evolution monitored by *in-situ* DRIFTS (**Figure 6.9**). Different from the phenomenon observed in Chapter 5 that CO_2 self-dissociates at the V_O site of Au/TiO_2 with the formation of CO*, there is no CO* peak emerging over $Au/\gamma\text{-}Al_2O_3$ either in dark or under green light irradiation. These experiments can reasonably rule out the redox mechanism for RWGS over Au/Al_2O_3.

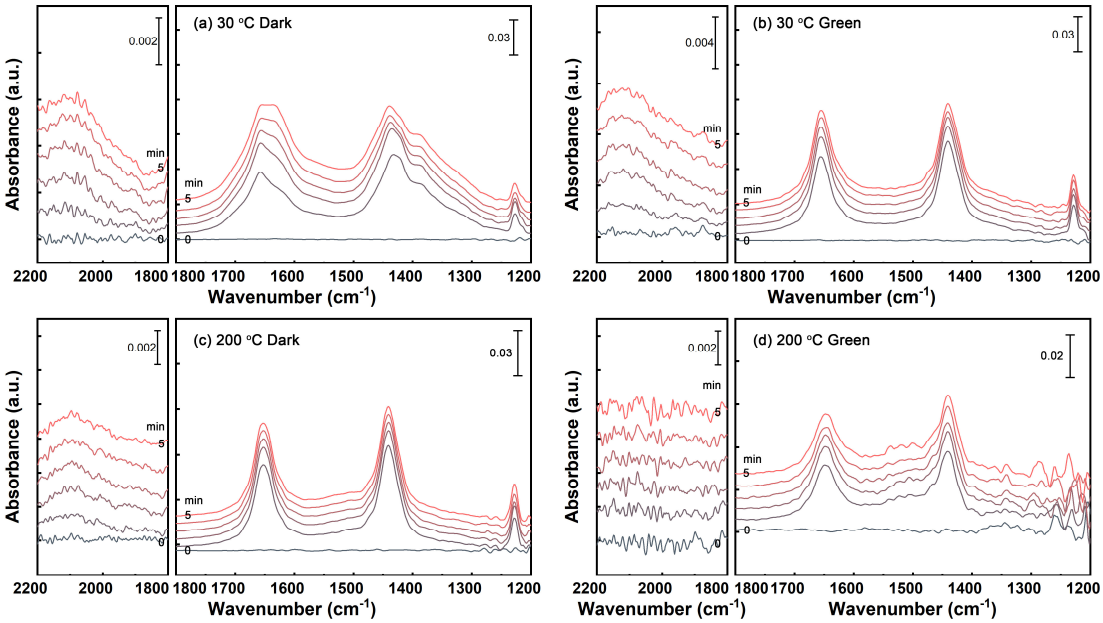

Figure 6.9. Time-resolved DRIFT spectra of CO_2 interaction with $Au/\gamma\text{-}Al_2O_3$ at 30 °C and 200 °C under dark or green light irradiation. The $Au/\gamma\text{-}Al_2O_3$ is pretreated in flowing Ar (30 sccm) at 400 °C for 1 h before CO_2 adsorption.

6.3.3.3 Confirmation of br-formate as reaction intermediate

It has been a long debate on the role of formate during the CO_2 hydrogenation reaction.[19-20] Because formate is easy to form from CO_2*, while difficult to be further dehydrated due to its high stability. Therefore, it is of great importance to prove that formate does contribute to the CO production in RWGS over Au/Al_2O_3, especially under photo-thermal coupled reaction condition. Here, I used the *in-situ* DRIFTS-MS technique to explicitly unravel the role of formate.

The key evidence to convince the formate pathway is to prove that the conversion of HCOO* will directly result to CO production. TPSR using isotope-labelled $^{13}CO_2$ was conducted with H^{13}COO* and effluent ^{13}CO monitored with DRIFTS-MS. The details of the experimental procedure are described in experimental section 6.2.3.2. It is important to use $^{13}CO_2$ rather than $^{12}CO_2$ to make the detection of CO by MS extremely sensitive (detection limit of ~100 ppb using our setup) and accurate, since the strong intervention from ambient N_2 can be ruled out. Note that unambiguous results cannot be achieved by using $^{12}CO_2$.

The experiments were conducted on Au/Al_2O_3-400 first. To demonstrate the br-HCOO* hydrogenation to CO* mechanism in dark, the TPSR experiments were conducted under flowing H_2/Ar. The important control group of TPSR in flowing Ar without H_2 was also performed. The corresponding DRIFTS-MS results are shown in **Figure 6.10**(a-d) and **Figure 6.10**(e-h), respectively. In both conditions, the br-H^{13}COO* can be clearly observed in DRIFT spectra contours (1546 cm^{-1}) after pretreatment with $^{13}CO_2/H_2$ at 300 °C for 20 min. Following purging for more than 30 min can effectively remove the gaseous H_2 from the reactor. The symmetric peak of 1546 cm^{-1} suggests that m-HCOO* is completely consumed during the purging step, which proves the high activity of m-HCOO*. To better illustrate the evolution of IR peak intensity of br-HCOO*, the derivative of absorbance with respect to temperature (∂Abs./∂Temp.) is plotted against temperature. In the TPSR under flowing H_2/Ar (**Figure 6.10**(a-d)), the consumption of br-HCOO* highly matches the effluence of ^{13}CO, with the peak at the temperature of ~340 °C. On the contrary, with the absence of H_2 (**Figure 6.10**(e-h)), the decomposition of br-HCOO* doesn't generate ^{13}CO. The observed $^{13}CO_2$ is believed to be derived from the direct decomposition of H^{13}COO* to $^{13}CO_2$* and H*. Moreover, there is no obvious formation of m-HCOO* during this experiment, which suggests the br-HCOO* might not have to first convert to m-HCOO*, then further produce CO. It is further supported by the DFT calculation result that br-HCOO* is more stable than m-HCOO* by 0.94 eV. From thermodynamics perspective, the equilibrium concentration ratio of br-HCOO* to m-HCOO* is rather low. Under Ar atmosphere, the

formation of m-HCOO* from br-HCOO* is also negligible, which proves this transformation is also kinetically unfavourable.

The similar comparison experiments were conducted under green light irradiation and the results are presented in **Figure 6.10**(i-l) and **Figure 6.10**(m-p). The same pronounced correlation between br-H^{13}COO* consumption and ^{13}CO production is found in H_2/Ar atmosphere, while no ^{13}CO is detected without H_2. In **Figure 6.10** (j), the ∂Abs./∂Temp. shows a centre at ~ 280 °C, which is significantly lower than the corresponding temperature of ~330 °C in dark. The TPSR experiments under green light further confirm that br-HCOO* is a reaction intermediate in photo-thermo coupled reaction condition too. Comparing the results under dark, the green light irradiation can lower the temperature of br-H^{13}COO* conversion to CO, which indicates this elementary step is activated by light-induced plasmonic effects.

To rule out the possibility that the effluent ^{13}CO is derived from the reaction between re-adsorbed $^{13}CO_2$* (due to HCOO* dehydrogenation) with H_2, another careful control experiment was conducted following the same procedure except only introducing $^{13}CO_2$/Ar (without H_2) in the first step. As shown in **Figure 6.11**(a), ^{13}HCOO* is not formed on the surface after flowing $^{13}CO_2$/Ar at 300 °C for 20 min. The physisorbed $^{13}CO_2$ desorption happens within the temperature range of 30 to 120 °C, as demonstrated by the corresponding MS spectrum (**Figure 6.11**(d)). While the chemisorbed CO_2 still remains on the surface in the temperature of this TPSR experiment. As shown in **Figure 6.12**, the chemisorbed CO_2 shows full desorption at temperature higher than 700 °C. During the whole TPSR process with flowing H_2, no ^{13}CO effluent is detected by MS (**Figure 6.11**(c)), which proves that the ^{13}CO is the product of br-H^{13}COO* and H_2.

The same formate TPSR experiments were conducted over the other two samples: Au/Al_2O_3-600 and Au/Al_2O_3-800. The corresponding DRIFTS contour and MS spectra are shown in **Figure 6.13**. The same phenomena were observed for Au/Al_2O_3-600 and Au/Al_2O_3-800: the CO production strongly correlates with br-HCOO* consumption. The green light can effectively lower

the temperature of br-HCOO* conversion to CO, which further proves that the LSPR can activate the br-HCOO* dehydration.

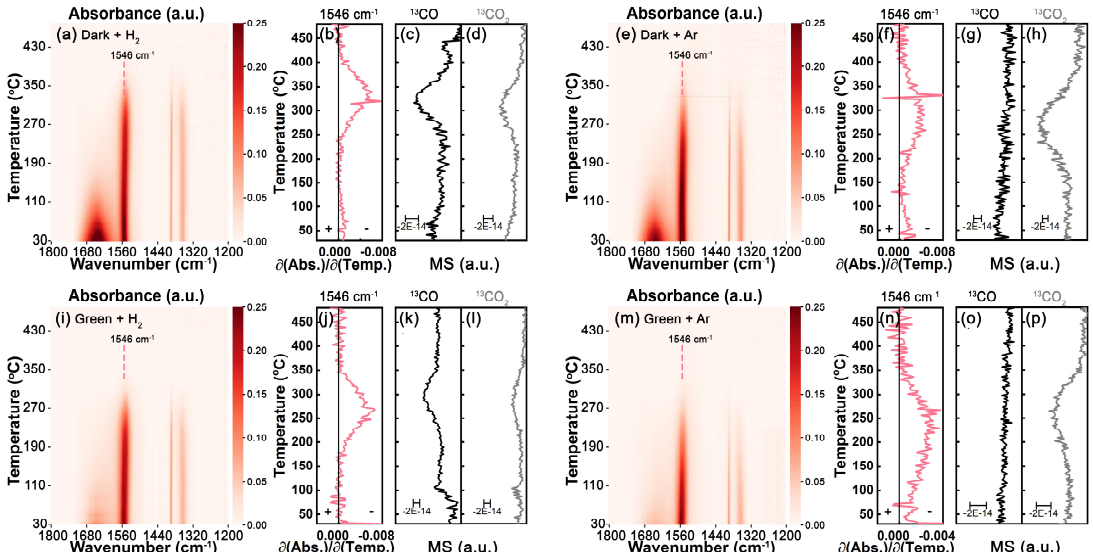

Figure 6.10. Temperature-programmed surface reaction (TPSR) results achieved with DRIFTS-MS at different atmospheres and irradiation conditions over Au/Al_2O_3-400. Temperature-resolved DRIFT contours of br-HCOO* reduction in (a) dark + H_2, (e) dark + Ar, (i) green light + H_2, (m) green light + Ar. (b, f, j, n) The corresponding derivatives of br-HCOO* IR peak (1546 cm^{-1}) intensity with respect to temperature are plotted against temperature. The corresponding time-resolved MS signals of (c, g, k, o) ^{13}CO and (d, h, l, p) $^{13}CO_2$. *m/z* = 29 and 45 are used for ^{13}CO and $^{13}CO_2$ MS measurements, respectively.

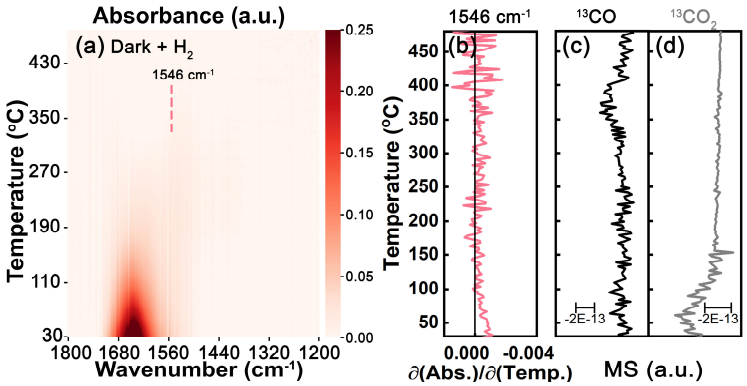

Figure 6.11. Control group temperature-programmed surface reaction (TPSR) results achieved with DRIFTS-MS without br-formate pre-adsorbed on the surface over Au/Al_2O_3-400: (a) Temperature-resolved FTIR contour, (b) corresponding derivatives of br-HCOO* IR peak (1546 cm^{-1}) intensity with respect to temperature, (c, d) MS signals of ^{13}CO and $^{13}CO_2$.

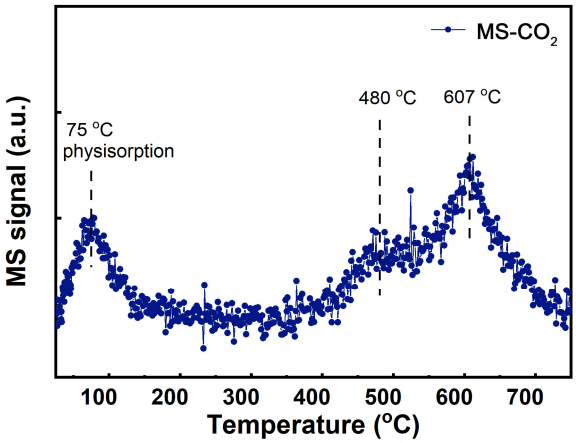

Figure 6.12. CO_2-TPD profile of Au/Al_2O_3-400 in dark.

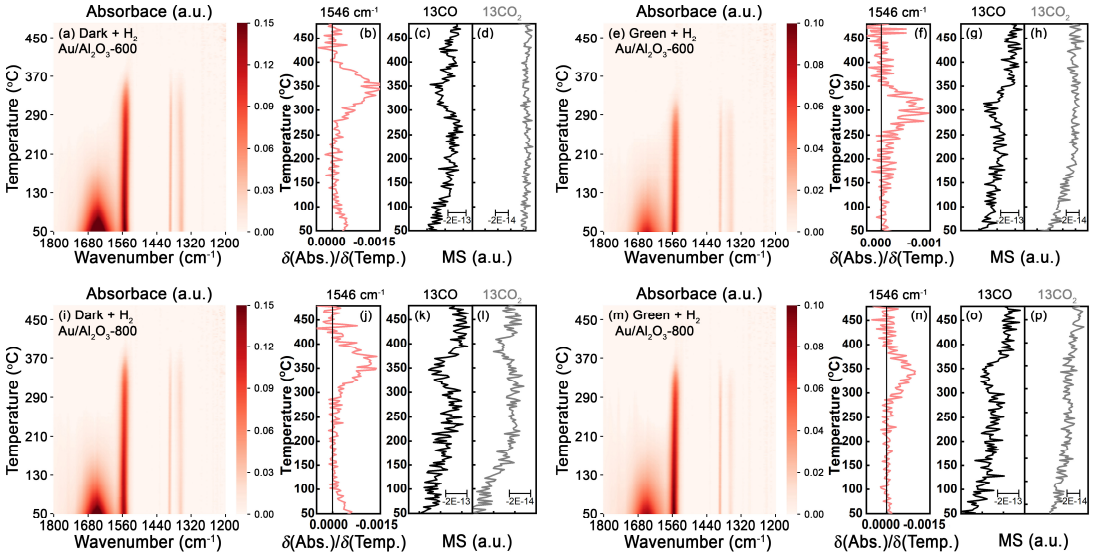

Figure 6.13. Temperature-programmed surface reaction (TPSR) results achieved with DRIFTS-MS at different irradiation conditions. Temperature-resolved DRIFT contour plots of br-HCOO* reduction in (a) Au/Al_2O_3-600 in dark, (e) Au/Al_2O_3-600 in green, (i) Au/Al_2O_3-800 in dark, (m) Au/Al_2O_3-600 in green. (b, f, j, n) The corresponding derivatives of br-HCOO* IR peak (1546 cm^{-1}) intensity with respect to temperature are plotted against temperature. The corresponding time-resolved MS signals of (c, g, k, o) ^{13}CO and (d, h, l, p) $^{13}CO_2$. *m/z* = 29 and 45 are used for ^{13}CO and $^{13}CO_2$, respectively.

6.3.3.4 m-HCOO* Reaction pathway unravelled by TP-DRIFTS-MS

To unravel temperature-dependent prevailing surface intermediates, the TP-DRIFTS-MS experiments were conducted in both dark and green light irradiation condition. $^{13}CO_2$ was used in this experiment to achieve a highly accurate and sensitive MS signal for CO product. The corresponding contours

are presented in **Figure 6.14**. As shown in **Figure 6.14**(a), the prevailing surface species are $^{13}CO_3$*, $H^{13}CO_3$* and H_2O* at temperature below 170 °C. **Figure 6.14**(b, d) demonstrates the evolutions of br-HCOO* and m-HCOO* IR peak intensities by plotting their first derivative of absorbance with respect to temperature (*∂*Abs./*∂*Temp.) as a function of temperature, respectively. The br-$H^{13}COO$* emerges at ~140 °C and reaches its peak intensity at around 305 °C. By contrast, the m-$H^{13}COO$* shows an abrupt increase at ~225 °C. The derivative of MS-^{13}CO with respect to temperature is plotted as a function of temperature to describe the evolution of ^{13}CO production. Note that the production of ^{13}CO starts from ~225 °C in dark, which is almost the same to the appearance of m-$H^{13}COO$* on the surface and much higher than the emerging of br-$H^{13}COO$*. It strongly indicates the close connection between m-$H^{13}COO$* and ^{13}CO product. Similar results are achieved for TP-DRIFTS-MS experiments conducted under green light irradiation. As shown in **Figure 6.14**(e-h), the ^{13}CO starts to effluent at temperature of ~185 °C, which is the same to the temperature of m-$H^{13}COO$* formation (185 °C) but significantly higher than the br-$H^{13}COO$* (~96 °C). Although the formation temperature of br-$H^{13}COO$ and m-$H^{13}COO$*, CO all decreases due to light irradiation, the consistency between the emergences of m-$H^{13}COO$* and ^{13}CO product remains valid. The disagreement between br-$H^{13}COO$* and ^{13}CO formation temperature suggests the br-$H^{13}COO$* can easily forme on the surface but suffers from a high energy barrier to further reduce to CO. The generation of m-HCOO* might be either derived from the transformation from br-HCOO* to m-HCOO* at high temperature[12] or reaction between m-CO_2* and H*. Note that during the br-HCOO* TPSR-DRIFTS experiments (**Figure 6.10** and **Figure 6.13**), no m-HCOO* can be observed. Therefore, it is more plausible of the direct formation of m-HCOO* from CO_2* and H* rather than the transformation from br-HCOO*. m-HCOO* and br-HCOO* pathways are believed parallelly happening on the surface. However, the complete ruling out the br-HCOO*/m-HCOO* transformation needs more investigations, which is out of the scope of this chapter.

The same TP-DRIFTS-MS experiments were conducted over the other two samples with larger Au NPs. From **Figure 6.15** (Au/Al_2O_3-600), it can conclude that the consistency of CO generation temperature and m-HCOO* formation temperature is still valid. The green light irradiation can also significantly reduce the temperature of formate and CO formation. The same formation temperature strongly suggests the m-HCOO* pathway is still an important reaction pathway in dark and under green light irradiation over Au/Al_2O_3-600.In the case of Au/Al_2O_3-800 (**Figure 6.16**), the situation is slightly different. In **Figure 6.16**(a), the $H^{13}COO$* peak is quite symmetric, which suggests there is no observable m-$H^{13}COO$* peak during the TP-DRIFTS-MS experiment. It is also demonstrated by **Figure 6.16**(c). By contrast, under green light irradiation, the m-$H^{13}COO$* can be found in the ramping procedure (**Figure 6.16**(e)). Again, the formation temperature of m-$H^{13}COO$* and CO become consistent. The different behaviours of Au/Al_2O_3-800 in dark and under green light irradiation indicates the plasmonic electrons will significantly enhance the formation of m-HCOO* and facilitate the formate reaction pathway.

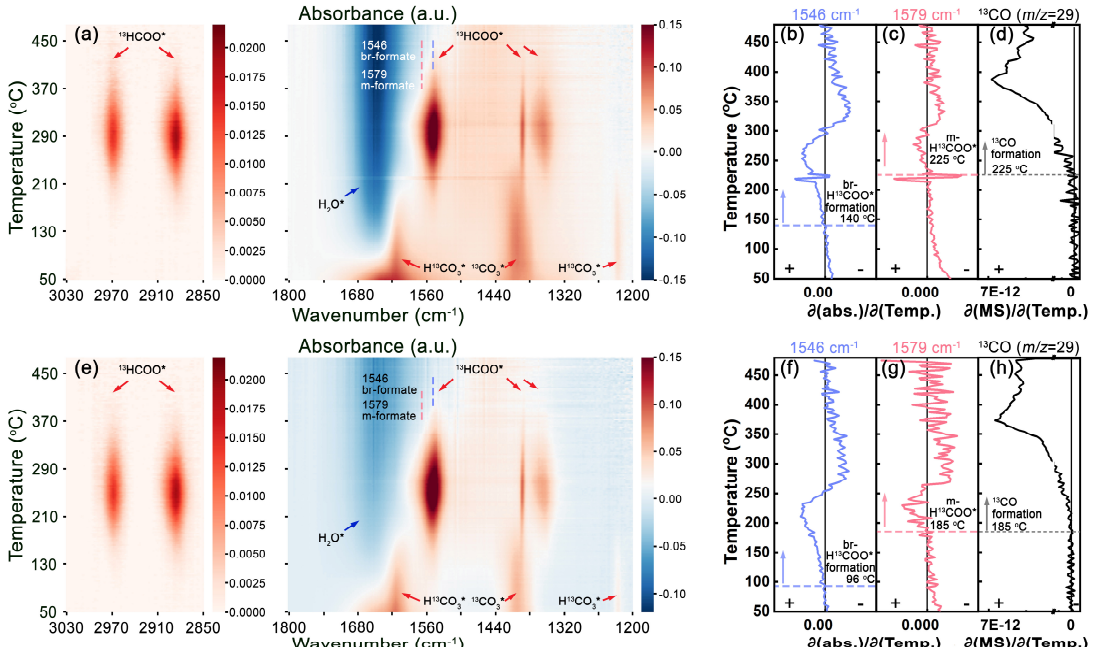

Figure 6.14. TP-DRIFTS-MS investigations on $^{13}CO_2$ hydrogenation from 50 to 480 °C over Au/Al_2O_3-400. (a) The DRIFTS contour, corresponding IR peak intensity evolution of (b) br-$H^{13}COO^*$ (1546 cm^{-1}), (c) m-$H^{13}COO$ (1579 cm^{-1}) and (d) first derivative of ^{13}CO-MS signal with respect to temperature as a function of temperature in dark. (e) The DRIFT contour, corresponding IR peak intensity evolution of (f) br-$H^{13}COO^*$ (1546 cm^{-1}), (g) m-$H^{13}COO^*$ (1579 cm^{-1}) and (h) first derivative of ^{13}CO-MS signal with respect to temperature as a function of temperature under green light irradiation. The MS signal of ^{13}CO has been calibrated against $^{13}CO_2$.

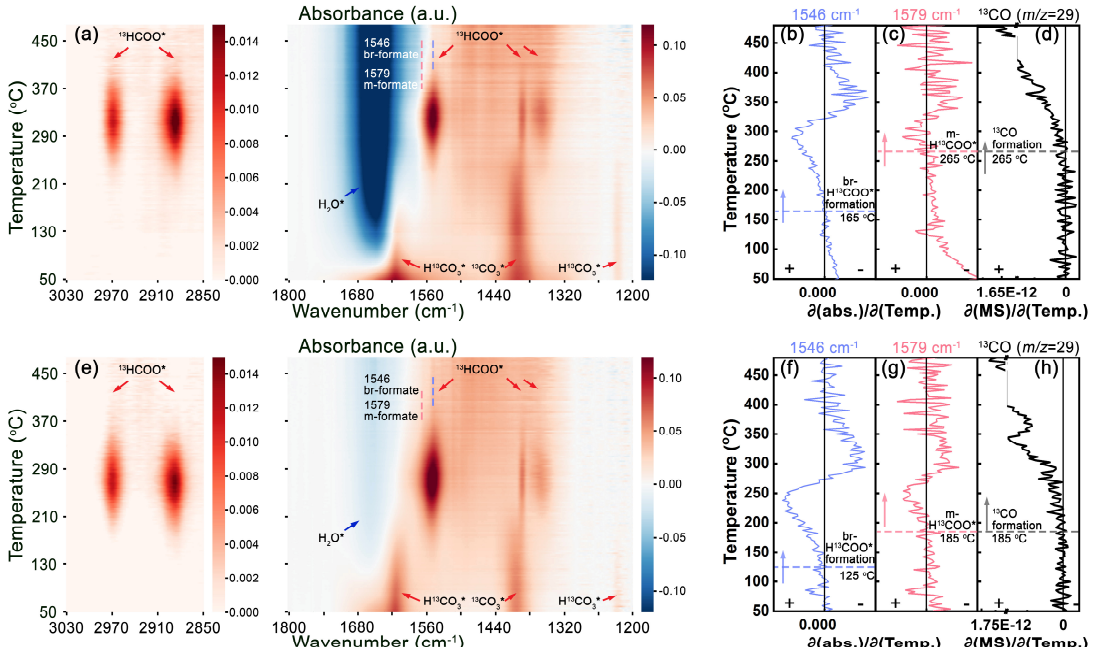

Figure 6.15. TP-DRIFTS-MS investigations on $^{13}CO_2$ hydrogenation from 50 to 480 °C over Au/Al_2O_3-600. (a) The DRIFTS contour, corresponding IR peak intensity evolution of (b) br-$H^{13}COO$* (1546 cm^{-1}), (c) m-$H^{13}COO$* (1579 cm^{-1}) and (d) first derivative of ^{13}CO-MS signal with respect to temperature as a function of temperature in dark. (e) The DRIFT contour, corresponding IR peak intensity evolution of (f) br-$H^{13}COO$* (1546 cm^{-1}), (g) m-$H^{13}COO$* (1579 cm^{-1}) and (h) first derivative of ^{13}CO-MS signal with respect to temperature as a function of temperature under green light irradiation. The MS signal of ^{13}CO has been calibrated against $^{13}CO_2$.

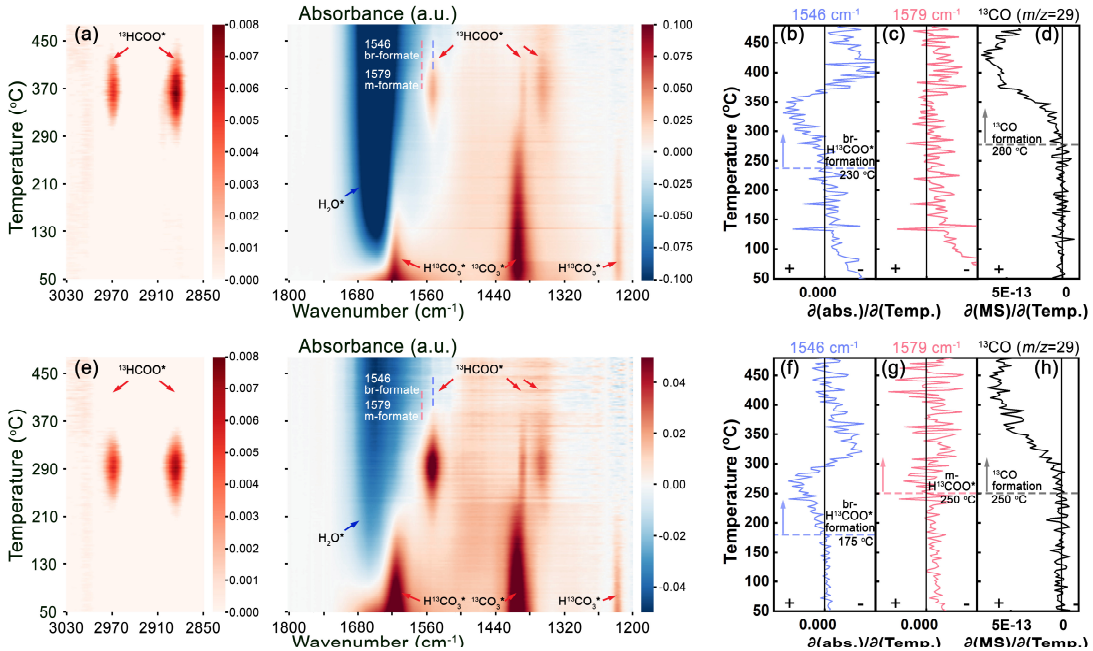

Figure 6.16. TP-DRIFTS-MS investigations on $^{13}CO_2$ hydrogenation from 50 to 480 °C over Au/Al_2O_3-800. (a) The DRIFTS contour, corresponding IR peak intensity evolution of (b) br-$H^{13}COO^*$ (1546 cm^{-1}), (c) m-$H^{13}COO^*$ (1579 cm^{-1}) and (d) first derivative of ^{13}CO-MS signal with respect to temperature as a function of temperature in dark. (e) The DRIFT contour, corresponding IR peak intensity evolution of (f) br-$H^{13}COO^*$ (1546 cm^{-1}), (g) m-$H^{13}COO^*$ (1579 cm^{-1}) and (h) first derivative of ^{13}CO-MS signal with respect to temperature as a function of temperature under green light irradiation. The MS signal of ^{13}CO has been calibrated against $^{13}CO_2$.

6.3.3.5 SSITKA-DRIFTS investigation on kinetics of HCOO*

SSTIKA-DRIFTS experiments can provide kinetic information of the key reaction intermediates HCOO* group at steady state. A typical temperature of 300 °C was chosen as the investigation temperature and $^{12}CO_2/^{13}CO_2$ with the identical flow rate were swiftly switched with a 4-way valve. The moment of isotope switch was denoted as t = 0 min in the DRIFTS contours (**Figure 6.17**, **Figure 6.18** and **Figure 6.19**). As shown in **Figure 6.17**(a, c), br-HCOO* and m-HCOO* can be observed on the surface of the Au/Al_2O_3-400, which agrees with the other DRIFTS contours shown in former sections. In dark (**Figure 6.17**(a, b)), the m-HCOO* decays significantly faster than br-HCOO*. The corresponding exponential decay fittings interpret the kinetic surface lifetimes of 10.76 and 8.13 min for br-HCOO* ad m-HCOO*, respectively. Under green light irradiation (**Figure 6.17**(c, d)), the kinetics of both br-HCOO* and m-

HCOO* are significantly facilitated with corresponding surface lifetimes of 3.95 and 3.22 min. The same SSITKA-DRIFTS experiments were conducted over Au/Al_2O_3-600 and Au/Al_2O_3-800 too (**Figure 6.18** and **Figure 6.19**). In both cases, the green light is proven to boost the kinetics of br-HCOO* and m-HCOO* too. The calculated kinetic surface lifetimes are summarised in **Table 6.3**.

To further unravel the correlation between LSPR strength and surface HCOO* kinetics, it is important to compare the light induced HCOO* kinetics facilitation across all three samples. Because the larger Au NPs can result in a stronger LSPR effect. During the SSITKA-DRIFTS characterization, it is believed the reaction stays at the constant rate and surface species with constant coverage. Therefore, the SSITKA experiment can measure the reaction activity of single species independent from its abundance on the surface.[12] The measured HCOO* surface lifetime is a reciprocal of the pseudo-first-order reaction rate constant *k*:

$$k = \tau^{-1} \tag{6.2}$$

Considering the plasmonic resonance doesn't change the active sites for each reaction intermediate, the plasmonic enhancement (*P*) on overall, m-HCOO* and br-HCOO* reaction rates can be represented by following equations:

$$P_{\text{overall}} = \frac{r_{\text{CO\_green}}}{r_{\text{CO\_dark}}} \tag{6.3}$$

$$P_{\text{m-HCOO}^*} = \frac{k_{\text{m-HCOO}^*\text{\_dark}}}{k_{\text{m-HCOO}^*\text{\_green}}} = \frac{\tau_{\text{m-HCOO}^*\text{\_green}}}{\tau_{\text{m-HCOO}^*\text{\_dark}}} \tag{6.4}$$

$$P_{\text{br-HCOO}^*} = \frac{k_{\text{br-HCOO}^*\text{\_dark}}}{k_{\text{br-HCOO}^*\text{\_green}}} = \frac{\tau_{\text{br-HCOO}^*\text{\_green}}}{\tau_{\text{br-HCOO}^*\text{\_dark}}} \tag{6.5}$$

As shown in **Figure 6.20**, the $P_{\text{m-HCOO}^*}$ and $P_{\text{br-HCOO}^*}$ are significantly larger than P_{overall}. Considering the reaction mechanism is a combination of HCOO* and COOH* pathway, this result clearly indicates the LSPR promotes HCOO* pathway more significantly than COOH* pathway in the reaction. Moreover, HCOO* kinetics enhancement also follows the same sequence of LSPR

effects strength. It is also worth noticing that the $P_{\text{br-HCOO}^*}$ is larger than $P_{\text{m-HCOO}^*}$ over Au/Al_2O_3-400 and Au/Al_2O_3-600 with relatively smaller Au NPs sizes. While in the case of Au/Al_2O_3-800 with significantly larger Au NPs, the $P_{\text{br-HCOO}^*}$ and $P_{\text{m-HCOO}^*}$ become similar. It can be plausibly explained by the combination of two enhancement mechanisms. For smaller Au NPs, the plasmonic resonance decay will excite hot electrons in higher energy, which act as the main enhancement mechanism. Due to the lower energy of antibonding states of br-HCOO* than m-HCOO* (**Figure 6.26**(c, d)), the hot electrons are more likely to inject into br-HCOO* rather than m-HCOO*. Therefore, the br-HCOO* kinetics is more enhanced by LSPR. For larger Au NPs, the LSPR induced strong electromagnetic field becomes the dominated enhancement mechanism, which is less electronic structure sensitive.[21]

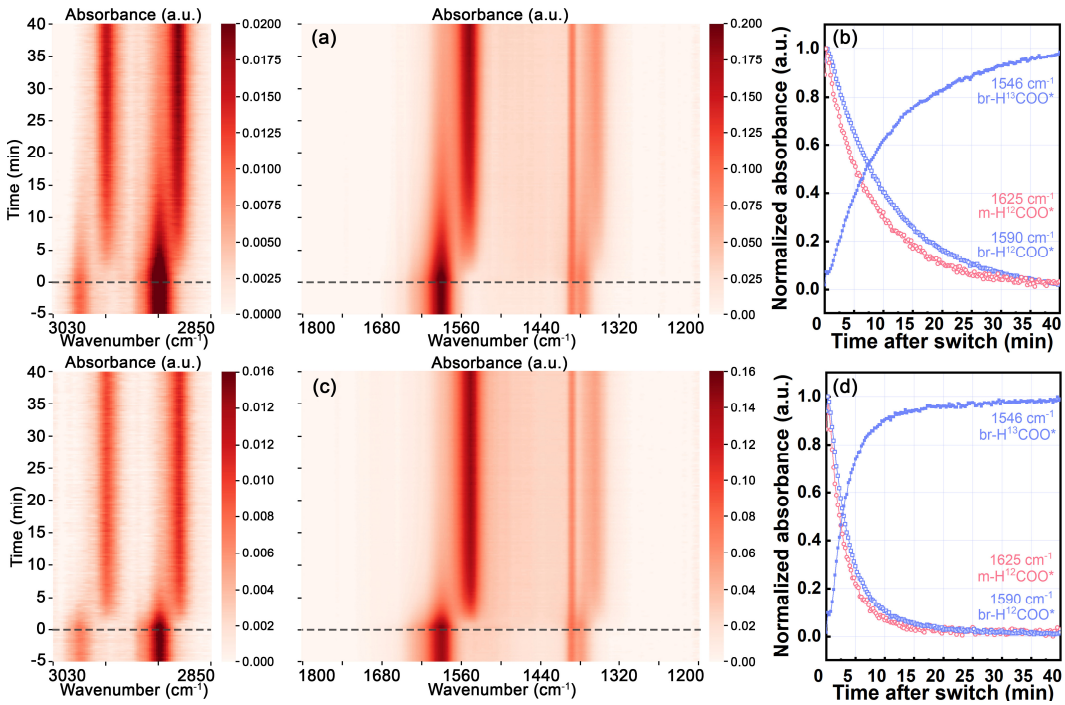

Figure 6.17. SSITKA-DRIFTS results of RWGS at 300 °C over Au/Al_2O_3-400. The SSITKA-DRIFTS contours in (a) dark and (c) green light irradiation. The corresponding intensity evolutions of m-HCOO* and br-HCOO* (b) in dark and (d) under green light irradiation.

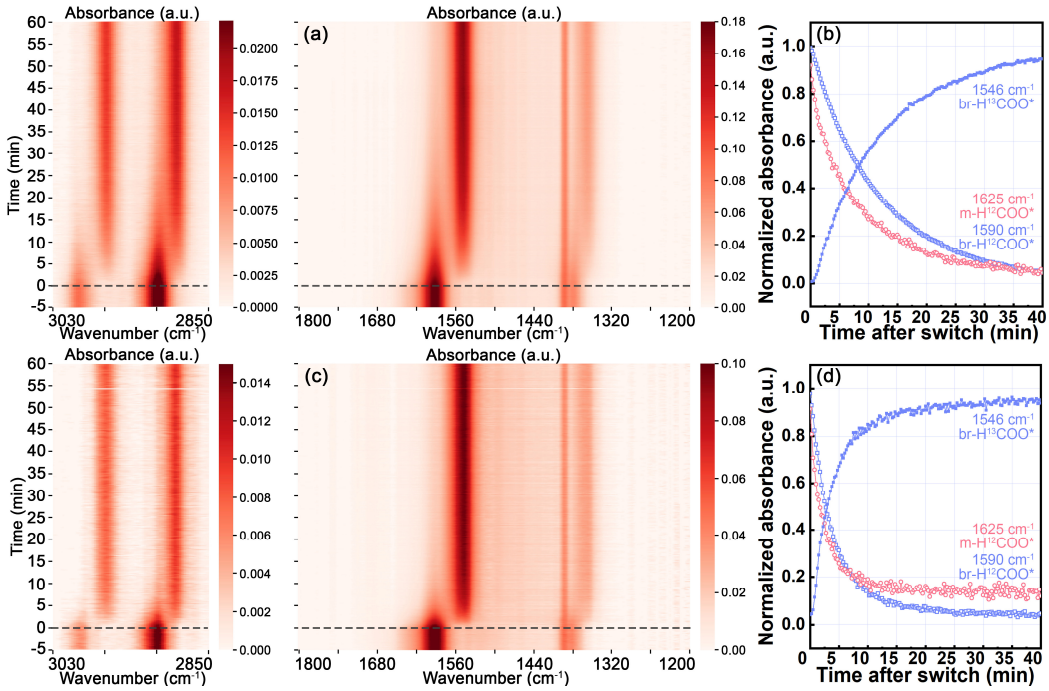

Figure 6.18. SSITKA-DRIFTS results of RWGS at 300 °C over Au/Al_2O_3-600. The SSITKA-DRIFTS spectra contours in (a) dark and (c) green light irradiation. The corresponding intensity evolutions of m-HCOO* and br-HCOO* (b) in dark and (d) under green light irradiation.

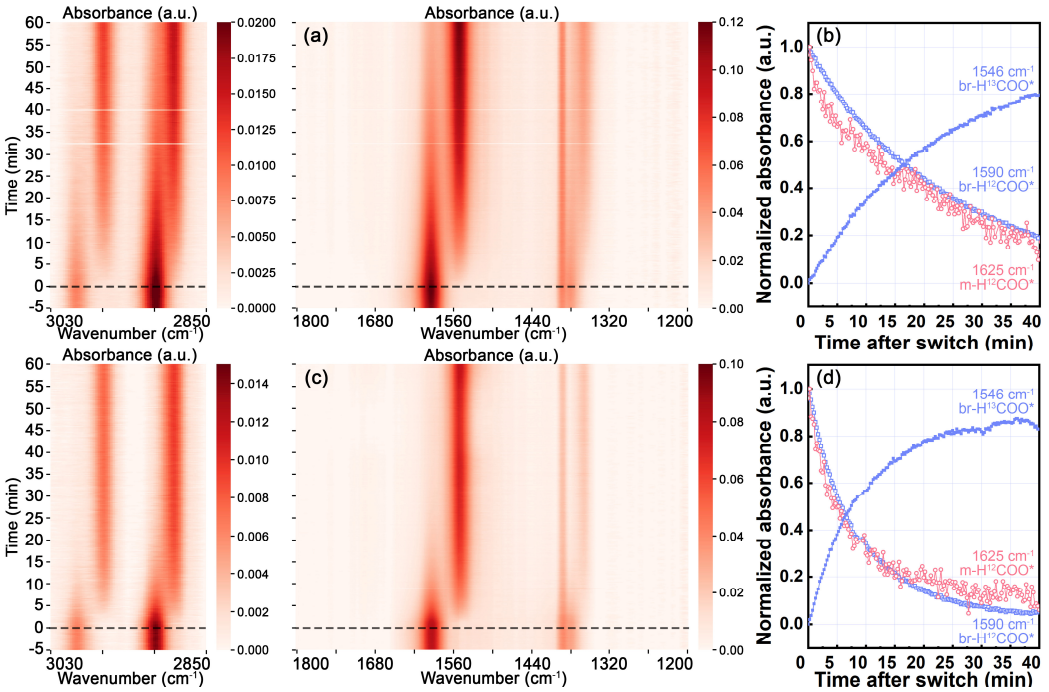

Figure 6.19. SSITKA-DRIFTS results of RWGS at 300 °C over Au/Al_2O_3-800. The SSITKA-DRIFTS spectra contours in (a) dark and (c) green light irradiation. The corresponding intensity evolutions of m-HCOO* and br-HCOO* (b) in dark and (d) under green light irradiation.

Table 6.3. Summaries of kinetic parameters derived from SSIKTA-DRIFTS experiments at 300 °C

Sample	Condition	GC	FTIR	
		CO yield (mmol g_{cat}^{-1} h^{-1})	$\tau_{br-HCOO^*}$ (min)	τ_{m-HCOO^*} (min)
Au/Al_2O_3-400	dark	0.47	11.04	8.74
	green	0.57	5.06	4.25
Au/Al_2O_3-600	dark	0.40	12.25	9.02
	green	0.60	5.17	4.30
Au/Al_2O_3-800	dark	0.17	26.65	24.67
	green	0.36	8.70	7.97

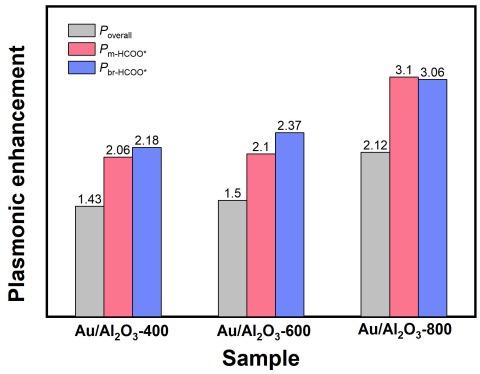

Figure 6.20. Plasmonic enhancement ratios on overall reaction rate, m-HCOO* and br-HCOO* kinetics.

6.3.4 H/D kinetic isotope effects and equilibrium isotope effects

KIE is an important kinetic method to shed light on reaction mechanism and the mechanism underpinning the plasmonic enhancement. As shown in **Figure 6.21**, the apparent KIEs are observed smaller than 1 both in dark or under green light irradiation at the temperature of 300 °C. Two results are worth emphases here: (1) Au/Al_2O_3-400 shows a less significant inverse KIE of 0.82 and 0.84 for dark or green-light promoted conditions. Comparatively, for larger Au NP size, the apparent inverse KIE becomes much more pronounced; (2) The green light irradiation results in larger apparent KIE values comparing with the counterparts in dark. The increases of apparent KIE values become greater on larger Au NPs. The larger KIE value under green light irradiation is a strong evidence of non-thermal effects of plasmonic enhancement. Because the heavier isotope is pushed less away from its equilibrium position than its lighter counterpart and gets less energy.[10, 22-23]

To determine the '*real*' KIE from the apparent one for the RDS interpretation, the EIE needs to be considered. The H/D EIE can be determined by comparing the concentration of HCO_3* and DCO_3* on catalysts surface. The detailed EIE determination procedure is described in the experimental section. The DRIFT spectra after reaching equilibrium are shown in **Figure 6.22**. Deuterated bicarbonate adsorbed on γ-Al_2O_3 has been reported to show IR peaks locating at 1659 and 1436 cm^{-1} corresponding to asymmetric and symmetric O-C-O vibrations, respectively.[24] For ν_s(O-C-O) mode, the vibration frequency is nearly free from the isotope effects, because this vibration mode doesn't involve isotope atom.[17, 25] The same principle applies to the corresponding extinction coefficient.[10] Therefore, EIE can be calculated by dividing the absorbance of ν_s(O-C-O) of HCO_3* by DCO_3*. Based on the spectra shown in **Figure 6.22**, the EIEs for different samples in dark and green light irradiation conditions are summarised in **Table 6.4**. After considering the EIE, the '*real*' KIE is proven to show a trend changing from insignificant for Au/Al_2O_3-400 to pronounced inverse for Au/Al_2O_3-800.

The reaction pathway and RDS can be interpreted based on the results above. The pronounced inverse KIE over Au/Al_2O_3-800 suggests the main reaction pathway is likely to be the COOH* pathway with COOH* formation as the RDS, which has also been reported in former investigations.[26-29] Comparatively, the insignificant KIE over Au/Al_2O_3-400 suggests the reaction mechanism is likely to be a combination of COOH* pathway and HCOO* pathway. The HCOO* pathway has been reported to show a normal KIE with its RDS of the dehydration step.[30-31] For reaction in dark, the inverse KIE becomes more pronounced from Au/Al_2O_3-400 to Au/Al_2O_3-800 indicate the contribution of HCOO* pathway to overall reaction rate drops when Au NPs becomes larger. In the case of reaction under green light irradiation, the KIE shifts from significant inverse to insignificant, which suggests the proportion of HCOO* pathway in overall reaction become larger due to plasmonic enhancements. The KIE value increasements also become more significant from Au/Al_2O_3-400 to Au/Al_2O_3-800, which agrees with the sequence of stronger LSPR effects on larger Au NPs. The evolution of formate and carboxyl mechanism contributions

to the overall reaction rate derived from KIE analyses are in consistent with the DRIFTS-SSIKTA analyses results in former section. The RDSs of formate and carboxyl pathways also agrees with our DFT calculation results, which will be further discussed in section 6.3.5.

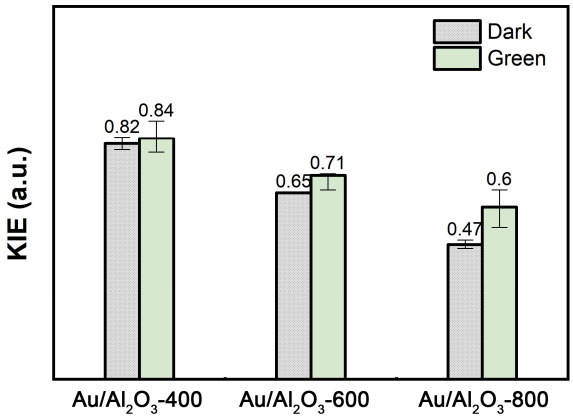

Figure 6.21. Apparent H/D kinetic isotope effects of RWGS over $Au/\gamma\text{-}Al_2O_3$ at different temperatures in dark or under green light irradiation.

Table 6.4. EIE values determined for different samples in dark or under green light irradiation

Sample	EIE in dark	EIE under green light irradiation
$Au/\gamma\text{-}Al_2O_3$-400	0.92	0.93
$Au/\gamma\text{-}Al_2O_3$-600	0.94	0.95
$Au/\gamma\text{-}Al_2O_3$-800	1.18	1.16

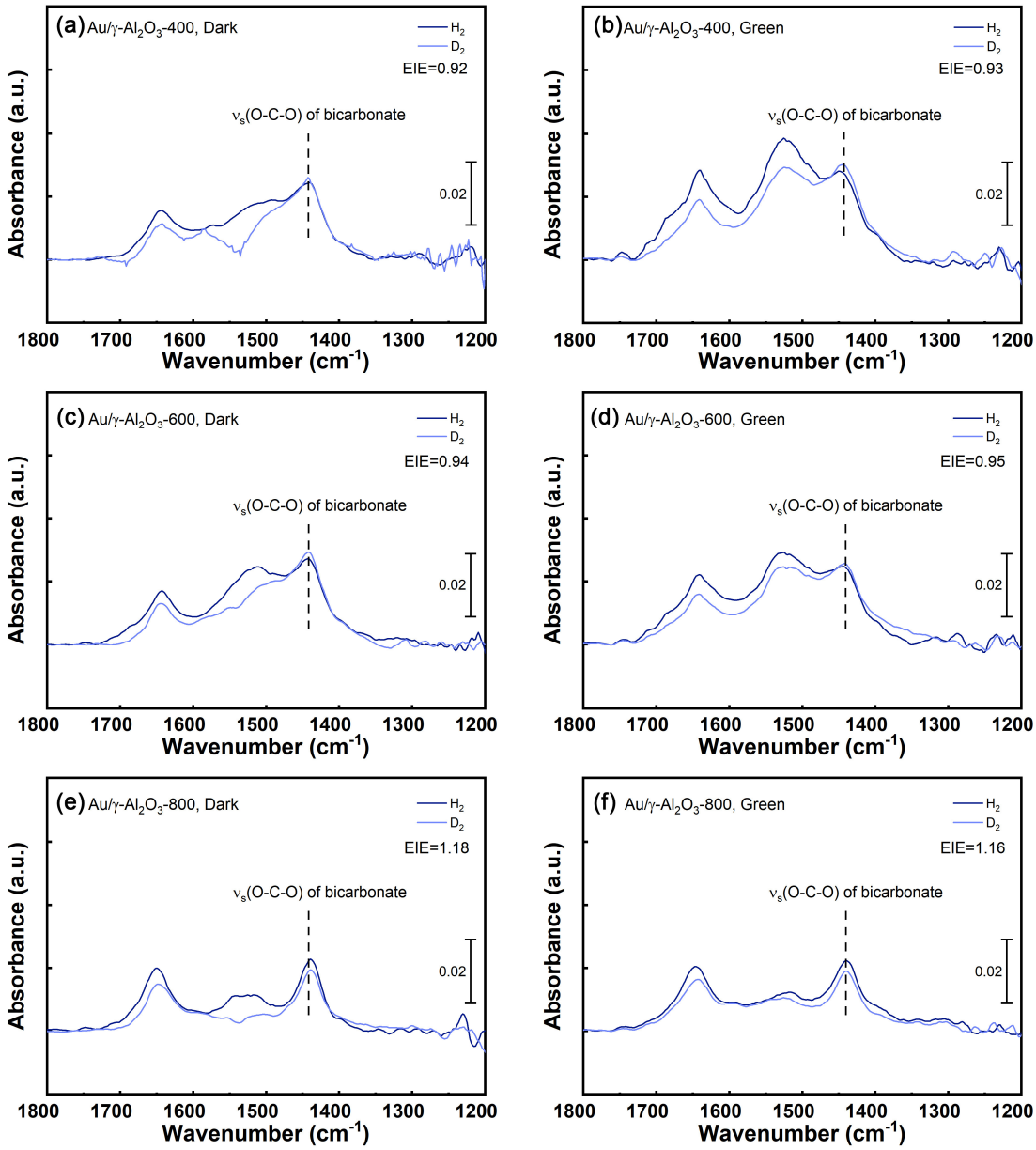

Figure 6.22. DRIFT spectra of H_2 or D_2 pre-treated $Au/\gamma\text{-}Al_2O_3$ after 20 min of CO_2 adsorption during the EIE determination experiments.

6.3.5 Theoretical calculation

The reaction pathway and plasmonic enhancement mechanism are further supported by the DFT calculation. Theoretical calculation can provide molecular level understanding, which is difficult for experiments.

6.3.5.1 Choice of supported cluster slab model

The γ-Al_2O_3 model used here is adopted from Digne et al.'s work.[32] The optimised bulk structure shows a *P*21/*m* space group symmetry and the lattice constants of a = 5.564 Å, b = 8.382 Å, c = 8.053 Å, α = γ = 90°, β = 90.57°. The calculated lattice constants are in high consistency with literature.[32-33] The (110) surface of γ-Al_2O_3 is found as the predominant facet with more than 70% of total surface area by experiments.[34] In addition, (110) surface also shows abundant tri-coordinate and four-coordinate Al (Al_{3C} and Al_{4C}) Lewis acid sites, which ensures its relatively high catalytic activity. Therefore, the slab model of γ-Al_2O_3 was built with dry (110) surface termination. The slab model is built in 2 × 2 supercell containing 4 Al-O layers, which consists 32 Al_2O_3 units and 160 atoms in total. A vacuum layer more than 18 Å was added above the top atoms on the surface. This periodic model shows lattice constants of 16.765, 16.106 and 23.0 Å along x, y, z axis, respectively. Bottom two layers were fixed during the relaxation to mimic the bulk effects. The optimised γ-Al_2O_3 (110) surface configuration is presented in **Figure 6.23**(a). For Au clusters in gas phase, the number of 13 is known as the magic number due to its higher stability. Therefore, it is widely used in DFT simulation to represent the supported Au cluster.[35-37] With icosahedral Au_{13} cluster as the starting configuration, *Ab initio* BOMD simulation in canonical (NVT) ensemble was used to investigate the stable configurations of Au_{13} cluster supported on γ-Al_2O_3 (110) surface. The BOMD was performed for 15 ps at the experimental calcination temperature of 673 K, which was controlled by a Berendsen thermostat. As shown in **Figure 6.23**(c), the system reaches equilibrium plateau after ~7 ps. 8 candidates were extracted from the equilibrated trajectory after 7 ps with a time interval of 1 ps and further relaxed at 0 K. The most stable Au_{13}/γ-Al_2O_3 configuration was determined by finding the configuration with the lowest energy (**Figure 6.23**(b)).

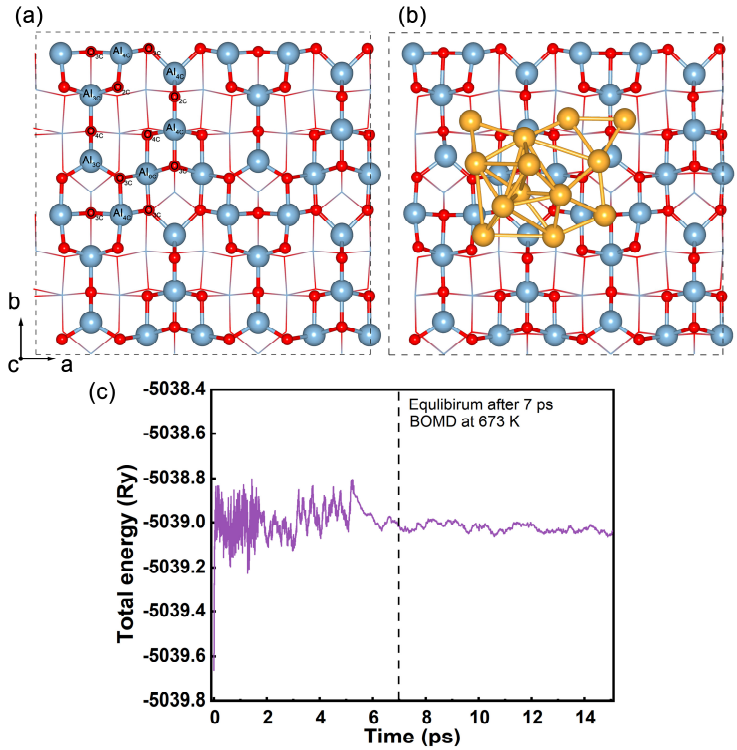

Figure 6.23. Optimised slab models of (a) γ-Al_2O_3 and (b) Au_{13}/γ-Al_2O_3 with (110) termination. (c) Energy evolution during the BOMD of Au_{13}/γ-Al_2O_3 slab model at 673 K. The blue, red, amber spheres represent Al, O and Au atoms, respectively.

6.3.5.2 Theoretical reaction mechanism investigation

There are two different kinds of CO_2* adsorbing at $Au/\gamma\text{-}Al_2O_3$ interface in monodentate and bridged configurations (m-CO_2* and br-CO_3*). The m-CO_2* and br-CO_3* function as the precursors to further form the m-HCOO* and br-HCOO* after adding an additional H*, respectively. The most energy-favourable m-CO_2* and br-CO_2* geometries are shown in **Figure 6.24** and the calculated CO_2 adsorption energies (E_{ad}) are -0.74 and -1.25 eV for m-CO_2* and br-CO_2*, respectively. The m-CO_2* adsorbs at the tricoordinate Al site (Al_{3C}), by contrast the br-CO_2* adsorbs at the interface with its two O atoms bonding with Al_{3C} and Al_{4C} (four-coordinated Al), respectively. The larger E_{ad} for br-CO_2* than m-CO_2* indicates the higher abundance of br-CO_2* than its counterpart m-CO_2*.

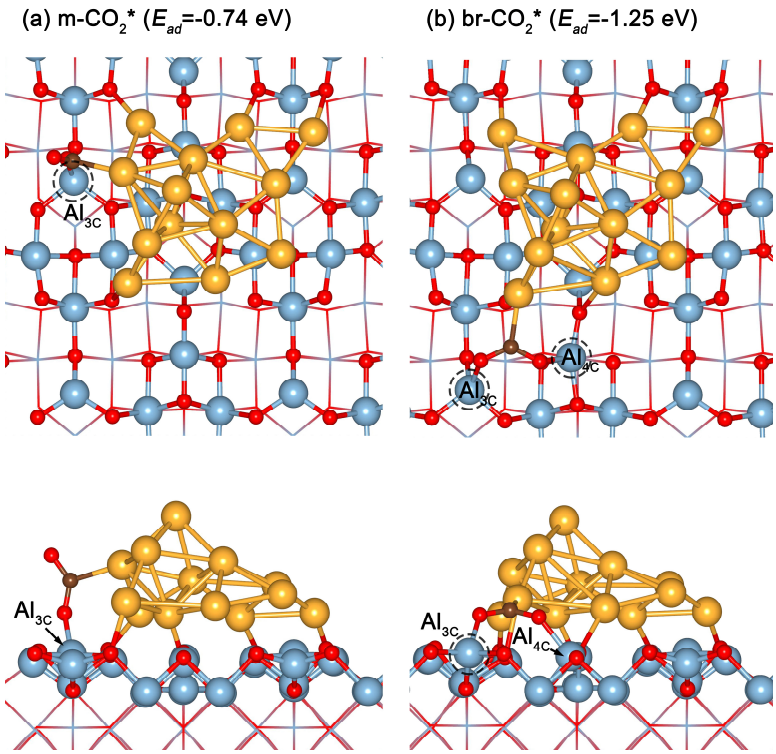

Figure 6.24. Geometries of (a) monodentate CO_2* (m-CO_2*) and (b) bridged CO_2* (br-CO_2*) in top and side views. The blue, red, amber, brown spheres represent Al, O, Au and C atoms, respectively.

Since the direct dissociation CO_2 mechanism is ruled out by experiments (**Figure 5.13** and **Figure 6.9**), the DFT calculation here focuses on the carboxyl and formate pathways. Based on the *in-situ* DRIFTS experimental results, the reaction pathways are categorised into monodentate formate/carboxyl and bridged formate/carboxyl pathways starting from m-CO_2* and br-CO_2* (**Figure 6.24**), respectively. The calculated reaction profiles are plotted in **Figure 6.25**(a, b) and the energetics are summarized in **Table 6.5** & **Table 6.6**. Whether reaction goes along formate or carboxyl pathways are determined by the first hydrogenation step of CO_2*. For m-CO_2*, the formation of monodentate trans-COOH* requires a high activation energy (E_a) of 1.38 eV; by contrast, the m-HCOO* only requires a smaller E_a of 0.65 eV after H* diffusion to the adjacent site of C with E_a of 0.74 eV. Similarly, the bridged trans-COOH* formed from br-CO_2* requires an even higher E_a of 1.74 eV and further transforms into bridged cis-COOH* with a small E_a of 0.16 eV; by contrast, the formation of br-HCOO* only requires an E_a of 0.53 eV.

Additionally, both m- and br-HCOO* are more stable than their COOH* counterparts by 0.93 and 1.19 eV, respectively. Therefore, it is energy-favourable to form HCOO* rather than COOH* over $Au_{13}/\gamma\text{-}Al_2O_3$ from both thermodynamic and kinetic perspectives.

Considering the full reaction profile, for COOH* pathways, the overall RDS is likely to be the elementary step of COOH* formation; Different from COOH*, the RDS for HCOO* pathway is the HCOO* decomposition to CO* and OH* for both monodentate and bridged configurations showing the E_a of 0.97 and 2.56 eV, respectively. The following H_2O* formation step for both monodentate and bridged configurations only show small E_a of 0.50 and 0.55 eV. The small E_a of formation and remarkably large E_a of decomposition make the br-HCOO* accumulate on the surface. On the contrary, the smallest overall E_a of m-HCOO* pathway makes it the most plausible candidate from the perspective of kinetics. It also explains the much higher IR peak observed for br-HCOO* than m-HCOO* in DRIFTS experiments (**Figure 6.14**, **Figure 6.15** and **Figure 6.16**).

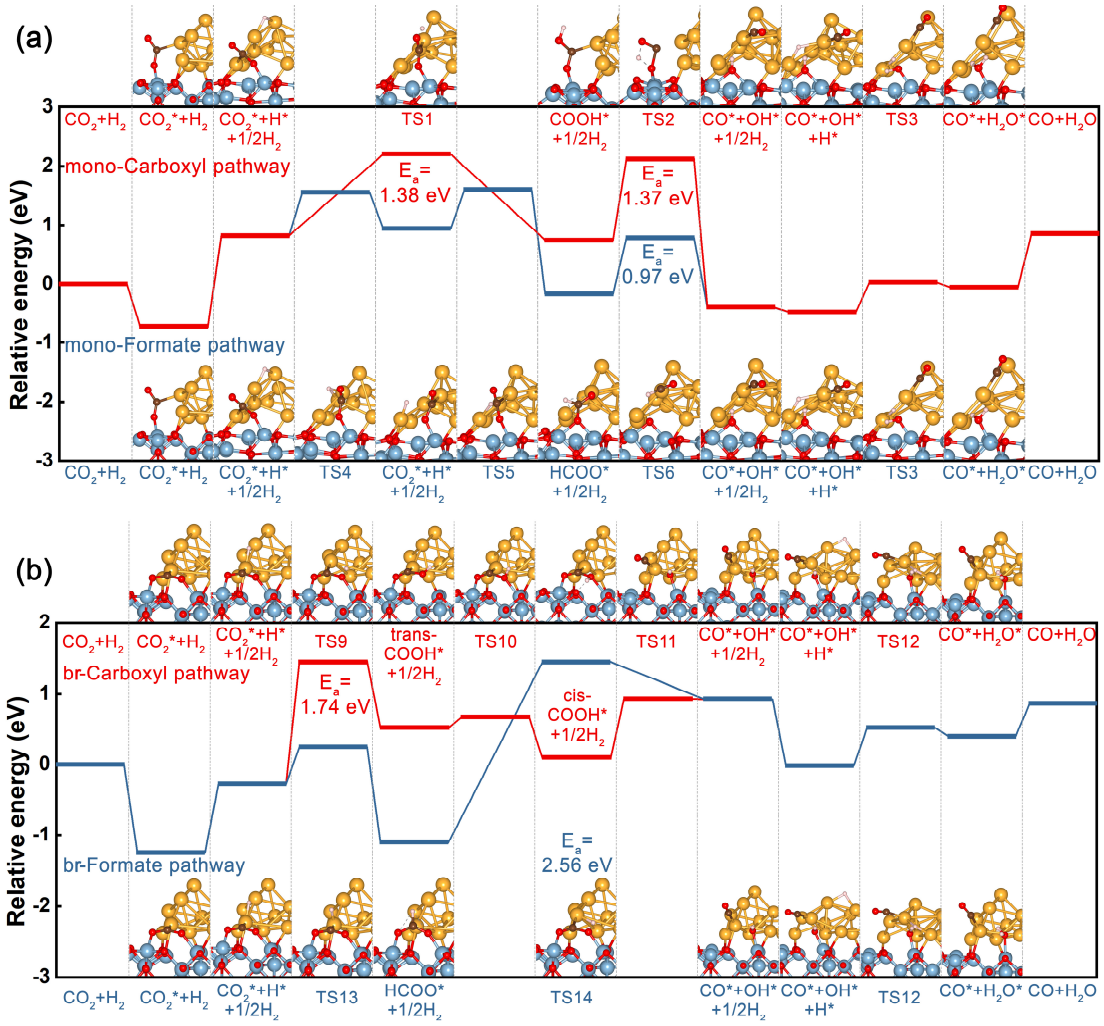

Figure 6.25. Calculated reaction profiles of (a) m-formate, m-carboxyl and (b) br-formate, br-carboxyl reaction pathways over $Au_{13}/\gamma\text{-}Al_2O_3(110)$. The calculated configurations of each elementary steps are presented at the top and bottom of the images. The activation energy (E_a) of RDS in their corresponding reaction pathway is also depicted in the plots. The blue, red, amber, brown and pink spheres represent Al, O, Au, C and H atoms, respectively.

Table 6.5. Energetics for reaction steps along m-formate and br-formate reaction pathways.

Reaction steps	m-formate pathway		br-formate pathway	
	Reaction energy (eV)	E_a (eV)	Reaction energy (eV)	E_a (eV)
$CO_2 + H_2 \rightarrow CO_2^* + H_2$	-0.74		-1.25	
$CO_2^* + H^* + 1/2\ H_2 \rightarrow CO_2^* + H^* + 1/2\ H_2$ (H^* diffusion on Au)	+0.13	+0.74		
$CO_2^* + H^* + 1/2\ H_2 \rightarrow HCOO^* + 1/2\ H_2$	-1.12	+0.65	-0.83	+0.53
$HCOO^* + 1/2\ H_2 \rightarrow CO^* + OH^* + 1/2\ H_2$	-0.23	+0.97	+2.03	+2.56
$CO^* + OH^* + H^* \rightarrow CO^* + H_2O^*$	+0.42	+0.49	+0.43	+0.55
$CO^* + H_2O^* \rightarrow CO + H_2O$	+0.91		+0.44	

Table 6.6. Energetics for reaction steps along m-carboxyl and br-carboxyl reaction pathways.

Reaction steps	m-carboxyl pathway		br-carboxyl pathway	
	Reaction energy (eV)	E_a (eV)	Reaction energy (eV)	E_a (eV)
$CO_2 + H_2 \rightarrow CO_2^* + H_2$	-0.74		-1.25	
$CO_2^* + H^* + 1/2\ H_2 \rightarrow$ trans-$COOH^* + 1/2\ H_2$	-0.07	+1.38	+0.79	+1.74
trans-$COOH^* + 1/2\ H_2 \rightarrow$ cis-$COOH^* + 1/2\ H_2$			-0.43	+0.16
$COOH^* + 1/2\ H_2 \rightarrow CO^* + OH^* + 1/2\ H_2$	-1.15	+1.37	+0.83	+0.85
$CO^* + OH^* + H^* \rightarrow CO^* + H_2O^*$	+0.42	+0.49	+0.43	+0.55
$CO^* + H_2O^* \rightarrow CO + H_2O$	+0.91		+0.44	

Electronic structure analyses can provide insights on plausible plasmonic hot electrons-induced enhancement. The PDOS plots of important surface species including CO_2*, HCOO* and COOH* in their monodentate and bridged configurations are presented in **Figure 6.26**(a, b) and **Figure 6.27**(a-d). The grey dash lines indicated the energy of 2.4 eV, which is the highest possible energy the plasmonic hot electron can achieve under 532 nm light irradiation. m-HCOO* shows nearly no unoccupied states above Fermi energy level (E_f); by contrast, there is a major C2p-O2p orbitals below the upper energy limit of 2.4 eV for br-HCOO*. The difference in electronic structure suggests the hot electrons are much more likely to inject into and activate the br-HCOO* than m-HCOO*. Since the further conversion of br-HCOO* is the plausible RDS for this reaction pathway, the plasmonic hot electron injection is likely to significantly enhance the overall reaction kinetics. There is no fundamental difference in electronic structures between m-CO_2*, br-CO_2*. Both of the two types of CO_2* are expected to be activated and the negatively charged CO_2* is more easily for further conversion,[38-39] which explains the lower formation temperature for br- and m-HCOO*. Similarly, both br-COOH* and m-COOH* are plausible to be activated by hot electron injection from the perspective of electronic structure. However, the RDS for carboxyl pathway is likely the formation rather the decomposition and unoccupied orbitals of CO_2* below 2.4 eV are in very small density (**Figure 6.27**(a, b)), which results in a weak excitation. Therefore, the plasmon-enhancement on COOH* pathway is less pronounced.

To further deduce how hot electron injection activates the br-HCOO* dehydration, the COHP analyses of O-Al bonds of br-HCOO* and m-HCOO* are plotted in **Figure 6.26**(c, d) with configurations shown in **Figure 6.26**(e, f), respectively. Since the bond population is presented in -COHP, the bonding and antibonding states are shown in right and left side of the plot, respectively. Note the C-O antibonding states of m-HCOO* located above 2.4 eV, the stability of m-HCOO* is expected less affected by hot electrons. On the contrary, in the case the br-HCOO*, the C-O shows much higher antibonding state populations than $O\text{-}Al_{4C}$, which are both underneath the 2.4 eV limit. The electronic structure of br-HCOO* suggests the plasmonic hot electron can much more efficiently activate the br-HCOO* dehydration than m-HCOO*.

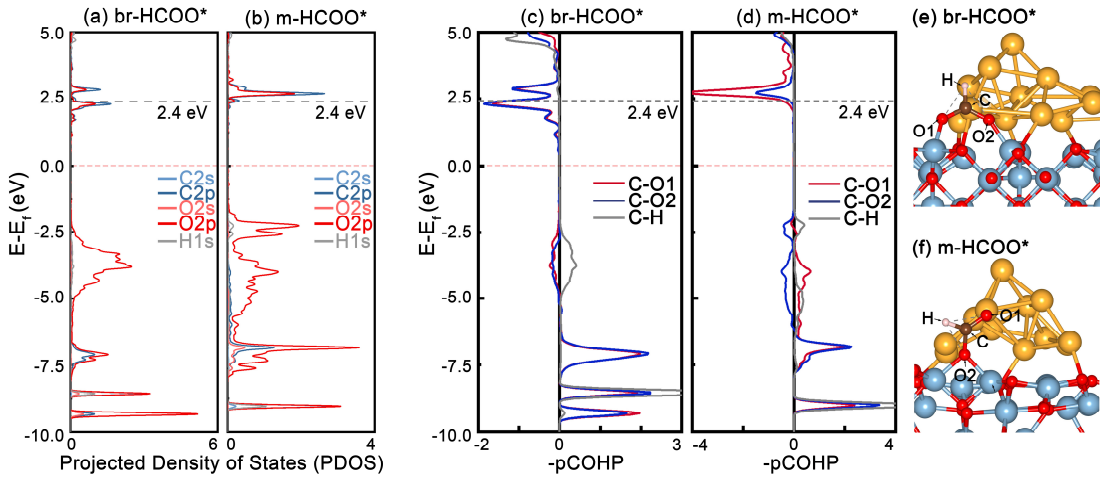

Figure 6.26. PDOS of reaction intermediates adsorbed on $Au_{13}/\gamma\text{-}Al_2O_3(110)$: (a) br-HCOO* and (b) m-HCOO*. Projected crystal orbital Hamilton population (pCOHP) analyses of (c) br-HCOO* and (d) m-HCOO*. The corresponding configurations of (e) br-HCOO* and (f) m-HCOO*. The blue, red, amber, brown and pink spheres represent Al, O, Au, C and H atoms, respectively. Since the spin-up and spin-down state/bond populations are similar, only spin-up curves are presented here.

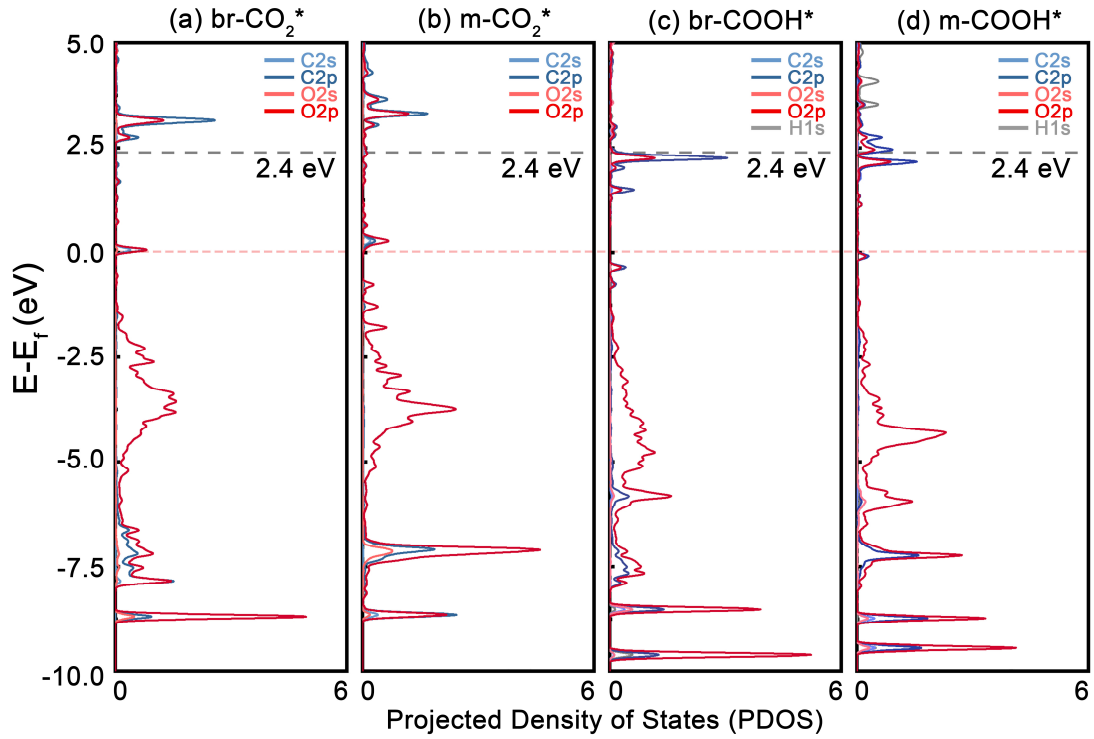

Figure 6.27. PDOS of reaction intermediates adsorbed on $Au_{13}/\gamma\text{-}Al_2O_3(110)$: (a) br-$CO_2$* and (b) m-$CO_2$*, (c) br-COOH* and (d) m-COOH*.

In summary, DFT calculation results suggest the RWGS reaction prefers to follow the formate pathway way over $Au/\gamma\text{-}Al_2O_3$ under both dark and light irradiation conditions. The limiting step for br-formate pathway is its decomposition to CO* and OH*. Comparatively, the m-HCOO* shows the smallest overall E_a, while its abundance is limited by thermodynamics. Under green light irradiation, the plasmon-excited electrons are more likely to inject into unoccupied orbitals of br-HCOO* than m-HCOO* and facilitate its further dehydration to CO*. Considering the model in DFT calculation can well represent the small Au clusters on Al_2O_3, these calculation results highly agree with the *in-situ* DRIFTS and SSITKA experimental results in dark and under green light irradiation over Au/Al_2O_3-400.

6.4 Summary

CO_2 hydrogenation reaction were investigated over Au/Al_2O_3 with different Au NPs sizes under pure thermal and photo-thermo coupled reaction conditions.

The smaller Au NPs shows higher reaction activity than larger Au NPs in dark. While under external green light irradiation, the plasmonic enhancement to thermal reaction is more significant over larger Au NPs. A maximum of 229% reaction rate enhancement is achieved by external light induced plasmonic effects. The reaction mechanisms are proven to be a combination of formate and carboxyl pathways via *in-situ* DRIFTS/SSITKA and KIE analyses. Moreover, the proportion of formate pathway contribution is higher on smaller Au NPs. Green light irradiation shows preferred promotion effects on formate intermediate kinetics. The main plasmon-thermo coupling mechanisms are likely to be hot electrons injection for smaller Au NPs and electromagnetic-field enhancement for larger Au NPs.

6.5 References

1. Giannozzi, P.; Andreussi, O.; Brumme, T.; Bunau, O.; Buongiorno Nardelli, M.; Calandra, M.; Car, R.; Cavazzoni, C.; Ceresoli, D.; Cococcioni, M.; Colonna, N.; Carnimeo, I.; Dal Corso, A.; de Gironcoli, S.; Delugas, P.; DiStasio, R. A.; Ferretti, A.; Floris, A.; Fratesi, G.; Fugallo, G.; Gebauer, R.; Gerstmann, U.; Giustino, F.; Gorni, T.; Jia, J.; Kawamura, M.; Ko, H. Y.; Kokalj, A.; Kucukbenli, E.; Lazzeri, M.; Marsili, M.; Marzari, N.; Mauri, F.; Nguyen, N. L.; Nguyen, H. V.; Otero-de-la-Roza, A.; Paulatto, L.; Ponce, S.; Rocca, D.; Sabatini, R.; Santra, B.; Schlipf, M.; Seitsonen, A. P.; Smogunov, A.; Timrov, I.; Thonhauser, T.; Umari, P.; Vast, N.; Wu, X.; Baroni, S., *J. Phys.: Condens. Matter* **2017,** 29 (46), 465901.
2. Perdew, J. P.; Burke, K.; Ernzerhof, M., *Phys. Rev. Lett.* **1996,** 77 (18), 3865-3868.
3. Grimme, S.; Antony, J.; Ehrlich, S.; Krieg, H., *J. Chem. Phys.* **2010,** 132 (15), 154104.
4. Dal Corso, A., *Comput. Mater. Sci.* **2014,** 95, 337-350.
5. Smidstrup, S.; Pedersen, A.; Stokbro, K.; Jonsson, H., *J. Chem. Phys.* **2014,** 140 (21), 214106.
6. Maintz, S.; Deringer, V. L.; Tchougreeff, A. L.; Dronskowski, R., *J. Comput. Chem.* **2016,** 37 (11), 1030-1035.
7. Momma, K.; Izumi, F., *J. Appl. Crystallogr.* **2011,** 44 (6), 1272-1276.
8. Rotole, J. A.; Sherwood, P. M. A., *Surf. Sci. Spectra* **1998,** 5 (1), 18-24.
9. Wang, K.; Lu, J.; Lu, Y.; Lau, C. H.; Zheng, Y.; Fan, X., *Appl. Catal., B* **2021,** 292, 120147.
10. Wang, K.; Cao, M.; Lu, J.; Lu, Y.; Lau, C. H.; Zheng, Y.; Fan, X., *Appl. Catal., B* **2021,** 296, 120341.
11. Bobadilla, L. F.; Santos, J. L.; Ivanova, S.; Odriozola, J. A.; Urakawa, A., *ACS Catal.* **2018,** 8 (8), 7455-7467.
12. Nelson, N. C.; Nguyen, M.-T.; Glezakou, V.-A.; Rousseau, R.; Szanyi, J., *Nat. Catal.* **2019,** 2 (10), 916-924.
13. Wang, X.; Shi, H.; Kwak, J. H.; Szanyi, J., *ACS Catal.* **2015,** 5 (11), 6337-6349.
14. Szanyi, J.; Kwak, J. H., *Phys. Chem. Chem. Phys.* **2014,** 16 (29), 15117-15125.
15. Baumgarten, E.; Zachos, A., *Spectrochim. Acta, Part A* **1981,** 37 (2), 93-98.
16. Busca, G.; Lorenzelli, V., *Mater. Chem.* **1982,** 7 (1), 89-126.

17. Baltrusaitis, J.; Jensen, J. H.; Grassian, V. H., *J. Phys. Chem. B* **2006,** 110 (24), 12005-12016.
18. Olympiou, G. G.; Kalamaras, C. M.; Zeinalipour-Yazdi, C. D.; Efstathiou, A. M., *Catal. Today* **2007,** 127 (1-4), 304-318.
19. Burch, R., *Phys. Chem. Chem. Phys.* **2006,** 8 (47), 5483-5500.
20. Meunier, F. C.; Tibiletti, D.; Goguet, A.; Shekhtman, S.; Hardacre, C.; Burch, R., *Catal. Today* **2007,** 126 (1-2), 143-147.
21. Seemala, B.; Therrien, A. J.; Lou, M.; Li, K.; Finzel, J. P.; Qi, J.; Nordlander, P.; Christopher, P., *ACS Energy Lett.* **2019,** 4 (8), 1803-1809.
22. Wang, Z. J.; Song, H.; Liu, H.; Ye, J., *Angew. Chem., Int. Ed.* **2020,** 59 (21), 8016-8035.
23. Christopher, P.; Xin, H.; Marimuthu, A.; Linic, S., *Nat. Mater.* **2012,** 11 (12), 1044-1050.
24. Zhao, K.; Wang, L.; Moioli, E.; Calizzi, M.; Züttel, A., *J. Phys. Chem. C* **2019,** 123 (14), 8785-8792.
25. Bernitt, D. L.; Hartman, K. O.; Hisatsune, I. C., *J. Chem. Phys.* **1965,** 42 (10), 3553-3558.
26. Yu, S.; Jain, P. K., *Angew. Chem., Int. Ed.* **2020,** 59 (50), 22480-22483.
27. Loiland, J. A.; Wulfers, M. J.; Marinkovic, N. S.; Lobo, R. F., *Catal. Sci. Technol.* **2016,** 6 (14), 5267-5279.
28. Karelovic, A.; Galdames, G.; Medina, J. C.; Yévenes, C.; Barra, Y.; Jiménez, R., *J. Catal.* **2019,** 369, 415-426.
29. Kunkes, E. L.; Studt, F.; Abild-Pedersen, F.; Schlögl, R.; Behrens, M., *J. Catal.* **2015,** 328, 43-48.
30. Kwon, S.; Lin, T. C.; Iglesia, E., *J. Catal.* **2020,** 383, 60-76.
31. Kwon, S.; Lin, T. C.; Iglesia, E., *J. Phys. Chem. C* **2020,** 124 (37), 20161-20174.
32. Digne, M.; Sautet, P.; Raybaud, P.; Euzen, P.; Toulhoat, H., *J. Catal.* **2002,** 211 (1), 1-5.
33. Digne, M., *J. Catal.* **2004,** 226 (1), 54-68.
34. Nortier, P.; Fourre, P.; Saad, A. B. M.; Saur, O.; Lavalley, J. C., *Appl. Catal.* **1990,** 61 (1), 141-160.
35. Liu, L.; Liu, Z.; Sun, H.; Zhao, X., *Appl. Surf. Sci.* **2017,** 399, 469-479.
36. Hong, S.; Rahman, T. S., *J. Am. Chem. Soc.* **2013,** 135 (20), 7629-7635.
37. Kim, H. Y.; Lee, H. M.; Henkelman, G., *J. Am. Chem. Soc.* **2012,** 134 (3), 1560-1570.
38. Taifan, W.; Boily, J.-F.; Baltrusaitis, J., *Surf. Sci. Rep.* **2016,** 71 (4), 595-671.
39. Wang, K.; Fu, J.; Zheng, Y., *Appl. Catal., B* **2019,** 254, 270-282.

Chapter 7. General Conclusion and Perspective

7.1 Conclusions

This thesis focuses on how the CO_2 reduction is driven by external light on the surface of promising catalysts. The key factors influencing CO_2 reduction performance are demonstrated. *In-situ* spectroscopy methods including *in-situ* UV-Vis DRS/DRIFTS, isotope kinetic analyses and DFT calculations were used to provide understandings and insights of the reaction mechanisms. Detailed conclusions are listed as follows:

(1) Increasing the CO_2 activation capability is the key to improve the activity of photocatalytic CO_2 reduction with H_2O. In Chapter 3, CO_2 photocatalytic reduction with H_2O was conducted over environmentally friendly g-C_3N_4 catalysts. Optimising the molecular and electronic structures of g-C_3N_4 by co-doping K, B and N_V can improve the photocatalytic CO_2 reduction to CO and CH_4 by 527% and 161%, respectively. A strong correlation has been found between activated $CO_2^{\cdot-}$ concentration on surface and photocatalytic CO_2 reduction rate. It suggests the design of g-C_3N_4 should aim to increase the amount of activated $CO_2^{\cdot-}$ adsorbing on the surface.

(2) The excitation mechanism shows significant effects on photocatalytic CO_2 reduction product selectivity. In Chapter 4, it is found the primary product of CO is formed by UV light-driven (bandgap excitation) CO_2 reduction with H_2O over Au/TiO_{2-x} with abundant V_O. By contrast, green light-driven (plasmonic excitation) CO_2 reduction over the same catalyst produces 20% C_2H_6. The *in-situ* IR spectroscopy of CO molecule probe adsorption experiments proves that the bandgap and plasmonic excitation result in negatively and positively charged Au NPs, which

determines the adsorption to the key reaction intermediate CO*. The stability of CO* determined the final product selectivity.

(3) CO_2 shows the dissociative adsorption on the V_O of Au/TiO_2. A series of *in-situ* DRIFTS and isotope kinetic analyses prove that the RWGS follows the redox pathway at 200 °C both in dark and under green light irradiation. On the contrary, the CO_2 hydrogenation to CO over Au supported by γ-Al_2O_3, a typical non-reducible support, is proven to follow a mixture of carboxyl and formate reaction mechanisms at 300 °C in dark and thermo-photo coupled reaction conditions.

(4) CO_2 hydrogenation to CO shows significantly higher activity over Au supported by reducible support (TiO_2) than Au supported by non-reducible support (γ-Al_2O_3) in pure thermocatalytic condition. It is due to the involvement of V_O of TiO_2 in the reaction. Additionally, the plasmonic enhancement is more pronounced over Au/TiO_2 than Au/Al_2O_3. It is attributed to the significantly higher efficiency of charge separation across Au/TiO_2 interface.

(5) The plasmonic enhancement shows preferential promotion on specific reaction intermediate and pathway. Moreover, the plasmonic enhancement mechanism to thermocatalytic RWGS is different over Au/TiO_2 and Au/Al_2O_3. For reducible TiO_2, the enhancement mechanism is largely ascribed to the ‘hot electron’ injected into TiO_2, which facilitates the V_O generation. By comparison, for non-reducible Al_2O_3, the ‘hot electrons’ primarily inject into the orbitals of adsorbed formate, which significantly accelerates the kinetics or formate reaction pathway.

7.2 Perspective

Pure photocatalytic CO_2 conversion has been investigated extensively over the last 30 years. The primary issue preventing the practical application in industry-scale is its slow reaction rate. Most of the reports with appealing

photocatalytic performance rely on the consumption of hole scavengers, which is not an economical or green strategy. To promote the reaction activity, one of the promising strategies is to introduce external green energy sources including but not limited to electric fields, magnetic fields, thermal fields etc.

Another general issue is the product selectivity of photocatalysis. How to further improve the selectivity to more desired products is believed to be a fascinating topic in the future. In the case of photocatalysis, the product selectivity is determined by two main factors: (a) incident light energy (thermodynamics) and (b) adsorption to key reaction intermediates (kinetics). From thermodynamics perspective, the incident light energy determines if the reaction for specific product is possible. However, majority of the excited electrons/holes possess the energy of CBM/VBM, which is independent from the incident light energy. Therefore, varying the incident light energy is a possible but not efficient way to alter the product selectivity. For the kinetics factor, it is very similar to the traditional thermocatalysis. The selectivity to specific product is largely affected by the adsorption to a specific key intermediate. Because the stability of the key intermediate determines the possibility of reaction pathways to the desired products. Since the adsorption to key reaction intermediate is mainly influenced by the composition of the catalysts (electronic structure), modifying and optimising the composition of the catalyst is still the most efficient way to alter the product selectivity. It is worth emphasizing that for photo-thermo coupled reaction condition the influence of incident light on product selectivity is a promising way to alter the product selectivity of traditional thermocatalysis. The effects of incident light on product selectivity alteration can be explained from two aspects: (i) the incident light will alter the electronic structure of the catalyst, which shows great influences to the adsorption of key reaction intermediates; (ii) the external light energy can promote the catalysts into excited states, which could activate some reaction pathways not feasible in pure thermocatalytic condition. In the specific case of CO_2 photocatalytic reduction with H_2O. There are still fundamental issues not fully resolved. H_2O is proven as a poor proton donor in this reaction, since it competes with CO_2 for excited electrons. Traditionally

believed proton generation mechanism, H_2O oxidation by photo-excited holes, are not fully persuasive. More investigations are recommended to work on the design of photocatalysts with better H_2O dissociation and proton supplying capabilities. Another issue regarding H_2O is the generation of O_2. As OH* or O* are highly affiliated to conventional photocatalysts surface, especially for sulphides, the generation of O_2 is indeed a sluggish elementary step with slow kinetics. In the worst situation, the surface of photocatalysts can be oxidised by these species, which causes the degradation of the performance.

The mechanism of photo-thermo coupled reaction is still at very early stage. Current researches usually prefer reporting the enhanced reaction activity while less attentions on the underpinning light enhancement mechanism. Suggestions are presented as follows on future works on this area.

Most of the researches including the works in this thesis use conventional powder catalysts. However, the UV-Vis light can only penetrate ~1 μm into the catalysts, which makes the most of the catalysts packed in the fixed bed not exposed to light irradiation. It is the main reason why the light enhancement cannot be accurately measured. The conventional way is to address this issue is to reduce the packing thickness of the catalysts. However, this method comes with an important trade-off of the low product yields.

It is still a great challenge to decouple the thermal effects and non-thermal effects of external light irradiation. Possibly the best way is to use pulsed laser in fs scale. However, it can only be afforded by very few catalysis research groups. I believe in the near future, an unambiguous consensus on the clear decoupling of thermal and non-thermal effects are hardly achieved. For future investigations, it will be the best to focus on the effects of external light on the product selectivity changes. If external light irradiation can alter the selectivity while elevating the temperature can’t, it will be both scientifically and practically valuable.

Further optimising the setup for photo-thermo coupled reaction is another key topic for future researches. An ideal setup is supposed to show the following

features: (i) catalysts are in a thin layer structure ensuring all the catalysts can be equally excited by incident light and thermal field; (ii) *in-situ* temperature measurement with high accuracy. The accurate measurement of catalysts temperature is indispensable for decoupling thermal and nonthermal effects. The prevailing method to measure the temperature with thermocouple in literature shows obvious shortage of accuracy. For future setup design, *in-situ* spectroscopy thermometry method is a promising way to simultaneously elucidate the information on temperature as well as reaction mechanism; (iii) the optimised gas diffusion and interaction with catalysts. Since the catalysts are supposed to be in thin-layer format, the engineering of the reactor needs to be conducted. The optimal reactor will be likely to contain microchannels to ensures a long enough interaction time between reactants and catalysts. (iv) light source with homogenous output spatial distribution. It will ensure a consistent light-induced temperature contribution. Polarized light source is promising for more insightful mechanism investigation. (v) Products quantitative analyses with high sensitivity. Since the catalysts are supposed to be in an ultrathin layer structure, the loading per unit area is relatively low resulting a low conversion. Microchannel reactor engineering can partially solve this issue. While using high-sensitive universal detectors such as BID, HID etc. will definitely benefit to a more comprehensive investigation.

This thesis has demonstrated the external light irradiation will preferentially promote specific reaction intermediates and reaction pathways. The “hot carriers” related promotion can be clearly explained by the electronic structures, which is usually in high consistent with the experimental results. However, the enhancement caused by intensified electromagnetic field is far less clearly understood by either experimental or theoretical approaches. Future works on investigating the correlation of enhanced electromagnetic field, molecular configuration of reaction intermediate and preferentially promoted reaction rate are highly attractive.

Ab-initio calculation is an excellent way that can help to interpret the experimental results at the molecular level. It can provide invaluable insights

on the reaction pathway and electronic structure of reactants/intermediates. While most of the researches including the works in this thesis in this area still rely on the calculation at ground state, which cannot represent the real external light-irradiated reaction condition in excitation states. Especially for reaction pathway calculation, the excitation state reaction pathway could be different from the ground state. In recent years, several emerging methods have been reported to reduce the excitation-state calculation cost to make it practical on larger systems. It is extremely important for heterogeneous catalysis investigations, because both the transition metal clusters and the transition metal oxides supports function in the reaction. Such techniques include embedded CASSCF, Δ-SCF-DFT, Nonadiabatic MD, TDDFT-MD etc.